THE PENNSYLVANIA STATE UNIVERSITY
SCHREYER HONORS COLLEGE

DEPARTMENT OF BIOENGINEERING

FLUID DYNAMIC STUDY OF THE FDA BENCHMARK MODEL UNDER PULSATILE FLOW

JOSHUA KESSLER
SUMMER 2017

A thesis
submitted in partial fulfillment
of the requirements
for baccalaureate degrees
in Biomedical Engineering and Mechanical Engineering
with honors in Bioengineering

Reviewed and approved* by the following:

Keefe Manning
Professor of Bioengineering and Surgery
Thesis Supervisor

William Hancock
Professor of Biomedical Engineering
Honors Advisor and Faculty Reader

Peter Butler
Professor of Biomedical Engineering
Faculty Reader

* Signatures are on file in the Schreyer Honors College.
The Pennsylvania State University

ABSTRACT

Pulsatile flow through a simplified benchmark model was analyzed as a part of the FDA's Critical Path Initiative, which intends to evaluate the accuracy of computational fluid dynamics (CFD) in the study of medical devices. The benchmark nozzle model mimics the flow characteristics of common medical devices. In one orientation, the model consists of a rapid contraction followed by a narrowed throat region and a conical diffuser. In the other orientation, the model comprises a gradual contraction followed by a narrow throat and a sudden expansion, from which flow exits as a jet with significant areas of recirculation. The *in vitro* data collected using the benchmark model provides a reliable method for validating CFD simulations. Of particular significance is the validation of Reynolds shear stresses, which are used to predict blood damage. Laser Doppler velocimetry (LDV) was used to collect two-component velocity data within the benchmark model under pulsatile flow at locations with pertinent flow characteristics. The measured velocities were used to calculate principal Reynolds stresses, maximum Reynolds shear stresses, turbulence intensities, viscous shear stresses, and wall shear stresses during mid-acceleration, systole, mid-deceleration, and diastole. Axial velocities during systole were compared with previous data taken using LDV. Shear stresses near the wall of the nozzle throat, at the boundary of the free shear layer within the conical diffuser and downstream of the sudden expansion, and within the recirculation regions during diastole exceeded accepted thresholds for the onset of hemolysis, indicating that the model geometry may induce blood damage under certain flow conditions. Combined with the results of previous studies of the benchmark model, the results presented in this study indicate that the model provides a useful comparison for computational simulations that seek to predict hemolysis in medical devices.

TABLE OF CONTENTS

LIST OF FIGURES

LIST OF TABLES

ACKNOWLEDGEMENTS

I would like to thank each member of my thesis committee for providing the time and guidance to ensure that this thesis was a success: Dr. Keefe B. Manning, Dr. William O. Hancock, and Dr. Peter J. Butler. In particular, I would like to thank my thesis advisor, Dr. Keefe Manning, for providing all of the time, patience, and guidance that was necessary for me to complete this work.

I would also like to thank my family and friends for the constant support that they have provided through this experience. My parents, Dr. Steven Kessler and Lisa Kessler, and my brother, Eli Kessler, have provided the love and support that has been necessary to lift me through the writing of this thesis and college in general. It goes without saying, but I would not have accomplished anything without them.

I would also like to thank all of the professors within the Biomedical Engineering department and the Mechanical Engineering department for teaching me so much over the past five years, and for preparing me for the world ahead. I would also like to recognize the entire staff of the Biomedical Engineering department, and Dr. Cheng Dong in particular, for leading the department and helping it to thrive. Additionally, I would like to express my appreciation for Erin Ammerman, Gene Gerber, and Gary Meyers, who have helped me solve more problems than I can count. Finally, I would like to thank all the members of the Artificial Heart and Cardiovascular Fluid Dynamics Lab for their assistance, particularly Josh Taylor, Bryan Good, Grant Rowlands, Jeremy Myslowski, Josh Riley, and Tice Harkins.

Chapter 1

Introduction

1.1 Clinical Background

Cardiovascular disease is the leading cause of death in the United States, responsible for 31.9% of all deaths in 2010 [1]. A large number of diseases fall within the designation of cardiovascular disease, many of which are individually significant. Coronary heart disease alone accounts for one out of every six deaths, and strokes account for one out of every nineteen deaths [1]. Mitral valve diseases such as mitral valve prolapse occur in 5% of the population [2]. The annual incidence of pulmonary embolism is between 300,000 to 600,000 cases, with a 30-day mortality rate of 10%-20% [3]. These diseases, along with all other cardiovascular diseases, account for nearly 800,000 deaths annually [4].

To address this monumental health concern, companies are developing new medical devices that can potentially extend longevity. For example, patients with advanced heart failure are successfully receiving ventricular assist devices that can extend their lifetime by as much as 3.7 years [5]. Another successful device is the sirolimus-eluting Bx Velocity stent, which had a four-year survival rate of 97%, but still a 13% incidence of major cardiovascular events [6]. Similarly effectual technologies include vena cava filters [7] and bioprosthetic aortic valves [8], among others.

Many devices that treat cardiovascular disease come into direct contact with blood, disturbing the hemodynamics and presenting an acute risk for certain complications such as thrombosis and hemolysis. The CardioWest Total Artificial Heart is a noteworthy example of a device that presents significant blood complications. Although it is highly successful, resulting in a 70% one-year survival rate compared to a 31% survival rate in the control group [9], it often induces anemia in patients due to hemolysis, or damage of red blood cells. In addition, it can cause ineffective erythropoiesis and increase inflammation [10].

Other examples of complications induced by medical devices are the HeartMate II left ventricular assist device (LVAD), for which the most common failure mode is thrombosis, leading to a mortality rate without treatment of 48.2% [11]. In addition, patients with the HeartMate II frequently exhibit acquired von Willebrand syndrome, which leads to severe gastrointestinal bleeding [12]. Similarly, prosthetic mitral valves present a risk of thrombosis [13], the MicroMed Debakey LVAD causes elevated levels of platelet activation [14].

1.2 Blood Damage and Hemolysis

Implantable medical devices present an acute risk of several complications including humoral dyscrasias, hemolysis, thrombosis, infection, inflammation, and transient immunal compromise [15]. Hemolysis, the destruction of red blood cells, results in the release of hemoglobin into the blood plasma, reducing the blood's capacity to transport oxygen and resulting in anemia. Hemolysis occurs because of the magnitude of shear stress acting on an erythrocyte and the cell's exposure time to that stress. A plot from Chandran *et al.* illustrating the effect of shear stress and exposure time on hemolysis and platelet activation is given in Figure 1. As shown in the figure, platelet activation has a similar dependence on shear stress and exposure time. Hemolysis and platelet activation can occur at relatively low shear stresses given a long enough exposure time, or can occur during very short time durations given a high enough shear stress [16].

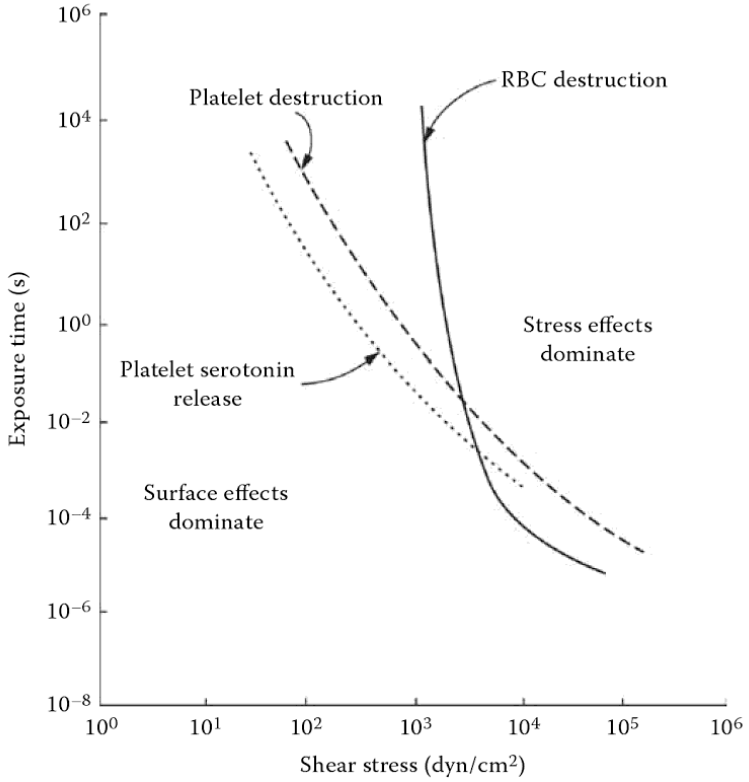

Figure 1. Shear stress vs. Exposure Time Plot of Hemolysis and Platelet Destruction, Adapted from Chandran *et al.* [16]

A number of studies have sought to determine the Reynolds shear stress threshold necessary to induce hemolysis. In one study by Sallam and Hwang [17], a laser Doppler anemometer system was used to obtain shear stress values, and free-hemoglobin was measured to assess hemolysis. This study found that hemolysis occurred when cells were exposed to a Reynolds shear stress of 400 Pa at an exposure time of 1 ms. For comparison, shear stress values in the human body during normal circulation are around 10 Pa [18]. This value was obtained using a one-component laser Doppler anemometer system, and the major Reynolds principal shear stresses were not used to determine the value [19]. Another assessment of Sallam and Hwang's data by Grigioni *et al.* [20] determined that the 400 Pa threshold was likely underestimated, and used a 3D stress analysis to estimate that the hemolytic threshold is 600 Pa. In a subsequent assessment by Lu *et al.* [19], which used a two-component laser Doppler anemometer system

and calculated the major principal Reynolds shear stress, the reevaluated threshold for hemolysis was 800 Pa at an exposure time of 1 ms.

In another study, erythrocytes were fixed using glutaraldehyde fixation as the shear stress was gradually increased, allowing for the examination of changes in cell shape. The hemolytic threshold established using this method was 250 Pa for an exposure time of four minutes. In addition, it was found that the destruction of erythrocytes was dependent upon the kinematics of the shear flow. In Couette flows with smaller gaps, deformation was greater for the same ranges of shear stress. The study also found that fragmentation of red blood cells appeared to occur in the bulk flow rather than near the walls [21].

Leverett *et al.* [22] used a rotational viscometer to induce hemolysis, and found that the threshold for hemolysis was 150 Pa at an exposure time of 10^2 seconds. The study also found that hemolysis did not depend on the surface-to-volume ratio of the viscometer, indicating that blood damage does not result from interaction of the cells with walls of the test apparatus.

Nevaril *et al.* [18] subjected erythrocytes to shear stress, pressure variation, and direct impact of solid surfaces. Pressure variation appeared to have little impact on hemolysis. Impact of cells with solid surfaces was evaluated using the Starr-Edwards valve. Hemolysis increased with increasing force, but hemolysis levels reached an asymptotic value at 3 pounds of force. Finally, using a concentric cylinder viscometer to induce shear stress, the study found that the threshold for hemolysis occurs at 150 Pa for an exposure time of two minutes. In addition, the measured level of hemolysis was independent of the blood viscosity.

Other studies have found higher thresholds for hemolysis when exposure times were significantly shorter. In a study conducted by Forstrom [23] using a jet fragility test, the onset of hemolysis was 4000 Pa for an exposure time of 10^{-6} seconds.

The shear stress values and exposure times necessary to induce hemolysis are summarized in Table 1.

Table 1. Shear Stresses and Exposure Times Necessary to Induce Hemolysis

	Shear Stress (Pa)	Exposure Time (s)
Leverett *et al.* [22]	150	10^2
Nevaril *et al.* [18]	150	10^2
Sutera and Mehrjardi [21]	250	10^2
Sallam and Hwang [17]	400	10^{-3}
Grigioni *et al.* [20]	600	10^{-3}
Lu *et al.* [19]	800	10^{-3}
Forstrom [23]	4000	10^{-6}

1.3 Modeling Blood Damage

As demonstrated in the previous studies, hemolysis occurs in erythrocytes due to a combination of shear stress and exposure time [22], causing damage to the cell membrane and the release of hemoglobin [24]. The total damage accrued by an erythrocyte depends on both the current level of damage and the damage that has accumulated over the entire lifetime of the cell [24]. The most common model of hemolysis is a power law function given by Equation 1, where D is the damage fraction of a cell, τ is the shear stress, t is the exposure time, and α and β are constants [25].

$$D = Ct^{\alpha}\tau^{\beta} \quad (1)$$

Various computational simulations have implemented Equation 1 using either Eulerian or Lagrangian coordinates. Using the Eulerian approach, a damage index is integrated over the domain of cells [24], as in the approach taken by Garon and Farinas given by Equations 2 and 3. In these equations, D_I is the linear damage function, σ is the rate of hemolysis production per unit time, and the constants are

determined experimentally. Comparing numerical results using this approach with experimental results for hemodialysis cannulas yielded fairly good agreement [26].

$$\frac{d}{dt}D_I = \left(\frac{\partial}{\partial t} + \bar{u} * \nabla\right) D_I = \sigma \quad (2)$$

$$\sigma = (3.62 * 10^{-7})^{1/0.785} \tau^{2.416/0.785} \quad (3)$$

Grigioni *et al.* employed a Lagrangian approach to track an erythrocyte moving along a fluid pathline. Accounting for the load history of the cell, Grigioni et al. arrived at Equation 4 to describe blood damage, where BDI is the blood damage index, and a, b, and C are constants. The trends predicted by this model match experimental data [27]. Although Grigioni et al. had success used the Lagrangian approach to predict hemolysis, this approach encounters computational issues obtaining pathlines at near-zero velocities and in recirculation regions, and it does not necessarily consider the entire flow field [24].

$$d(BDI) = Ca\left(\int_{t_0}^{t} t(\xi)^{b/a} d\xi + D(t_0)\right)^{a-1} \tau(t)^{b/a} dt \quad (4)$$

Another complication that has arisen due to biomedical devices is platelet activation, which can lead to the formation of blood clots [24]. Alemu and Bluestein modeled the platelet damage index, given by Equation 5, which measures the total damage sustained by the platelet due to varying stress levels. The damage index includes the initial damage accumulation, the stress loading history, and the dependence on the loading rate. In this equation, *D* is the damage index representing the level of platelet activation and damage, σ is the scalar stress value, *k* is the turbulent kinetic energy, and *r* and σ_0 are nonlinear characteristic constants [28].

$$\dot{D}(t) = \left(\frac{\sigma}{\sigma_0}\right)^r \frac{1}{[1-D(t)]^k} \quad (5)$$

Using these models, it may be possible to predict hemolysis and platelet activation in biomedical devices. This insight would allow engineers to improve the design of implantable devices, reducing the risk of blood complications and increasing patient longevity.

1.4 Standard Hemolysis Experimental Models

Continuum-based models are the most common method for experimental study of hemolysis [29]. Two prominent models based on the power law given by Equation 6 are Heuser and Opitz [30] for porcine blood and Giersiepen *et al.* [25] for human blood. IH is the index of hemolysis, t is the exposure time, τ is the shear stress, and α and β are constants. These models were based on experimental data consisting of shear stress ranging from 57-255 Pa and exposure time ranging from 7-700 ms.

$$IH = t^{\alpha}\tau^{\beta} \quad (6)$$

Other studies have found that this model over-predicts hemolysis by a factor of 25 [31]. The model has also been used to study changes in hemolysis rates as a result of medical devices. Goubergrits and Affeld used computational fluid dynamics to predict that the Bjork-Shiley mechanical heart valve increased the hemolysis index by 7% [31].

Another model developed by Arora *et al.* [32] examines the strain on individual blood cells and correlates it to an experimental steady flow blood damage data. The erythrocytes are modeled as droplets, and the model includes phenomena such as tank-treading and ellipsoidal deformation. The model agrees well with experimental data in simple shear flow. The study then applies the model in the examination of hemolysis in the Gyro blood pump, finding that blood cells in regions of highly fluctuating shear stress do not undergo significant damage. In addition, the model predicts that conical centrifugal pumps with

constant shear stress result in higher levels of hemolysis than vaned centrifugal pumps, which cause erythrocytes to undergo long periods of low shear stress with occasional periods of high shear stress [32].

In a study by Arvand *et al.* [33], rather than using path-line stress/strain characteristics, mean values for shear stress, exposure time, and other important factors were calculated in order to develop a power law equation defined by mean blood damage characteristics. Unknown values were determined using regression analysis and experimentally determined hemolytic curves. Predictions calculated with this model were validated using *in vitro* hemolysis indices for multiple pump configurations using the MicoDiagonal Pump, and the predicted results agreed well with the experimental data [33].

Finally, Chen and Sharp [34] developed a constitutive model relating hemolysis to fluid stresses. The data necessary to define the constitutive relation were derived from an experiment using a small chamber and Poiseuille flow. Red blood cells were passed through the chamber, and shear stress was calculated with a derivative of Equation 7, where v is the cell velocity, $\bar{v}$ is the mean velocity, H is the half height of the channel, W is the half width of the channel, and $y^{"}$ is the distance from the cell's centroid to the center of the channel. A viscoelastic membrane model was then developed to predict the strain exerted on an erythrocyte. The results obtained from this model provide predictions at a larger range of stresses and exposure times and better predict experimental results than the power law models outlined earlier [34].

$$\frac{v}{\bar{v}} = \frac{48}{\pi^3}\frac{\sum_{i=1,3,5\ldots}(-1)^{(i-1)/2}\left[1-\frac{\cosh\left(\frac{i\pi y^{"}}{2H}\right)}{\cosh\left(\frac{i\pi W}{2H}\right)}\right]i^{-3}}{1-\frac{192H}{\pi^5 W}\sum_{i=1,3,5\ldots}\frac{\tanh\left(\frac{i\pi W}{2H}\right)}{i^5}} \tag{7}$$

1.5 FDA Benchmark Nozzle Model and Steady Experiments

If the predictions produced by computational fluid dynamics (CFD) are inaccurate, they may lead to faulty conclusions and incorrect design-related decisions. To prevent this risk, it is crucial that the results of CFD are rigorously and comprehensively validated. Therefore, the Food and Drug Administration (FDA) initiated a multilaboratory study to systematically validate the use of CFD [35]. This study was included in the Critical Path Initiative, which is the FDA's "strategy to drive innovation in the scientific processes through which medical products are developed, evaluated, and manufactured" [36].

In order to compare experimental results with computational results, a benchmark nozzle model was developed. This model shares many characteristics with common blood-carrying medical devices including blood tubing, hemodialysis sets, and catheters [37]. The geometry of the benchmark nozzle model, shown in Figure 2, includes areas of contraction, expansion, flow recirculation, and local high shear stresses. Using the flow direction shown in Figure 2, the nozzle model acts as a conical concentrator followed by a sudden expansion (SE). Reversing the flow direction, the nozzle model then resembles a sudden contraction followed by a conical diffuser (CD). Thus, the design of the model enables the analysis of four flow geometries. In addition, the geometry is simple enough to allow for CFD analysis [35].

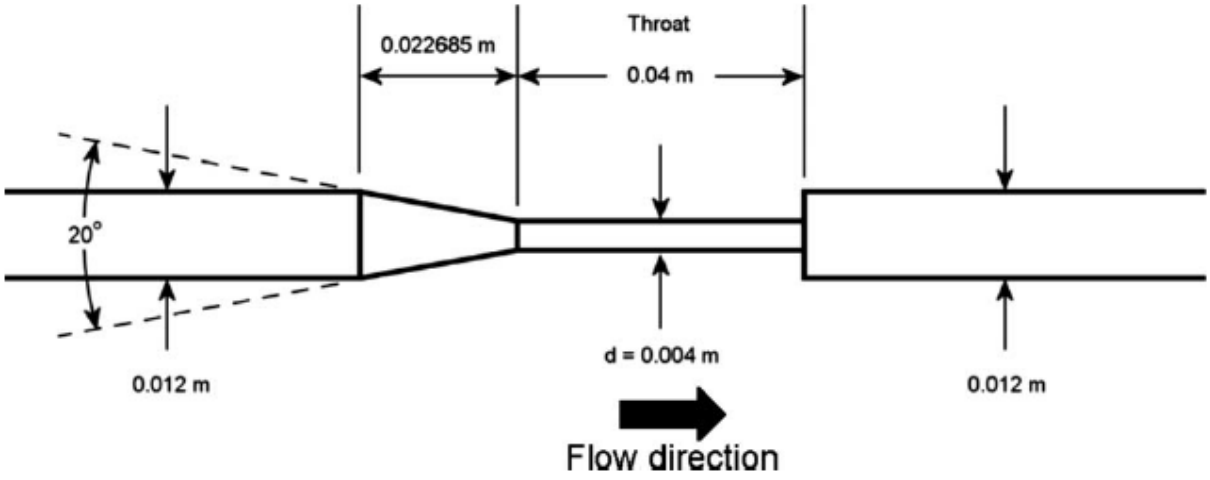

Figure 2. Dimensioned benchmark nozzle model [35]

In the conical diffuser configuration, the flow encounters a continuously varying adverse pressure gradient. This configuration is relevant for devices in which flow decelerates. Conversely, flow entering the conical concentrator models devices in which flow accelerates. In addition, the sudden contraction models implants that contain orifices such as gaps between heart valve leaflets. Upstream of the sudden contraction, it is difficult to predict wall shear stress values, which are important for the calculation of hemolysis. Thus, the prediction of wall shear stress in the regions of flow upstream of the sudden contraction provides a worthwhile assessment of the accuracy of CFD [38]. Finally, flow exiting the sudden expansion separates from the wall, introducing regions of recirculation and forming a reattachment site downstream before returning to fully developed flow. Flow through the sudden expansion models fluid exiting a stenosis or another similar geometry, after which recirculation regions develop [39].

To thoroughly validate the current state of CFD, experimental *in vitro* data were compared with computational data. To collect experimental data, three research groups measured steady flow through the benchmark nozzle model using particle image velocimetry (PIV). The goals of these groups were to develop a standard operating protocol for performing PIV measurements to validate CFD simulations, to

present aspects of the measured data that deserved further evaluation, and to disseminate these data to the scientific community for use in future CFD validation studies. The standard operating procedure successfully minimized user error and interlaboratory bias by controlling model orientation, fluid temperature, fluid properties, cavitation effects, and boundary conditions. For laminar and turbulent flow regimes, the variance in velocity measurements was ~10%. In the transitional flow regime, the velocity measurements varied more, agreeing by ~15% at the entrance, conical concentrator, throat, and sudden expansion regions of the model. The centerline velocity measurements near the reattachment region had an uncertainty of ~60%, primarily due to differences in reattachment length in the transitional regime. The cause of variation between laboratories was due to differences in fluid properties, flow rate, PIV algorithms, and inlet boundary conditions [35].

Alongside the experimental groups, twenty-eight research groups from around the world conducted computational studies for five flow rates that include laminar, transitional, and turbulent flow regimes [37]. The computational results showed significantly more variation than the experimental results, with a standard deviation greater than 60% of the mean value, and just four of the twenty-eight studies falling within the confidence interval of the experimental data [35]. For the laminar flow regime (Re_t = 500), most laminar simulations fell within $CI_{95\%}$ of the experimental values. In the transitional flow regime (Re_t = 500), just one simulation using the k-ω model fit within the $CI_{95\%}$ of the PIV data. For the turbulent flow regime, none of the simulation models fell within the confidence interval obtained experimentally. Overall, no single turbulence model was demonstrably more accurate than any of the others. Several sources of error among the computational groups include turbulence model underestimations of velocity measurements in certain regions, along with inability to accurately predict velocity and shear stress measurements in recirculation regions. This wide variation, particularly among wall shear-stress distributions, casts doubt on the ability of CFD to accurately model blood damage [37].

1.6 Study Objective

Alongside the original study commissioned by the FDA, additional studies are necessary to validate other conditions such as pulsatility, secondary flows, and short or curved inlets and outlets [37]. The work presented here examines the case of pulsatile flow through the original benchmark model using the standard operating protocol developed previously. Axial and radial velocity data are obtained at pertinent cross sections in the flow, from which viscous shear stresses, turbulent Reynolds stresses, and turbulence intensities are calculated. The results of the study are made available for comparison with computational simulations to evaluate the capability of CFD to accurately predict pulsatile fluid flow through medical devices.

Chapter 2

Fluid Dynamics of Nozzle Model

2.1 Sudden Expansions

The benchmark nozzle model can be oriented in two directions. In the sudden expansion orientation, the model geometry changes abruptly from a smaller sectional area to a larger sectional area, as demonstrated in Figure 3. At point 1, the incoming wall shear layer separates, developing a free shear layer downstream of the sudden expansion. The free shear layer then reattaches at some point downstream of the sudden expansion. Following the point of reattachment, the flow continues to decelerate until fully developed flow is reached. Flow entrapment in the free shear layer forms a primary recirculation zone, with the flow moving in the upstream direction near the wall at a velocity of 10-20% of the inlet velocity. A smaller secondary vortex is also formed near the corner. The distance x_{r1} is determined by the entrainment rate and the growth of the shear layer, which depend on whether the shear layer is laminar or turbulent [40].

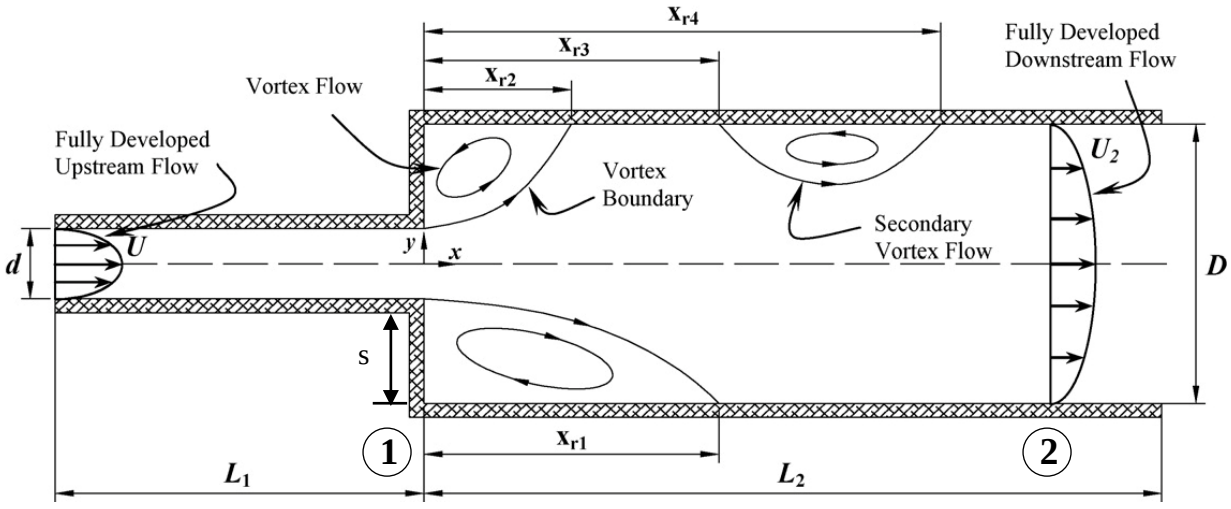

Figure 3. Flow Through a Sudden Expansion, adapted from Rocha *et al.* [41]

In a symmetric planar sudden expansion, at low Reynolds numbers, the flow is symmetric about the central axis, and the separation zones are similar in size. However, at higher Reynolds numbers, the flow becomes asymmetric, with one separation zone significantly larger than the other. In addition, at higher Reynolds numbers, additional separation zones occur further downstream [42]. In axisymmetric flows, the separation zone following the sudden expansion is nearly axisymmetric, and the reattachment length is a linear function of the Reynolds number for a D/d ratio of 4:1 [43].

The transition of the shear layer from laminar to turbulent is a function of the Reynolds number. For $Re_h < 570$ the shear layer is laminar, for $570 < Re_h < 3170$ the shear layer is transitional, and for $Re_h > 3170$ the shear layer is fully turbulent [44]. Once the shear layer is fully turbulent, its reattachment length becomes independent of the Reynolds number, and instead fluctuates about a mean value. Turbulence intensity and turbulent shear stress increase as the shear layer develops, and reach a maximum value near the reattachment point [40].

A Bordan-Carnot analysis is used to obtain the pressure rise across a sudden expansion. Neglecting shear at the walls and assuming that the static pressure is uniform across both planes, Equation 8 can be used to predict the pressure rise, where AR is the area ratio. The pressure reaches a steady value approximately 20 step sizes downstream (given by dimension *s* in Figure 3) of the sudden expansion, well after the reattachment zone [40].

$$\frac{(p_1 - p_2)}{\frac{1}{2}\rho {U_1}^2} = \left(\frac{2}{AR}\right)\left(1 - \frac{1}{AR}\right) \quad (8)$$

A study conducted by Smyth [45] examined turbulence intensities upstream and downstream of a sudden expansion using tap water and a Reynolds number of 30,210. As shown in Figure 4a, upstream of the sudden expansion turbulence intensities were maximum near the walls. Figures 4b and 4c show the turbulence intensities downstream of the sudden expansion. Within those regions, the turbulence intensity at the center of the duct reached a minimum value of 0.065, rising to a maximum value of approximately 0.195 at the boundary of the free shear layer before dropping again closer to the walls. In the figure, x is the distance downstream of the sudden expansion, y is the distance radially from the center of the duct, L

is the duct height downstream of the step, and $\sqrt{u^2}/U_0$ is the streamwise turbulence intensity. Farther downstream of the sudden expansion, the turbulence intensity curves begin to resemble curves observed during fully developed flow, where the turbulence intensity is at its minimum near the center of the duct and reaches its maximum value near the walls. The shear stress in the region downstream of the sudden expansion follows a similar trend; it is negligible near the center of the duct, and increases to its maximum value at the edge of the recirculation zone. The minimum recorded shear stress was -15 x 10^{-3} of U_0^2, where U_0 is the mean inlet velocity. Farther downstream of the sudden expansion, the shear stress curve becomes more flat, remaining low across the entire cross section.

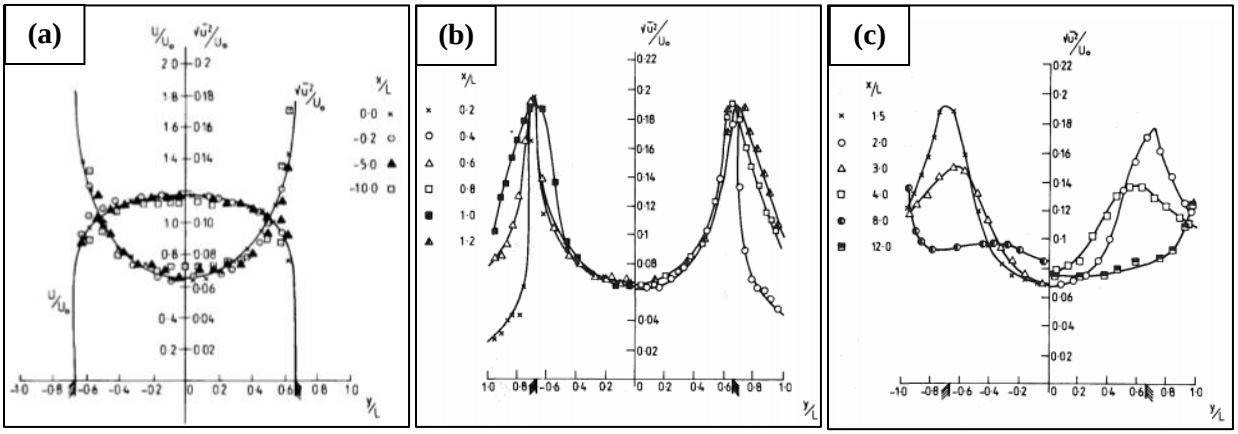

Figure 4. (a) Streamwise Velocity and Turbulence Intensity Upstream of Sudden Expansion, (b) Turbulence Intensity Downstream of Sudden Expansion, and (c) Turbulence Intensity Far Downstream of Sudden Expansion, Adapted from Smyth [45]

2.2 Diffusers

Diffusers, also known as diverging ducts, consist of a gradual expansion in cross sectional area, which causes fluid velocity to decrease and the static pressure to increase (also known as pressure recovery). Thus, diffusers are frequently used to convert kinetic energy to pressure [46]. As the fluid decelerates and produces a rise in pressure, the wall shear layer undergoes an adverse pressure gradient. This pressure gradient causes the wall boundary layer to thicken and separate from the diffuser walls, which creates areas of regurgitant flow. This formation of areas of regurgitant flow creates a blockage of

the flow area, reducing the effective flow area and thus reducing the pressure rise through the diffuser [46].

The type of diffuser geometry in the benchmark nozzle model is a conical diffuser, shown in Figure 5. The diffuser inlet, also called the diffuser throat, is the location at which the geometry begins to expand [46]. The diffuser outlet is the location where the gradual expansion ends.

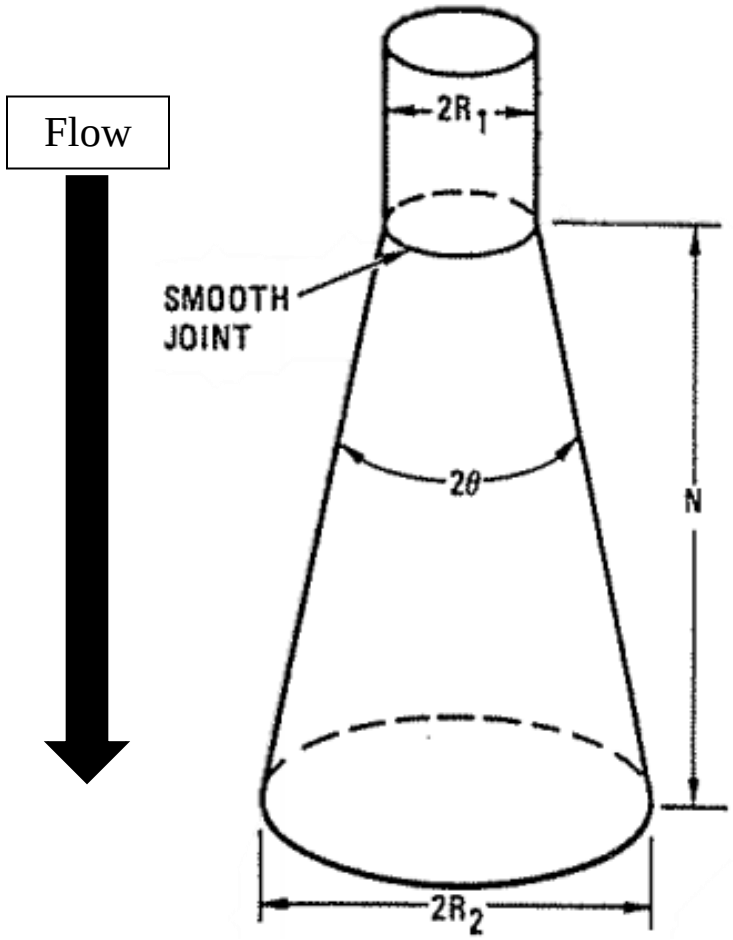

Figure 5. Conical Diffuser Geometry, adapted from the *Applied Fluid Dynamics Handbook* [47]

Since mass is conserved along the diffuser, it follows that the decrease in velocity is proportional to the ratio of the inlet to outlet areas. The rise in static pressure is given by the Bernoulli equation, Equation 9, where P_t is the total pressure, P_s is the static pressure, and $\frac{1}{2}\rho {V_1}^2$ is the dynamic pressure. The

static pressure remains constant from the inlet to the outlet, so as the velocity decreases, the static pressure must increase. Static pressure acts perpendicularly to the streamlines and is a measure of the thermal energy of the fluid [48].

$$P_{t1} = P_{s1} + \frac{1}{2}\rho {V_1}^2 = P_{s2} + \frac{1}{2}\rho {V_2}^2 = P_{t2} \quad (9)$$

Several dimensionless parameters are useful in describing conical diffusers. The first is the area ratio, or *AR*, which is the ratio of diffuser exit to inlet areas. *AR* measures the theoretical pressure recovery expected from the diffuser. The next parameter is the dimensionless diffuser length, which is defined as N/R_1. The third parameter is the wall divergence angle, 2θ. Equation 10 relates these three parameters [46].

$$AR = \left(1 + \left(N/R_1\right)\tan\theta\right)^2 \quad (10)$$

Diffuser performance is given by the pressure recovery coefficient, C_p, given by Equation 11, where p_e is the exit pressure, p_i is the inlet pressure, ρ is the density, and U_i is the mean inlet velocity. Note that this equation only holds for uniform inlet and outlet pressures; a similar equation using mean inlet and outlet pressures is necessary for non-uniform pressure distributions [46].

$$C_p = \frac{p_e - p_i}{\frac{1}{2}\rho {U_i}^2} \quad (11)$$

The ideal pressure recovery C_{pi}, given by Equation 12, is the maximum pressure recovery possible for a diffuser assuming inviscid flow, where *AR* is the aspect ratio. The diffuser effectiveness η is a measure of diffuser performance and is given by Equation 13 [46].

$$C_{pi} = 1 - 1/AR^2 \quad (12)$$

$$\eta = C_p/C_{pi} \quad (13)$$

Assuming that the velocity profile at the inlet is flat and the boundary layer is thin, Equation 14 gives the pressure loss coefficient, which measures the total pressure loss through the diffuser.

$$\zeta = C_{pi} - C_p \quad (14)$$

Diffuser performance is determined by the inlet wall boundary layer. Turbulent inlet boundary layers result in better performance, as they can sustain a longer adverse pressure gradient and thus a greater pressure rise. If the duct leading to the diffuser is long enough for fully developed flow to develop, then for Re > 10^4, the inlet flow is turbulent. If the duct is not long enough for fully developed flow to develop, then the Reynolds number must be higher for the inlet flow to be turbulent [46]. The most effective parameter used to correlate the inlet boundary layer with diffuser performance is the blockage parameter B, defined by Equation 15, where U is the average velocity and U_c is the maximum velocity [49]. In general, increasing blockage reduces the diffuser performance [46].

$$B = 1 - {}^{U}/_{U_c} \tag{15}$$

A study by Okwuobi and Azad [50] examined turbulence intensities in a conical diffuser with a Reynolds number of 293,000. The normalized turbulence intensities in the streamwise direction are shown in Figure 6, where y/R is the distance from the wall, ${}^{\overline{u_1}}/_{U_*}$ is the axial normalized turbulence intensity, and the numbers 1-10 above the curves indicate increasing distance from the diffuser inlet. The results show that the peak turbulence intensity is near the wall at the diffuser inlet, and moves outward toward the center of the flow in the streamwise direction. In addition, turbulence intensities increase in value farther from the diffuser inlet. The station reference is taken upstream of the diffuser inlet, and the turbulence intensities at that location are nearly flat.

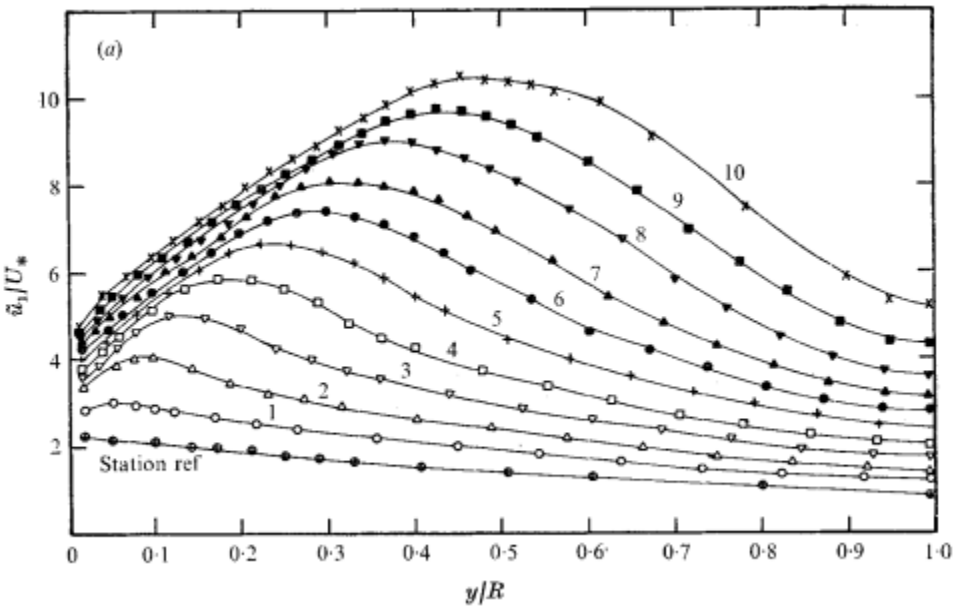

Figure 6. Turbulence Intensity Distribution, Adapted from Okwuobi and Azad [50]

2.3 Turbulent Flow

Unsteady turbulent flow can lead to hemolysis and thrombus formation in the circulatory system. Blood damage due to turbulence is related to the magnitude of Reynolds stresses [51].

Turbulent flow consists of random fluctuations in flow parameters. Figure 7 shows the random fluctuations in velocity in a turbulent flow in the x_1 and x_2 directions. The instantaneous velocity is $\tilde{u}_i$, the mean velocity is U_i, and the fluctuating velocity is u_i [52].

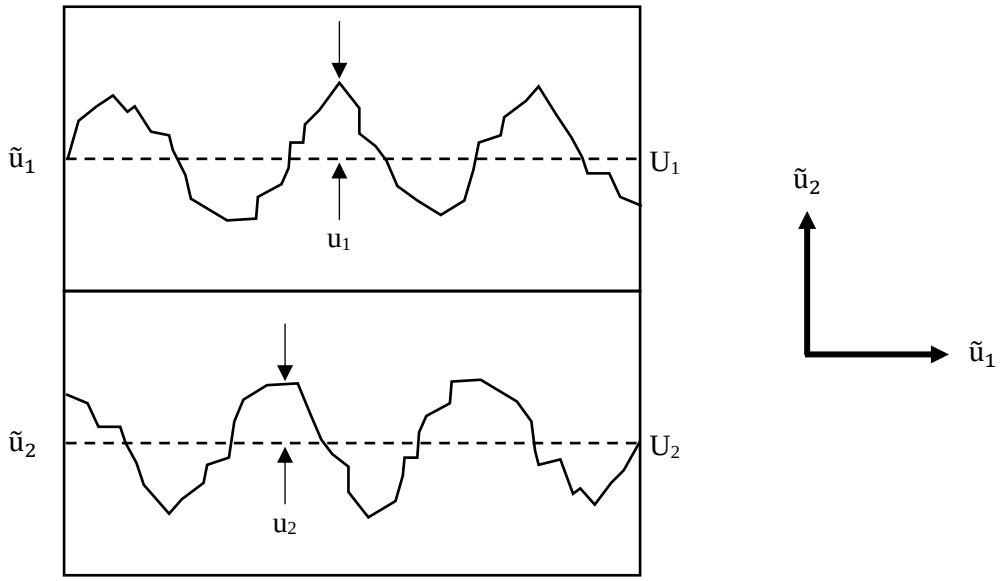

Figure 7. Turbulent Flow

Statistical methods are necessary to study the randomness of turbulent flow. Using the Reynolds decomposition technique, the instantaneous velocity can be written as a function of the mean and fluctuating velocities, shown in Equation 16 [52].

$$\tilde{u}_i = U_i + u_i \tag{16}$$

The root-mean-square (rms) velocity, given by Equation 17, measures the magnitude of velocity fluctuations in one direction. Highly turbulent flows have significant rms velocities in at least one direction [52].

$$u_{i,rms} = \sqrt{\overline{u_i^2}} \tag{17}$$

2.3.1 Reynolds Stresses

Reynolds stresses result from the mixing of fluid in the direction transverse to the flow direction. Fluid that originates in a low-velocity zone near the viscous sublayer and moves into a higher-velocity zone in the bulk flow decelerates fluid in the higher-velocity zone. Similarly, higher velocity fluid swept

into a region of lower velocity accelerates the lower velocity fluid. Although this process is a momentum exchange phenomenon, it has the same effect on the fluid as applying a shear stress. Thus, these "stresses" are known as apparent shear stresses or Reynolds stresses [53].

For flows with steady mean velocities, Reynolds decomposition can be used to average the Navier-Stokes equations, generating the Reynolds momentum equation given by Equation 18. $\sum ij$ and S_{ij} are given by Equations 19 and 20, respectively. ρ is the fluid density, P is the mean pressure, μ is the fluid viscosity, δ_{ij} is the Kronecker delta function, and U_i, U_j, u_i, u_j, x_i, and x_j are the velocities and directions described by Figure 7 [54].

$$U_j \frac{\partial U_i}{\partial x_j} = \frac{1}{\rho} \frac{\partial}{\partial x_j} \left(\sum ij - \overline{\rho u_\iota u_j} \right) \tag{18}$$

$$\sum ij = -P\delta_{ij} + 2\mu S_{ij} \tag{19}$$

$$S_{ij} = \frac{1}{2} \left[\frac{\partial U_i}{\partial x_j} + \frac{\partial U_j}{\partial x_i} \right] \tag{20}$$

Equation 17 is identical to the Navier-Stokes equation for laminar flow, but with the extra term $-\overline{\rho u_\iota u_j}$, which is the Reynolds stress tensor. The off-diagonal elements ($-\overline{\rho u_\iota u_j}$; $i \neq j$) are the six Reynolds shear stresses (RSS), and the diagonal elements ($-\overline{\rho u_\iota u_\iota}$) are the three Reynolds normal stresses (RNS). Simultaneous measurements are necessary in the *i* and *j* directions to calculate Reynolds shear stresses [52]. Equation 21 gives the Reynolds stress tensor for two-dimensional flow. The tensor is symmetric, so the off-diagonal components are equivalent and are equal to the Reynolds shear stress [55].

$$\begin{bmatrix} -\rho\overline{u^2} & -\rho\overline{uv} \\ -\rho\overline{uv} & -\rho\overline{v^2} \end{bmatrix} \tag{21}$$

Since the Reynolds stress is the rate of mean momentum transfer by turbulent fluctuations, the Reynolds shear stress $\rho_0 \overline{u_\iota u_j}$ can be thought of as the average flux of j-momentum in the i-direction, or as the average flux of i-momentum in the j-direction [55].

The Reynolds decomposition method has been used to calculate the rms velocities and Reynolds stresses in turbulent flows using an ensemble average of the velocity in a period of flow over a large

number of cycles [56]. The mean velocity can be calculated using Equation 22, where U' is the mean velocity, N is the number of measurements, and $\widetilde{u'}_n$ is the measured velocity. A similar calculation can be performed to calculate the mean velocity V' in the orthogonal direction [52].

$$U' = \frac{\sum_1^N \widetilde{u'}_n}{N} \tag{22}$$

The Reynolds normal stress ($-\overline{\rho u'u'}$) is calculated using Equation 23. The RNS in the orthogonal direction ($-\overline{\rho v'v'}$) is calculated with the same formula, but using the instantaneous velocities and mean velocity for that direction instead [52].

$$-\overline{\rho u'u'} = \frac{-\rho \sum_1^N \left(\widetilde{u'}_n - U'\right)^2}{N} \tag{23}$$

The Reynolds shear stress ($-\overline{\rho u'v'}$) is calculated using simultaneous velocity fluctuations in both directions using Equation 24 [52].

$$-\overline{\rho u'v'} = \frac{-\rho \sum_1^N (\widetilde{u'}_n - U')(\widetilde{v'}_n - V')}{N} \tag{24}$$

After calculating both RNSs and the RSS, the principal Reynolds stress (PRS) and the maximum Reynolds shear stress (MRSS) can be calculated using Equations 25 and 26, respectively [57].

$$PRS = \frac{(\overline{\rho u'u'}) + (\overline{\rho v'v'})}{2} \pm \sqrt{\left[\frac{(\overline{\rho u'u'}) - (\overline{\rho v'v'})}{2}\right]^2 + (\overline{\rho u'v'})^2} \tag{25}$$

$$MRSS = \sqrt{\left[\frac{(\overline{\rho u'u'}) - (\overline{\rho v'v'})}{2}\right]^2 + (\overline{\rho u'v'})^2} \tag{26}$$

2.3.2 Turbulence Intensities

Although turbulence intensities (TIs) are not conventionally used to gauge hemolysis or thrombosis, they can provide a normalized measurement of turbulent velocity fluctuations which are necessary for the calculation of Reynolds stresses. Axial turbulence intensity is calculated using Equation 27, where u' is the measured turbulent velocity at a given spatial and temporal location, N is the number

of measurements, and $U_{throat,avg}$ is the average velocity in the throat. Radial turbulence intensity is calculated using the same equation, but replacing *u'* with *v'* [57].

$$TI_{axial} = \frac{\sqrt{\sum_{n=1}^{N} \frac{(u')^2}{N}}}{U_{throat,avg}} \quad (27)$$

2.3.3 Viscous Shear Stress and Wall Shear Stress

Another measurement used to evaluate shear stress is the viscous shear stress (ϵ), which is calculated using Equation 28. μ is the dynamic viscosity, U_j and U_{j+1} are mean velocities at adjacent measurement locations, and *d* is the distance between the two measurements [57].

$$\epsilon = \mu \frac{U_j - U_{j+1}}{d} \quad (28)$$

Wall shear stress (WSS) is an important metric used to predict hemolysis and thrombosis in medical devices. Equation 28 is also used to estimate the WSS, by assuming that the surface-normal velocity gradient near the wall is linear. The velocity at the nearest measurement location to the wall is used for U_j, and the velocity at the wall (0 m/s) is used for U_{j+1} [57].

Chapter 3

Theory

3.1 Laser Doppler Velocimetry

Laser doppler velocimetry (LDV) is a non-intrusive technique that uses light scattered by small diameter particles to determine fluid flow velocity. These fluid particles are small and dilute enough to enable them to accurately capture the natural flow of the fluid. Interference between two laser beams generates a probe volume within the flow several hundred microns in diameter. Each velocity sample is collected within the span of a few microseconds, allowing for the measurement of the highest frequencies of the turbulence spectrum [58]. Figure 8 shows the basic technique of LDV, demonstrating the scattering of laser light by small particles, which are then detected by a photodetector.

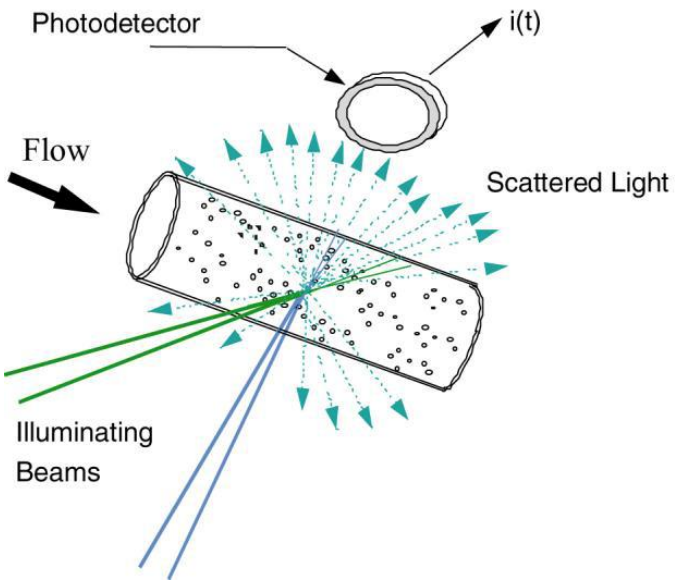

Figure 8. Laser Doppler velocimetry schematic, adapted from [59]

3.1.1 Seed Particles

The seed particle's capacity to follow the flow is governed by its aerodynamic diameter, which is the diameter of a unit density sphere with the same settling velocity as the particle, and which is related to the relaxation time of the particle. The relaxation time (τ) is given by Equation 29, where ρ is the particle's density, *d* is its diameter, and μ is the dynamic viscosity of the blood analog fluid [59].

$$\tau = {\rho d^2}/{18\mu} \tag{29}$$

The relaxation time is used to calculate the Stokes number (*St*), which is the dimensionless ratio of the particle relaxation time to the characteristic time of the fluid flow. The equation necessary to calculate the Stokes number is given by Equation 30, where u_∞ is the fluid velocity far from the particle and *d* is the obstacle's diameter. If the Stokes number is significantly lower than unity (St << 1), the seed particles can change directions without altering flow conditions and imposing their own flow [60].

$$St = {\tau u_\infty}/{d} \tag{30}$$

3.1.2 Fringe Pattern

For each component of velocity measured, the intersection of two beams generates a fringe pattern, the amplitude of which is a Gaussian intensity distribution as shown in Figure 9. The fringe spacing is given by Equation 31, where d_f is the fringe spacing, λ is the wavelength of light, and κ is the half angle of the beams [59].

$$d_f = {\lambda}/{2\sin\kappa} \tag{31}$$

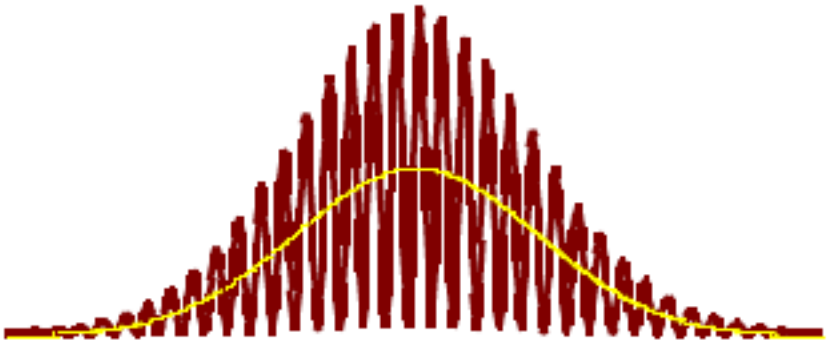

Figure 9. LDV Fringe Pattern, adapted from [59]

The fluid particles scatter light crossing the bright fringes, resulting in an oscillating pattern of scattered light intensity with a frequency proportional to the velocity of the particles. The distance between the fringes and the time necessary for the particle to pass between fringes (the inverse of the signal frequency) are known, enabling the calculation of the particle velocity using Equation 32, where f_D is the Doppler frequency, u is the velocity, and δ_f is the fringe spacing [61].

$$u = \delta_f f_D \tag{32}$$

3.1.3 Measurement Volume Calculation

The measurement volume is contained within an ellipsoidal surface, shown in Figure 10. The maximum intensity is at the center of the measurement volume. The boundaries of the measurement volume are defined by the surface where the light intensity is $1/e^2$ of the maximum intensity [59].

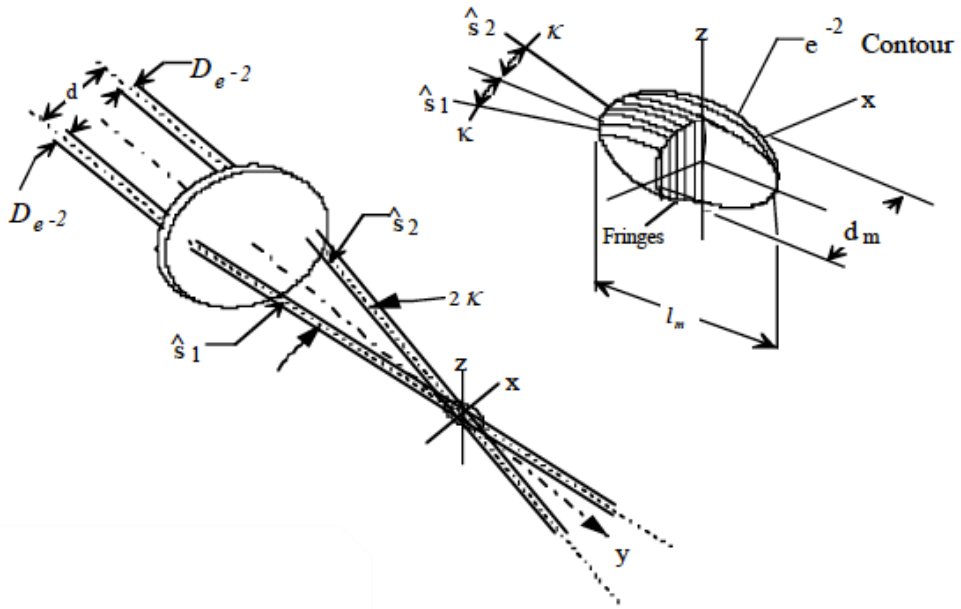

Figure 10. Measurement Volume, adapted from [59]

Equation 33 gives the diameter d_m of the measurement volume, Equation 34 gives the length of the measurement volume l_m, and Equation 35 gives the volume V of the measurement volume. $d_{e^{-2}}$ is related to the beam diameter $D_{e^{-2}}$ shown in Figure 10, and is defined by Equation 36. κ is the half angle of the beams, f is the focal length of the lens, and λ is the laser wavelength [59].

$$d_m = {d_{e^{-2}}}/{\cos\kappa} \tag{33}$$

$$l_m = {d_{e^{-2}}}/{\sin\kappa} \tag{34}$$

$$V = {\pi {d_{e^{-2}}}^3}/{(6\cos^2\kappa\sin\kappa)} \tag{35}$$

$$d_{e^{-2}} = {4f\lambda}/{\pi D_{e^{-2}}} \tag{36}$$

3.1.4 Beam Shifting

If the two interfering laser beams have the same frequency, then particles moving in one direction across the fringe pattern may have the same frequency as particles moving in the opposite direction, making it impossible to discern the direction of the particle's motion. To solve this problem, one of the two laser beams is shifted 40 MHz in frequency by a Bragg cell. If a particle is moving in the opposite direction as the fringes, it will have a frequency of 40 MHz plus the Doppler frequency, and if it is moving in the same direction as the fringes it will possess a frequency of 40 MHz minus the Doppler frequency. In addition, this frequency shift enables collection of near-zero velocity data, as without the shift there would be no fluctuating pattern of light [61].

Chapter 4

Methods

4.1 Mock Circulatory Flow Loop

In order to simulate the circulatory system *in vitro*, a mock circulatory flow loop was constructed which contained features that model the human circulatory system. The flow loop, shown in Figure 11, consisted of a pulsatile pump, stagnation chamber, flow straightener, two stainless steel pipes, a flow probe, a heat exchanger, a reservoir, and Tygon tubing [35].

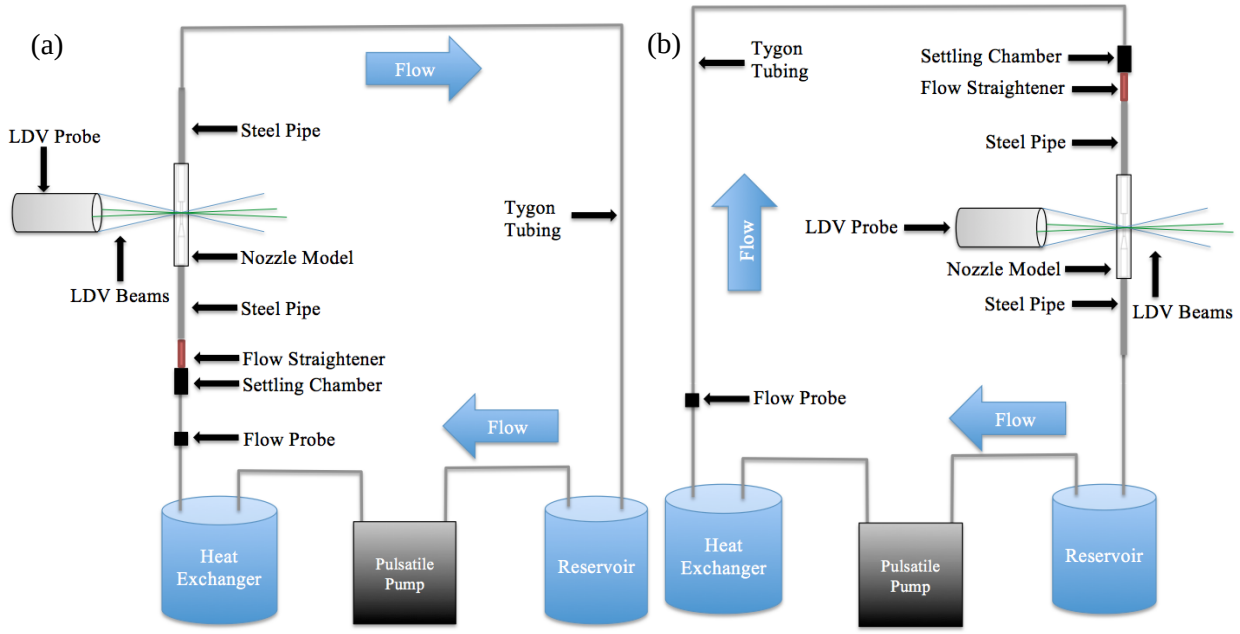

Figure 11. Mock Circulatory Flow Loop for (a) Sudden Expansion Orientation, (b) Conical Diffuser Orientation

A pulsatile blood pump (model 1423, Harvard Apparatus, Holliston, MA, USA) maintained a pulse rate of 73.11 beats per minute with 33% systolic duration and a mean flow rate of 1.61 L/min, corresponding to a mean Reynolds number of 2040, a systolic Reynolds number of 4300, and a diastolic Reynolds number of 300.

After exiting the pump, the fluid moved through Tygon tubing (Lima, OH, USA) and entered a Haake K10 heat exchanger and a Haake CD30 pump (Thermo Electron Corporation, Waltham, MA, USA), which were used to control the fluid temperature, maintaining constant viscosity [35]. The fluid temperature was measured using a True RMS Multimeter model 116 (Fluke Corporation, Everett, WA, USA). After exiting the heat exchanger, fluid entered a stagnation chamber, which decelerates and mixes it. The fluid then entered a flow straightener, which disrupts residual disturbances in the flow and ensures that the velocity profile is symmetric. After exiting the flow straightener, the fluid entered a 120 cm steel pipe. This entrance length was long enough to ensure that the velocity profile was parabolic and fully developed at the nozzle model inlet. After exiting the nozzle model, the fluid flowed through a 100 cm

steel pipe. The exit length was long enough to prevent disturbance in the reattachment point in the model [35].

A Transonic Systems Inc. (Ithaca, NY, USA) flow probe monitored the flow rate and transmitted the flow information to the Transonic Tubing Flow Module TS410. This signal was then split and transmitted to the Lecroy Wavesurfer 500 MHz Oscilloscope (model 3054, Teledyne, Thousand Oaks, CA, USA) and to the IOtech WaveBook/516E 16-bit 1MHz Data Acquisition System with Ethernet Interface (National Instruments, Austin, TX, USA). The trigger signal from the oscilloscope, which indicates the temporal location within the waveform, was also transmitted to the WaveBook. Both of these signals were then acquired in the WaveView Portable Data Acquisition System 32-bit Windows software, version 7.15.19 (National Instruments, Austin, TX, USA). This software enabled confirmation that the trigger and flow rate were correct.

4.2 Nozzle Model

The nozzle model, shown in Figure 12, consists of a 20° conical section that reduces the inlet diameter from 12 mm to 3 mm in the nozzle throat. After the throat region, the nozzle experiences a sudden increase in diameter to 12 mm. The nozzle model itself is 16.5 cm long, and contains 15 cm acrylic extenders both proximal and distal to the model. The nozzle model was fabricated from cast acrylic with an MB-46VAE three-axis CNC milling machine. To relieve residual material stress, the part was internally machined and annealed. The part was then polished to enable optical access to the internal geometry. To meet geometric specifications, internal features of the model were hand and vapor polished. Gauge pins, a metrology rubber, and an optical comparator were used to ensure that nozzle dimensions were within 1% of the specification. The root-mean-square roughness of the inner surface was less than $5*10^{-4}$ mm, and the radius of curvature at the sudden expansion was less than 0.025 mm [35].

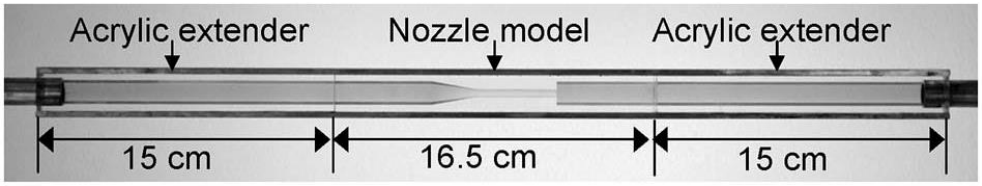

Figure 12. Benchmark Nozzle Model [35]

4.3 Fluid

To simulate native flow through the circulatory system, a blood analog with similar viscoelastic properties to those of blood was used. The composition of the fluid was 50 wt % saturated aqueous sodium iodide solution, 20 wt % glycerin, and 30 wt % water. The refractive index of the analog was 1.4834, measured using the Abbe Mark III Refractometer (Ametek Reichert Technologies, Depew, NY, USA). The dynamic viscosity was 6.95 cP at 25°, measured using the Vilastic 3 Viscoelasticity Analyzer (Vilastic Scientific Inc., Austin, Texas, USA). Finally, the specific gravity was 1.664, and was calculated by weighing 1 mL of fluid using the ME303E scale (Mettler Toledo, Columbus, OH, USA). The mean Reynolds number of the throat, 2044, was calculated using the nozzle throat diameter and average throat velocity. The Reynolds number of the inlet and exit pipes was one-third of the throat value. The fluid was seeded with 10μm glass spheres with a specific gravity of 1.1 for flow visualization [35]. These particles were calculated to have a Stokes number of 4.51×10^{-4} using Equation 18, which is low enough to prevent them from altering flow conditions.

4.4 LDV System

The imaging system used in this study was a TSI Inc. LDV System (Shoreview, MN, USA), shown in Figure 13. The laser was an Argon-ion laser (Innova 70c, Coherent Inc., Santa Clara, CA, USA). The laser system consists of a laser head, a plasma tube that amplifies the laser light, and a wavelength selector that holds the prism and high reflector optics [62]. A Coherent Components Group

Laserpure 20 heat exchanger was used to regulate the laser system's temperature. The Fiberlight™ Multicolor Beam Generator (TSI Inc., Shoreview, MN, USA) separates the laser beam into separate blue and green wavelengths at a total power of 1.8 W. The fiberoptic probe used to transmit and collect the laser light is the TR260-X10 (TSI Inc., Shoreview, MN, USA). A NOVA (Ophir, Jerusalem, Israel) power meter measured the power of the beams emitted by the probe. The probe positioning in the x, y, and z directions was controlled using the Motion Controller Model ESP301 (Newport Corporation, Irvine, CA, USA). The photo detector module (PDM 1000, TSI Inc., Shoreview, MN, USA) was setup in backscatter mode, and received optical signals from the fiberoptic probe. The signal processor (FSA3500/4000, TSI Inc., Shoreview, MN, USA) determined information including frequency, phase, burst transit time, and burst arrival time. After processing a burst, the signal was sent to a computer, where it was analyzed using FlowSizer™ software (TSI Inc., Shoreview, MN, USA) [63]. FlowSizer was also used to set the parameters given in Table 2.

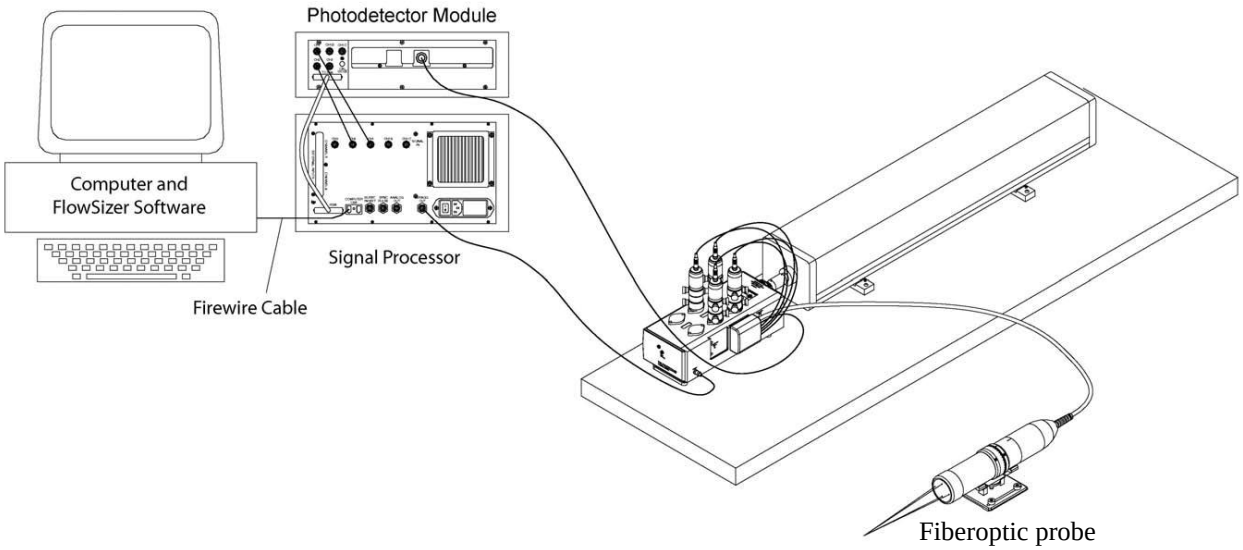

Figure 13. Components of LDV System, adapted from [64]

4.4.1 LDV Data Acquisition

LDV measurements were taken at fifteen separate planes within the nozzle model, seven in the sudden expansion direction and eight in the conical diffuser direction corresponding to pertinent locations within the test section, shown in Figures 14 and 15. The naming convention for each plane used in Figures 14 and 15, and throughout this paper, are adopted from Hariharan *et al.* [35]. These locations enable velocity measurements within the entrance region, the conical diffuser, the nozzle, the recirculation region following the sudden expansion, and the exit region. Nine planes that were collected in the original steady-flow experiment were not collected in this study: SE1, SE3, SE4, SE9, SE11, CD1, CD3, CD4, and CD12.

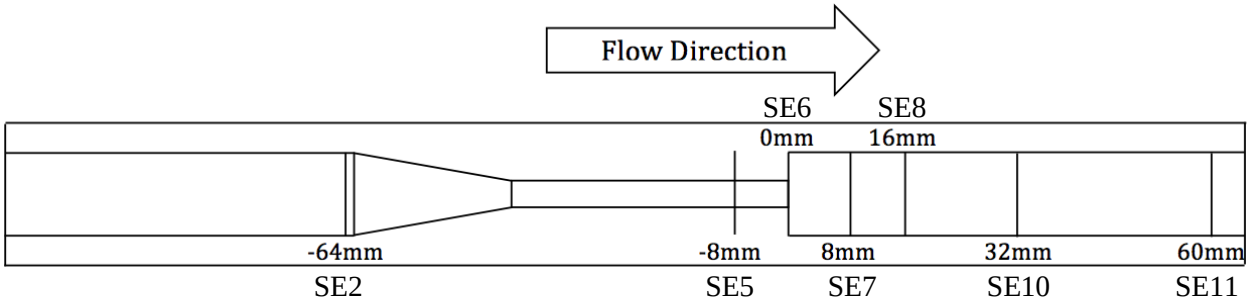

Figure 14. Data Collection Locations, Sudden Expansion Direction

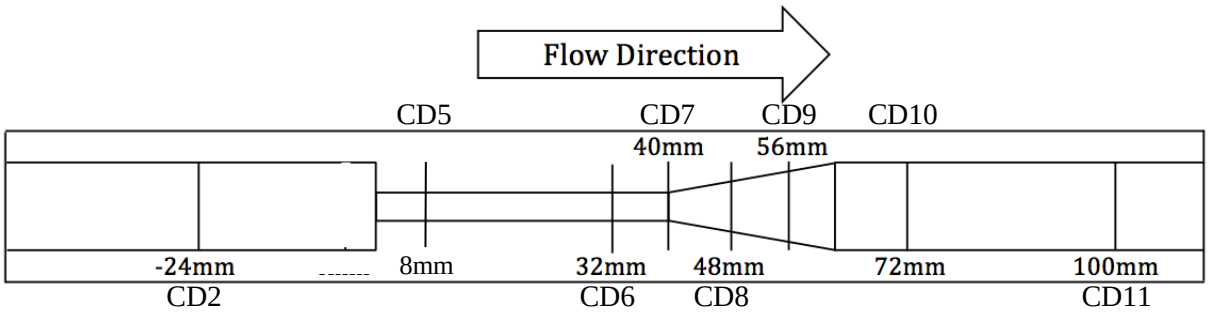

Figure 15. Data Collection Locations, Conical Diffuser Direction

For each plane outside of the throat, data were collected in coincidence mode every 0.3 mm from one end of the model to the other as shown in Figure 16. Within the throat, data were collected every 0.2

mm from one end of the model to the other. Separate two-component velocity data points were taken at each spatial location.

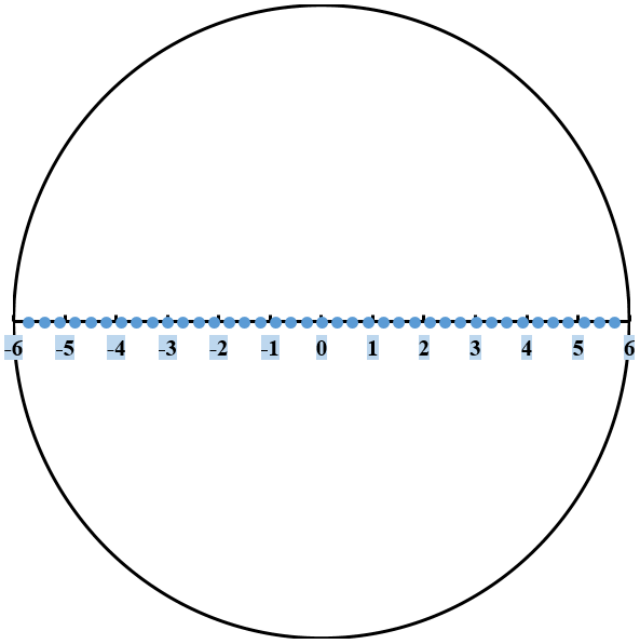

Figure 16. Data Collection Locations for Each Plane

Table 2 lists the FlowSizer and FSA parameters used to collect data, along with the probe measurement diameter, length, and volume, calculated using Equations 19-22 [65].

Table 2. FlowSizer and FSA Parameters [60]

Processor Controls	**Channel 1**	**Channel 2**
PMT Voltage	400-650 V	500-700 V
Burst Threshold	60-85 mV	50-100 mV
Band Pass Filter	1-10 MHz	1-10 MHz
Downmix Frequency	38.5 MHz	37.5-38.1 MHz
Gate Scale Coincidence	100%	100%
Minimum Possible Velocity	-0.71 m/s	-2.96 m/s
Maximum Possible Velocity	12.01 m/s	9.38 m/s
Measurement Volume Diameter	34 µm	34 µm
Measurement Volume Length	0.18 mm	0.18 mm
Measurement Volume	1.09×10^{-13} m^3	1.09×10^{-13} m^3

4.4.2 LDV Post Processing

As in Baldwin *et al.*, an elliptical filter removed data points outside of 3.5 standard deviations [66]. An example of the elliptical filter is shown in Figure 17. A MATLAB (MathWorks, Natick, MA, USA) program developed in-house filtered the data and then calculated principal Reynolds stresses (PRS), maximum Reynolds shear stresses (MRSS), and normalized turbulence intensities (TI) using equations 25, 26, and 27. A similar MATLAB script was used to analyze the steady flow data. Viscous shear stresses (VSS) and wall shear stresses (WSS) were then calculated in Microsoft Excel using Equation 28 and the dynamic viscosity of blood used in the CFD study (3.5 cP) [57]. The mean and standard deviation of the WSS was calculated using the velocities from the four measurement locations closest to the wall (one at either side of the model).

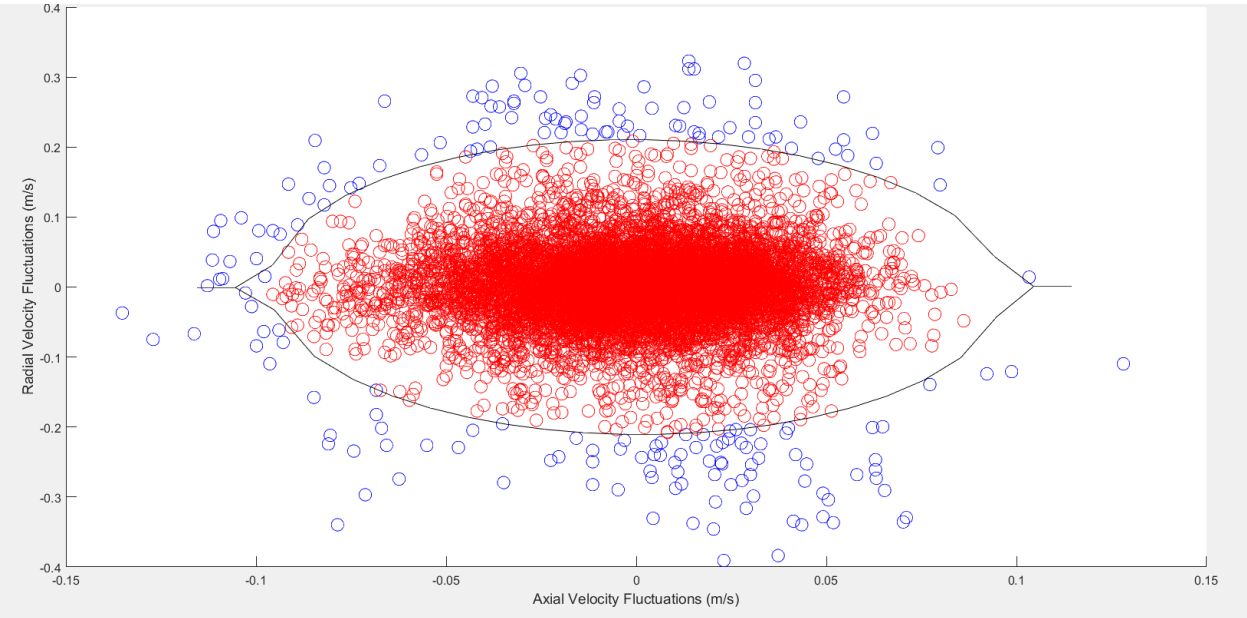

Figure 17. Elliptical Representation of Points Removed

4.5 Operating Procedure

The procedure used in this study was similar to the standard operating protocol developed by Hariharan *et al.* [35]. The model was oriented vertically to avoid bubbles and settling of tracer-particles in

recirculation regions. A heat exchanger maintained the temperature to within ±0.5°C to ensure that the fluid properties were constant. The flow rate was adjusted with variations in fluid properties so that the Reynolds number remained constant. To ascertain that the flow rate measurement was accurate, the ultrasonic flow meter was verified using a beaker and stopwatch. Finally, the inlet boundary conditions were controlled using a long entrance length (100D), and a stagnation chamber and flow straightener [35].

Steady flow data were initially collected using a Variable Speed Pump Drive (Cole-Parmer Instrument Company, Vernon Hills, IL, USA). Data were collected at planes 2, 5, and 8 in the sudden expansion direction. These data were then compared with PIV and LDV steady flow data taken by Hariharan *et al.* [35] and Taylor *et al.* [57]. The comparison of steady data with previous data enabled the verification that the experimental setup described above yielded results consistent with previous experiments.

In order to compare experimental data with computational data at specific locations within the model, data were collected at seven planes in the sudden expansion direction and eight planes in the conical diffuser direction. The velocity, Reynolds stress, Reynolds shear stress, and normalized turbulence intensity were calculated for both the axial and radial directions at each of the fifteen planes.

The mean Reynolds number in the throat of the model was 2040, the maximum Reynolds number during peak systole was 4300, and the minimum Reynolds number was 300. A trigger was set on the oscilloscope to enable post-processing software to know the location on the flow waveform where data were collected. Several flow periods, along with the location of the trigger, are shown in Figure 18.

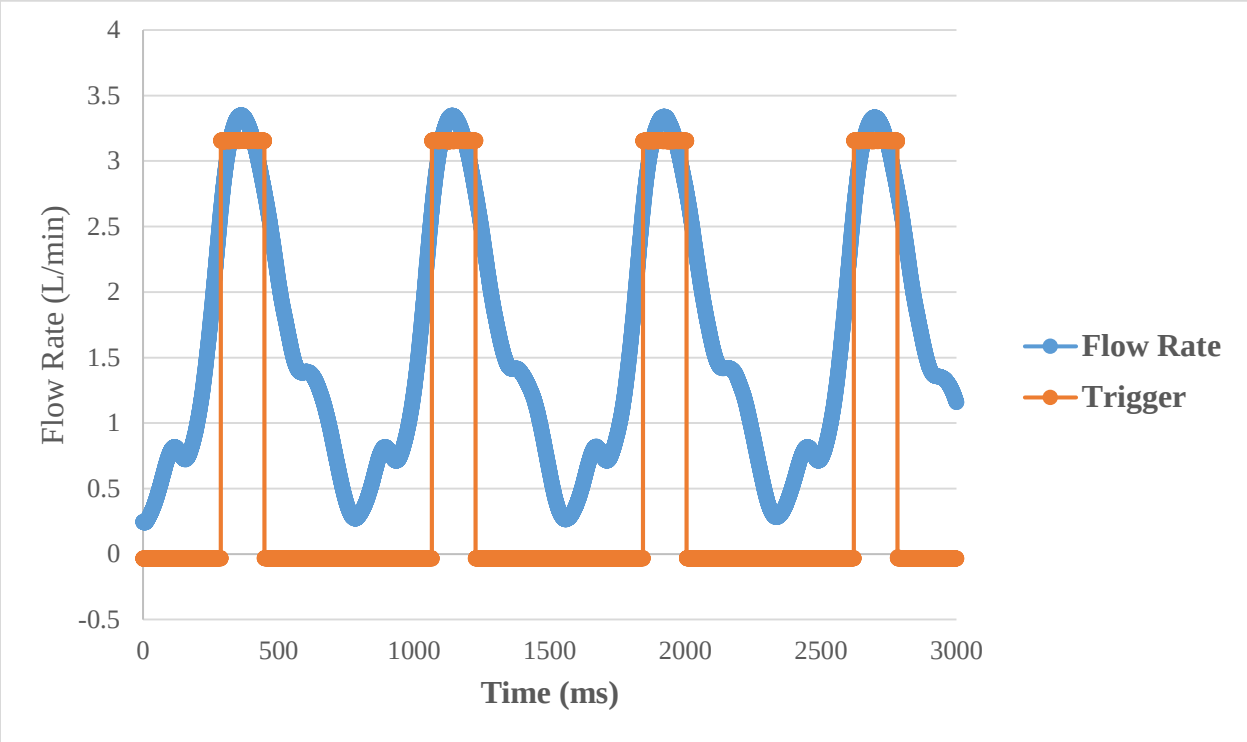

Figure 18. Flow Waveform and Trigger

Chapter 5

Results

LDV was used to measure the velocity for three planes using a steady flow pump, and fifteen planes using a pulsatile pump. For the pulsatile flow data, RSSs, RNSs, and TIs were calculated and evaluated at each plane.

5.1 Steady Flow Results

To verify the experimental setup, steady flow data were collected at plane 2 (-64mm), plane 5 (-8mm), and plane 8 (16mm) for Reynolds numbers of 2000 and 6500 in the sudden expansion direction and compared with data from Hariharan *et al.* [35] and Taylor *et al.* [57]. Only PIV data were available for comparison for a Reynolds number of 6500. Figure 16 shows the comparison between the newly collected LDV data and the previous LDV and PIV data collected at Penn State for all three planes and both Reynolds numbers. All velocity data shown in Figure 19 were normalized with respect to the average inlet velocity, as shown in Equations 37 and 38, where $\bar{u}_{inlet}$ is the average inlet velocity, Q is the flow rate, r_{inlet} is the inlet radium, and $\bar{u}_{measured}$ is the measured velocity [35].

$$\bar{u}_{inlet} = \frac{Q}{\pi {r_{inlet}}^2} \tag{37}$$

$$u_{normalized} = \frac{u_{measured}}{\bar{u}_{inlet}} \tag{38}$$

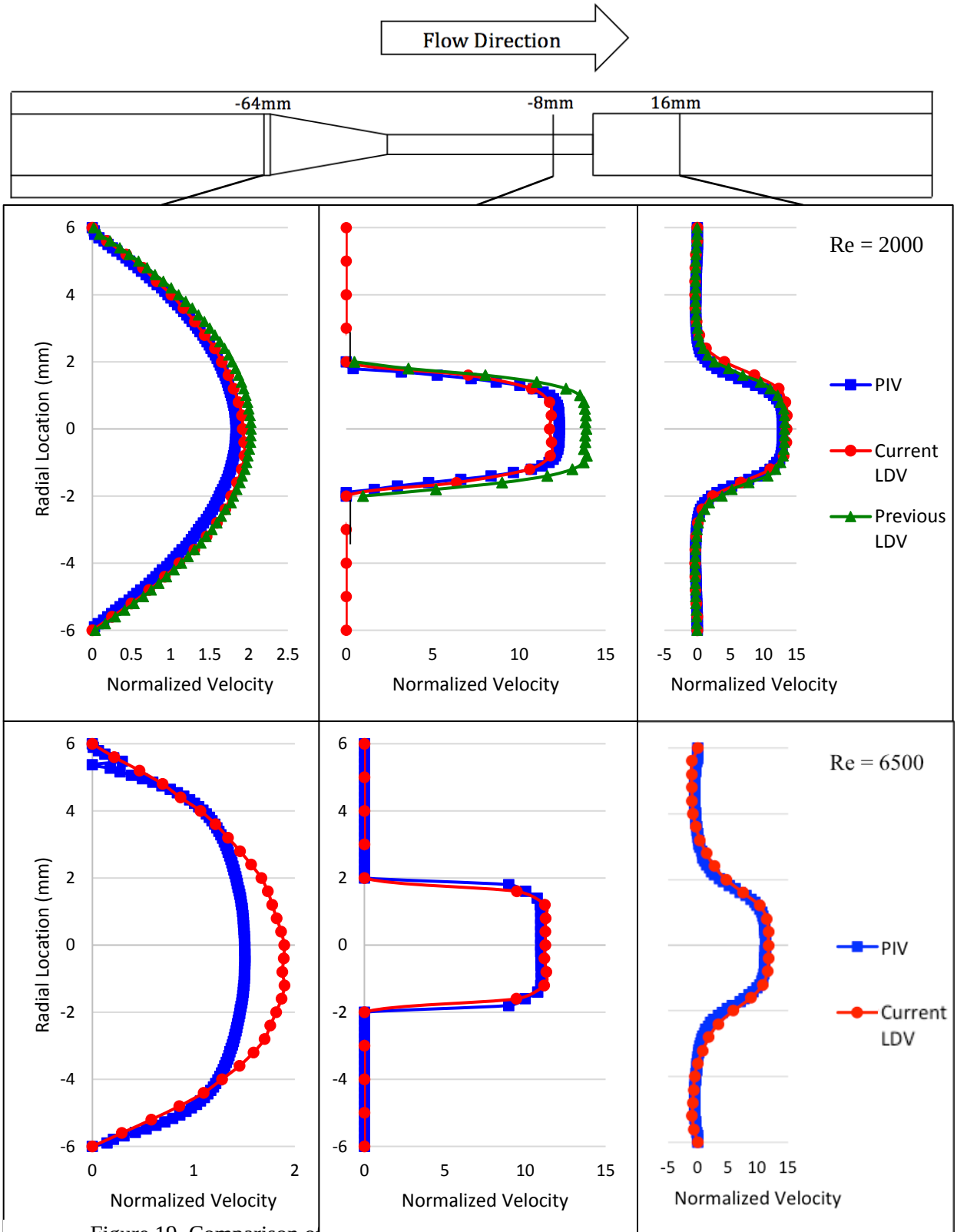

Figure 19. Comparison of LDV and PIV data for planes 2, 5, and 8 at Reynolds numbers 2000 and 6500

As shown in Figure 20, the new LDV data agrees well with the previous data for all planes and Reynolds numbers except for plane 2 at a Reynolds number of 6500. This discrepancy is likely due to a minute difference between the model used by Penn State in the original study and the model used to collect the new data. This aberration was detected in the original study, in which Lab 1 observed different results at plane 2, Re = 6500, than the other two labs. This original graph from Hariharan *et al.* is shown in Figure 17 [35]. As shown in the figure, the results obtained by Lab 1 are similar to the new results obtained in this experiment. See Appendix A for more detailed graphs of the steady flow data displaying error bars.

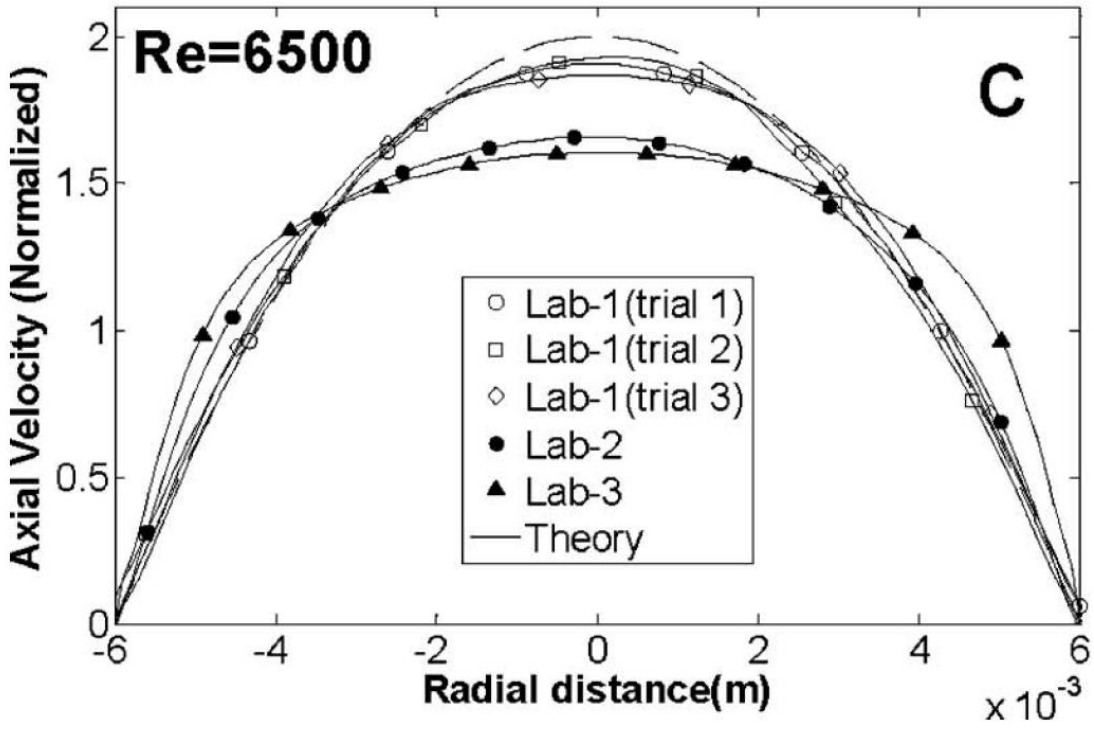

Figure 20. Axial Velocity vs. Radial Distance for Plane 2, Re = 6500, adapted from Hariharan *et al.* [35]

5.2 Pulsatile Results

5.2.1 Axial Velocity

Figure 21 shows the evolution of the flow profile as fluid moves through the model in the sudden expansion orientation. The development of the jet downstream of the sudden expansion, and the subsequent reattachment of the flow profile to the wall, are evident in the flow profiles during mid-acceleration, systole, and mid-deceleration (Figures 21a, 21b, and 21c). The development of recirculation regions in the separation zone downstream of the sudden expansion is visible in the diastolic velocity curves (Figure 21d). Immediately following the sudden expansion, recirculation regions begin to develop, growing in size and reaching a maximum at SE10, before declining again as the flow reattaches to the wall.

The flow profiles at each plane measured in the conical diffuser orientation are given in Figure 22. The gradual deceleration of the fluid as it exits the diffuser is shown in the mid-acceleration, systolic, and mid-deceleration velocity curves (Figures 22a, 22b, and 22c). Although the jet that develops is not as pronounced as in the sudden expansion orientation, flow still clearly separates from the wall downstream of the diffuser. The diastolic velocity curve in Figure 22d shows the recirculation regions that develop within and downstream of the conical diffuser. Unlike the sudden expansion orientation, where recirculation reached a maximum far downstream of the expansion, in this orientation maximum recirculation occurs within the diffuser.

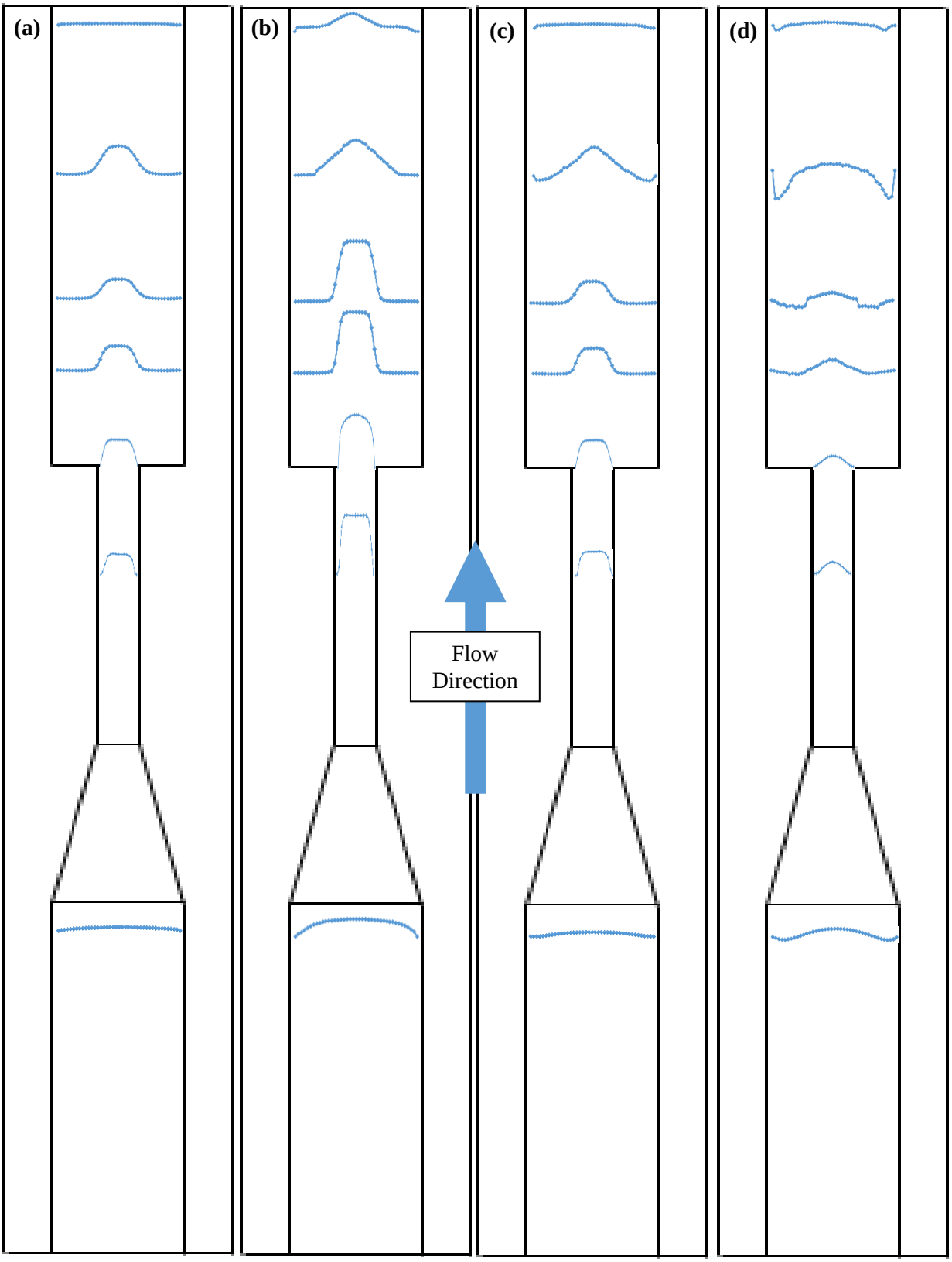

Figure 21. Velocities across the Nozzle Model in the Sudden Expansion Orientation during (a) Mid-Acceleration, (b) Systole, (c) Mid-Deceleration, and (d) Diastole. Note that Diastolic Velocities are Scaled Differently, and that Velocities in the Throat are Stretched for Scale.

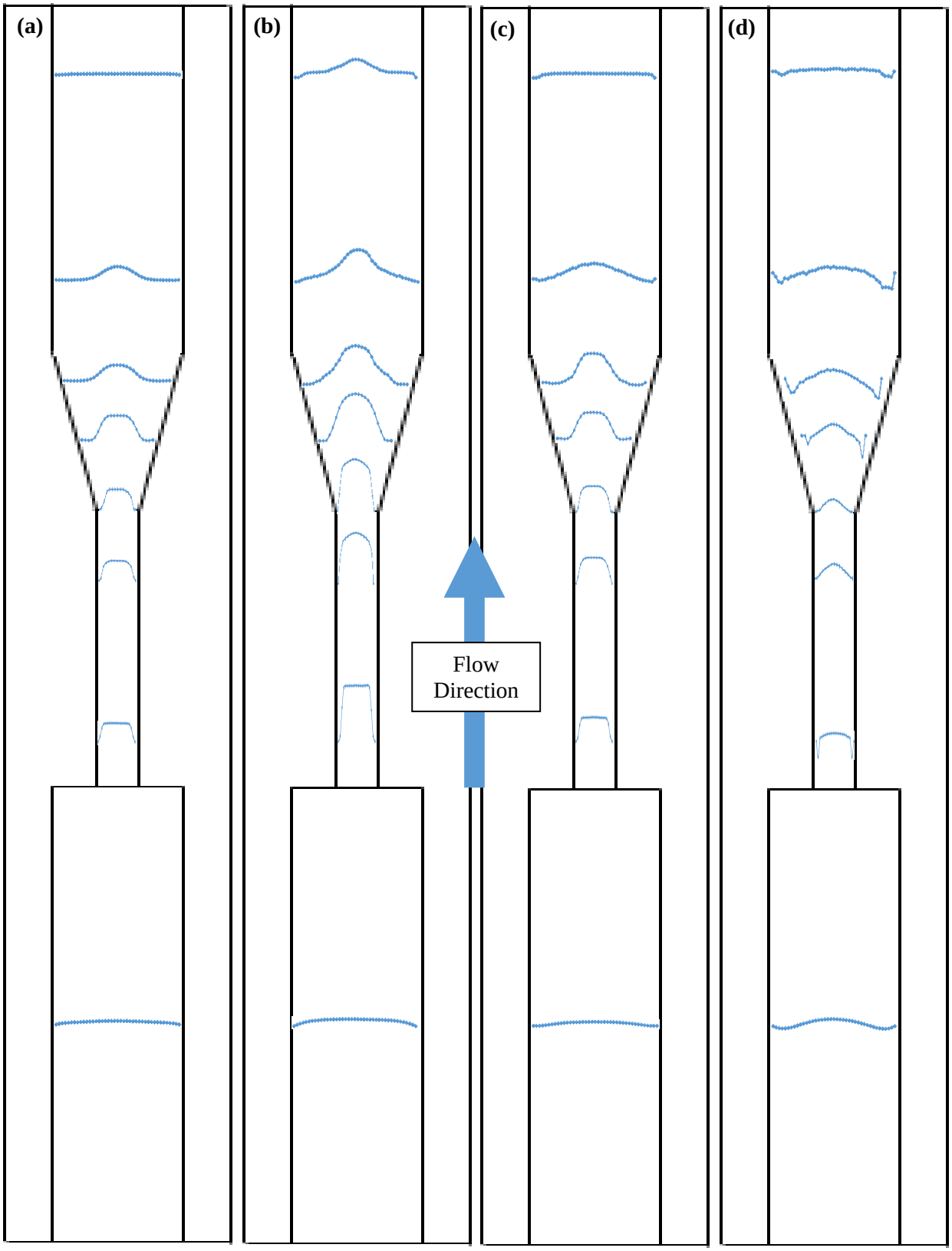

Figure 22. Velocities across the Nozzle Model in the Conical Diffuser Orientation during (a) Mid-Acceleration, (b) Systole, (c) Mid-Deceleration, and (d) Diastole. Note that Diastolic Velocities are Scaled Differently, and that Velocities in the Throat are Stretched for Scale

Figures 23-38 show the axial mid-acceleration, systolic, mid-deceleration, and diastolic velocities for the following planes: SE planes 2, 5, 6, 7, 8, 10, and 11, followed by CD planes 2, 5, 6, 7, 8, 9, 10, and 11, respectively. Note that the dimensions given in these figures are relative to the sudden expansion in the sudden expansion orientation, and to the sudden contraction in the conical diffuser orientation. All velocity data are scaled using Re similarity to correct for the viscosity of blood using Equation 38, where ν_{blood} is 3.314 cSt, which is the kinematic viscosity of blood used by the CFD studies [57]. All data are normalized using Equations 37 and 38 and the mean throat velocity over an entire cycle of 2.135 m/s. The plots of mid-acceleration, systolic, mid-deceleration, and diastolic velocities all show standard deviations at each point, represented by error bars. Note that for several plots, standard deviations are too low to visibly observe on the plots.

$$U_{blood} = U_{NaI} * \frac{\upsilon_{blood}}{\upsilon_{NaI}} \tag{38}$$

The radial velocities, axial and radial Reynolds normal stresses, and Reynolds shear stresses for mid-acceleration, systole, mid-deceleration, and diastole for each plane are included in Appendix B.

Figure 23 shows the centerline velocity and the velocities during mid-acceleration, systole, mid-deceleration, and diastole at SE2. This area of flow is ahead of the gradual contraction region. The flow has not yet entered the area of the model that undergoes geometry change, so it is fully developed with a parabolic shape and a peak of 0.63 m/s during systole. During diastole, there are some areas of recirculation near the walls. Near the center of the plane, the diastolic velocity curve is parabolic, with a maximum value of 0.17 m/s. As the flow is accelerating and decelerating, it has a flow profile that is parabolic, with a maximum value of 0.37 m/s during deceleration and of 0.32 m/s during acceleration. There are small areas of recirculation during mid-deceleration near the walls.

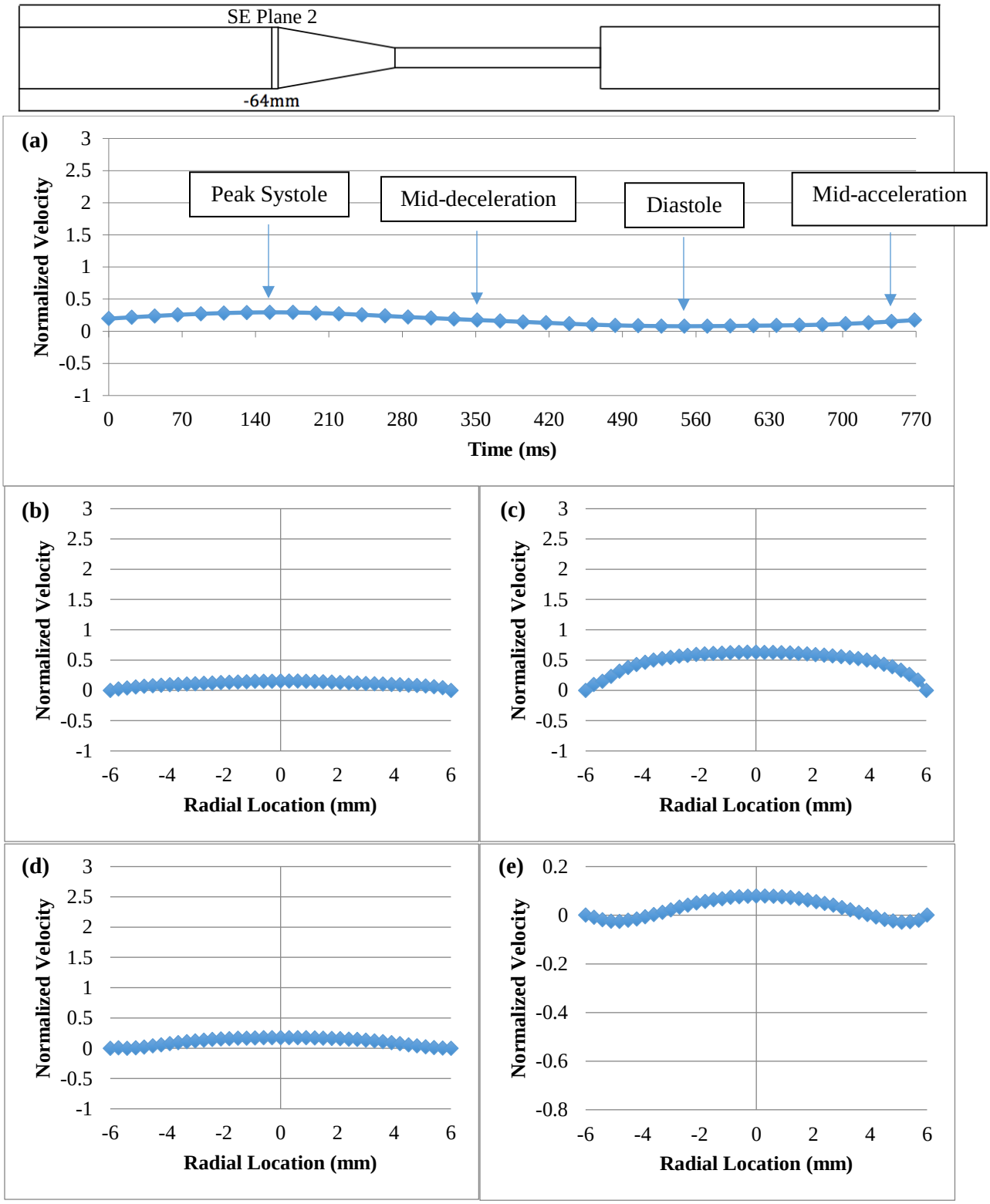

Figure 23. (a) Centerline Velocity, (b) Mid-acceleration, (c) Systolic, (d) Mid-deceleration, and (e) Diastolic Velocity for Sudden Expansion Plane 2. Note that Diastolic Velocity is at Different Scale.

Figure 24 shows the pertinent velocities at SE5, which is within the throat region of the model. During systole, the flow is blunted in shape, with a maximum velocity of 4.9 m/s across most of the plane, dropping off to 0 m/s at the walls. During diastole, the flow is parabolic and positive across the entire plane, with a maximum value of 0.30 m/s. The shape of the velocity curves during mid-acceleration and mid-deceleration are similar to the shape of the systolic velocity curve. The mid-acceleration curve peaks at 2.0 m/s, and the mid-deceleration curve peaks at 2.5 m/s.

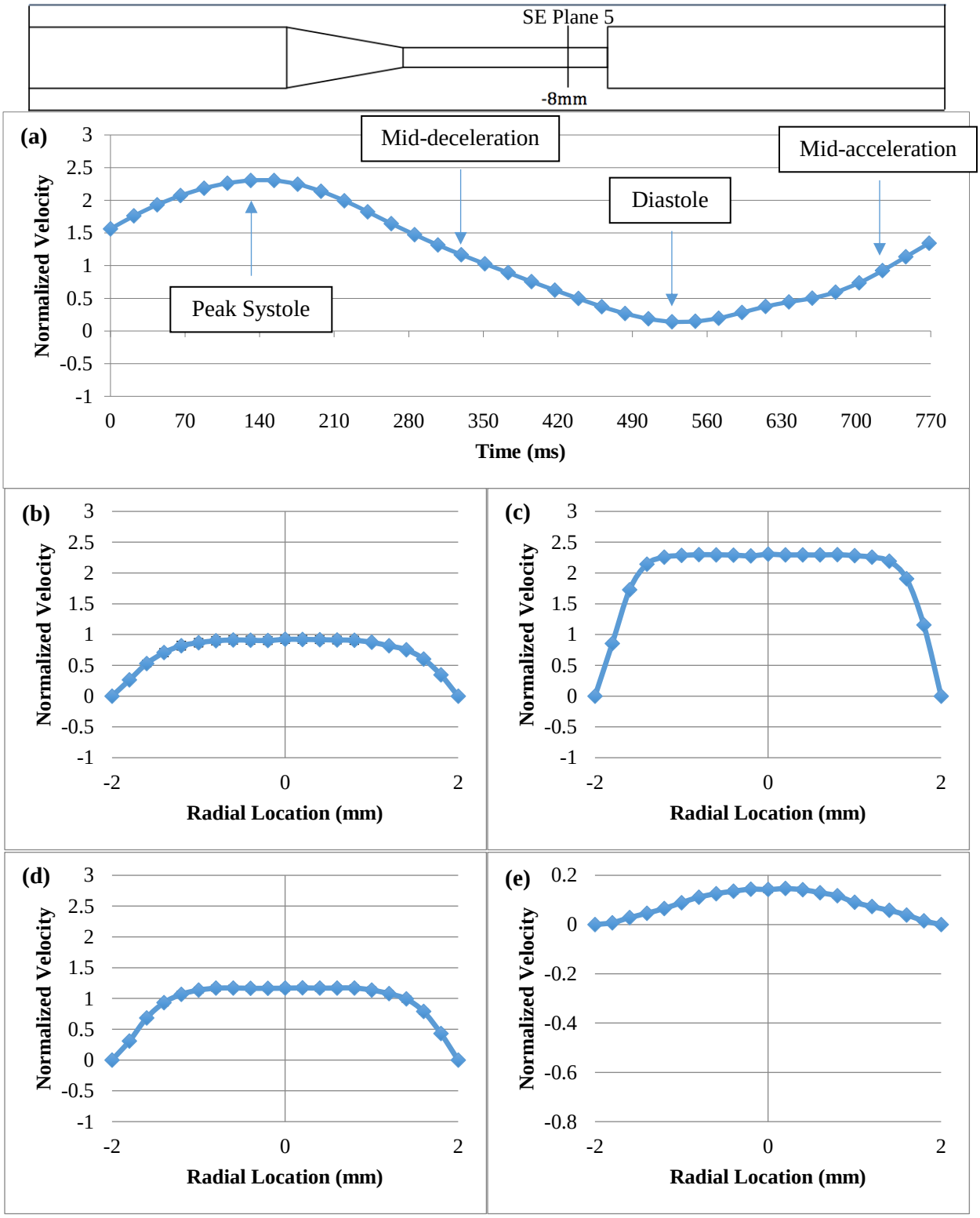

Figure 24. (a) Centerline Velocity, (b) Mid-acceleration, (c) Systolic, (d) Mid-deceleration, and (e) Diastolic Velocity for Sudden Expansion Plane 5. Note that Diastolic Velocity is at Different Scale.

The relevant velocities for SE6 are shown in Figure 25. SE6 is located at the sudden expansion region as the throat opens up to a larger diameter. The flow profiles are similar in shape to SE5, but the velocities have increased slightly.

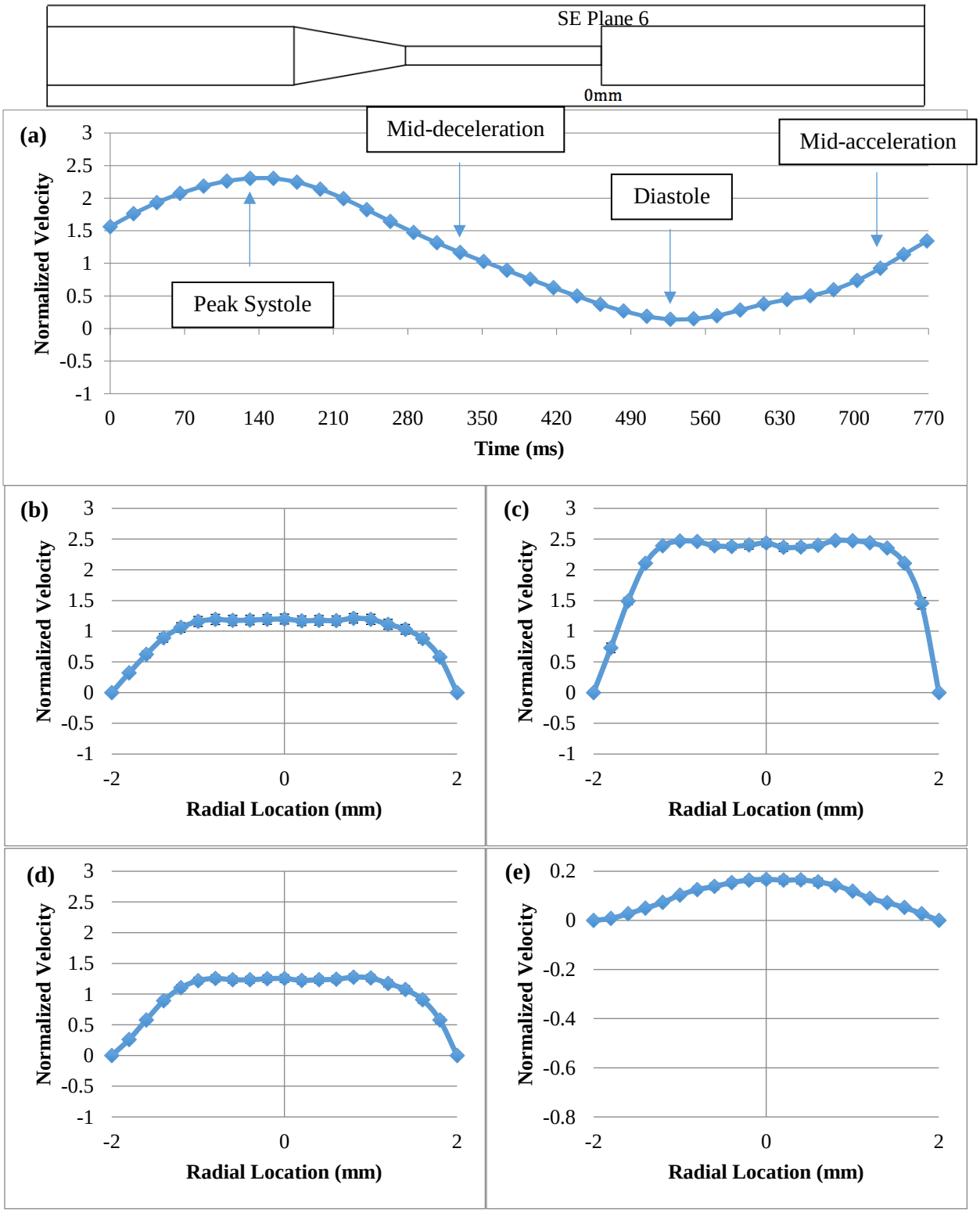

Figure 25. (a) Centerline Velocity, (b) Mid-acceleration, (c) Systolic, (d) Mid-deceleration, and (e) Diastolic Velocity for Sudden Expansion Plane 6. Note that Diastolic Velocity is at Different Scale.

Figure 26 shows the systolic, diastolic, mid-acceleration, and mid-deceleration velocities at SE7, which is located just beyond the sudden expansion. After exiting the sudden expansion, a jet forms with a similar shape and maximum velocity to the throat region. The systolic velocity curve is near-constant at 5 m/s near the center of the plane, declining to 0 m/s outside of +/-2 mm from the center. Outside of the central jet, the flow has separated, indicated by the areas of recirculation during diastole. The standard deviation in the recirculation regions during diastole is significant. The mid-acceleration and mid-deceleration curves are similar in shape to the systolic velocity curve. The mid-acceleration curve has a maximum velocity of 2.4 m/s, and the mid-deceleration curve has a maximum velocity of 2.5 m/s. Both the acceleration and deceleration curves are near-zero outside of the central jet.

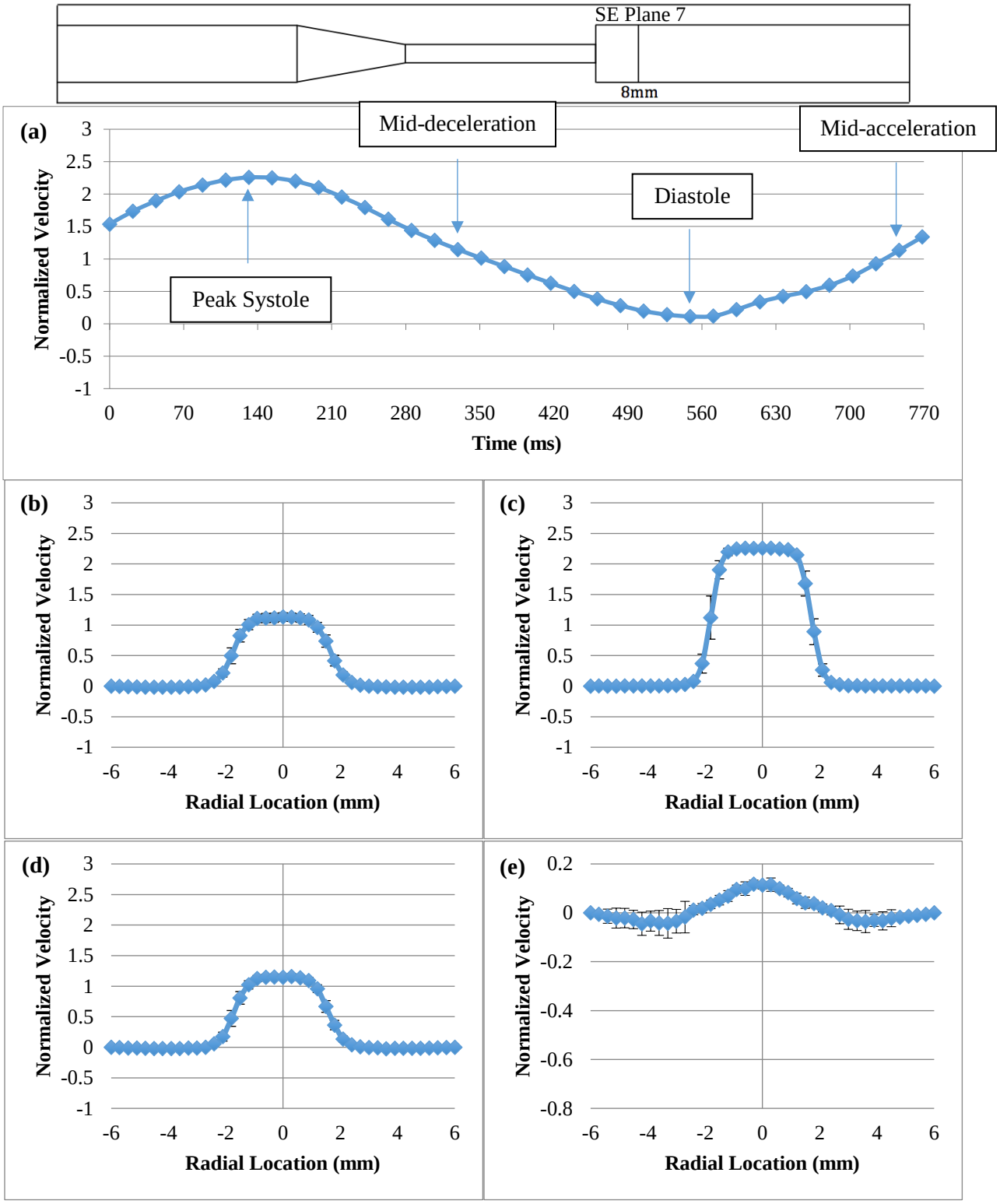

Figure 26. (a) Centerline Velocity, (b) Mid-acceleration, (c) Systolic, (d) Mid-deceleration, and (e) Diastolic Velocity for Sudden Expansion Plane 7. Note that Diastolic Velocity is at Different Scale.

Figure 27 shows the relevant velocities for SE8, which is 8 mm farther downstream than SE7. There is still a central jet flow evident by the systolic velocity curve, although the curve has become slightly more parabolic and decreased to a maximum value of 4.7 m/s. The areas of recirculation during diastole have increased in size and magnitude, reaching -0.2 m/s. The standard deviation in the areas of recirculation during diastole have also increased. The mid-acceleration and mid-deceleration curves are again near-zero outside of the central jet.

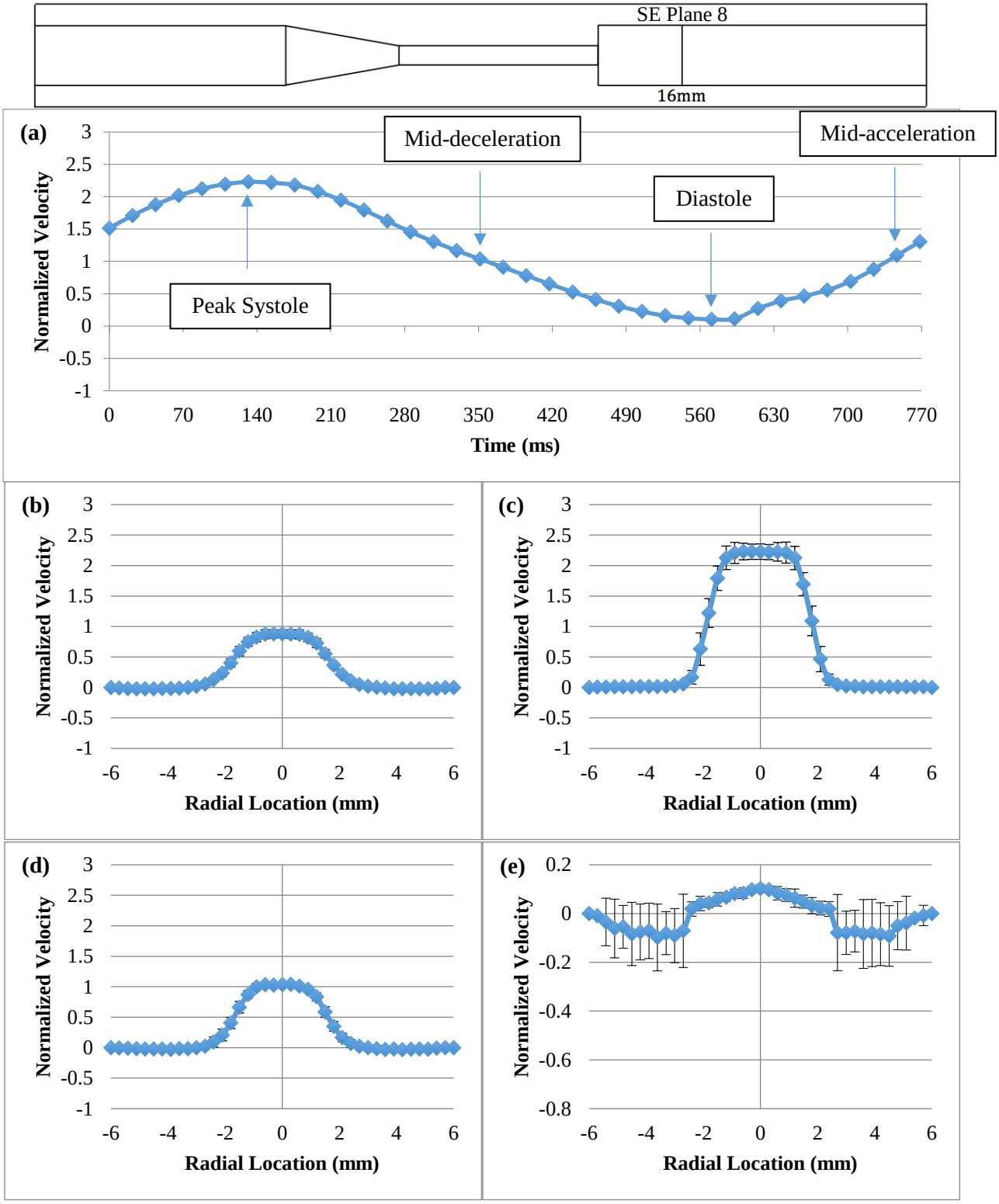

Figure 27. (a) Centerline Velocity, (b) Mid-acceleration, (c) Systolic, (d) Mid-deceleration, and (e) Diastolic Velocity for Sudden Expansion Plane 8. Note that Diastolic Velocity is at Different Scale.

The velocities for SE10 are shown in Figure 28, which is another 16 mm farther downstream from the throat than SE8. The flow in this region is beginning to reattach, as is indicated by its more parabolic and wide-spread shape during systole. During diastole, the width of the recirculation region has decreased, also indicating that the flow is reattaching. The regurgitant flow during diastole has significantly increased in magnitude, reaching -0.69 m/s. The mid-acceleration curve is very similar to mid-acceleration at SE8, with a central jet surrounded by near-zero flow. The mid-deceleration curve is significantly different from mid-deceleration at SE8, with no central jet or areas of near-zero flow. The velocity profile during mid-deceleration is more spread out, indicating that it is reattaching to the wall. In addition, it is negative near the walls, reaching a minimum of -0.39 m/s. The standard deviation is significant in the parabolic region of the systolic curve, mid-deceleration curve, and in the recirculation regions of diastole, indicating that the flow is unstable at this plane. Instability during systole is also evident in the centerline velocity curve, which fluctuates around peak systole rather than having a parabolic shape.

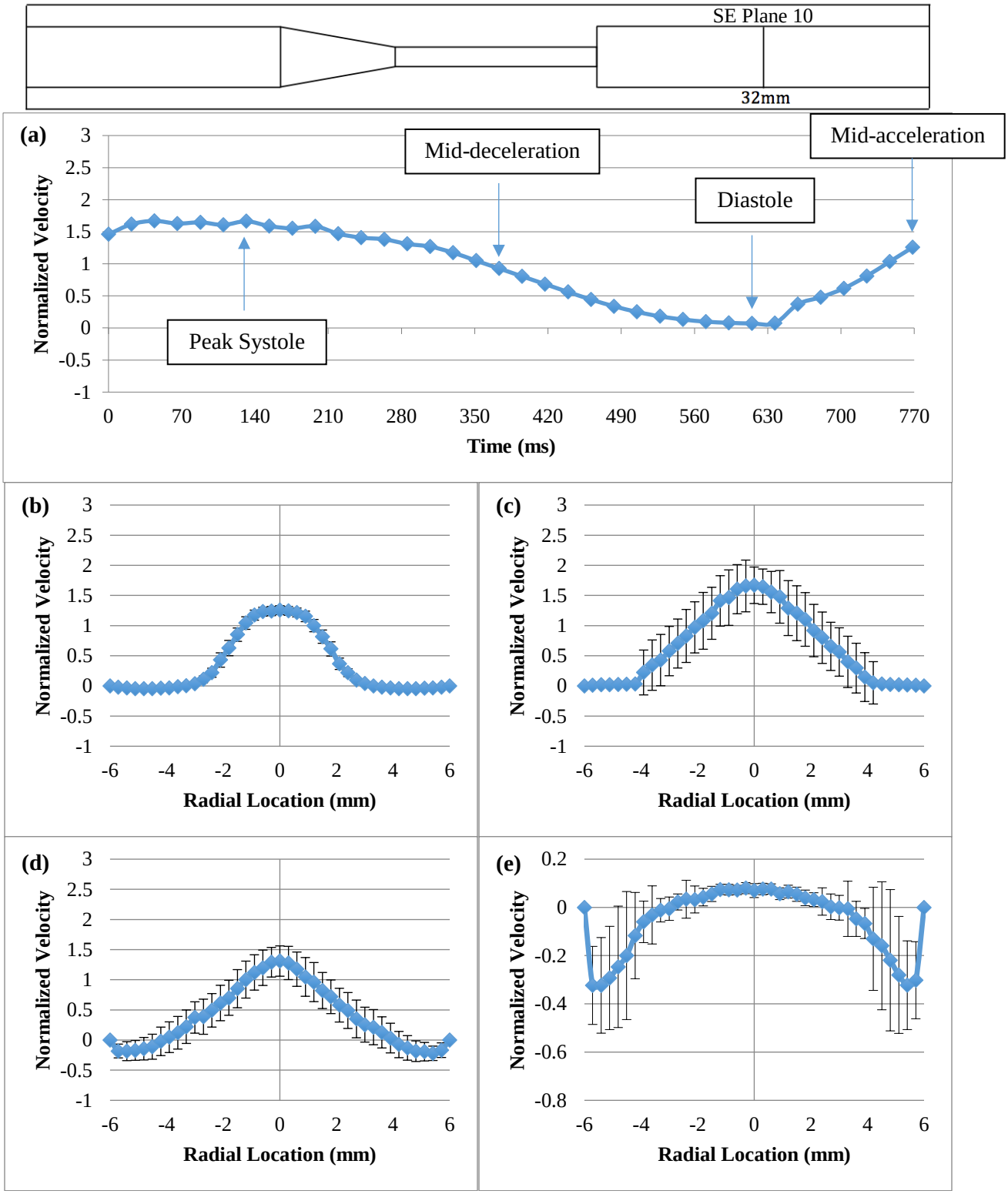

Figure 28. (a) Centerline Velocity, (b) Mid-acceleration, (c) Systolic, (d) Mid-deceleration, and (e) Diastolic Velocity for Sudden Expansion Plane 10. Note that Diastolic Velocity is at Different Scale.

Figure 29 shows the systolic and diastolic velocities at SE11, which is 60 mm downstream from the throat region. The systolic velocity is closer to reattaching, with a peak value that has declined to 1.8 m/s. The diastolic velocity is nearly flat, with small areas of regurgitant flow near the walls. The mid-acceleration and mid-deceleration curves are parabolic with peak magnitudes of 0.12 m/s and 0.4 m/s, respectively. Standard deviations are significant during systole and diastole across the entire plane, indicating that flow is still unstable as it continues to reattach.

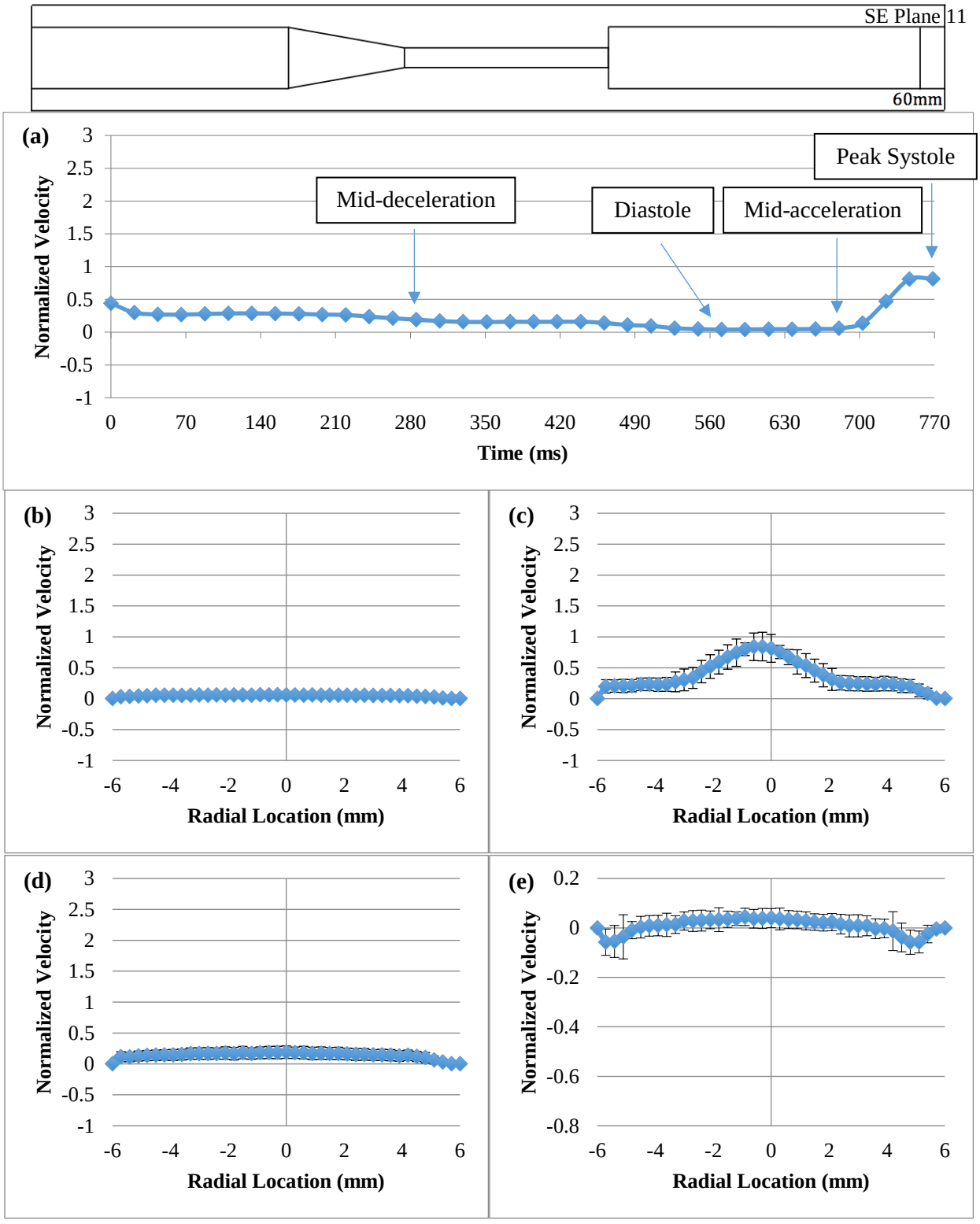

Figure 29. (a) Centerline Velocity, (b) Mid-acceleration, (c) Systolic, (d) Mid-deceleration, and (e) Diastolic Velocity for Sudden Expansion Plane 11. Note that Diastolic Velocity is at Different Scale.

The centerline, mid-acceleration, systolic, mid-deceleration, and diastolic velocities for CD2 are shown in Figure 30. This area of flow is ahead of the sudden contraction, so the flow is still fully developed. The flow profile during mid-acceleration, systole, mid-deceleration, and diastole all look very similar to those for SE2. The systolic velocity curve is parabolic, peaking at 0.62 m/s at the center of the model. This value is similar to the peak value found at SE2, which was 0.63 m/s. The diastolic velocity curve has a parabolic shape near the center of the plane with a maximum value of 0.17 m/s, which is the same peak value found at SE2. The diastolic velocity curve also has areas of regurgitant flow near the walls. The mid-acceleration and mid-deceleration curves both have a parabolic shape with peaks of 0.32 m/s and 0.38 m/s, respectively. The deceleration curve has small areas of negative flow near the wall.

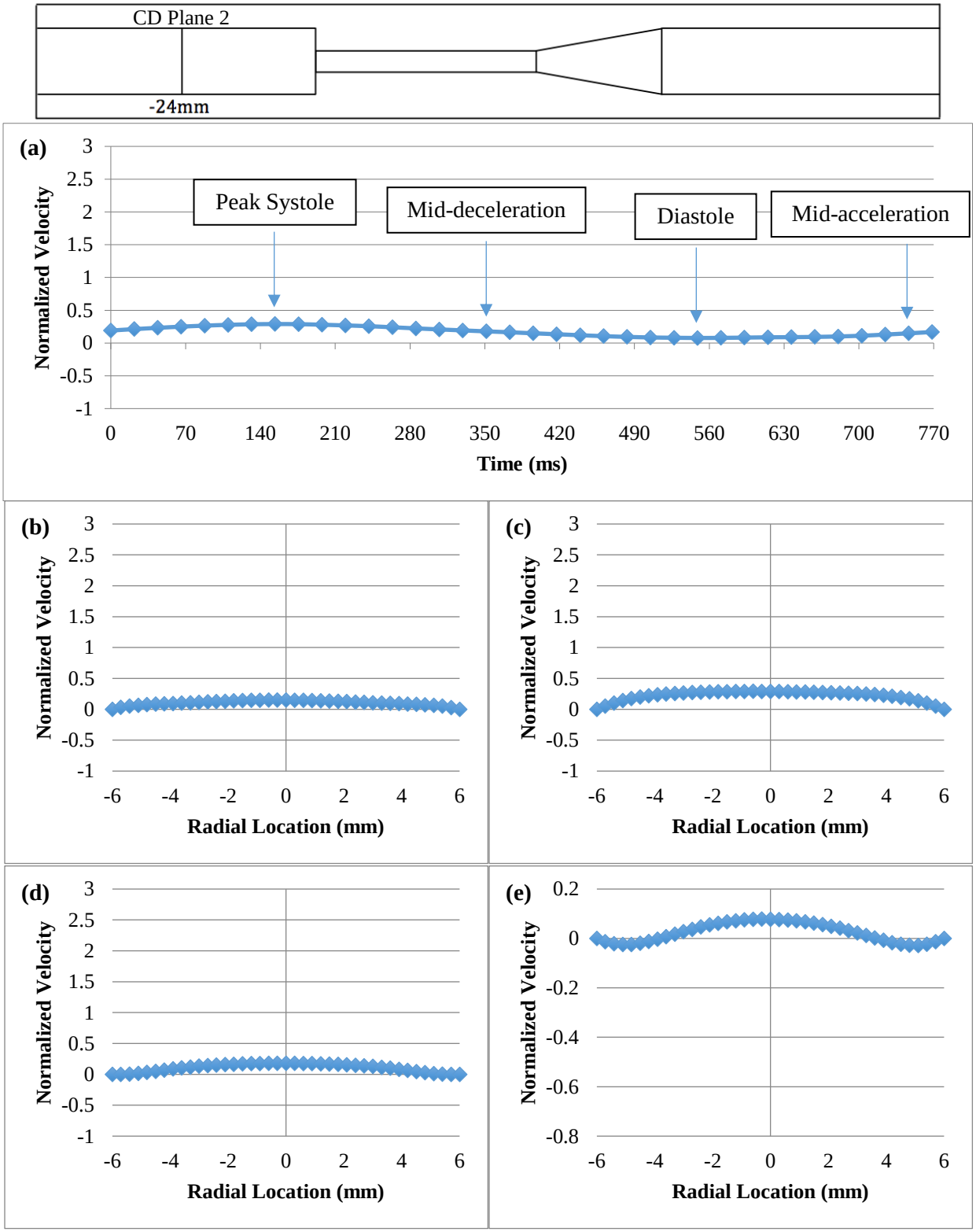

Figure 30. (a) Centerline Velocity, (b) Mid-acceleration, (c) Systolic, (d) Mid-deceleration, and (e) Diastolic Velocity for Conical Diffuser Plane 2. Note that Diastolic Velocity is at Different Scale.

Figure 31 shows the velocities at CD5, which is located just beyond the sudden contraction. Just after entering the contraction, the flow profile is very blunted across most of the cross section during each phase of flow, especially during mid-acceleration, systole, and mid-deceleration. The profile is still very blunted in the center of the cross section during diastole, but there are areas of negative flow close to the walls. The standard deviation is high near the walls during systole, and is particularly high within the recirculation regions of diastole.

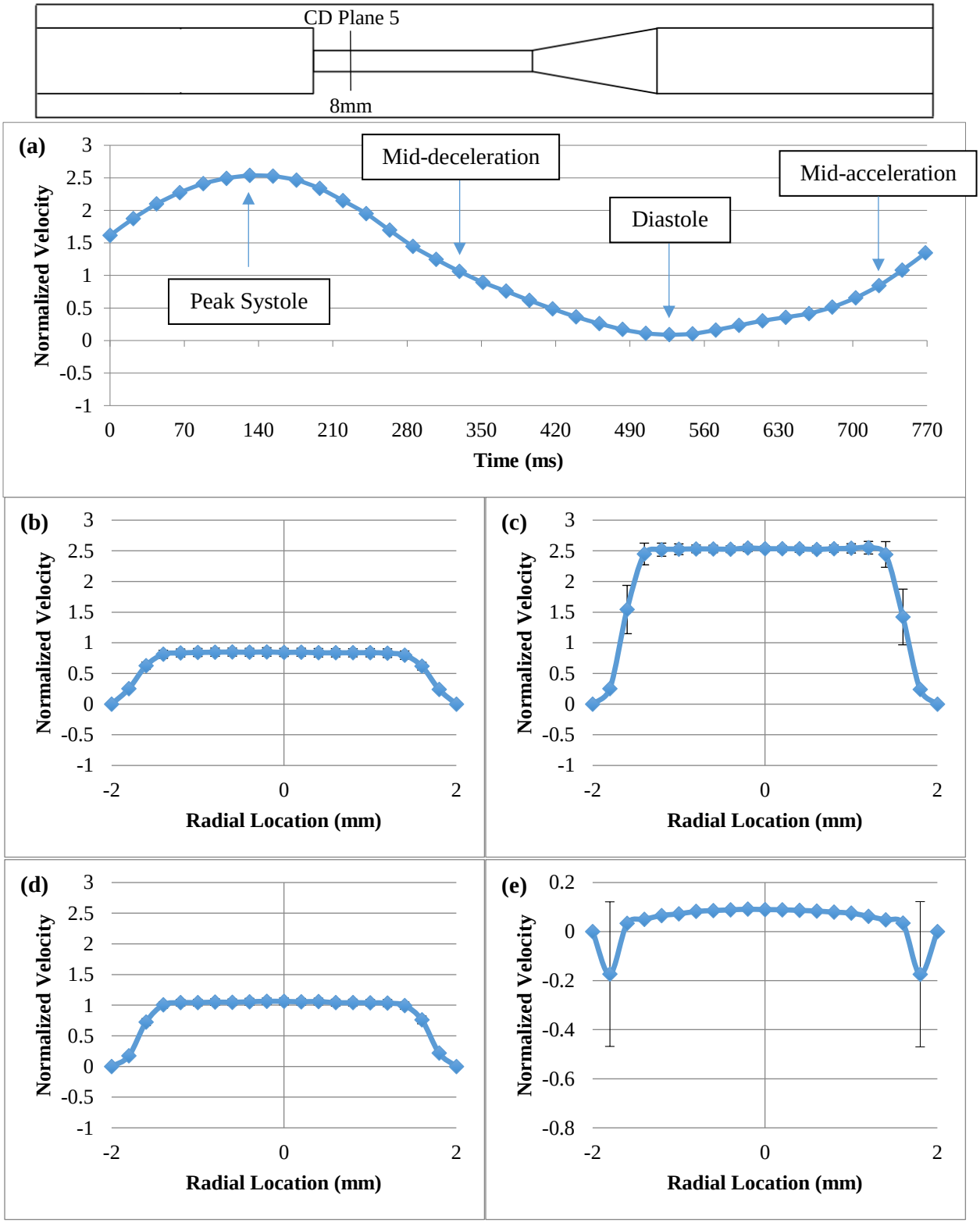

Figure 31. (a) Centerline Velocity, (b) Mid-acceleration, (c) Systolic, (d) Mid-deceleration, and (e) Diastolic Velocity for Conical Diffuser Plane 5. Note that Diastolic Velocity is at Different Scale.

The pertinent velocities at CD6 in the throat region are shown in Figure 32. The mid-acceleration, systolic, and mid-deceleration curves are blunted, but significantly less so than at CD5. The systolic velocity curve reaches a maximum velocity of 4.99 m/s at the center of the plane. This is similar to the peak velocity found during systole at SE5 of 4.92 m/s. The flow profile at CD6 is slightly less blunted in shape than at SE5, explaining the minor difference in peak velocities. During diastole, the flow profile is parabolic and positive across the entire plane, resembling the diastolic velocity curve at SE5. There are no longer any recirculation zones. The velocity during mid-acceleration and mid-deceleration both are flatter curves than the systolic velocity curve, and have maximum velocities of 2.0 m/s and 2.5 m/s, respectively. Standard deviations are somewhat large across the entire cross section during systole, particularly in the regions close to the walls.

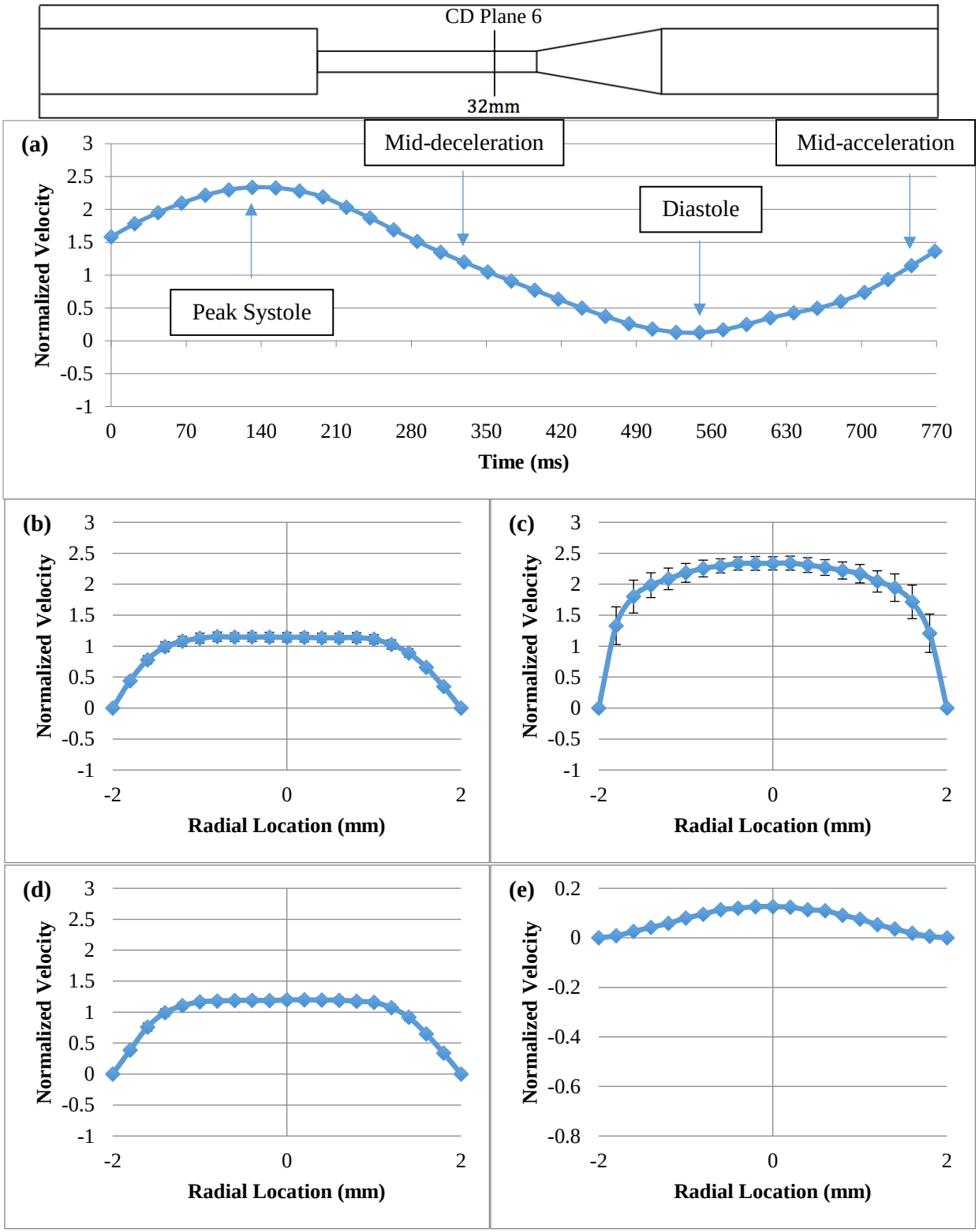

Figure 32. (a) Centerline Velocity, (b) Mid-acceleration, (c) Systolic, (d) Mid-deceleration, and (e) Diastolic Velocity for Conical Diffuser Plane 6. Note that Diastolic Velocity is at Different Scale.

Figure 33 shows the flow profiles for CD7, which is at the inlet of the conical diffuser. The flow profiles and velocity magnitudes are very similar to those of CD6.

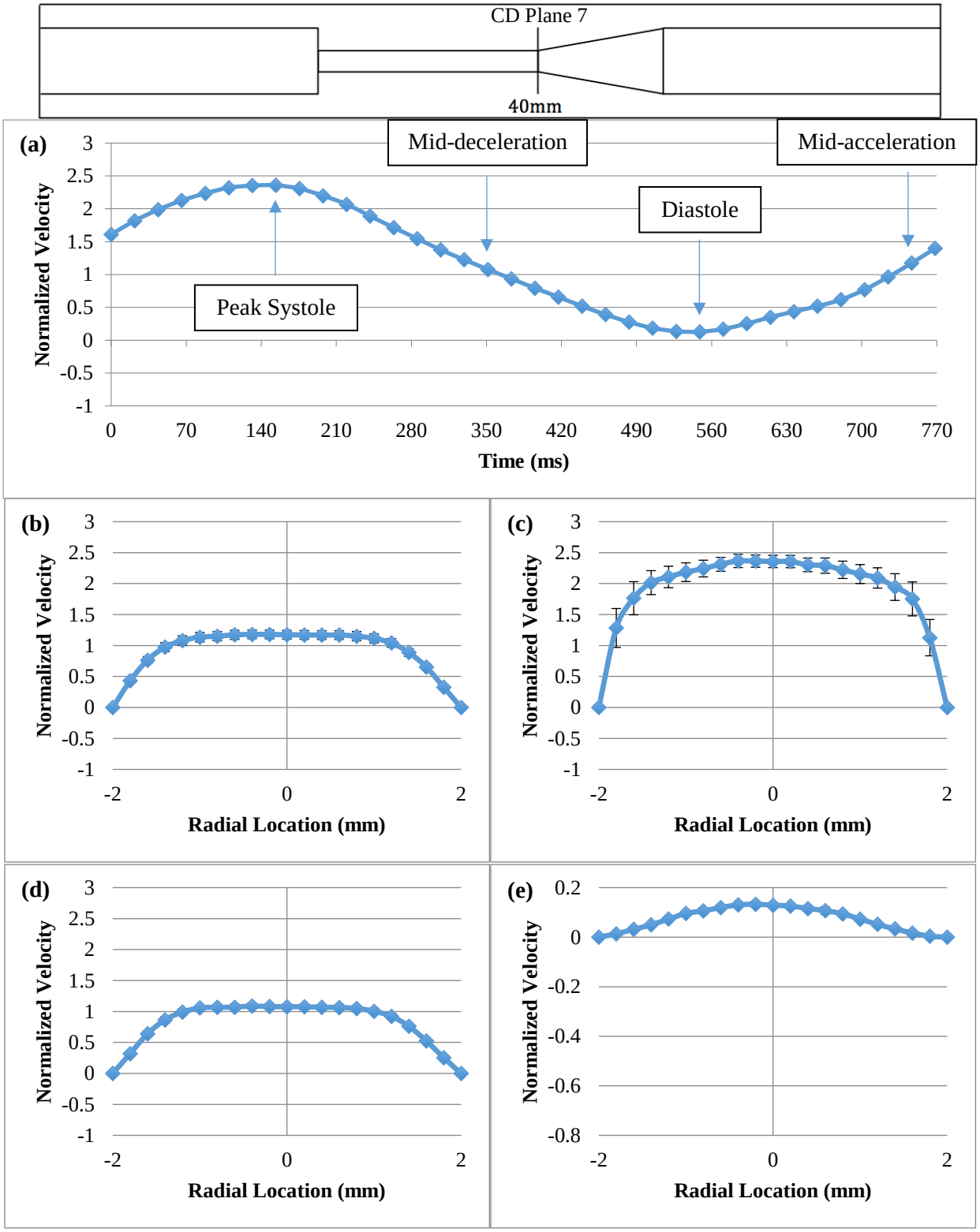

Figure 33. (a) Centerline Velocity, (b) Mid-acceleration, (c) Systolic, (d) Mid-deceleration, and (e) Diastolic Velocity for Conical Diffuser Plane 7. Note that Diastolic Velocity is at Different Scale.

Figure 34 shows CD8, which is located within the conical diffuser. As the diameter of the diffuser increases, the flow profile expands, and the maximum velocity decreases to 4.6 m/s during systole. Separation of the wall boundary layer has caused areas of recirculation to develop during diastole. Similar to the sudden expansion orientation, standard deviations are significant in the recirculation regions during diastole, indicating that flow is unstable in those regions. Mid-acceleration and mid-deceleration are flatter curves near the center of the plane, and are near-zero close to the walls. Asymmetry in the recirculation regions at this plane and at further planes downstream may be caused by disturbances created by the edge of the expansion [57].

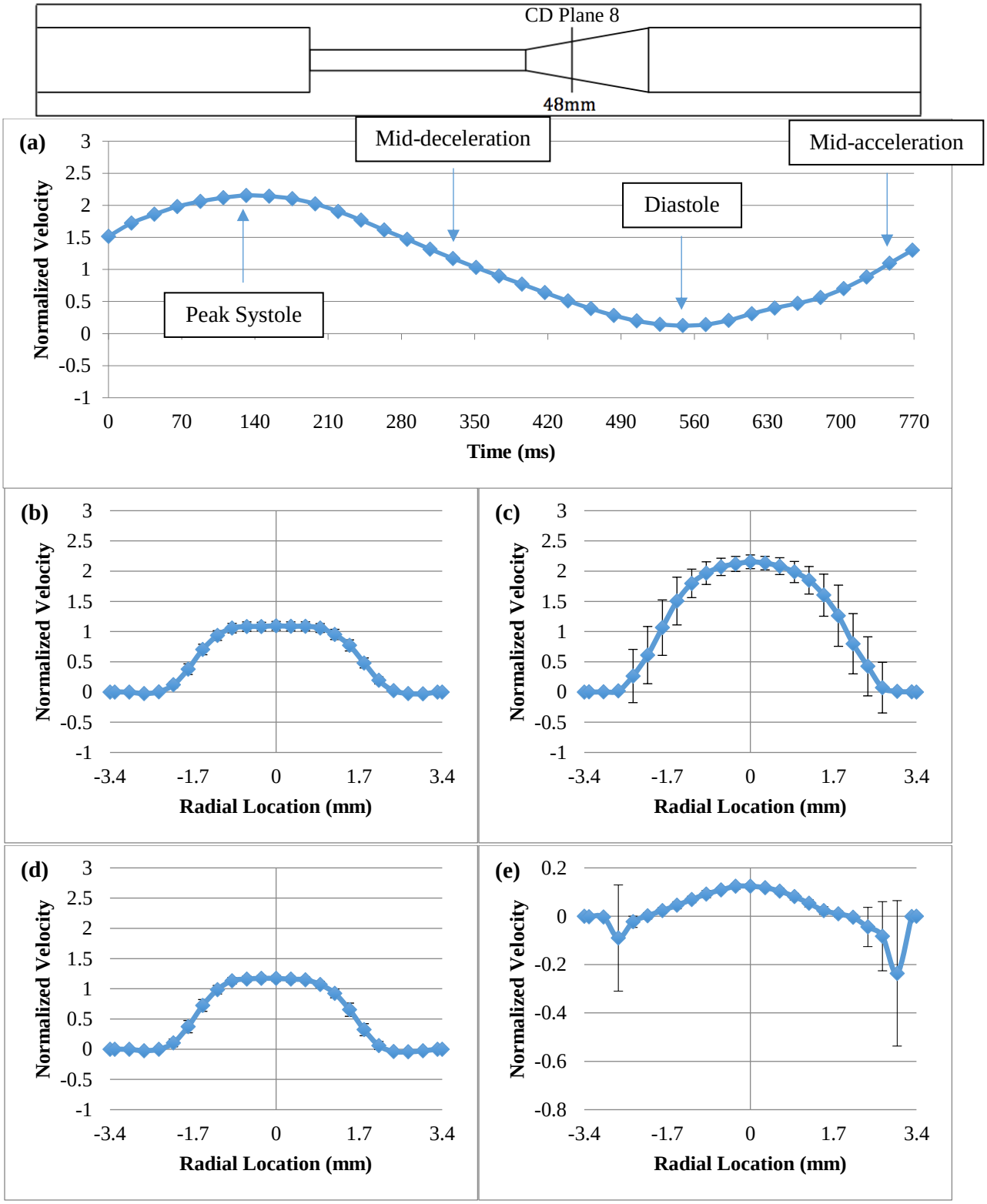

Figure 34. (a) Centerline Velocity, (b) Mid-acceleration, (c) Systolic, (d) Mid-deceleration, and (e) Diastolic Velocity for Conical Diffuser Plane 8. Note that Diastolic Velocity is at Different Scale.

CD9, shown in Figure 35, is located 8 mm farther downstream in the conical diffuser. Flow during mid-acceleration is flat at the center of the plane, and near-zero close to the walls. The velocity profile during systole has widened and decreased in magnitude, to 3.78 m/s at the centerline. Flow is near-zero close to the wall during systole, indicating that flow has separated from the wall. Mid-deceleration now has areas of negative flow reaching -0.1 m/s close to the walls. The recirculation regions during diastole have become more negative and grown wider than at CD8. Standard deviations are again significant in the areas of negative flow during diastole. The standard deviation is also significant during systole, indicating along with the fluctuating centerline velocity curve that the flow is unstable during systole.

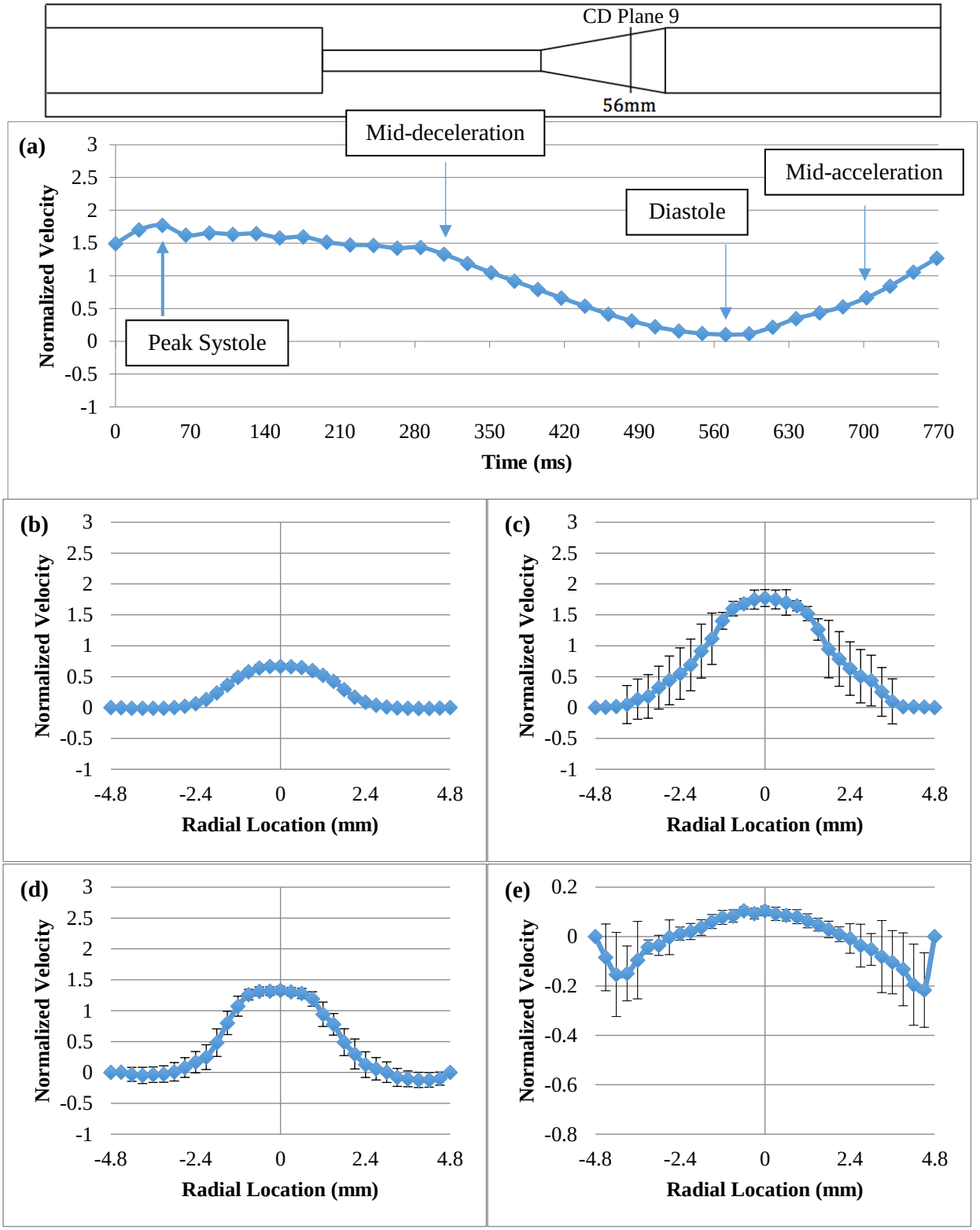

Figure 35. (a) Centerline Velocity, (b) Mid-acceleration, (c) Systolic, (d) Mid-deceleration, and (e) Diastolic Velocity for Conical Diffuser Plane 9. Note that Diastolic Velocity is at Different Scale.

Figure 36 shows CD10, which is located after the conical diffuser. The profile during mid-acceleration is similar to that of CD9, with positive parabolic flow in the center of the plane surrounded by near-zero flow close to the walls. The systolic velocity profile has begun to reattach, becoming more parabolic and decreasing in centerline magnitude to 3.0 m/s. The diastolic velocity curve still has areas of recirculation near the walls, although they have decreased in magnitude. Instabilities are high across the entire diastolic curve, especially in the recirculation regions. The mid-deceleration curve is significantly more spread out than the mid-acceleration curve, and the standard deviation is greater for the mid-deceleration curve. Flow has become even more unstable during systole, indicated by the inverse shape of the portion of the centerline velocity curve near peak systole and the significant standard deviation during peak systole.

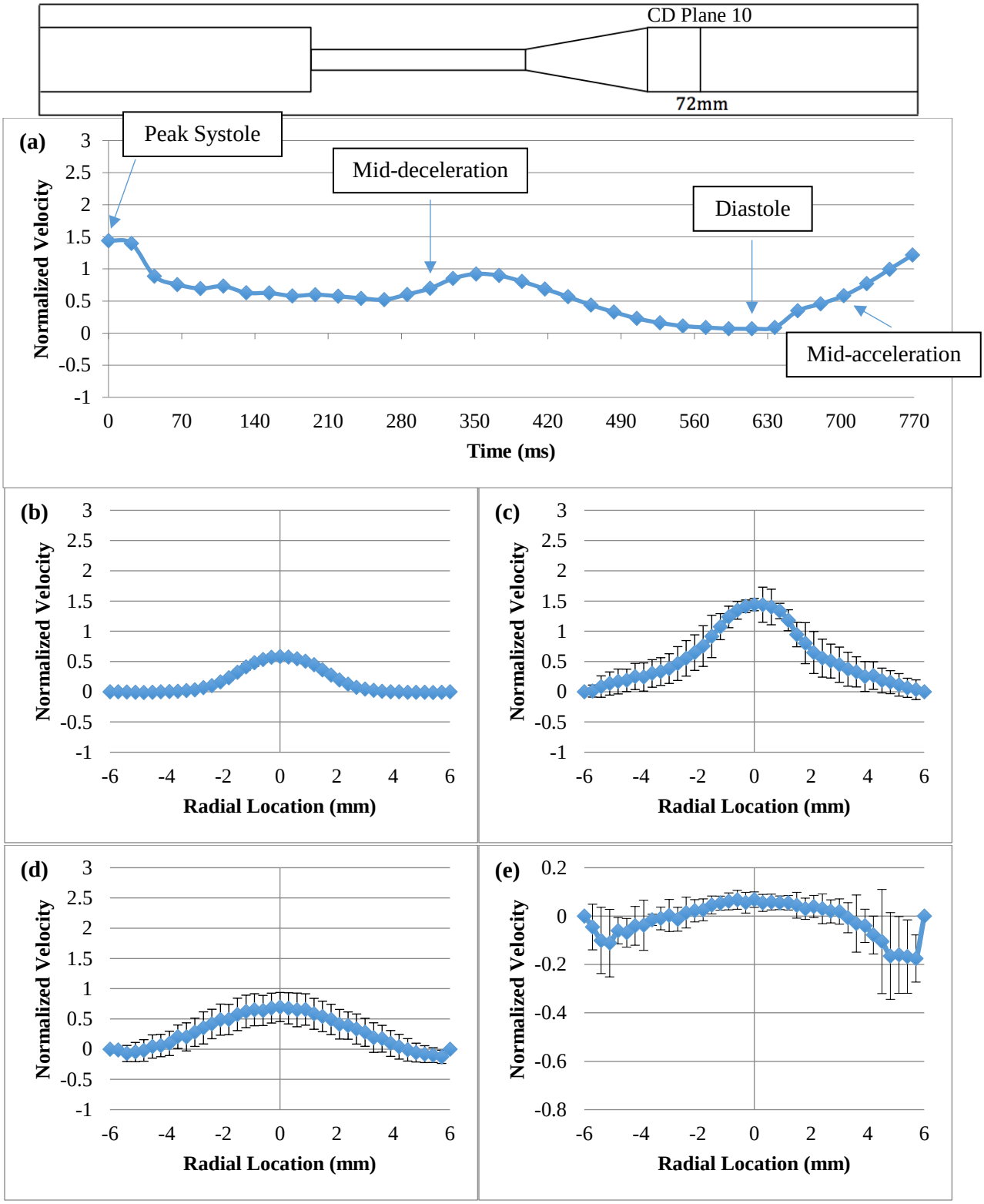

Figure 36. (a) Centerline Velocity, (b) Mid-acceleration, (c) Systolic, (d) Mid-deceleration, and (e) Diastolic Velocity for Conical Diffuser Plane 10. Note that Diastolic Velocity is at Different Scale.

Figure 37 shows the velocity curves at CD11, which is another 28 mm downstream from CD10. At this point in the model, the flow has nearly reattached, and the flow profiles have nearly returned to the fully developed shapes observed at CD2. The systolic velocity profile still shows some instability where the flow is reattaching. The maximum value at the center of the plane during systole is 1.68 m/s. The diastolic velocity is nearly zero across the entire plane with small regions of regurgitant flow near the walls. The standard deviation is significant across the entire plane during diastole. The mid-acceleration and mid-deceleration curves are parabolic with very small magnitudes, and near-zero standard deviations.

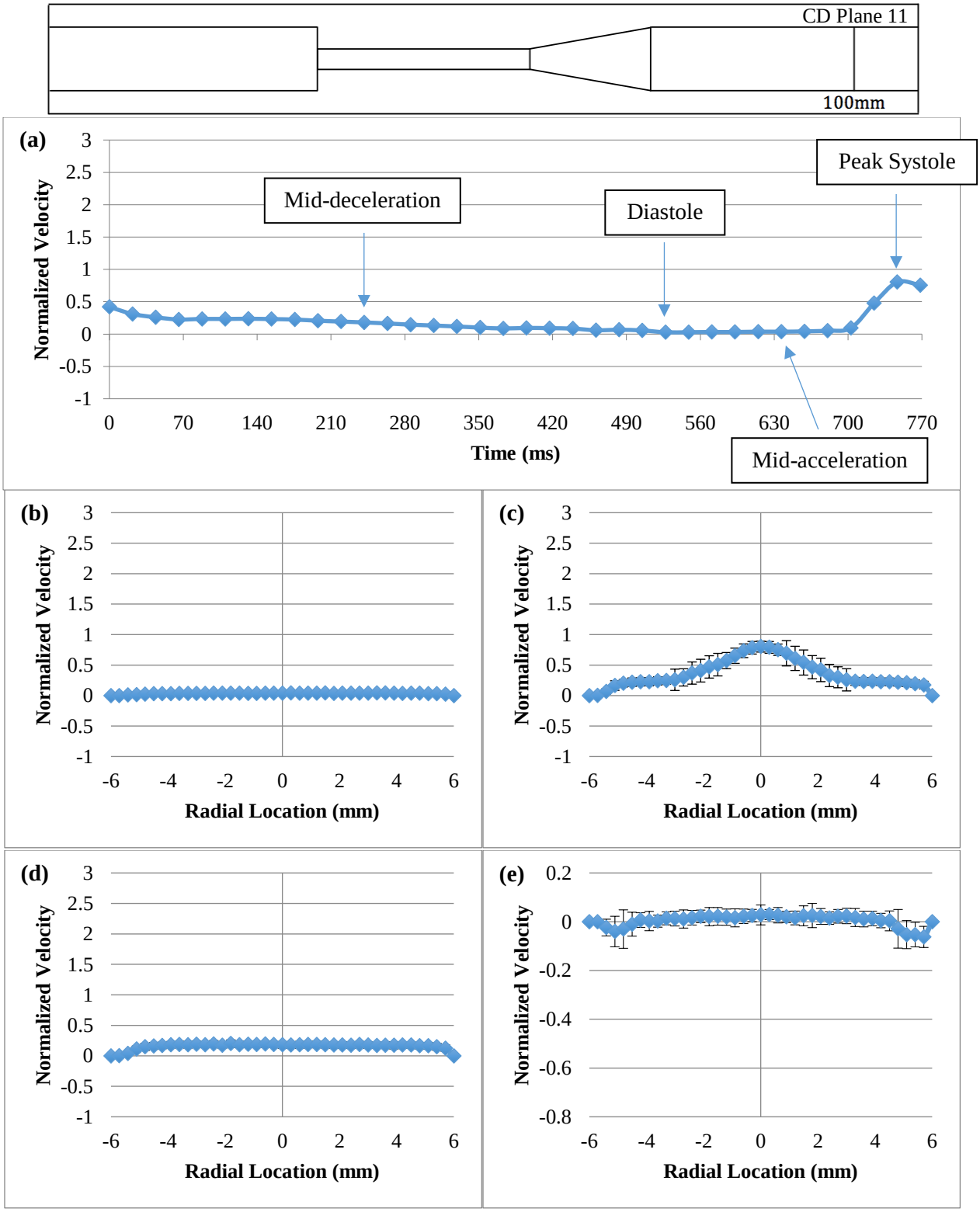

Figure 37. (a) Centerline Velocity, (b) Mid-acceleration, (c) Systolic, (d) Mid-deceleration, and (e) Diastolic Velocity for Conical Diffuser Plane 10. Note that Diastolic Velocity is at Different Scale.

5.2.2 Principal Reynolds Stresses (PRS)

Table 3 shows the PRSs measured at each plane and during each point within the cardiac cycle. The maximum PRS values calculated in the study were 1689.67 Pa and 1983.95 Pa at SE10 and CD7, respectively, both during systole. Both of these planes are located in the downstream regions following the sudden expansion and conical diffuser. Significant PRSs were also calculated within the throat in the conical diffuser orientation, particularly at CD5, where it reached 1674.4 Pa.

Table 3. Peak Reynolds Stresses in Pa at each Plane and for each Phase of the Cardiac Cycle

		Mid-Acceleration	Systole	Mid-Deceleration	Diastole
Sudden Expansion Orientation	**Plane 2**	1.72	8.65	0.83	0.54
	Plane 5	37.10	13.87	19.76	1.21
	Plane 6	45.44	65.03	28.57	2.10
	Plane 7	127.49	944.69	126.84	31.94
	Plane 8	70.34	535.32	69.54	186.04
	Plane 10	121.73	1689.67	230.93	683.38
	Plane 11	3.39	405.58	82.39	63.5
Conical Diffuser Orientation	**Plane 2**	0.95	1.67	0.68	0.46
	Plane 5	37.13	1674.4	29.98	673.36
	Plane 6	49.04	730.32	32.31	1.21
	Plane 7	43.99	751.50	19.65	1.56
	Plane 8	63.94	1983.95	90.55	718.82
	Plane 9	23.8	1640.89	447.05	221.86
	Plane 10	24.44	941.95	581.47	350.93
	Plane 11	3.84	328.61	28.43	49.25

Figure 38 shows the principal Reynolds stresses during mid-acceleration in the sudden expansion orientation. At SE2, PRSs are negligible. Within the throat, PRSs are slightly elevated near the center of the cross-section. Following the sudden expansion at SE7, SE8, and SE10, peak PRSs occur along the boundary of the free shear layer, reaching a maximum value of 127.49 Pa at SE7. By SE11, the flow has reattached sufficiently during mid-acceleration for the PRSs to become negligible.

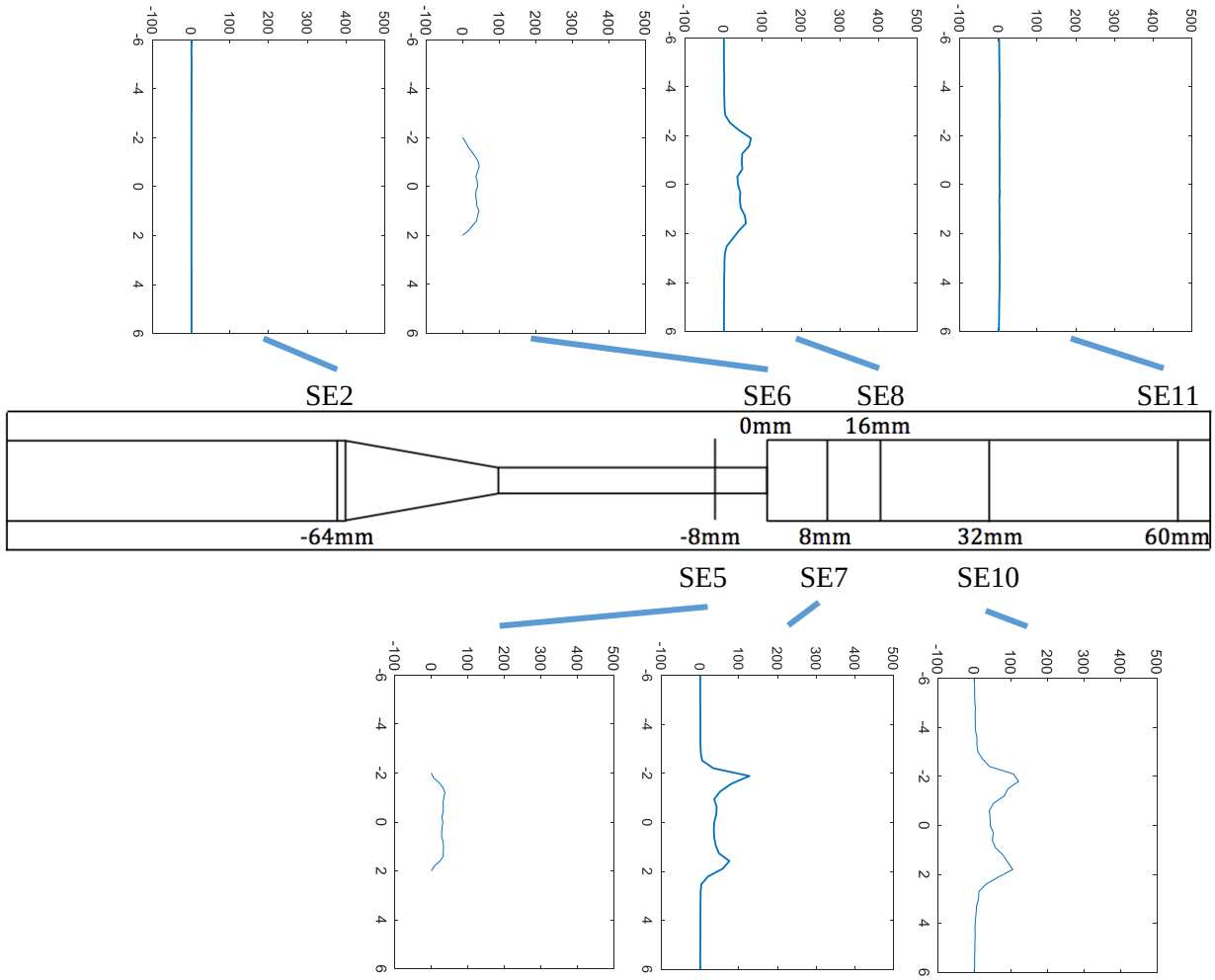

Figure 38. Principal Reynolds Stresses (in Pa, on Horizontal Axes) during Mid-Acceleration in the Sudden Expansion Orientation. Vertical Axes Show Radial Location in mm.

Figure 39 shows the PRSs at each plane in the sudden expansion direction during systole. PRSs are low in the fully-developed region and in the throat. Following the sudden expansion at SE7, there are spikes of high PRSs just outside the recirculation region and along the free shear layer. As flow moves farther from the sudden expansion, stress in the center of the plane begins to increase. At SE8, peak PRSs still occur at the edges of the recirculation regions, but stress has increased at the center of the plane. At SE10, stress is elevated across the entire plane outside of the recirculation regions, reaching a peak value of 1689.67 Pa. PRSs have declined by SE11, with slightly elevated values near the center of the plane.

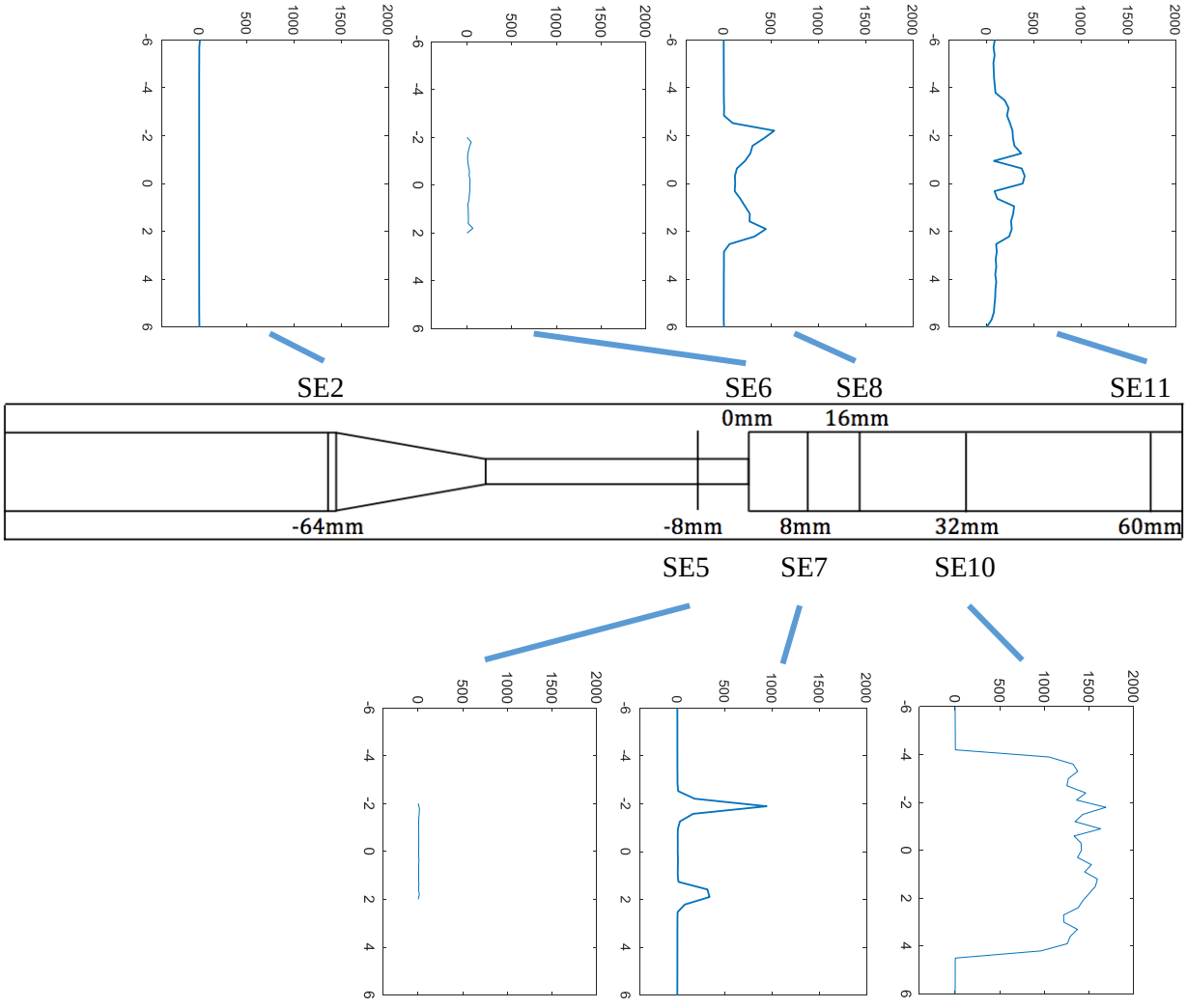

Figure 39. Principal Reynolds Stresses (in Pa, on Horizontal Axes) during Peak Systole in the Sudden Expansion Orientation. Vertical Axes Show Radial Location in mm.

Figure 40 shows the PRSs during mid-deceleration in the sudden expansion orientation. The trend during mid-deceleration mirrors the trends and values of mid-acceleration with the exception of SE10 and SE11, where they are more elevated. Following the sudden expansion, stress is highest along the free shear layer. As flow moves downstream, the peak stress on either side of the plane begins to converge. The peak stress of 230.93 Pa occurs at the boundary of the free shear layer at SE10.

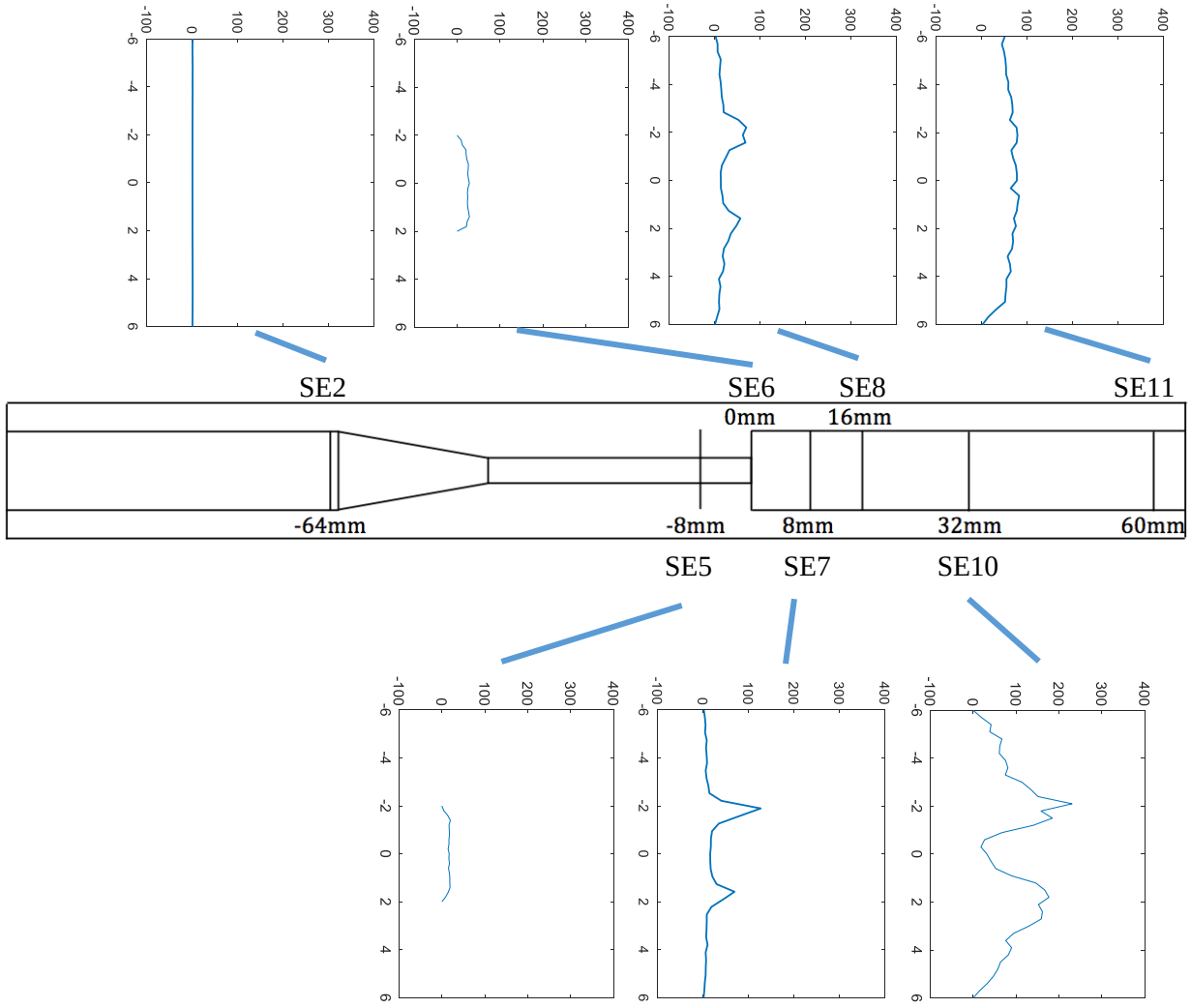

Figure 40. Principal Reynolds Stresses (in Pa, on Horizontal Axes) during Mid-Deceleration in the Sudden Expansion Orientation. Vertical Axes Show Radial Location in mm.

Figure 41 shows the PRSs during diastole in the sudden expansion orientation. Significant stresses occur at SE8 and SE10 within the recirculation regions. The recirculation observed during diastole at each of these planes was greater than at any other location in the sudden expansion orientation. Stresses are significantly higher at SE10 than at SE8, reaching a maximum value of 683.38 Pa. Commensurately, the regurgitant flow at SE10 is significantly greater in magnitude than at SE8.

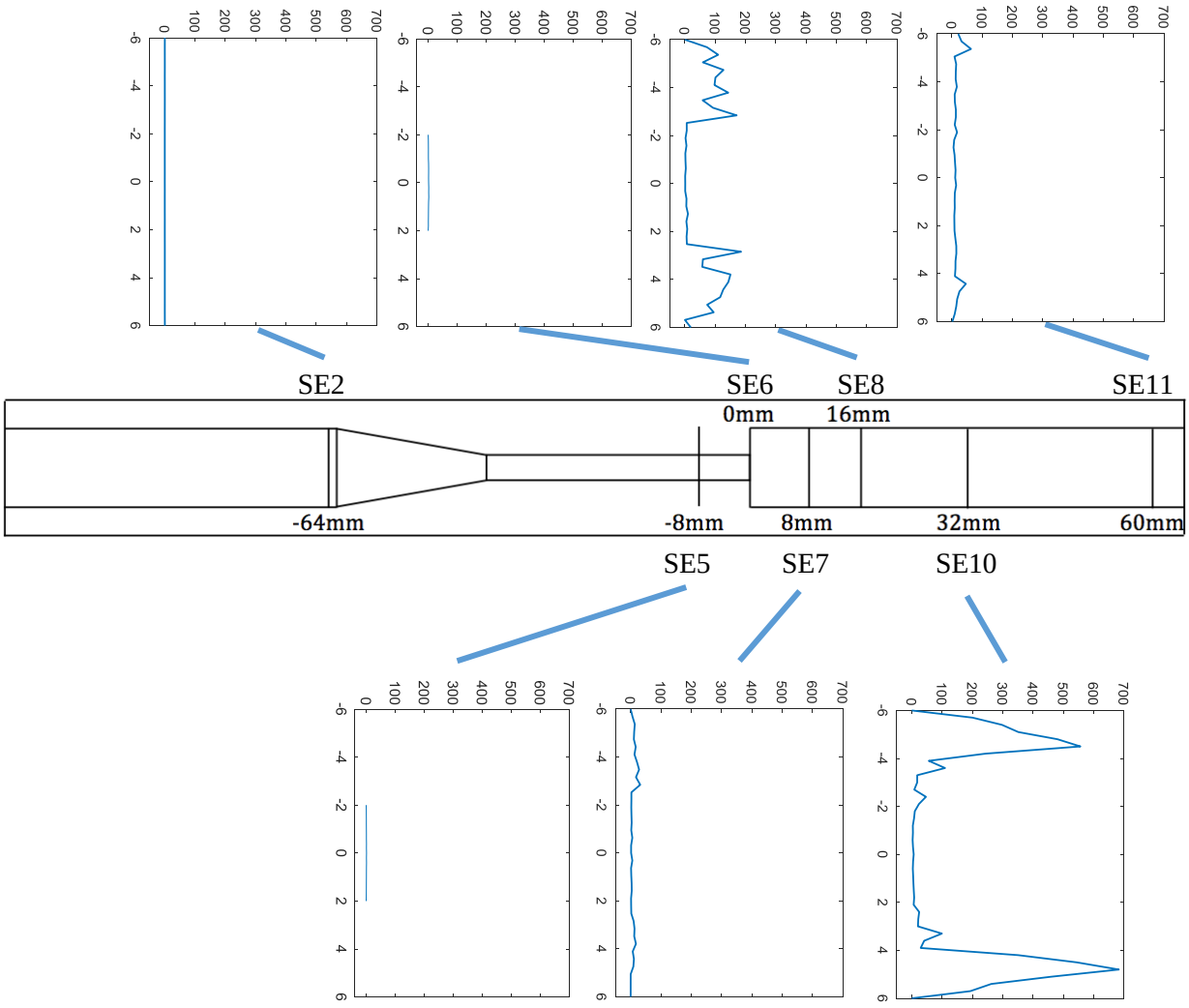

Figure 41. Principal Reynolds Stresses (in Pa, on Horizontal Axes) during Diastole in Sudden Expansion Orientation. Vertical Axes Show Radial Location in mm.

Figure 42 shows the PRSs during mid-acceleration in the conical diffuser orientation. Stresses are low at each plane, and are only slightly elevated within the throat and at the boundary of the free shear layer at CD8, where they reach a maximum value of 63.94 Pa.

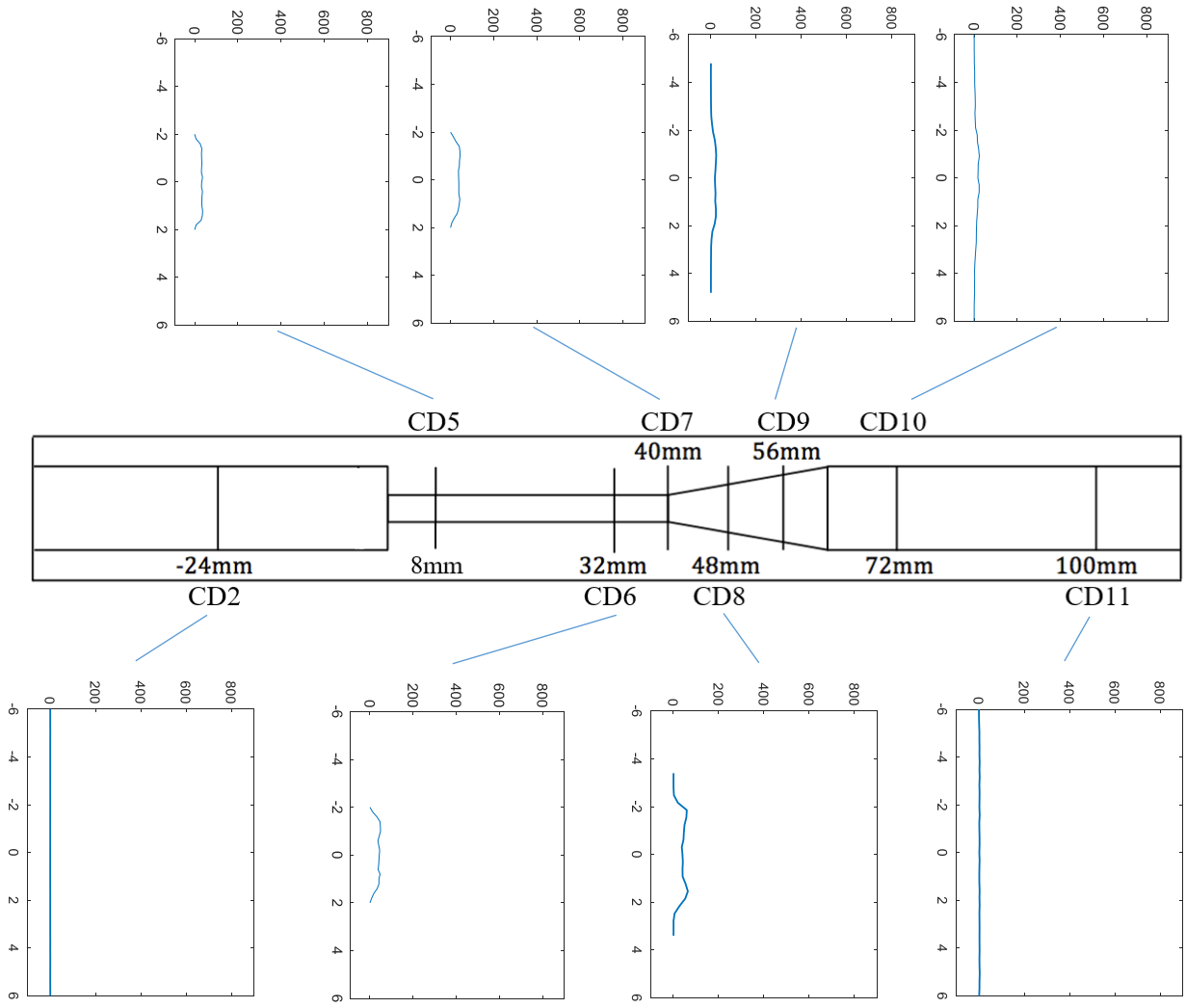

Figure 42. Principal Reynolds Stresses (in Pa, on Horizontal Axes) during Mid-Acceleration in Conical Diffuser Orientation. Vertical Axes Show Radial Location in mm.

Figure 43 shows the PRSs in the conical diffuser orientation during systole. At CD2, PRSs are negligible. Within the throat region, PRSs are maximum at the walls, peaking at 1674.4 Pa at CD5. Within the diffuser, PRSs reach peak values of 1983.95 Pa and 1640.89 Pa for CD8 and CD9, respectively, at the edges of the separation regions. At CD10, PRSs are still highest at the boundary of the separation region, but have declined in magnitude. At CD11, Reynolds stresses have declined substantially.

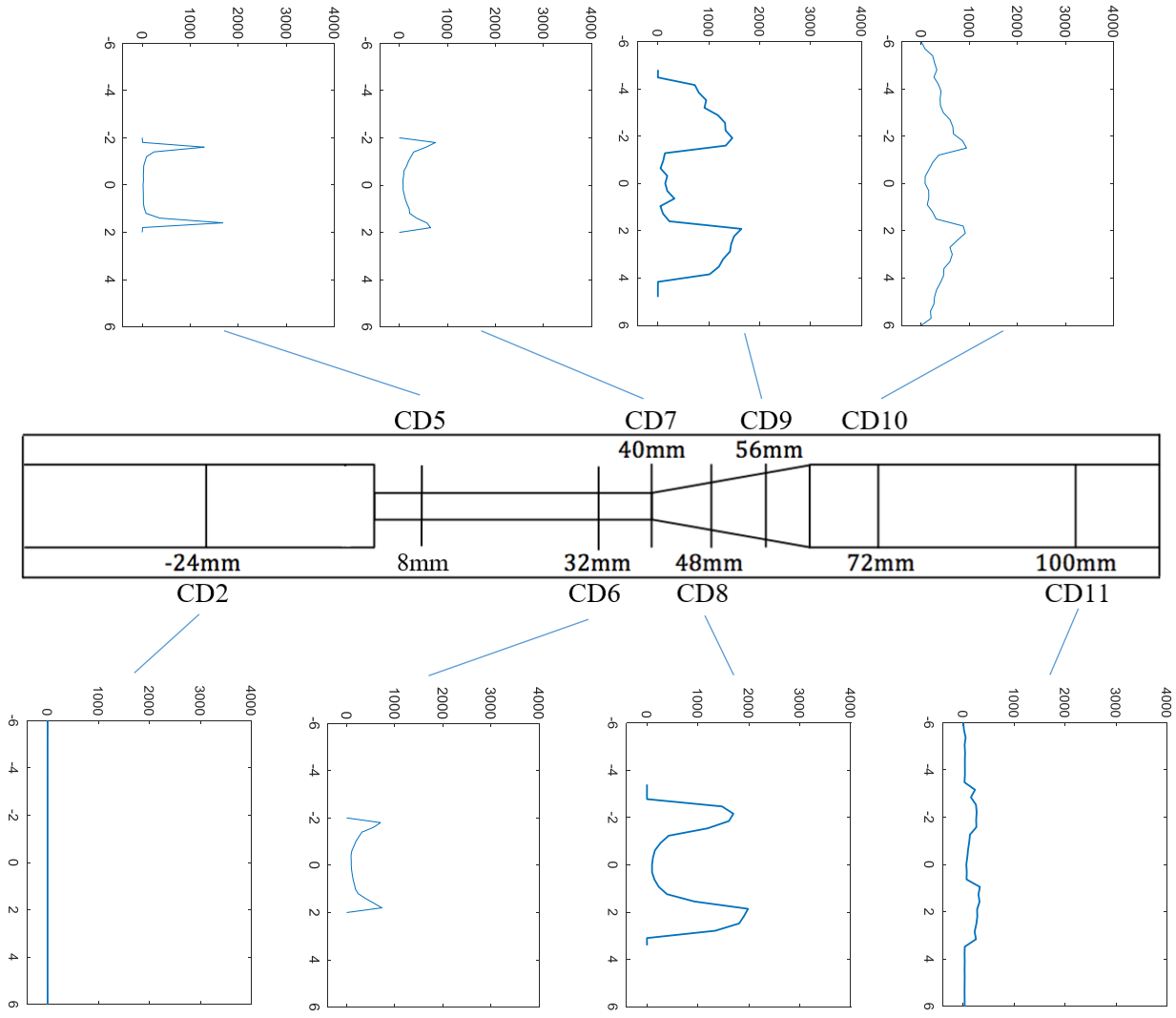

Figure 43. Principal Reynolds Stresses (in Pa, on Horizontal Axes) during Peak Systole in Conical Diffuser Orientation. Vertical Axes Show Radial Location in mm.

Figure 44 shows the PRSs during mid-deceleration in the conical diffuser orientation. Stress increases as fluid moves farther downstream from the conical diffuser inlet, reaching the peak value of 581.47 Pa at CD10 near the center of the plane.

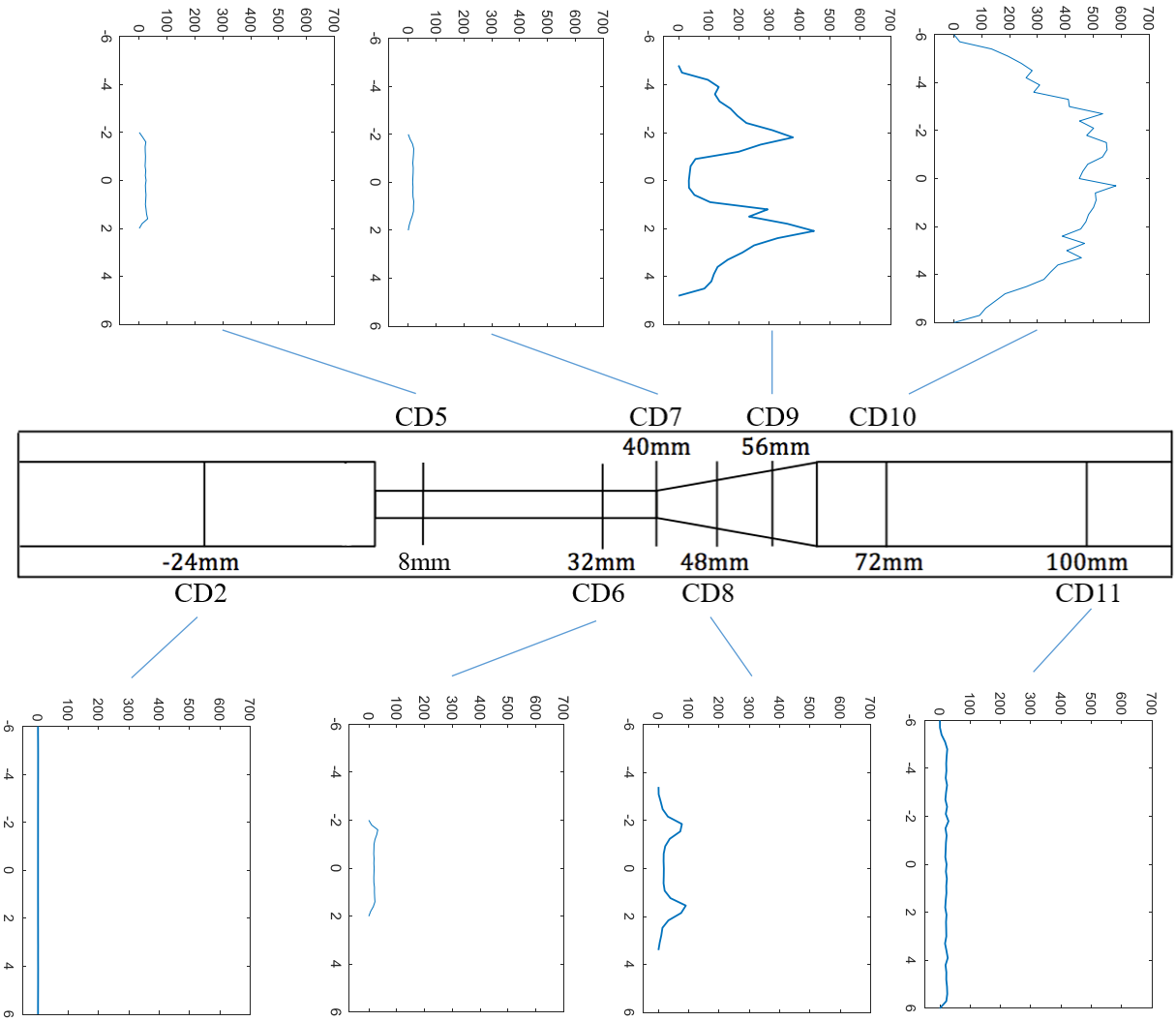

Figure 44. Principal Reynolds Stresses (in Pa, on Horizontal Axes) during Mid-Deceleration in Conical Diffuser Orientation. Vertical Axes Show Radial Location in mm.

PRSs during diastole are shown in Figure 45 for the conical diffuser orientation. Similar to the sudden expansion orientation, peak stress values occur within the recirculation regions. Stresses are particularly high near the walls at CD5 and CD8, where they are 673.36 Pa and 718.82 Pa, respectively.

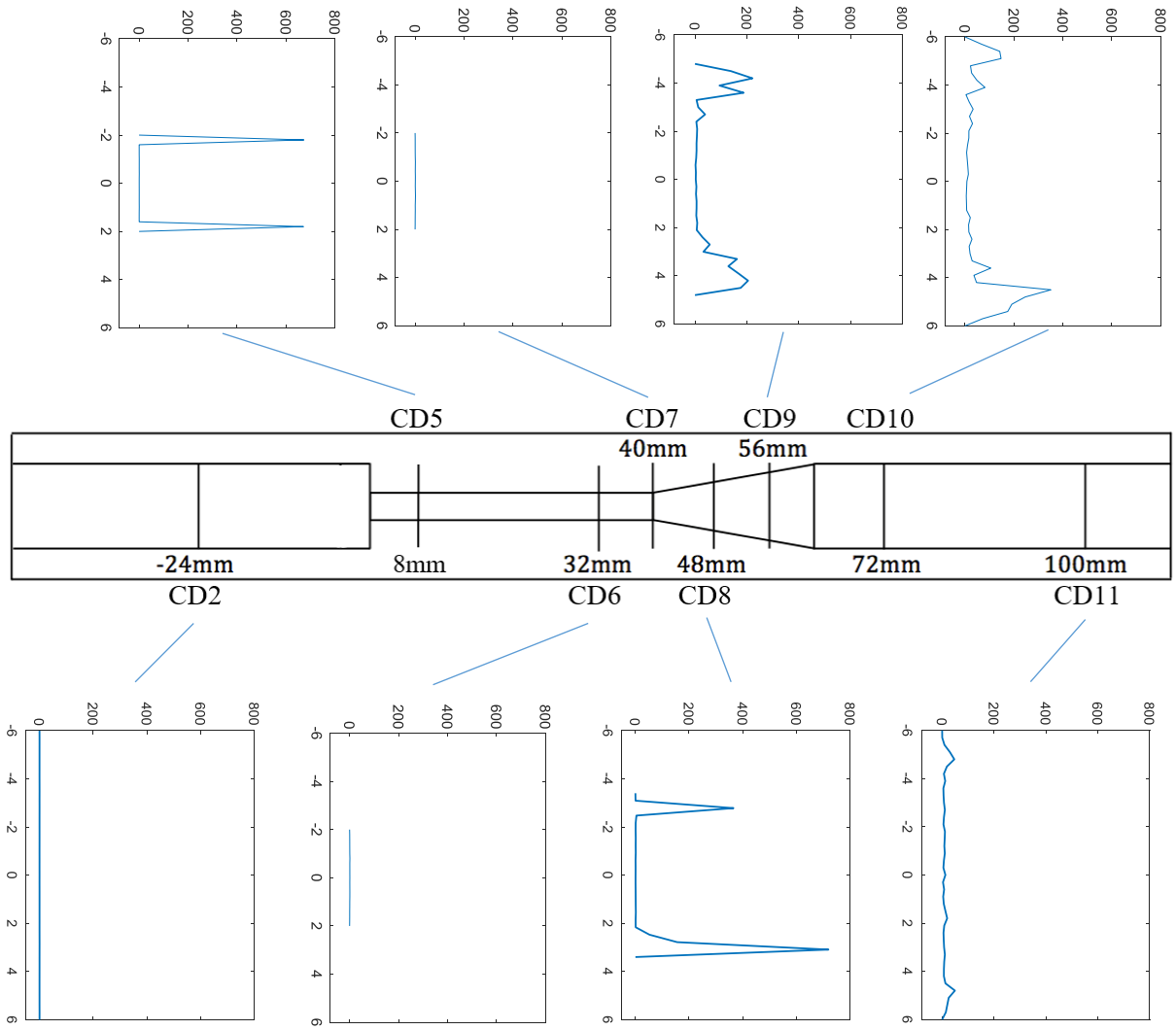

Figure 45. Principal Reynolds Stress (in Pa, on Horizontal Axes) during Diastole in Sudden Expansion Orientation. Vertical Axes Show Radial Location in mm.

5.2.3 Maximum Reynolds Shear Stresses (MRSS)

Table 4 shows the MRSSs at each plane and for each time within the cardiac cycle. Similar to the findings for the PRSs, the peak MRSSs occur at SE10 and CD8, and are equal to 953.17 Pa and 1772.19 Pa, respectively. As flow moves farther from the sudden expansion and the conical diffuser, MRSS values decline.

Table 4. Maximum Reynolds Shear Stresses in Pa at each Plane and for each Phase of the Cardiac Cycle

		Mid-Acceleration	Systole	Mid-Deceleration	Diastole
Sudden Expansion Orientation	**Plane 2**	0.85	4.31	0.39	0.24
	Plane 5	18.25	6.74	9.70	.5573
	Plane 6	22.50	31.85	13.87	1.02
	Plane 7	63.5	471.47	63.04	10.79
	Plane 8	34.88	220.82	33.68	65.55
	Plane 10	42.31	545.3	72.97	229.56
	Plane 11	1.26	159.59	20.6	16.82
Conical Diffuser Orientation	**Plane 2**	0.44	0.76	0.31	0.21
	Plane 5	18.43	752.88	14.70	308.52
	Plane 6	24.18	361.95	15.83	0.59
	Plane 7	21.44	372.04	9.55	0.76
	Plane 8	31.75	797.79	44.82	200.97
	Plane 9	11.78	538.7	153.03	60.24
	Plane 10	12.13	252.71	193.04	116.52
	Plane 11	1.4	116.43	8	15.87

Figure 46 shows the maximum Reynolds shear stresses at each plane measured in the sudden expansion orientation during mid-acceleration. Shear stresses are low until flow exits the sudden expansion, where shear stress is maximum at the edge of the recirculation region. The maximum recorded shear stress is 63.5 Pa at SE7. Shear stresses decline in magnitude as flow moves downstream.

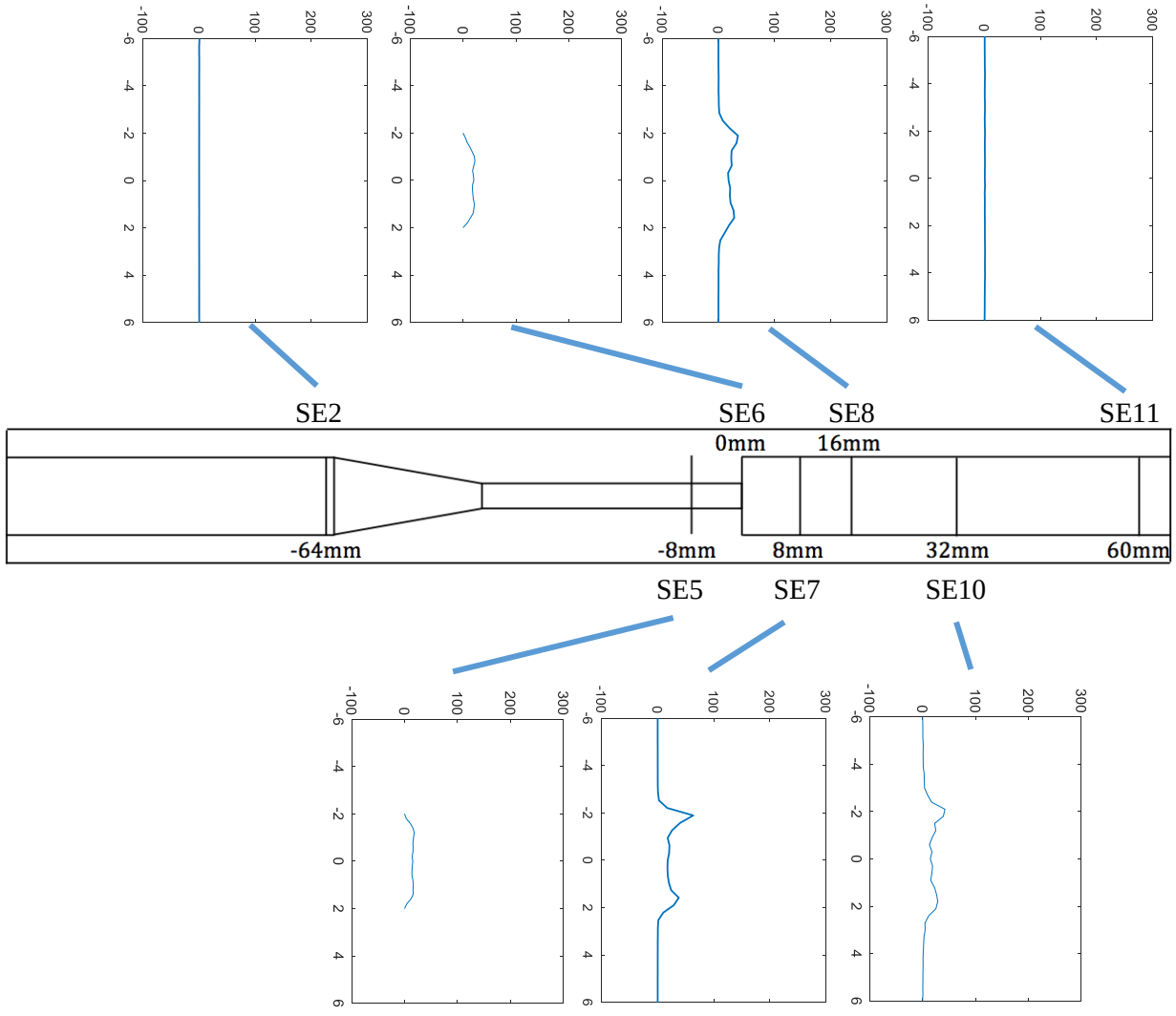

Figure 46. Reynolds Shear Stresses (in Pa, on Horizontal Axes) during Mid-Acceleration in Sudden Expansion Orientation. Vertical Axes Show Radial Location in mm.

Figure 47 shows the MRSS during peak systole in the sudden expansion orientation. Trends are similar to those for PRSs. Shear stress is low in the fully-developed region and within the throat. Downstream of the sudden expansion, peak MRSSs occur along the free shear layer. At SE7, stress is near-zero at all points aside from just outside of the recirculation region, where they reach 471.47 Pa. Moving farther downstream, these two peaks converge, until stress is elevated across the entire cross section at SE10. The peak stress value during systole is 545.3 Pa at SE10.

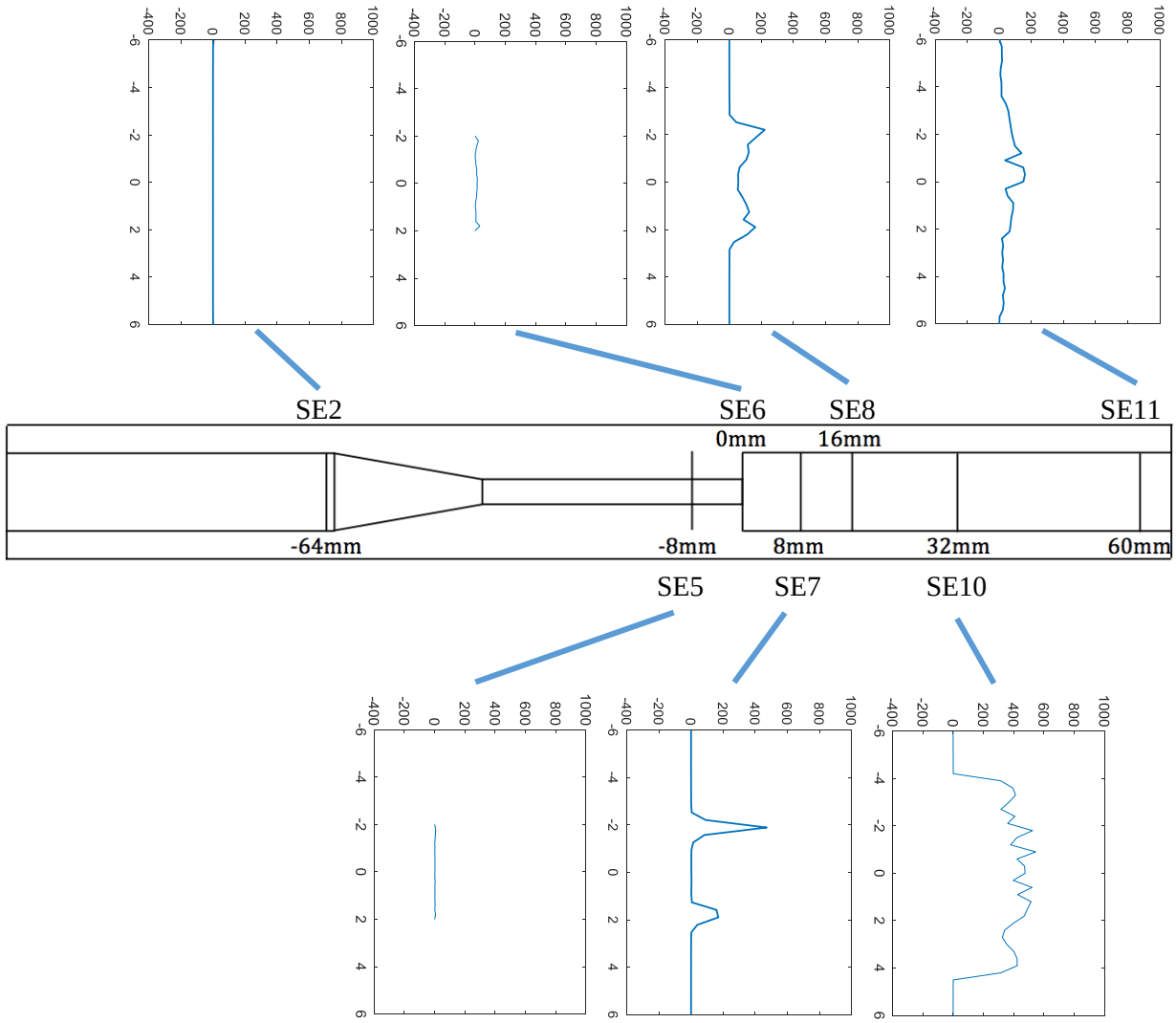

Figure 47. Maximum Reynolds Shear Stresses (in Pa, on Horizontal Axes) during Peak Systole in Sudden Expansion Orientation. Vertical Axes Show Radial Location in mm.

Figure 48 shows the MRSS during mid-deceleration in the sudden expansion orientation. Trends are very similar to those during mid-acceleration and systole. The stress values are similar to those during mid-acceleration as well, except for SE10 and SE11, where the values are higher during mid-deceleration. The peak stress during mid-deceleration was 72.97 Pa outside of the recirculation zone at SE10.

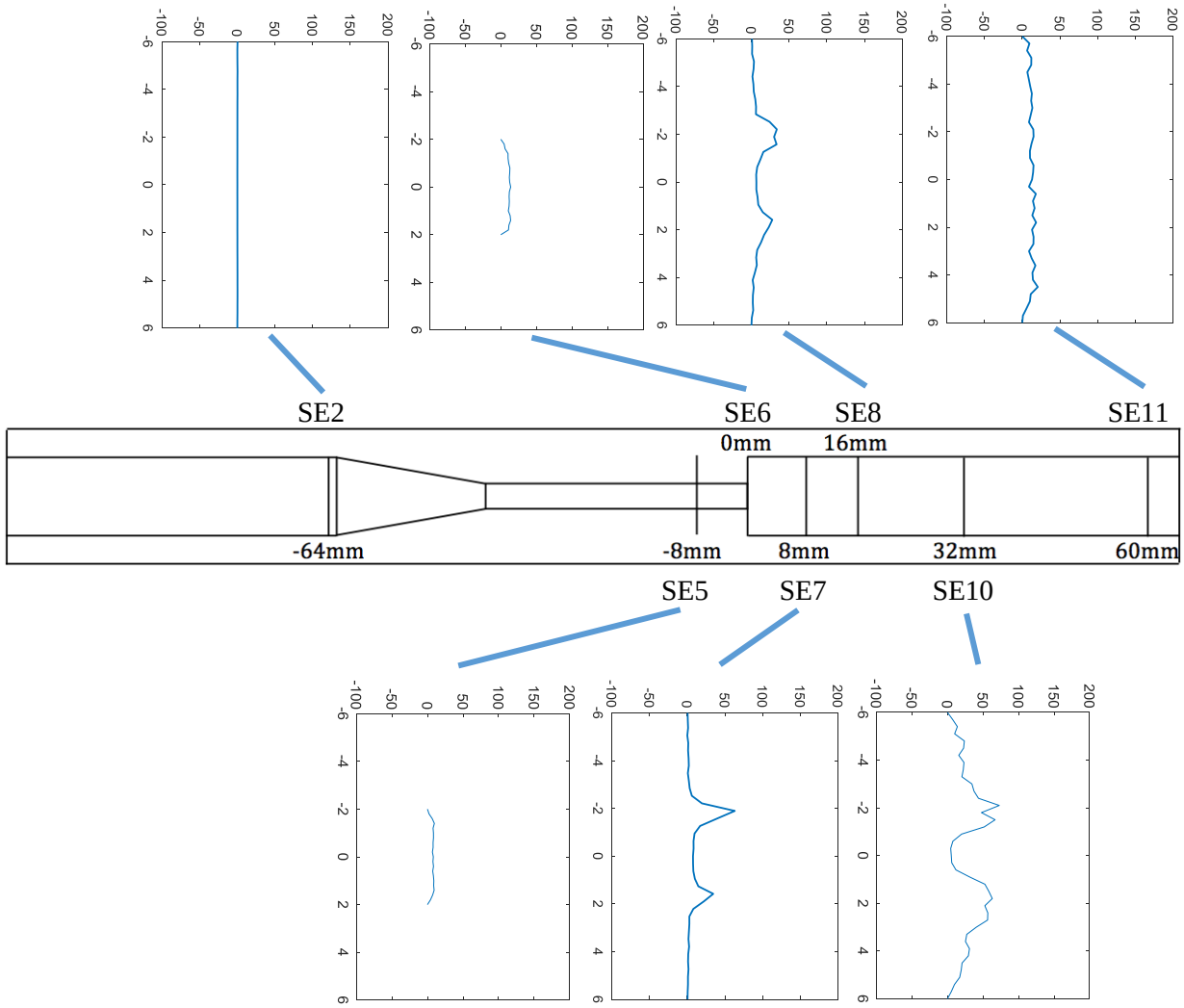

Figure 48. Maximum Reynolds Shear Stresses (in Pa, on Horizontal Axes) during Mid-Deceleration in Sudden Expansion Orientation. Vertical Axes Show Radial Location in mm.

Figure 49 shows the MRSS values during diastole. The maximum shear stresses occur within the recirculation regions of SE8 and SE10. SE10 showed significant areas of recirculation in the same area that high stress levels were calculated. The highest MRSS value calculated during diastole was 229.56 Pa at SE10.

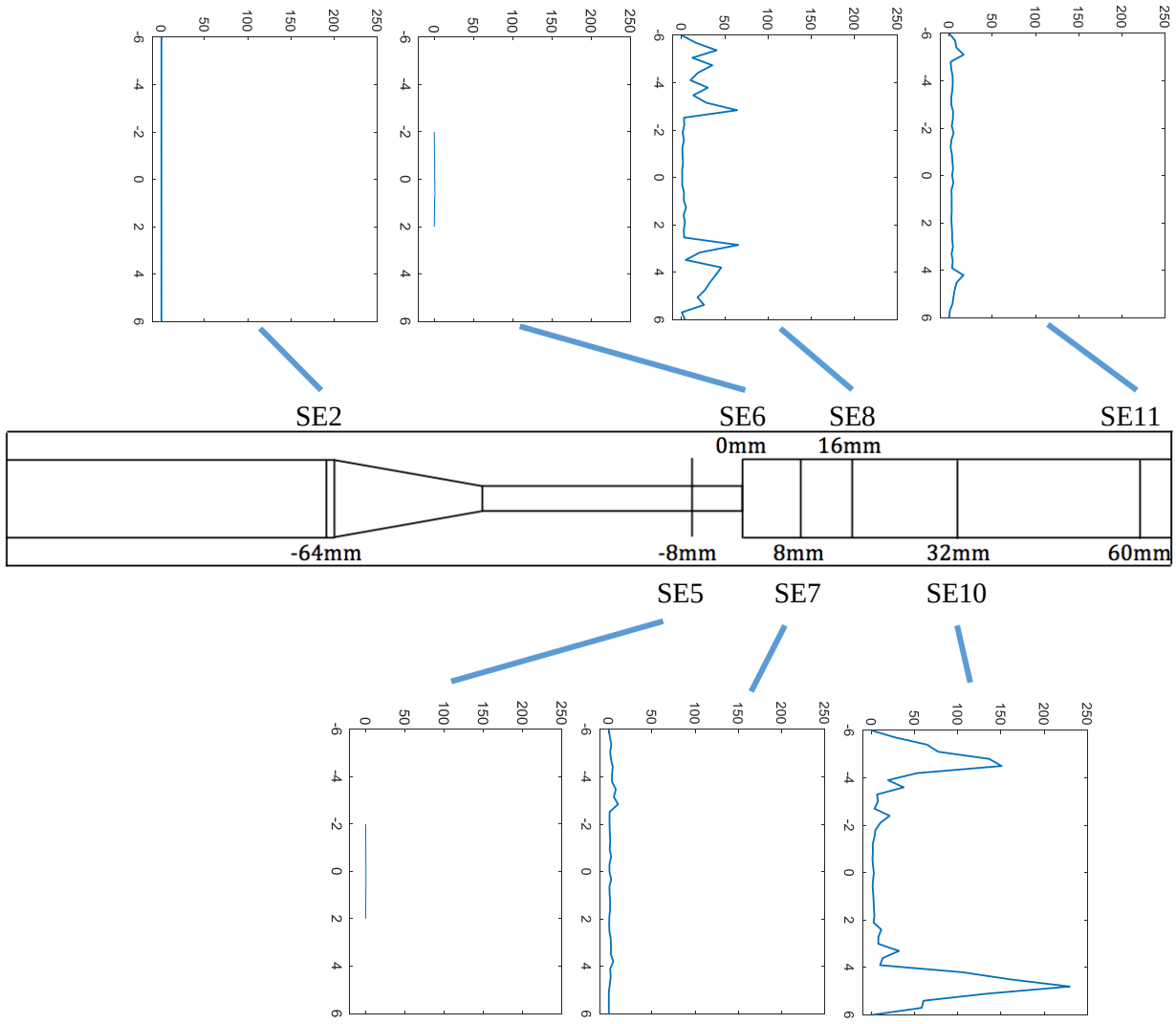

Figure 49. Maximum Reynolds Shear Stresses (in Pa, on Horizontal Axes) during Diastole in Sudden Expansion Orientation. Vertical Axes Show Radial Location in mm.

MRSS values during mid-acceleration in the conical diffuser orientation are shown in Figure 50. Shear stress values are relatively low across the entire model during mid-acceleration. The peak value of 24.18 Pa occurs at CD8.

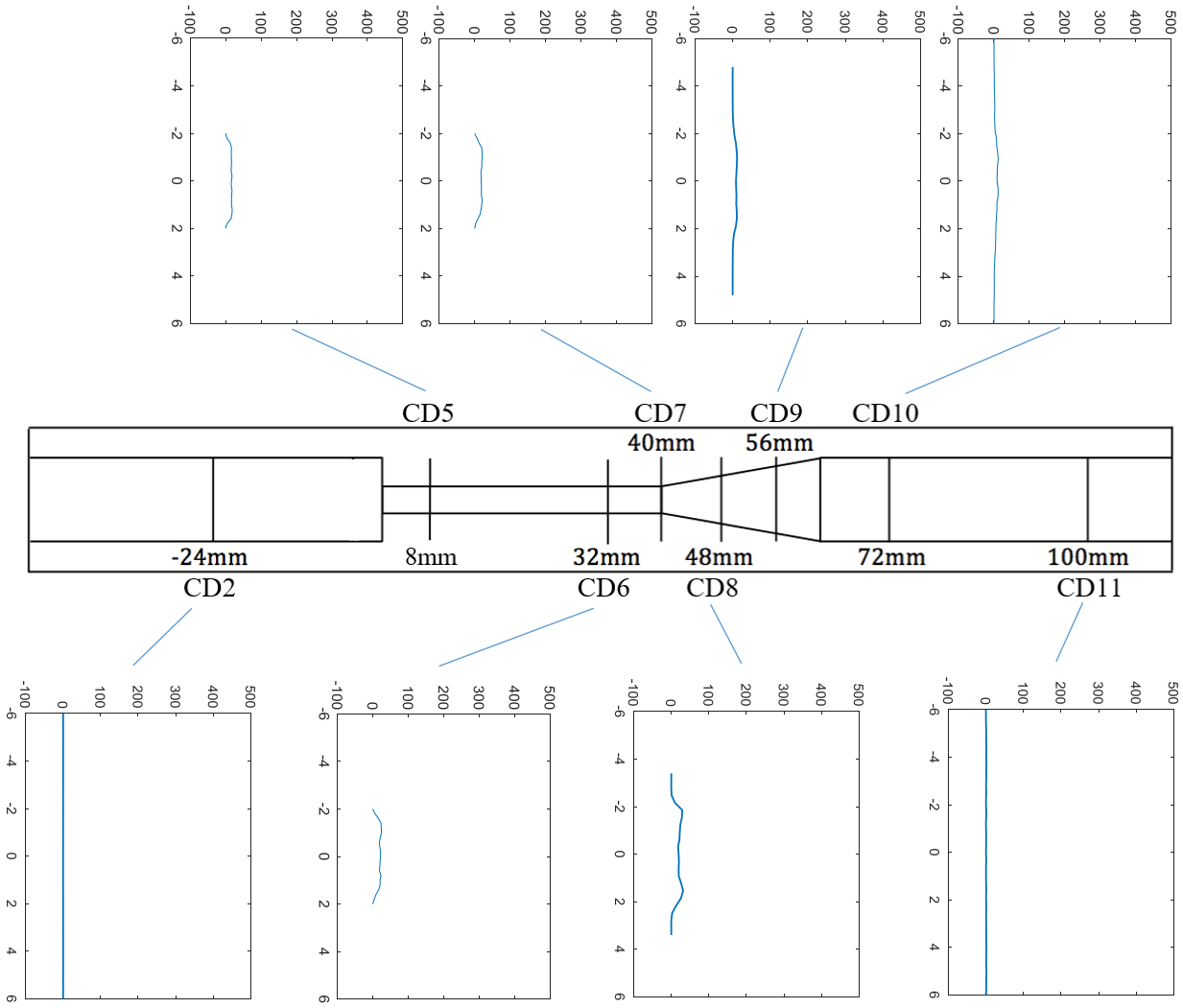

Figure 50. Maximum Reynolds Shear Stresses (in Pa, on Horizontal Axes) during Mid-Acceleration in Conical Diffuser Orientation. Vertical Axes Show Radial Location in mm.

Figure 51 shows the MRSSs at each plane in the conical diffuser orientation during peak systole. During fully developed flow at CD2, MRSSs are negligible. Shear stresses are elevated near the walls of the throat, reaching 752.88 Pa at CD5. Within the diffuser, MRSSs are maximum just outside of the separation region. The peak shear stress downstream of the throat is 797.79 at CD8. Stress values decline and move closer to the center of the plane as fluid moves away from the diffuser. At CD11, MRSSs have diminished to near-zero values across the entire plane.

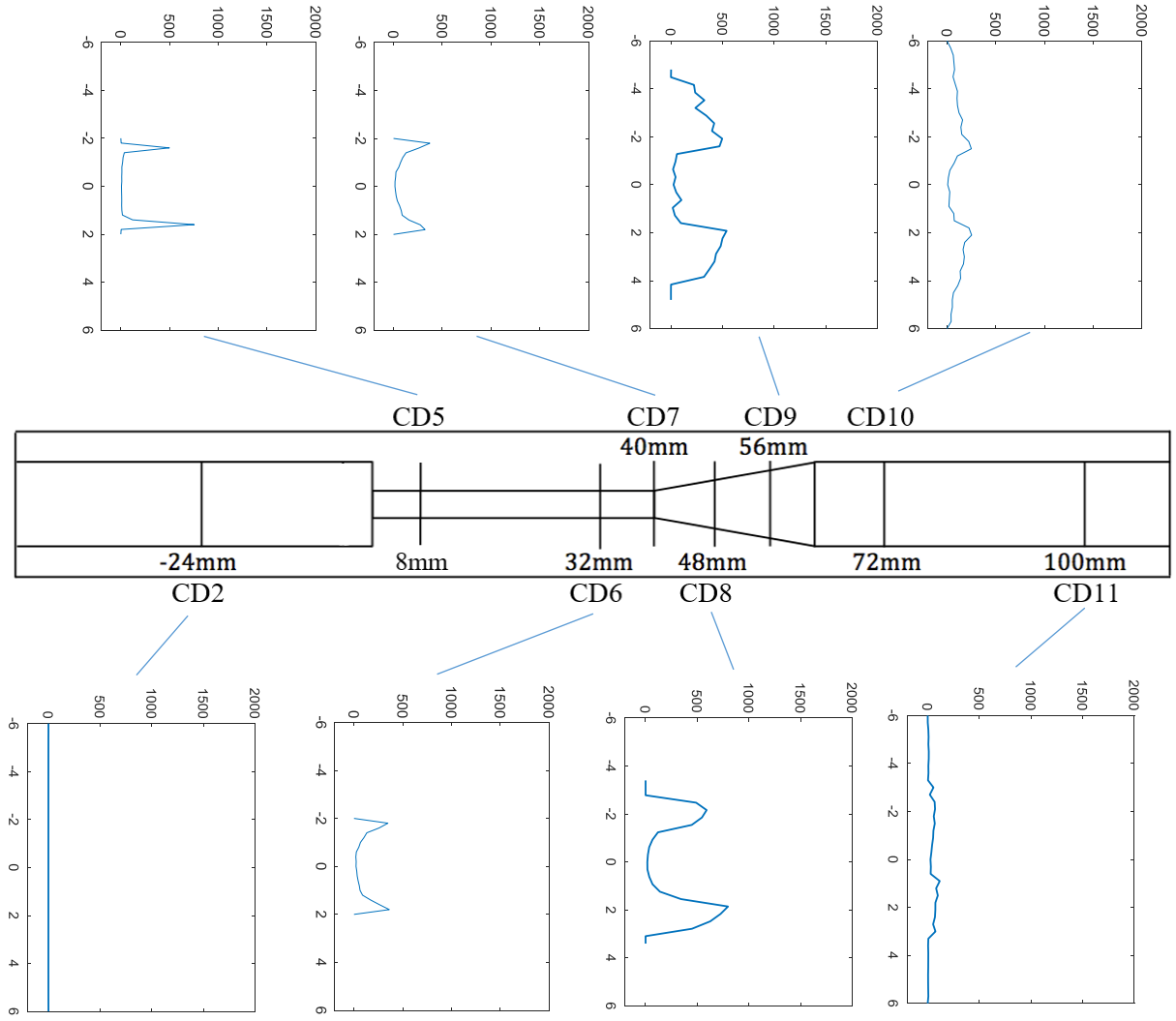

Figure 51. Maximum Reynolds Shear Stresses (in Pa, on Horizontal Axes) during Peak Systole in Conical Diffuser Orientation. Vertical Axes Show Radial Location in mm.

Figure 52 shows the MRSS values at each plane during mid-deceleration. Similar to other points in the cycle, stress values are elevated outside of the recirculation region at CD9. At CD10, stress values reach 153.03 Pa near the center of the plane. This is the maximum stress recorded at any plane during mid-deceleration, and is much higher than the stress at any plane during mid-acceleration. MRSS values were likely more significant during mid-deceleration than mid-acceleration due to higher instability during mid-deceleration. The standard deviation was much greater during mid-deceleration than during mid-acceleration at CD10.

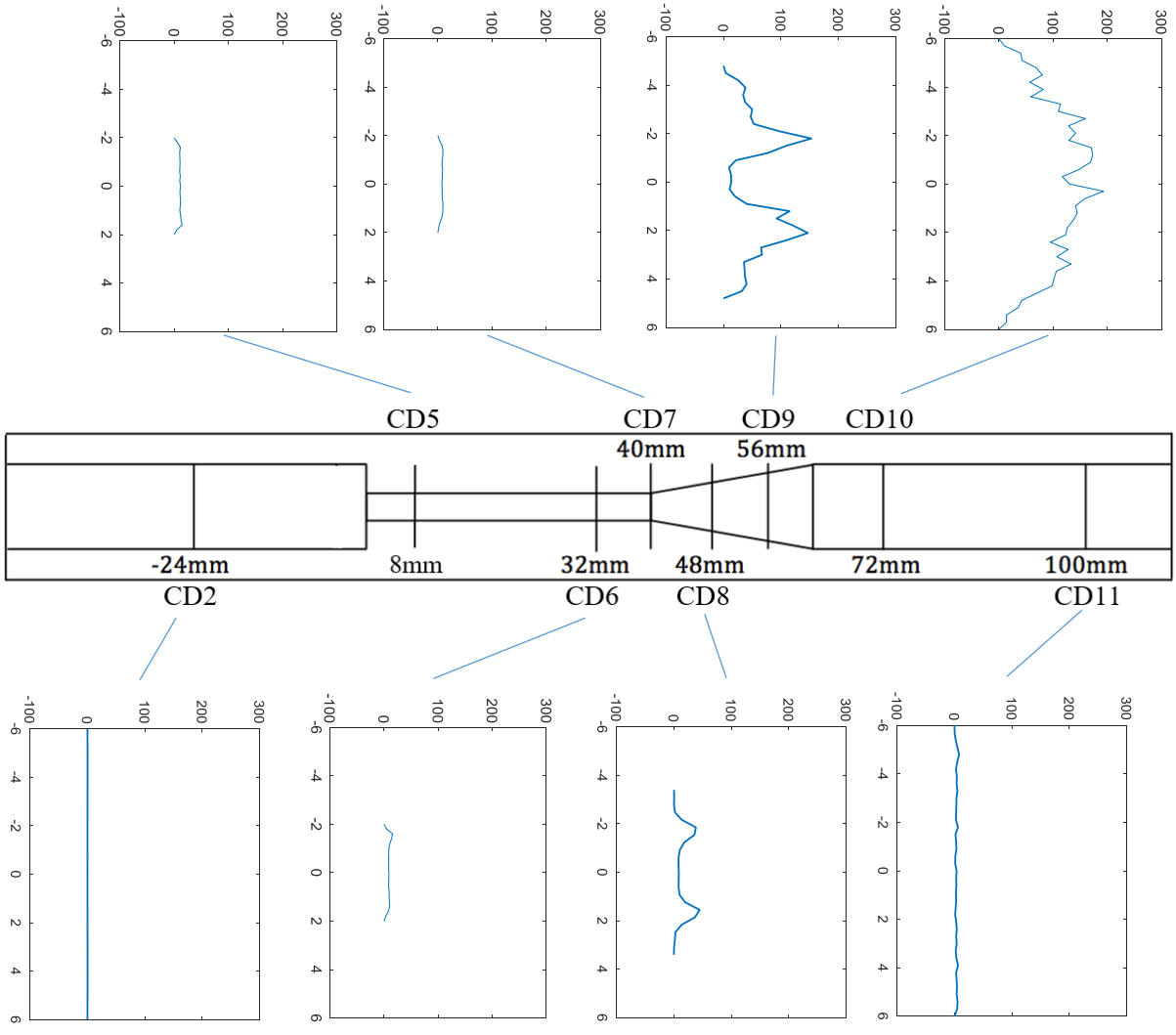

Figure 52. Maximum Reynolds Shear Stresses (in Pa, on Horizontal Axes) during Mid-Deceleration in Conical Diffuser Orientation. Vertical Axes Show Radial Location in mm.

Figure 53 shows the MRSS values during diastole in the conical diffuser orientation. Shear stresses are elevated within the recirculation regions, particularly at the entrance of the throat at CD5 and the entrance of the conical diffuser at CD8, where they were 308.52 Pa and 200.97 Pa, respectively. Considerable recirculation was observed at planes CD5, CD8, CD9, and CD10, and the standard deviation within those areas was significant.

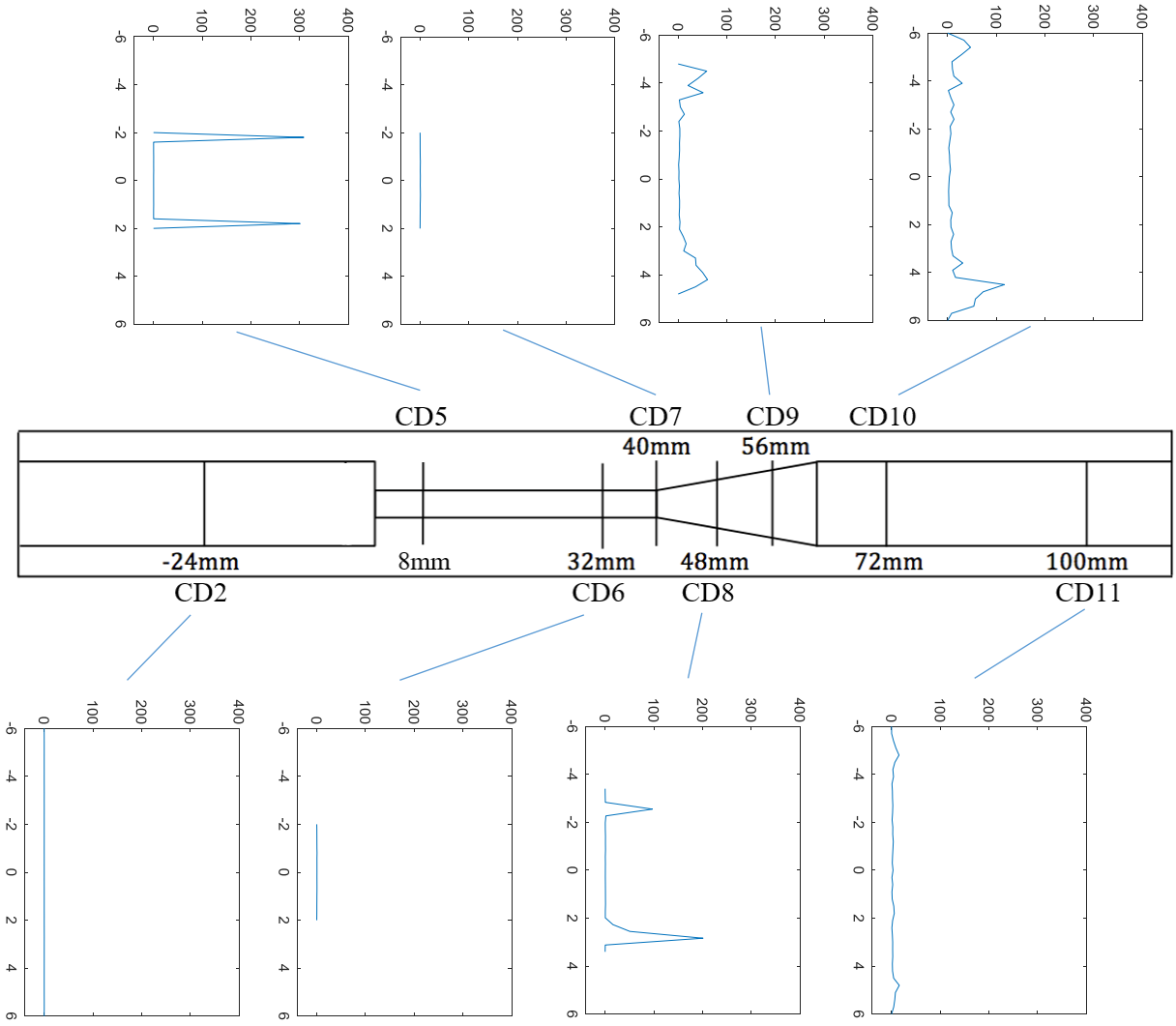

Figure 53. Maximum Reynolds Shear Stresses (in Pa, on Horizontal Axes) during Diastole in Conical Diffuser Orientation. Vertical Axes Show Radial Location in mm.

5.2.4 Turbulence Intensities

Table 5 shows the axial and radial TIs at each location and at each time within the cardiac cycle. Following the trends for the PRS and MRSS values, the peak axial TIs of 0.58 and 0.63 occur during systole at SE10 and CD8, respectively. Elevated axial TIs occur downstream of the sudden expansion and conical diffuser, and within the throat of the model in the conical diffuser orientation. Radial TIs are low within the throat, increasing in value downstream of the sudden expansion and conical diffuser inlet. The highest radial TIs were 0.38 at SE10 and 0.34 at CD8 and CD9, all during systole.

Table 5. Axial and Radial Turbulence Intensities at each plane and for each Phase of the Cardiac Cycle.

		Axial TIs				Radial TIs			
		Mid-Accel.	**Syst.**	**Mid-Decel.**	**Diast.**	**Mid-Accel.**	**Syst.**	**Mid-Decel.**	**Diast.**
Sudden Expansion Orientation	**Plane 2**	0.02	0.04	0.01	0.01	0.01	0.01	0.00	0.00
	Plane 5	0.09	0.05	0.06	0.02	0.01	0.03	0.01	0.00
	Plane 6	0.10	0.11	0.08	0.02	0.02	0.04	0.03	0.01
	Plane 7	0.16	0.44	0.16	0.08	0.01	0.02	0.04	0.06
	Plane 8	0.12	0.33	0.12	0.19	0.01	0.16	0.04	0.13
	Plane 10	0.16	0.58	0.22	0.36	0.1	0.38	0.13	0.24
	Plane 11	0.03	0.29	0.13	0.11	0.01	0.16	0.1	0.08
Conical Diffuser Orientation	**Plane 2**	0.01	0.02	0.01	0.01	0.00	0.01	0.00	0.00
	Plane 5	0.09	0.56	0.08	0.37	0.01	0.29	0.02	0.13
	Plane 6	0.10	0.38	0.08	0.02	0.02	0.12	0.02	0.00
	Plane 7	0.09	0.39	0.06	0.02	0.02	0.12	0.01	0.00
	Plane 8	0.11	0.63	0.14	0.37	0.01	0.34	0.05	0.27
	Plane 9	0.07	0.58	0.3	0.21	0.01	0.34	0.18	0.17
	Plane 10	0.07	0.43	0.34	0.27	0.01	0.30	0.21	0.15
	Plane 11	0.03	0.26	0.07	0.1	0.02	0.17	0.06	0.06

Figure 54 shows the axial and radial TIs during mid-acceleration in the sudden expansion orientation. TIs are low relative to the values during systole. The peak axial TI is 0.16 at SE7 and SE10, both at the boundary of the free shear layer. Both of these values are substantially lower than at the same plane during systole.

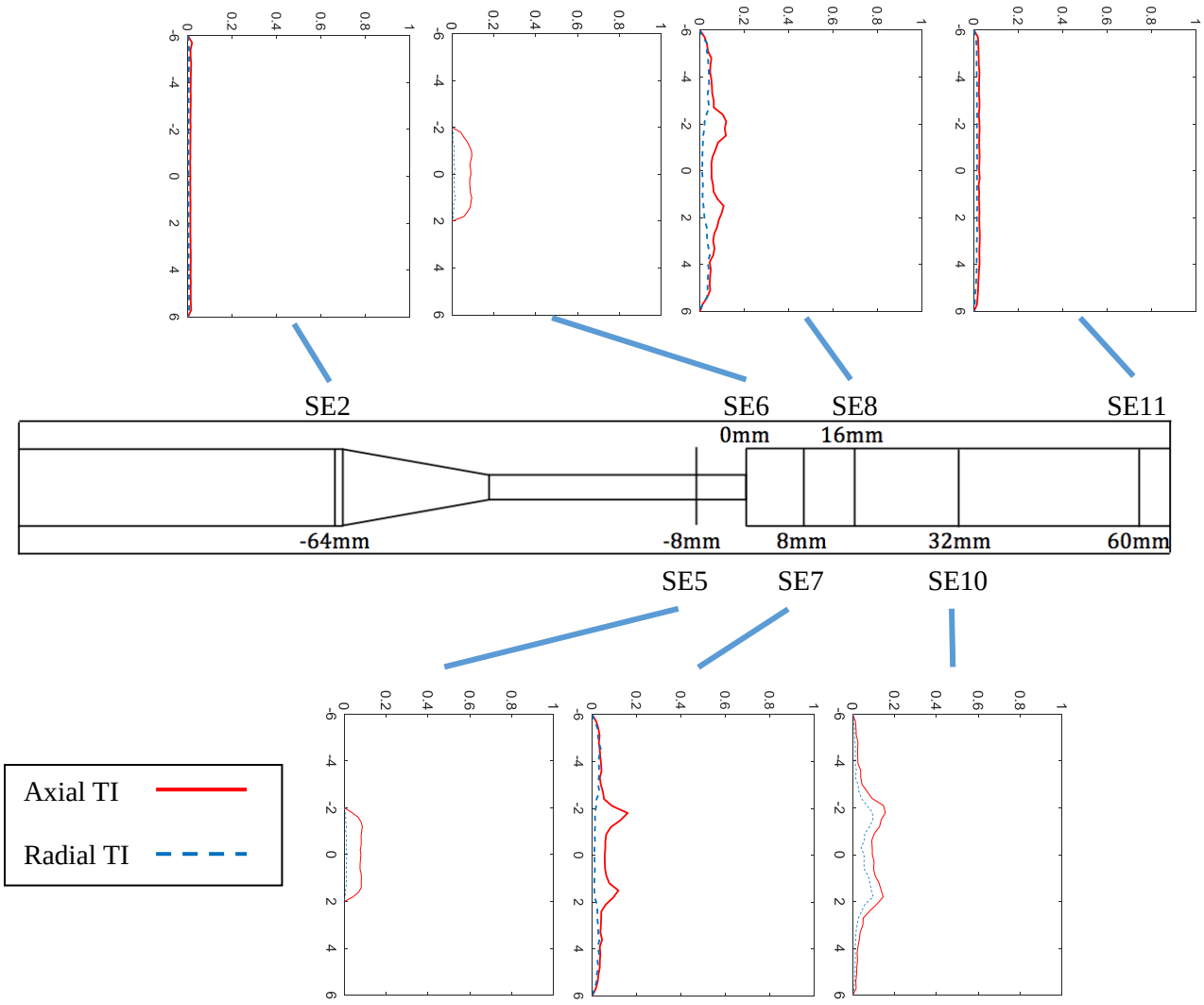

Figure 54. Turbulence Intensities (on Horizontal Axes) during Mid-Acceleration in Sudden Expansion Orientation. Vertical Axes is Radial Location in mm.

Figure 55 shows the TIs during peak systole in the sudden expansion orientation. TIs are higher during systole than during any other phase of the cardiac cycle. Following the sudden expansion, axial TIs are maximum in the area just outside of the recirculation region, where they are 0.44 and 0.33 at SE7 and SE8, respectively. Farther downstream at SE10, axial TIs are elevated across the entire cross-section outside of the recirculation region, reaching a peak of 0.58 near the center of the plane. TIs have declined by SE11, although are still higher than in the fully developed region. Radial TIs are negligible until SE8, after which they follow the same trends as axial TIs. The peak radial TI is 0.38 at SE10.

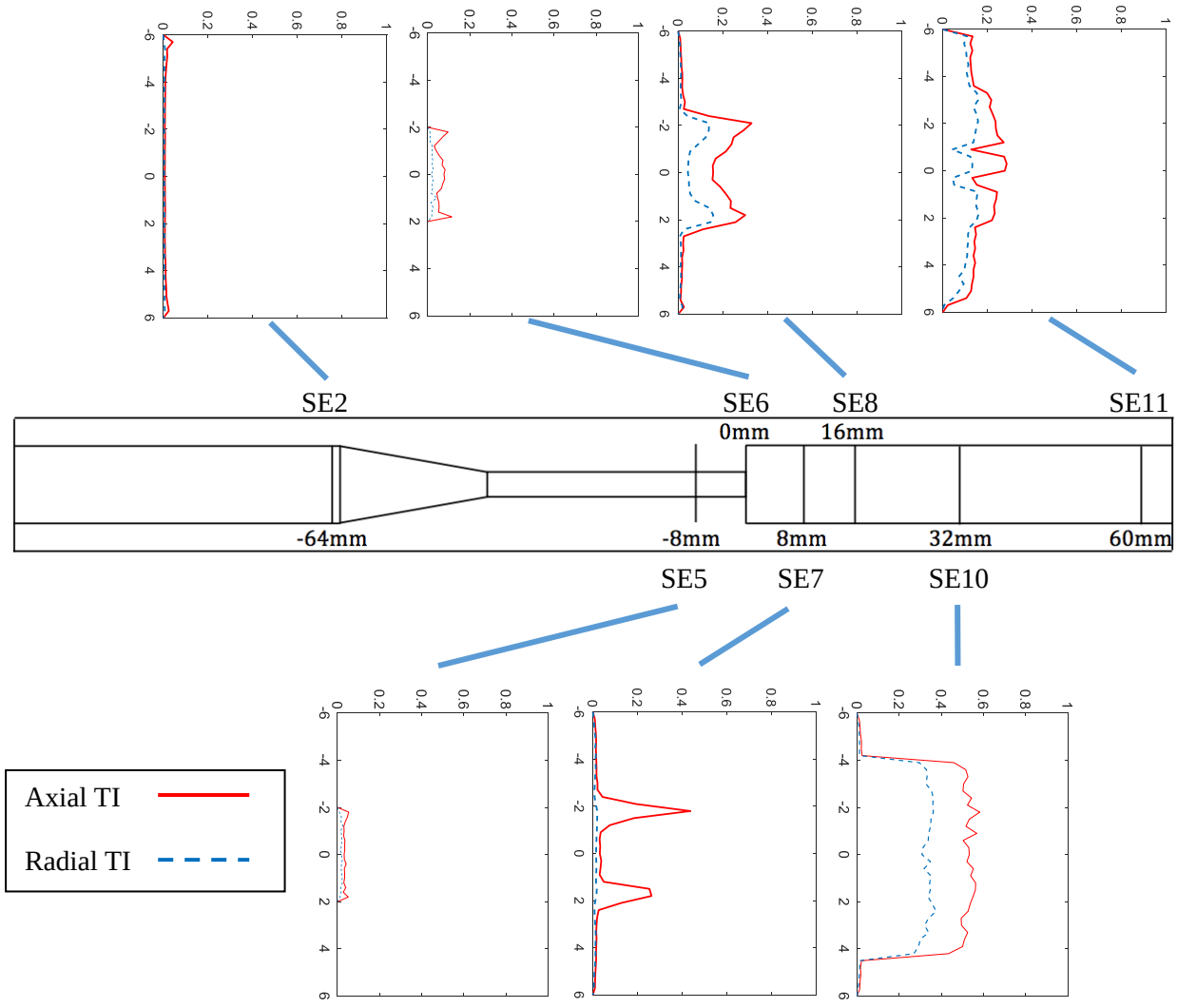

Figure 55. Turbulence Intensities (on Horizontal Axes) during Peak Systole in Sudden Expansion Orientation. Vertical Axes Shows Radial Location in mm.

Figure 56 shows the turbulence intensities during mid-deceleration in the sudden expansion orientation. TIs are substantially lower during mid-deceleration than during systole. The trends and values are very similar to those during mid-acceleration. The maximum axial TI at any plane is 0.22 at SE10, which is approximately three times lower than at the same location during systole.

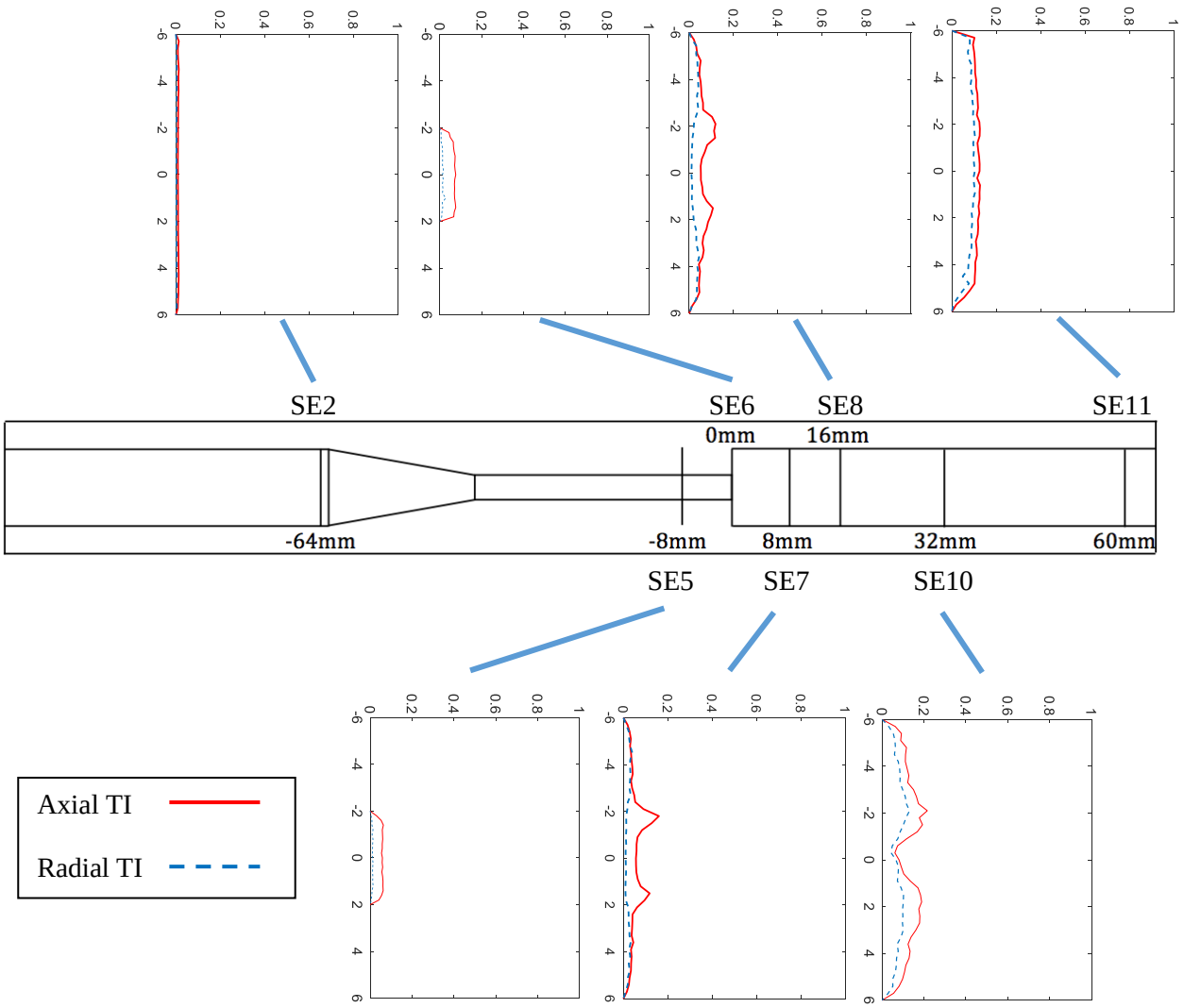

Figure 56. Turbulence Intensities (on Horizontal Axes) during Mid-Deceleration in Sudden Expansion Orientation. Vertical Axes Shows Radial Location in mm.

Figure 57 shows the turbulence intensities during diastole in the sudden expansion orientation. TIs are low at every plane with the exception of SE8 and SE10, which both have elevated axial and radial TIs within the recirculation regions. Axial TIs reach a peak value of 0.36 within the recirculation region at SE10, and radial TIs peak at 0.24 at the same location. Although higher than the TIs during mid-acceleration and mid-deceleration, these values are still substantially lower than during systole.

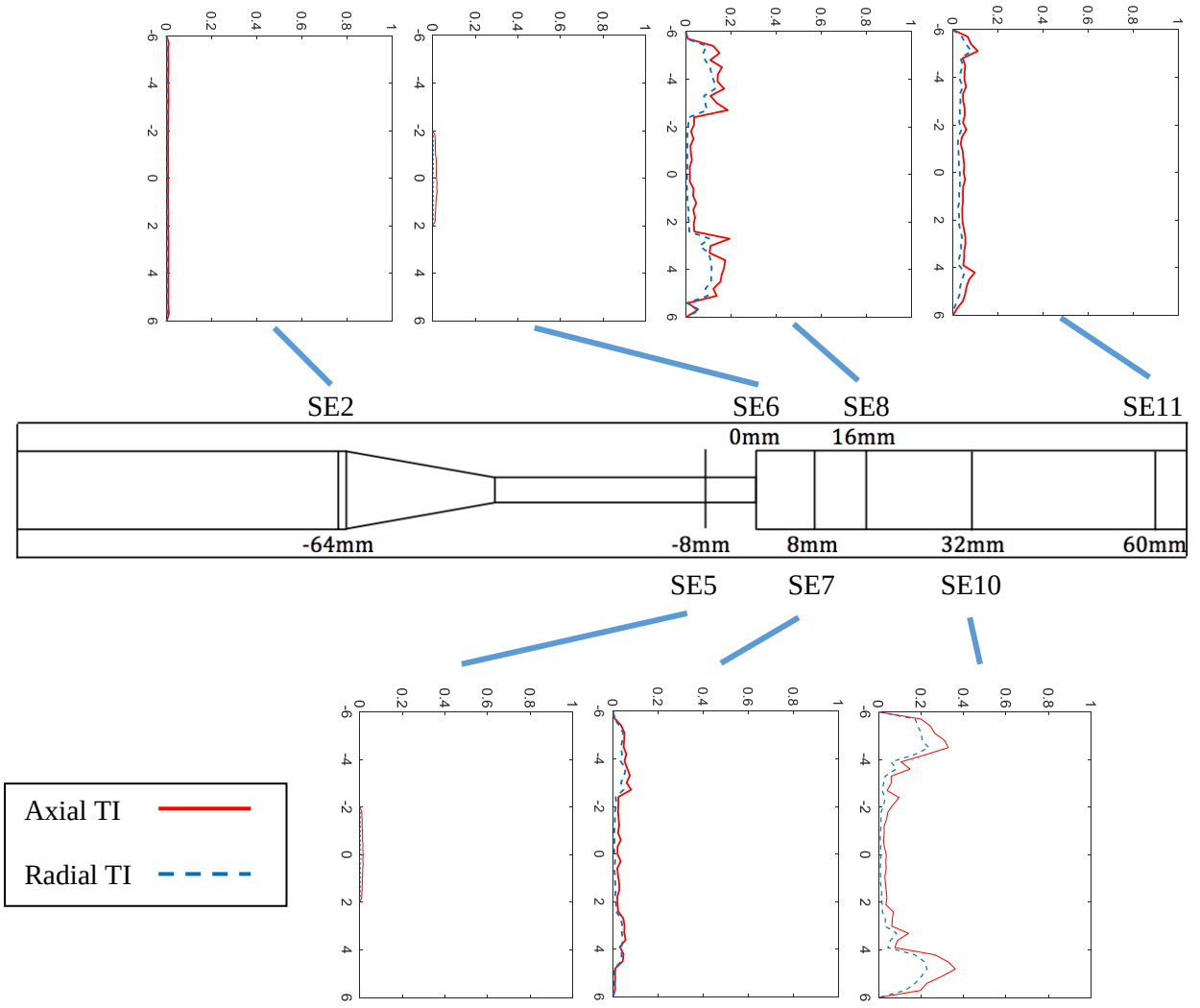

Figure 57. Turbulence Intensities (on Horizontal Axes) during Diastole in Sudden Expansion Orientation. Vertical Axes Show Radial Location in mm.

Figure 58 shows the turbulence intensities at each plane during mid-acceleration in the conical diffuser orientation. TIs are low relative to the values during systole at each plane. The highest axial TIs are within the diffuser, with values of 0.11 and 0.07 at the edges of the recirculation regions of CD8 and CD9, respectively. Axial TIs have declined substantially at CD10 and CD11. Radial TIs are negligible at every plane.

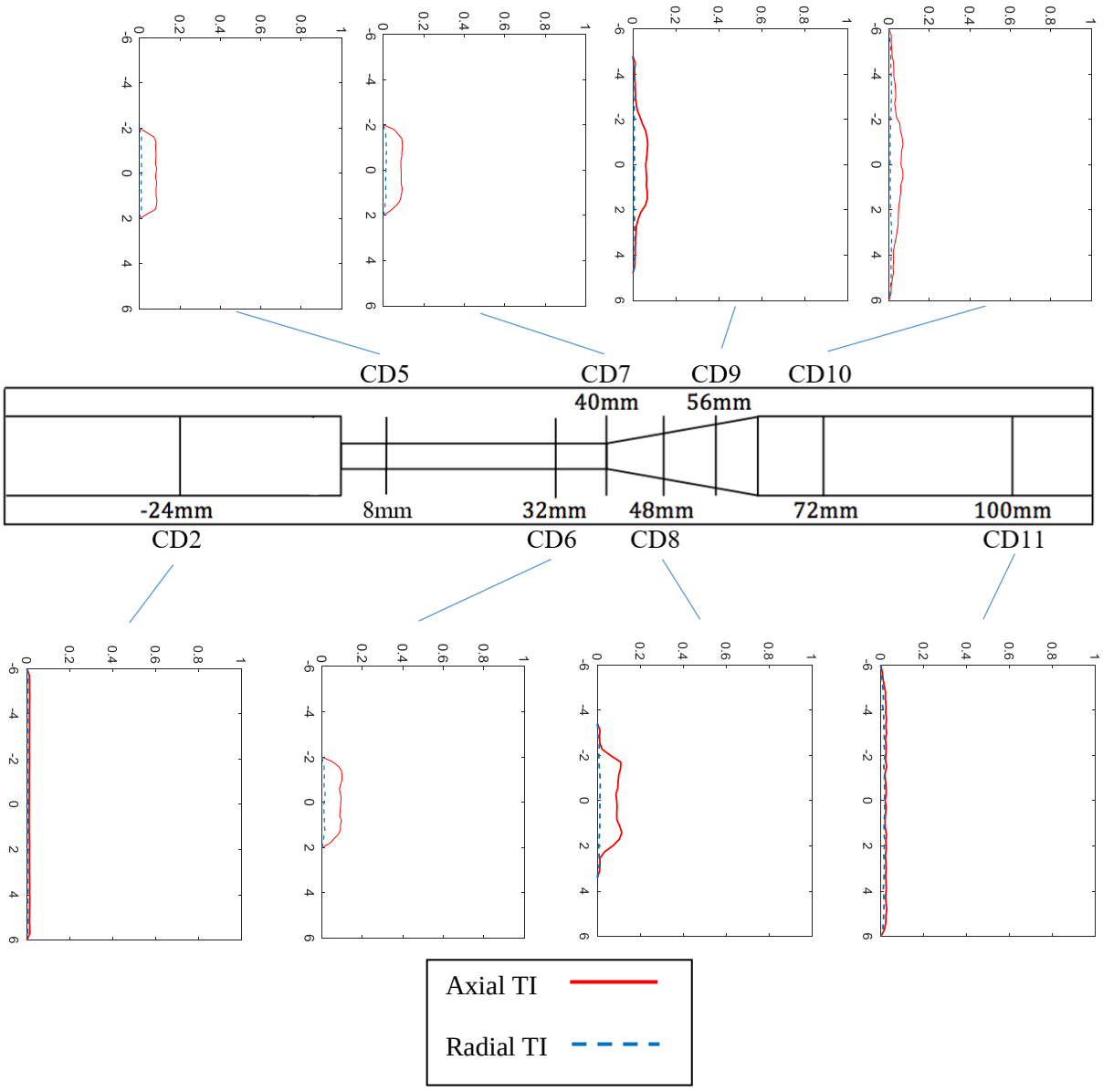

Figure 58. Turbulence Intensities (on Horizontal Axes) during Mid-Acceleration in Conical Diffuser Orientation. Vertical Axes show Radial Location in mm.

Figure 59 shows the TIs during peak systole in the conical diffuser orientation. TIs are substantially higher within the throat of the conical diffuser orientation than the sudden expansion orientation, reaching a maximum value of 0.56 at CD5. At CD8, axial TIs reach a peak for any plane in the sudden expansion orientation of 0.63, just outside of the recirculation region. At CD9, the axial TI declines to 0.58. Following the diffuser, axial TIs diminish to 0.43 at CD10 and 0.26 at CD11. Downstream of the diffuser inlet, radial TIs mirror the shape of the axial TIs but are lower in magnitude. TIs are substantially higher during systole than during the other phases of the cardiac cycle.

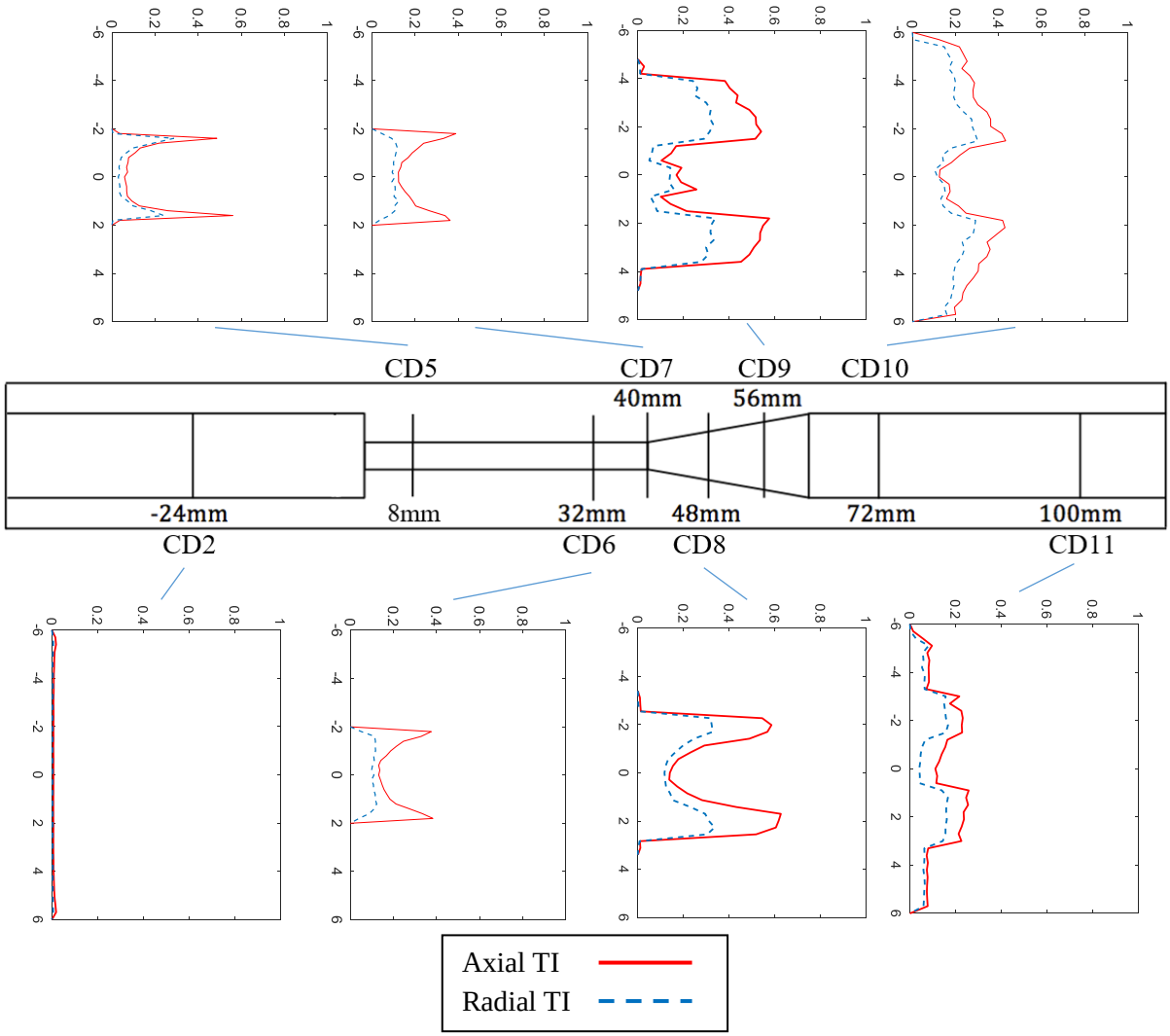

Figure 59. Turbulence Intensities (along Horizontal Axes) during Peak Systole in Conical Diffuser Orientation. Vertical Axes show Radial Location in mm.

Figure 60 shows the turbulence intensities during mid-deceleration in the conical diffuser orientation. TIs are much lower at each plane than during systole. Somewhat elevated axial TIs of 0.30 occur outside of the recirculation region at CD9, and of 0.34 near the center of the plane at CD10. Although lower than during systole, TIs were substantially higher at CD9 and CD10 than at those planes during mid-acceleration.

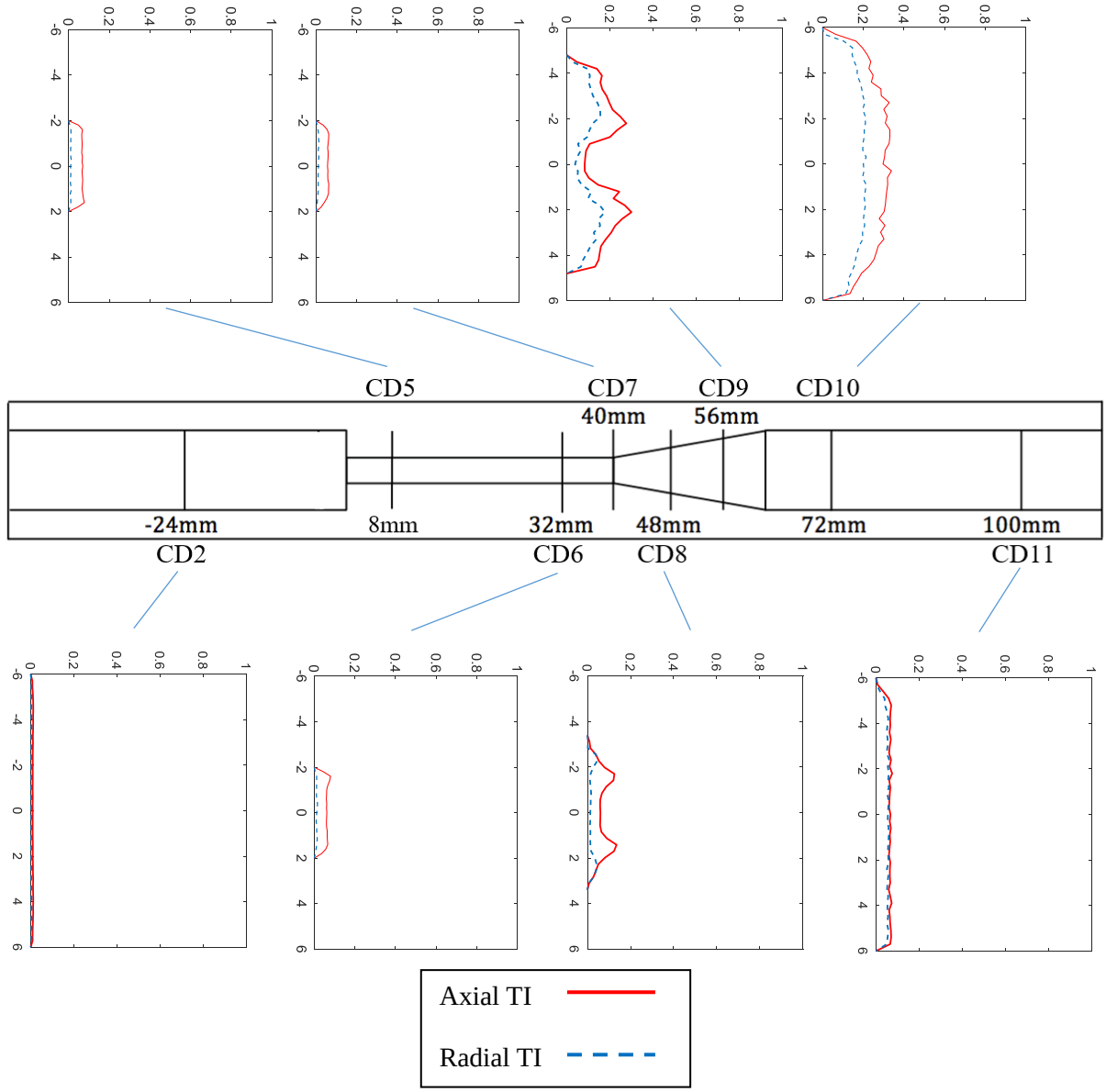

Figure 60. Turbulence Intensities (along Horizontal Axes) during Mid-Deceleration in Conical Diffuser Orientation. Vertical Axes show Radial Location in mm.

Figure 61 shows the turbulence intensities during diastole in the conical diffuser orientation. TIs are significant within the areas of recirculation. The peak TIs calculated during diastole occur at CD5 and CD8, where the axial TIs are 0.37. Although lower than the TIs during systole, TIs are higher within the recirculation regions of CD5 and CD8 than at any plane during mid-acceleration or mid-deceleration.

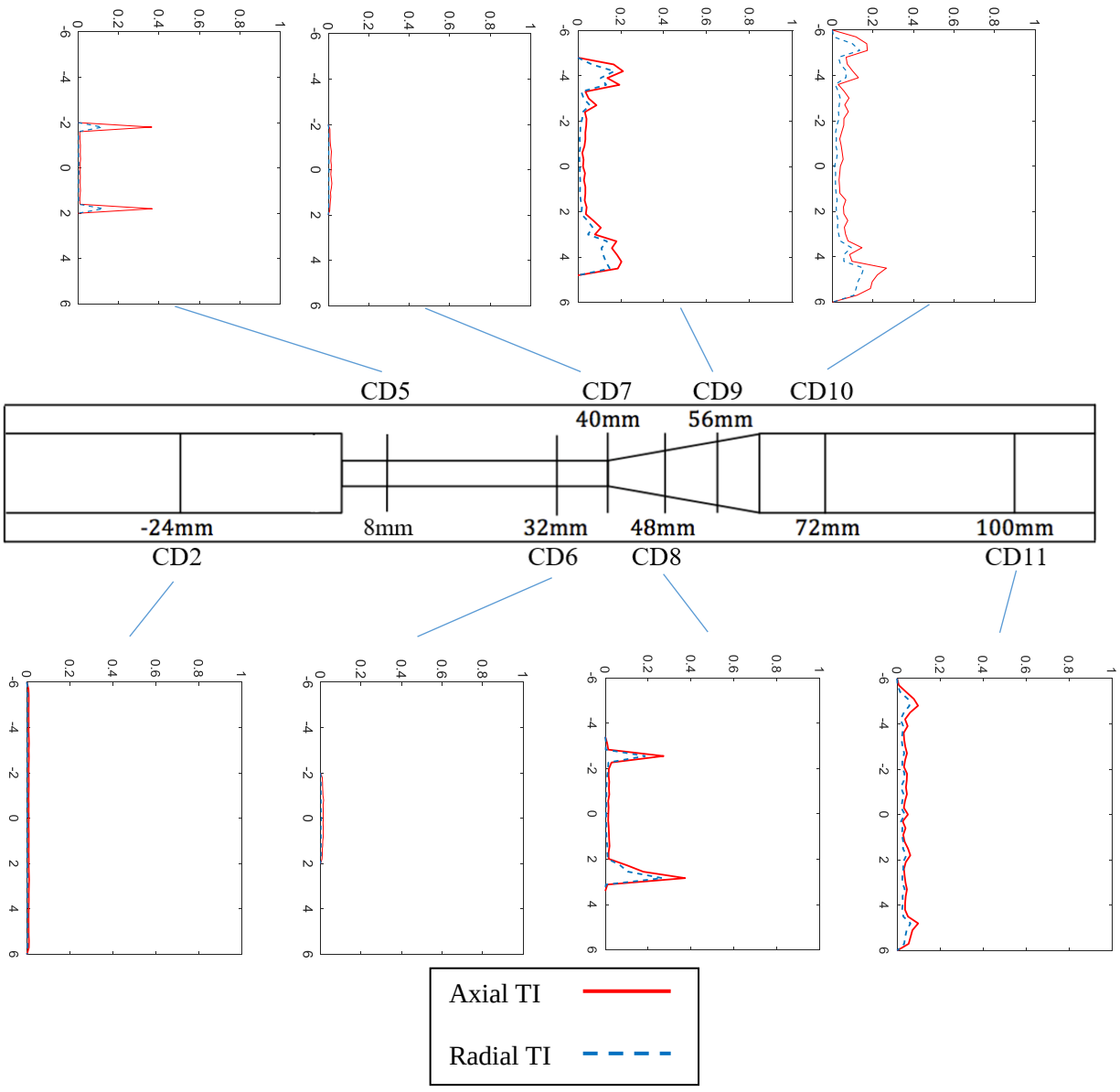

Figure 61. Turbulence Intensities (along Horizontal Axes) during Diastole in Conical Diffuser Orientation. Vertical Axes show Radial Location in mm.

5.2.5 Viscous Shear Stresses (VSS)

Table 6 shows the magnitudes of the maximum VSSs calculated at each plane and for each phase of the cardiac cycle. For both the sudden expansion and conical diffuser orientations, the peak VSSs occur within the throat, after which they gradually decline with distance from the sudden expansion or conical diffuser inlet. The peak VSSs calculated were 54.29 Pa at SE6 and 49.72 Pa at CD6, both during systole.

Table 6. Maximum VSSs in Pa at each Plane and for each Phase of the Cardiac Cycle

		Mid-Acceleration	Systole	Mid-Deceleration	Diastole
Sudden Expansion Orientation	Plane 2	1.10	2.03	0.49	0.52
	Plane 5	12.89	43.14	16.15	0.98
	Plane 6	21.62	54.29	21.57	1.11
	Plane 7	8.20	19.63	8.37	0.71
	Plane 8	4.79	15.58	6.42	2.41
	Plane 10	6.11	5.12	4.63	8.25
	Plane 11	0.81	5.08	2.96	1.47
Conical Diffuser Orientation	Plane 2	0.76	1.35	0.52	0.35
	Plane 5	14.20	48.30	20.57	7.77
	Plane 6	16.53	49.72	14.46	0.82
	Plane 7	16.11	47.95	11.96	0.87
	Plane 8	8.10	11.53	8.72	5.85
	Plane 9	3.32	7.90	7.94	5.50
	Plane 10	2.29	5.90	3.23	4.47
	Plane 11	0.55	4.40	3.23	1.58

Figure 62 shows the VSSs in the sudden expansion orientation during mid-acceleration. Within the throat region, viscous shear stresses are maximum near the walls, reaching a peak value of 21.62 Pa at SE6. Downstream of the sudden expansion, elevated VSS values are located outside of the jet. The peak VSS in the downstream portion of the model is 8.20 Pa at SE7. VSS values are diminished by SE10, and are negligible by SE11.

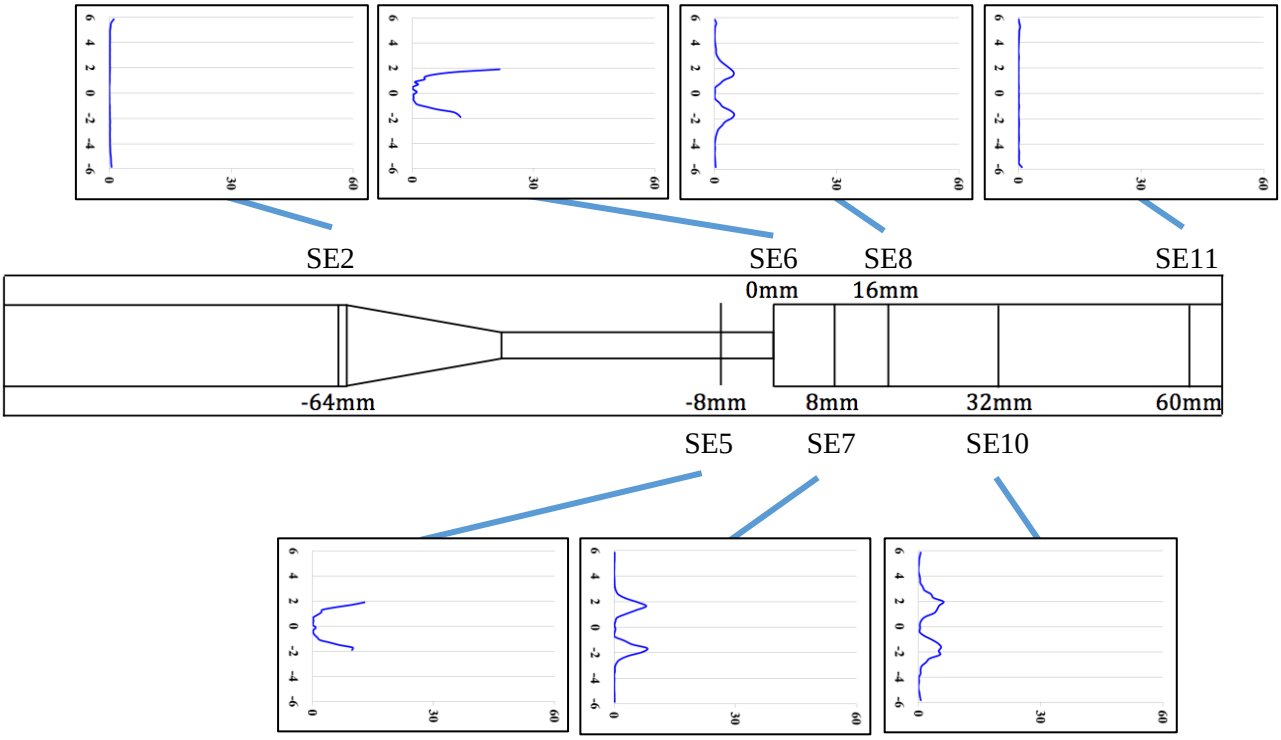

Figure 62. Viscous Shear Stress (in Pa, on Horizontal Axes) in Sudden Expansion Orientation during Mid-Acceleration. Vertical Axes Show Radial Location in mm.

Figure 63 shows the VSSs during systole in the sudden expansion orientation. Trends are very similar to those for mid-acceleration. The peak VSS for the entire model occurs near the walls at SE6, and is equal to 54.29 Pa. Downstream of the sudden expansion, VSSs are again elevated just outside of the central jet, peaking at 19.62 Pa at SE7. VSSs again decline by SE10 and SE11.

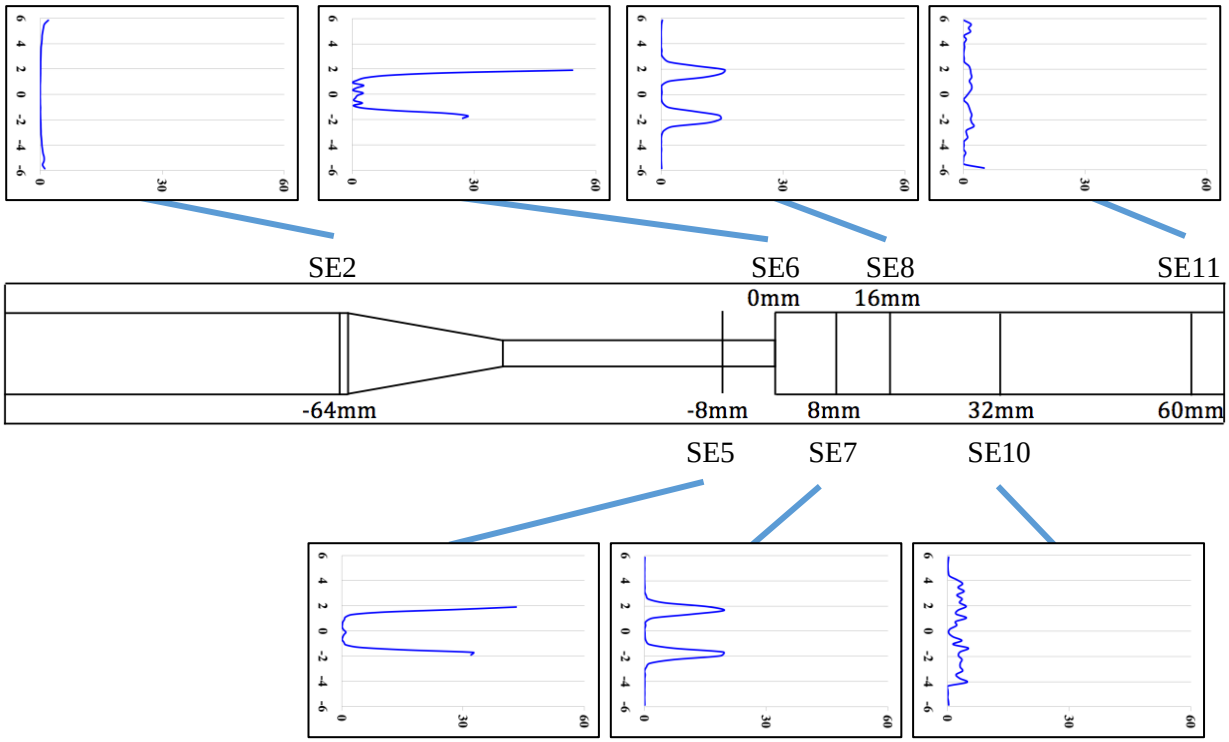

Figure 63. Viscous Shear Stress (in Pa, on Horizontal Axes) in Sudden Expansion Orientation during Systole. Vertical Axes Show Radial Location in mm.

Figure 64 shows the VSSs during mid-deceleration in the sudden expansion orientation. Trends mirror those for mid-acceleration and systole. The peak VSS during mid-deceleration is 21.57 Pa at SE6.

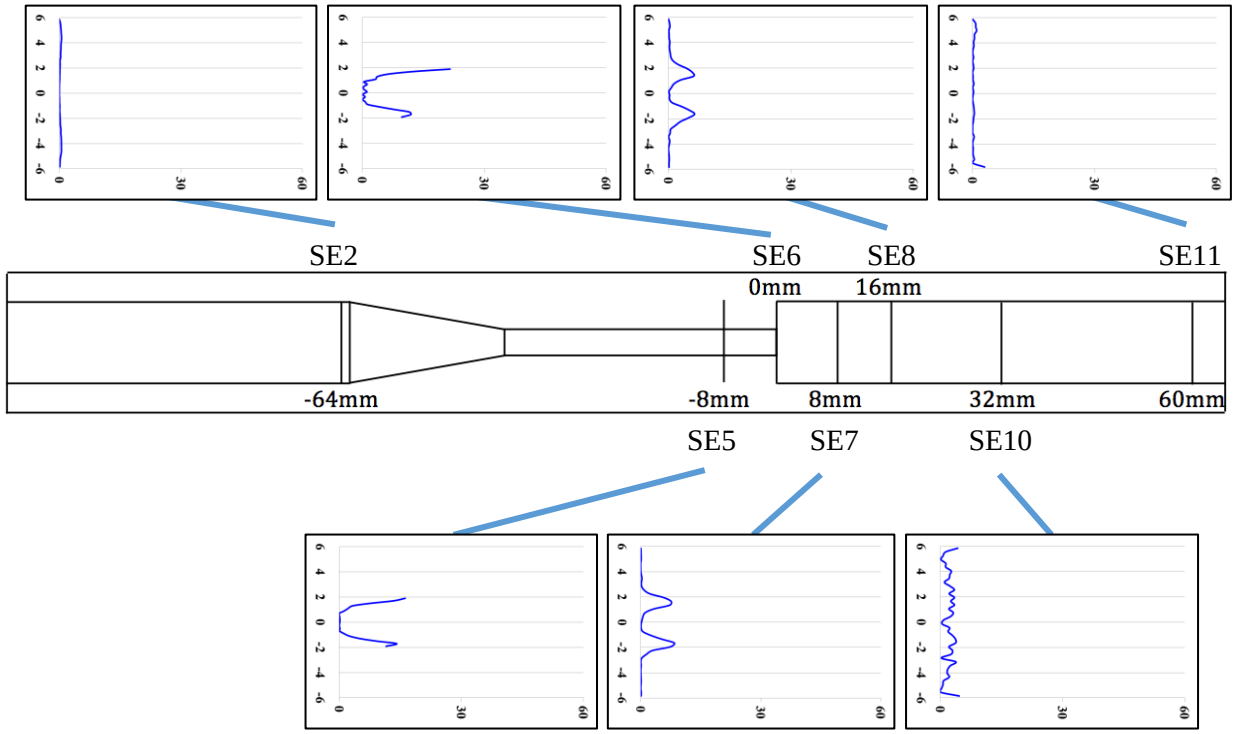

Figure 64. Viscous Shear Stress (in Pa, on Horizontal Axes) in Sudden Expansion Orientation during Mid-Deceleration. Vertical Axes Show Radial Location in mm.

Figure 65 shows the VSSs during diastole in the sudden expansion orientation. VSSs are very low at all planes except for SE10, where they are elevated within the recirculation regions near the walls. The peak VSS calculated at SE10 is 8.25 Pa.

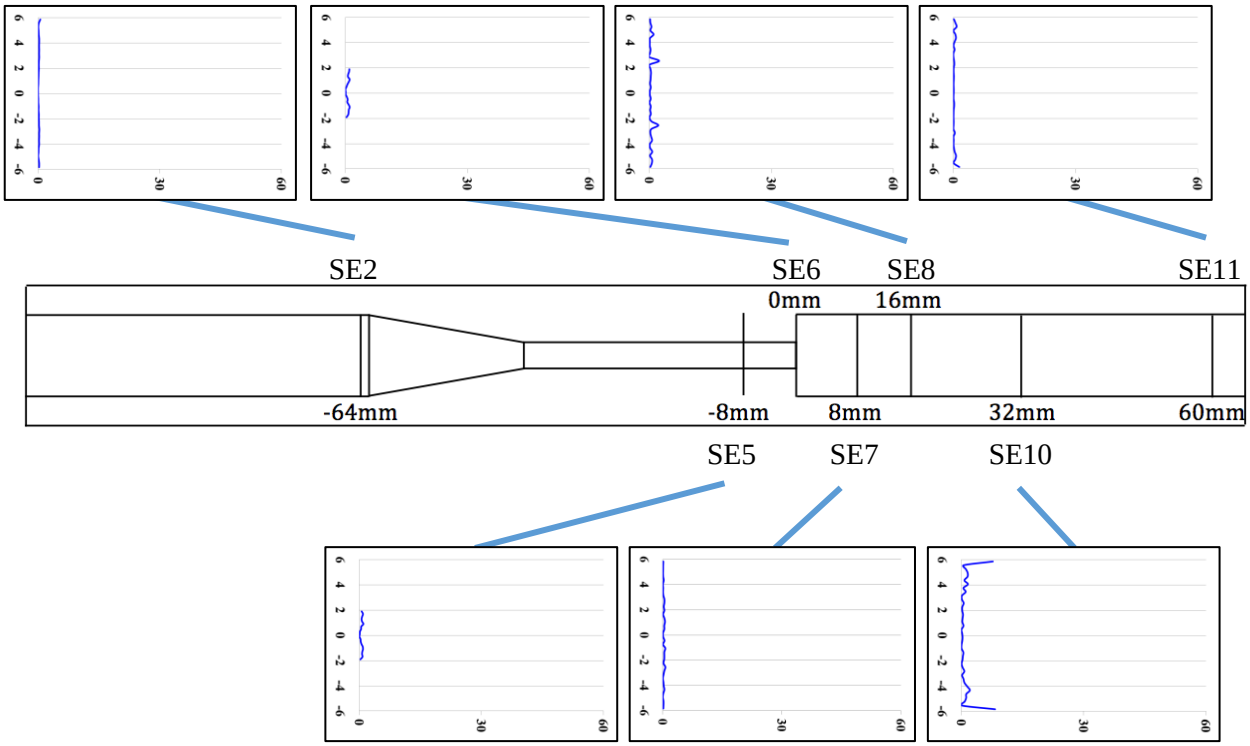

Figure 65. Viscous Shear Stress (in Pa, on Horizontal Axes) in Sudden Expansion Orientation during Diastole. Vertical Axes Show Radial Location in mm.

Figure 66 shows the VSSs during mid-acceleration in the conical diffuser orientation. Trends are similar to those seen in the sudden expansion orientation. VSSs are elevated near the walls of the throat, reaching a peak value of 16.53 Pa at CD6. Within the diffuser, VSSs are highest at the boundary of the separation zone. The highest VSSs downstream of the throat are at CD8, where they reach a peak value of 8.09 Pa. VSSs have declined by CD10, and are negligible at CD11.

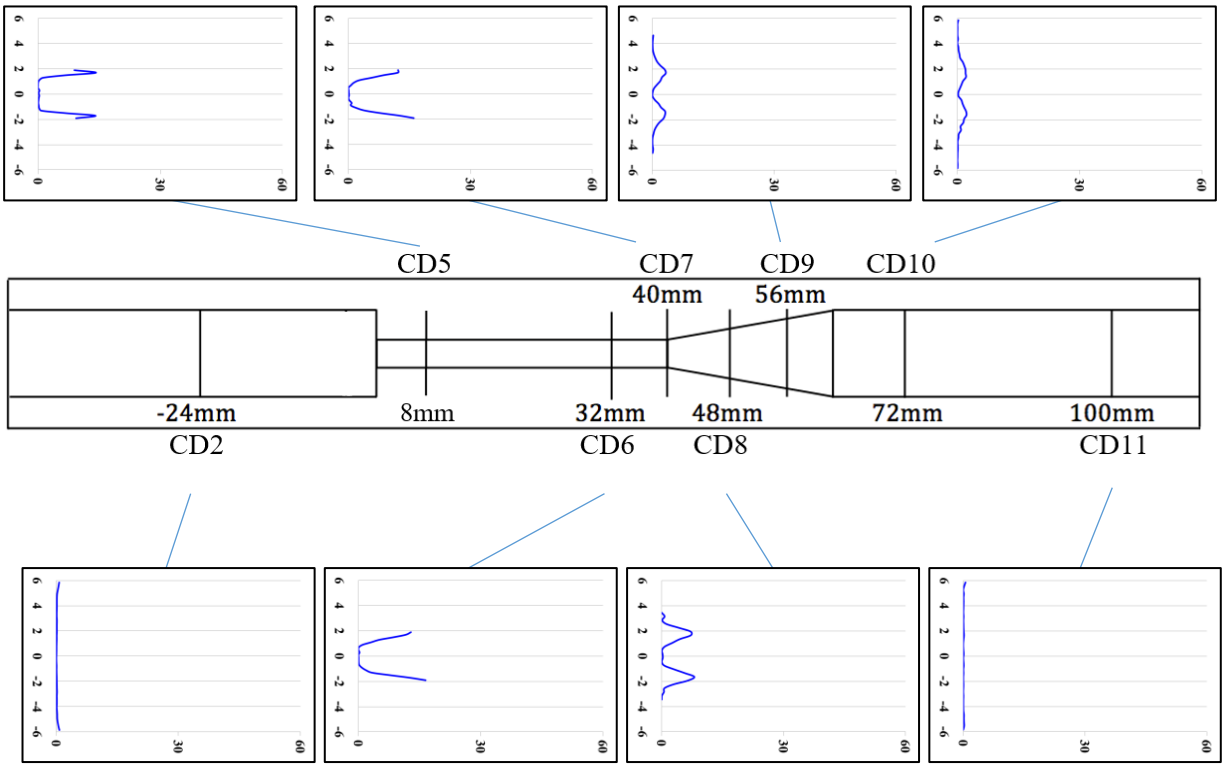

Figure 66. Viscous Shear Stress (in Pa, on Horizontal Axes) in Conical Diffuser Orientation during Mid-Acceleration. Vertical Axes Show Radial Location in mm.

The VSSs during systole in the conical diffuser orientation are shown in Figure 67. Trends mirror those described for mid-acceleration. The peak VSS within the throat is 49.72 Pa at CD6, and the peak VSS downstream of the diffuser inlet is 28.63 Pa at CD8.

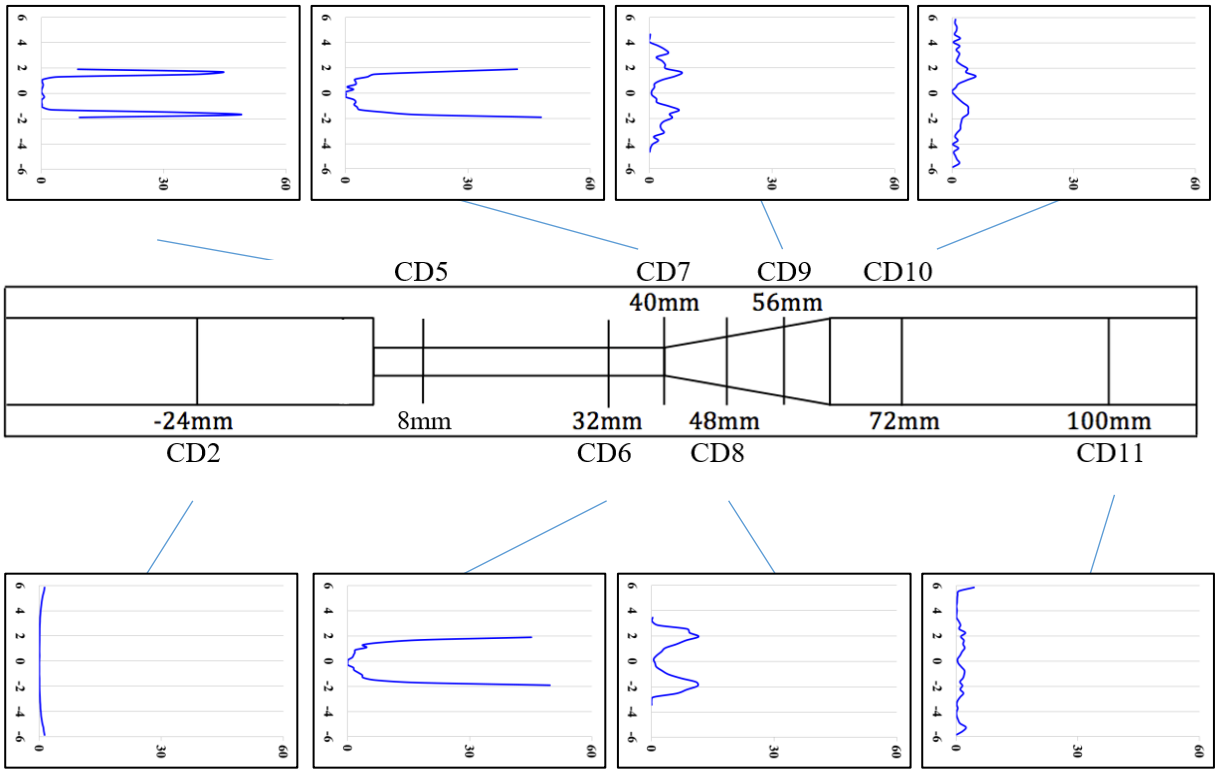

Figure 67. Viscous Shear Stress (in Pa, on Horizontal Axes) in Conical Diffuser Orientation during Systole. Vertical Axes Show Radial Location in mm.

Figure 68 shows the VSSs during mid-deceleration in the conical diffuser orientation. Trends and values are very similar to those for mid-acceleration, although values are generally slightly higher during mid-deceleration than during mid-acceleration. The peak VSS in the throat is 14.46 Pa at CD6, and the peak VSS downstream of the throat is 8.72 Pa at CD8.

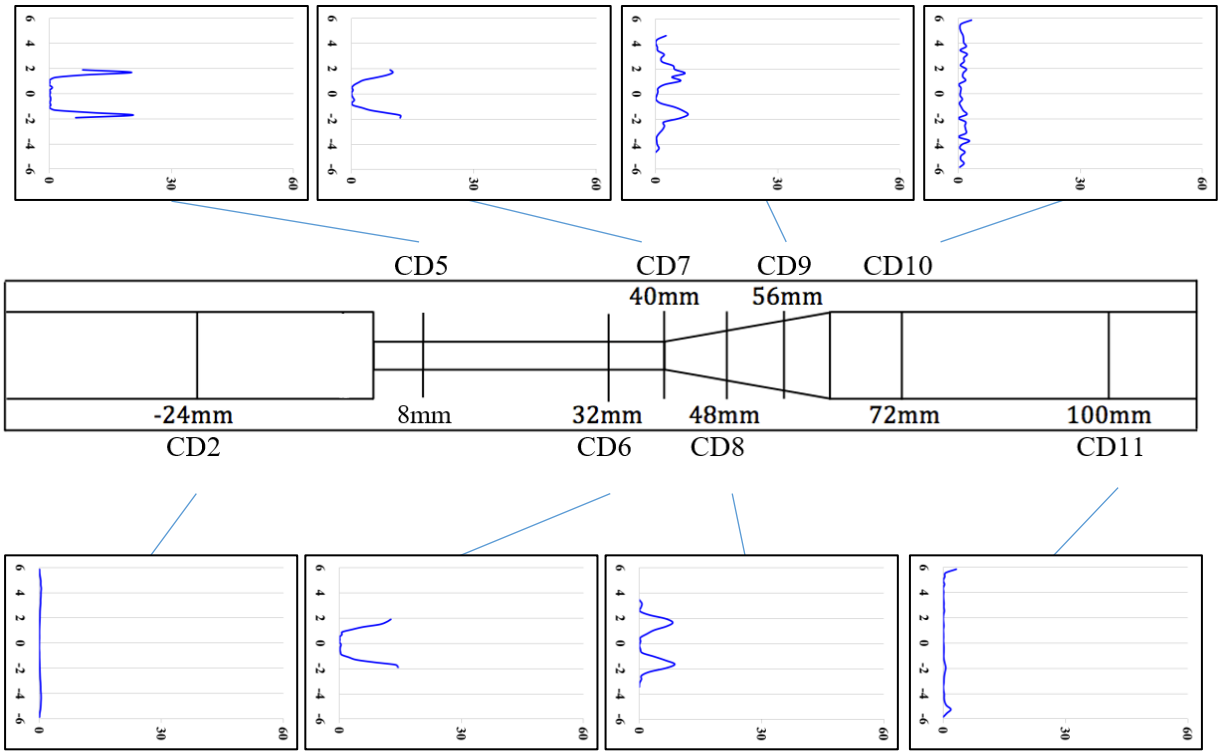

Figure 68. Viscous Shear Stress (in Pa, on Horizontal Axes) in Conical Diffuser Orientation during Mid-Deceleration. Vertical Axes Show Radial Location in mm.

Figure 69 shows the VSSs during diastole in the conical diffuser orientation. Values are low at all planes except for CD5, CD8, CD9, and CD10, where they are slightly elevated next to the walls in the recirculation regions. The peak VSS was 7.77 Pa at CD5.

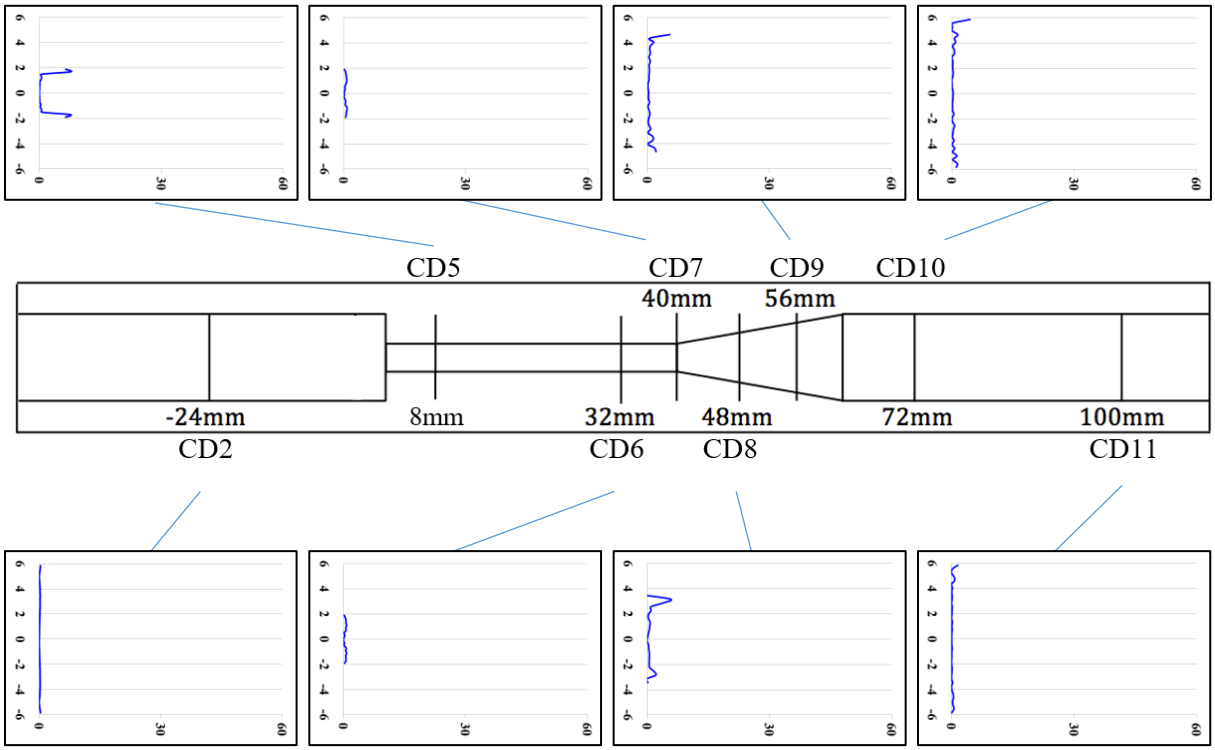

Figure 69. Viscous Shear Stress (in Pa, on Horizontal Axes) in Conical Diffuser Orientation during Diastole. Vertical Axes Show Radial Location in mm.

5.2.6 Wall Shear Stresses (WSS)

Table 7 shows the mean WSSs for each plane and during each phase of the cardiac cycle. During mid-acceleration, systole, and mid-deceleration, the peak WSSs for both the sudden expansion and conical diffuser orientations occur within the throat. During diastole, the WSSs are negative at all planes outside of the throat, reaching minimum values at SE10 and CD9.

Table 7. Mean WSSs in Pa at each Plane and for each Phase of the Cardiac Cycle

		Mid-Acceleration	Systole	Mid-Deceleration	Diastole
Sudden Expansion Orientation	Plane 2	0.72	1.40	0.06	-0.33
	Plane 5	10.95	35.74	13.79	0.53
	Plane 6	15.40	37.17	14.76	0.70
	Plane 7	-0.13	0.06	-0.10	-0.15
	Plane 8	-0.16	0.16	-0.11	-0.28
	Plane 10	-0.49	0.24	-3.50	-6.02
	Plane 11	0.35	2.23	1.21	-0.65
Conical Diffuser Orientation	Plane 2	0.69	1.31	-0.02	-0.32
	Plane 5	10.39	18.41	10.61	-2.93
	Plane 6	14.07	40.14	13.36	0.34
	Plane 7	13.71	38.94	10.82	0.39
	Plane 8	-0.15	0.14	-0.14	-1.21
	Plane 9	-0.15	0.18	-1.10	-3.00
	Plane 10	-0.15	0.77	-1.43	-2.25
	Plane 11	0.26	1.94	1.40	-0.64

Figure 70 shows the WSSs during mid-acceleration in the sudden expansion orientation. WSSs are low at all planes except for SE5 and SE6 within the throat, where they reach a peak of 15.40 Pa at SE6. Standard deviations are also large within the throat. In the regions downstream of the sudden expansion, WSSs are negative.

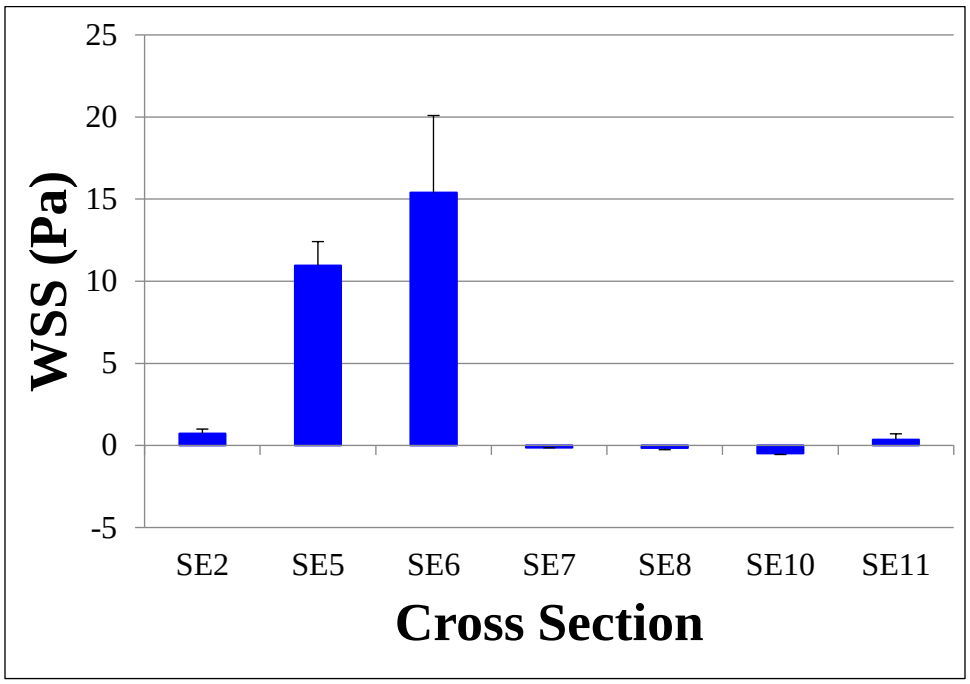

Figure 70. Wall Shear Stress during Mid-Acceleration in Sudden Expansion Orientation.

Figure 71 shows the WSSs during systole in the sudden expansion orientation. Similar to mid-acceleration, WSSs are highest within the throat, peaking at 37.17 Pa at SE6. Standard deviations are again high within the throat. Downstream of the sudden expansion, at the planes where a central jet has formed (SE7, SE8, and SE10), WSSs are near-zero.

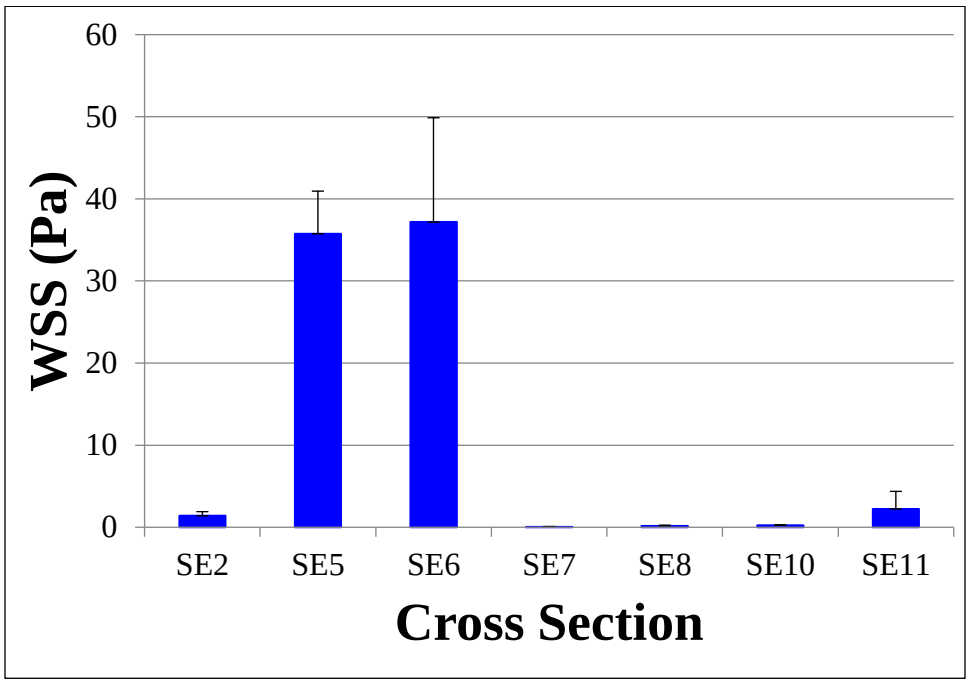

Figure 71. Wall Shear Stress during Systole in Sudden Expansion Orientation.

The WSSs during mid-deceleration in the sudden expansion orientation are given in Figure 72. The peak WSS of 14.76 Pa occurs at SE6. The standard deviations within the throat are large. WSSs are negative at SE7, SE8, and SE10. They reach a minimum value of -3.50 Pa at SE10, which is the location with greatest recirculation.

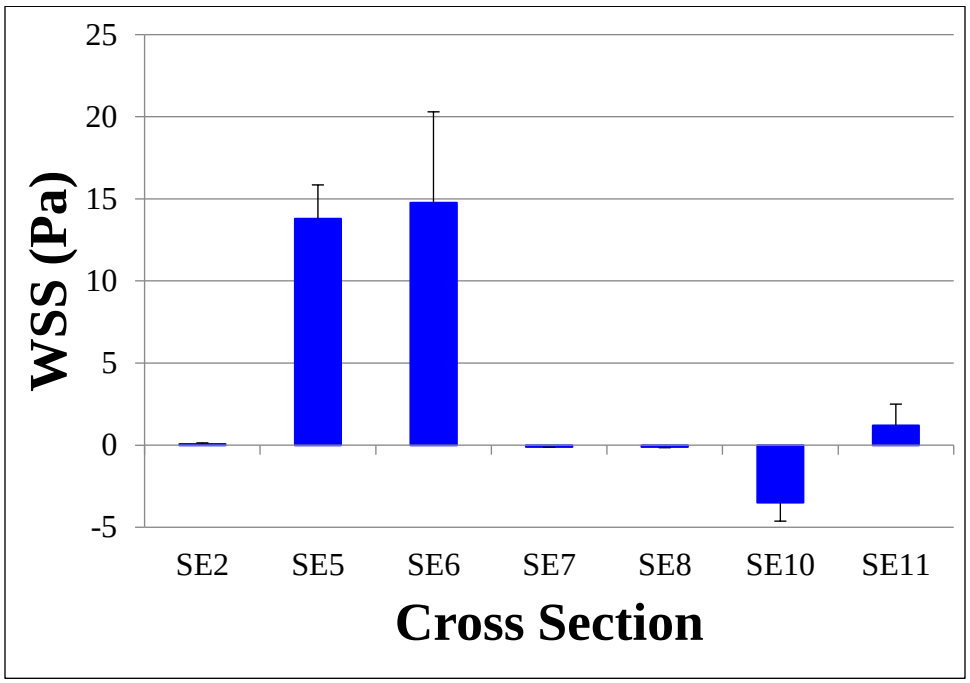

Figure 72. Wall Shear Stress during Mid-Deceleration in Sudden Expansion Orientation.

The WSSs during diastole in the sudden expansion orientation are given in Figure 73. WSSs are negative at all planes aside from SE5 and SE6 within the throat. The lowest WSS of -6.02 Pa was calculated at SE10. This plane was the location with the most recirculation. The standard deviation is also large at this plane.

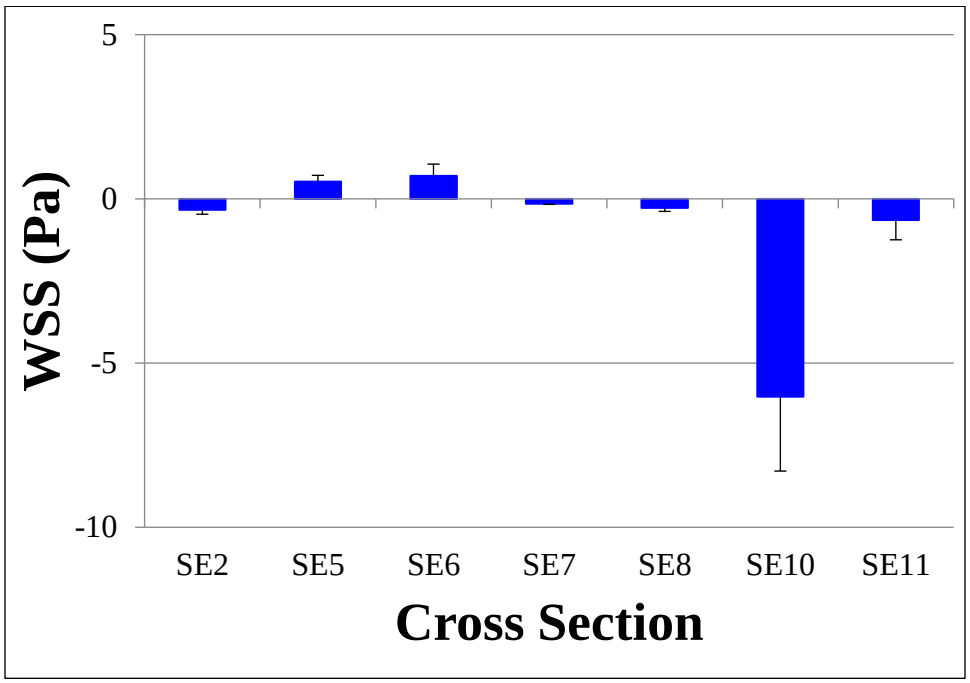

Figure 73. Wall Shear Stress during Diastole in Sudden Expansion Orientation.

Figure 74 shows the WSSs during mid-acceleration in the conical diffuser orientation. The trends and values are very similar to those of mid-acceleration in the sudden expansion orientation. The peak WSS of 14.07 Pa is within the throat at CD6. Downstream of the throat, WSSs are slightly negative. Standard deviations are again large within the throat, although not as large as during mid-acceleration in the sudden expansion orientation.

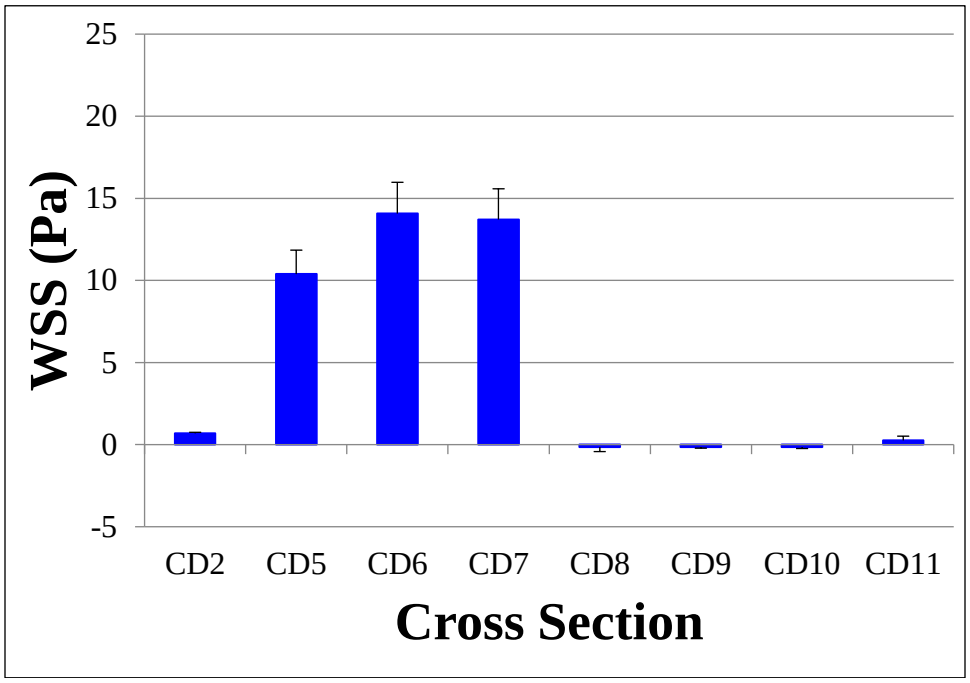

Figure 74. Wall Shear Stress during Mid-Acceleration in Conical Diffuser Orientation.

The WSSs during systole in the conical diffuser orientation are given in Figure 75. The trends are similar to those during systole in the sudden expansion orientation. The peak WSS of 40.14 Pa occurs at CD6. Within and following the diffuser, WSSs are very low. The standard deviations within the throat are high.

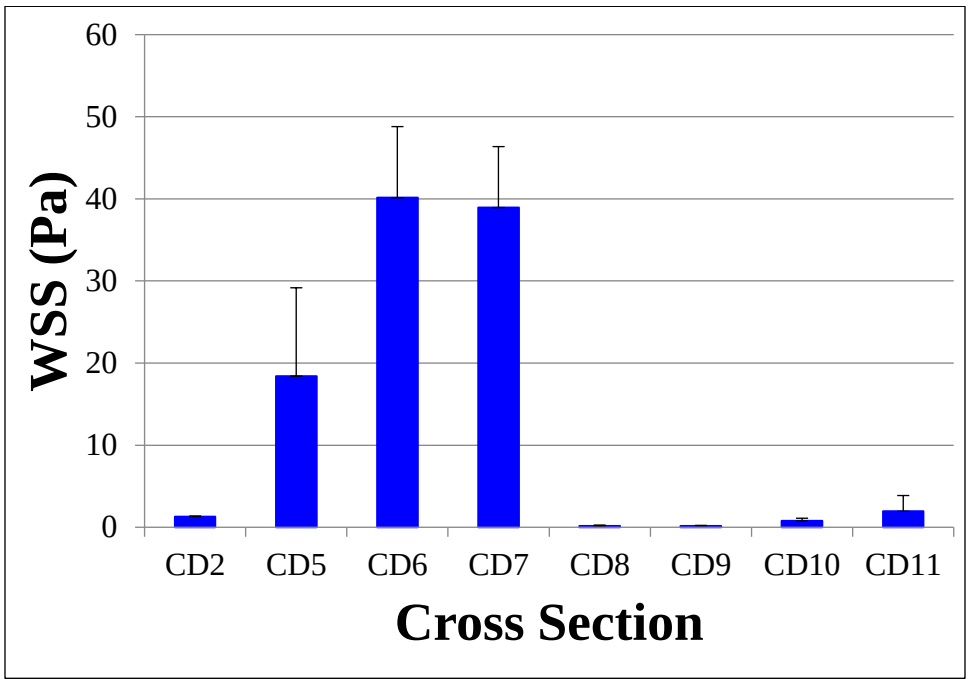

Figure 75. Wall Shear Stress during Systole in Conical Diffuser Orientation.

Figure 76 shows the WSSs during mid-deceleration in the conical diffuser orientation. The peak WSS is 13.36 Pa at CD6. At CD2, CD8, CD9, and CD10, the WSSs are negative, reaching a minimum of -1.43 Pa at CD10. The standard deviations are large at CD5, CD9, CD10, and CD11.

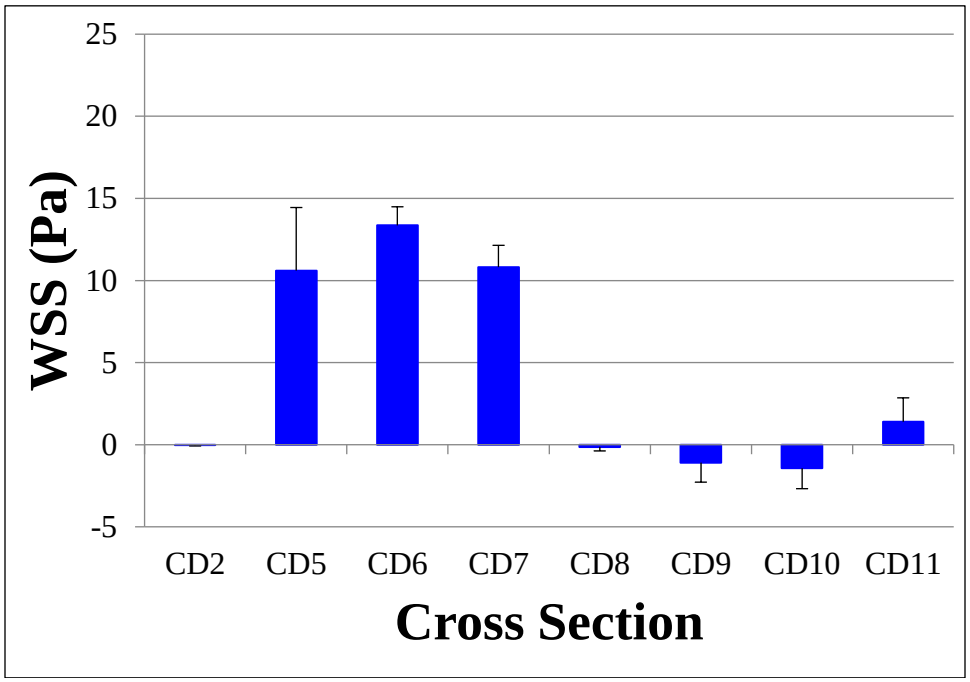

Figure 76. Wall Shear Stress during Mid-Deceleration in Conical Diffuser Orientation.

Figure 77 shows the WSSs during diastole in the conical diffuser orientation. WSSs are negative at all planes aside from CD6 and CD7. They are most negative at CD5, CD8, CD9, and CD10, where the recirculation is significant. The minimum value of -3.00 Pa is at CD9. Standard deviations are large at CD5, CD8, CD9, CD10, and CD11, exceeding the mean values at CD5, CD8 and CD11.

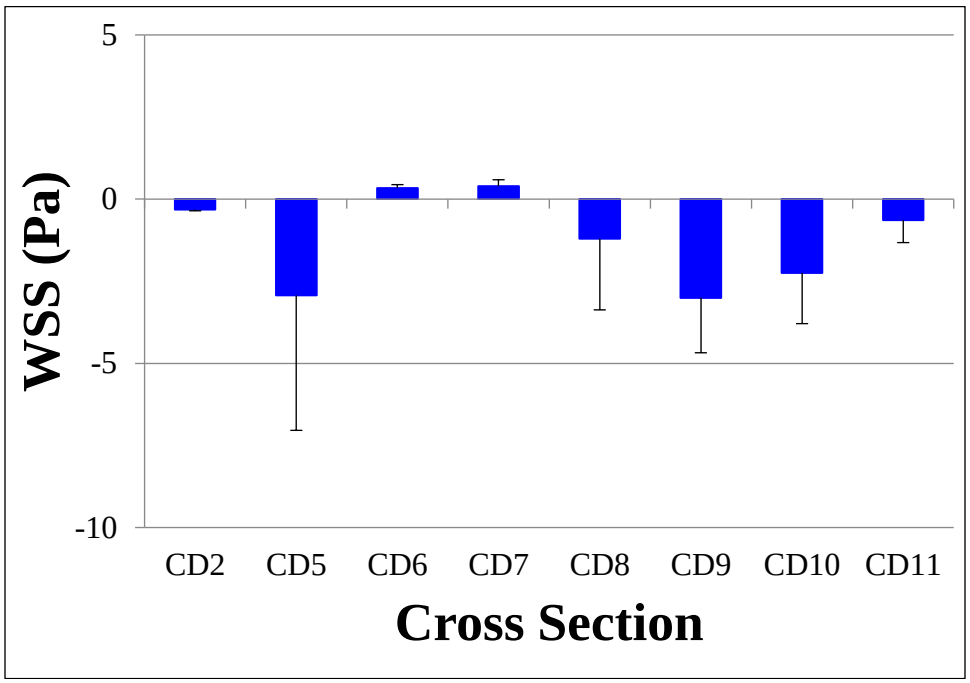

Figure 77. Wall Shear Stress during Diastole in Conical Diffuser Orientation.

Chapter 6

Discussion

6.1 Steady Velocity Comparison to Peak Pulsatile Flow

Figures 78 and 79 show the comparison of pulsatile data during peak systole with steady data at Reynolds numbers of 2000 and 5000 taken by Taylor *et al.* [57] in the sudden expansion orientation. The Reynolds number during peak systole is 4300. All data are normalized using equations 37 and 38. In Figure 78, the systolic pulsatile velocity curves are normalized using the mean throat velocity during peak systole, and the steady velocity curves are normalized using the mean throat velocity for Reynolds numbers of 2000 and 5000. In Figure 79, the data are normalized using the peak throat velocities for each curve's respective Reynolds number. For SE2, SE5, SE6, SE7, and SE8, all three curves lie very close to one another at each spatial location. At SE2 (Figures 78a and 79a), flow is fully developed for all three curves. At SE5 (Figures 78b and 79b) and SE6 (Figures 78c and 79c) within the throat, the flow profiles for all three curves are blunted.

At SE7 and SE8 (Figures 78d, 78e, 79d, and 79e), a jet has formed for all three curves with centerline velocity similar to those in the throat regions, and flow has separated from the walls. The three curves overlap in the center of the plane, but there is recirculation during steady flow at both Reynolds numbers and no recirculation during peak systole. This is also true at SE10 (Figures 78f and 79f) where there was significant recirculation for Re5000, and SE11 (Figures 78g and 79g) where there was significant recirculation for Re2000, but no recirculation during peak systole. During pulsatile flow, the fluid accelerates from near-zero during diastole to a mean value of 4.49 m/s in the throat during peak systole. Within that time, the central jet develops in the region downstream of the sudden expansion. The

recirculation regions surrounding the jet take time to develop, and the 373 ms over which the fluid is accelerating is not sufficient for recirculation regions to develop.

The reattachment length is a function of the Reynolds number. For both steady and pulsatile flow, the reattachment length is lower for higher Reynolds numbers, a trend supported by a study of flow over a backward facing step by Armaly *et al.* [44]. This is likely due to higher energy dissipation at higher Reynolds numbers, manifested in the higher turbulence stresses downstream of the sudden expansion [57]. At SE10, flow is reattaching for Re5000 and the systolic velocity curve, but it remains fully separated for Re2000. At SE11, the flow has fully reattached at Re5000, but is still reattaching for the pulsatile flow and for Re2000. The Reynolds number is higher during peak systole, so the flow is closer to reattaching for the systolic velocity curve than for the Re2000 curve.

Taylor *et al.*[57] determined the error between the measured flow rate and the flow rate calculated from the velocity data at SE11 for Re2000 by integrating the velocity profile over the entire cross section. The calculated flow rate was 5% lower than the flow rate measured by the flow probe. In the original PIV study by Hariharan *et al.* [35], the calculated flow rate was 26.1% lower than the measured flow rate. In the present study, the calculated flow rate at SE11 is 13.4% lower than the measured flow rate. The chaotic flow profile from the breakdown of the jet explains the error between the calculated flow rate and measured flow rate at this plane [57].

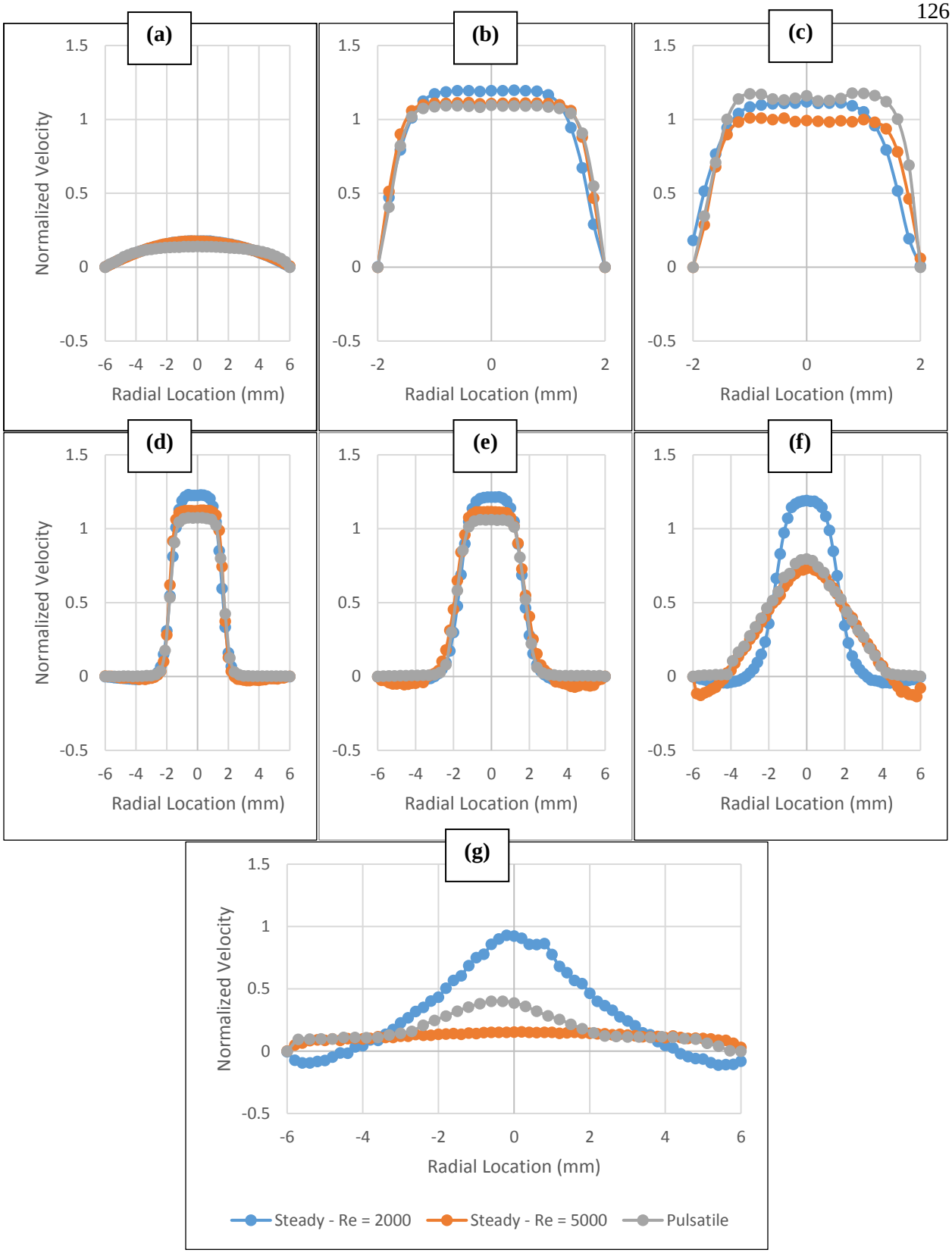

Figure 78. Comparison of Steady Data at Re2000 and Re5000 with Pulsatile Data during Peak Systole, all normalized by mean throat velocity, at (a) SE2, (b) SE5, (c) SE6, (d) SE7, (e) SE8, (f) SE10, (g) SE11

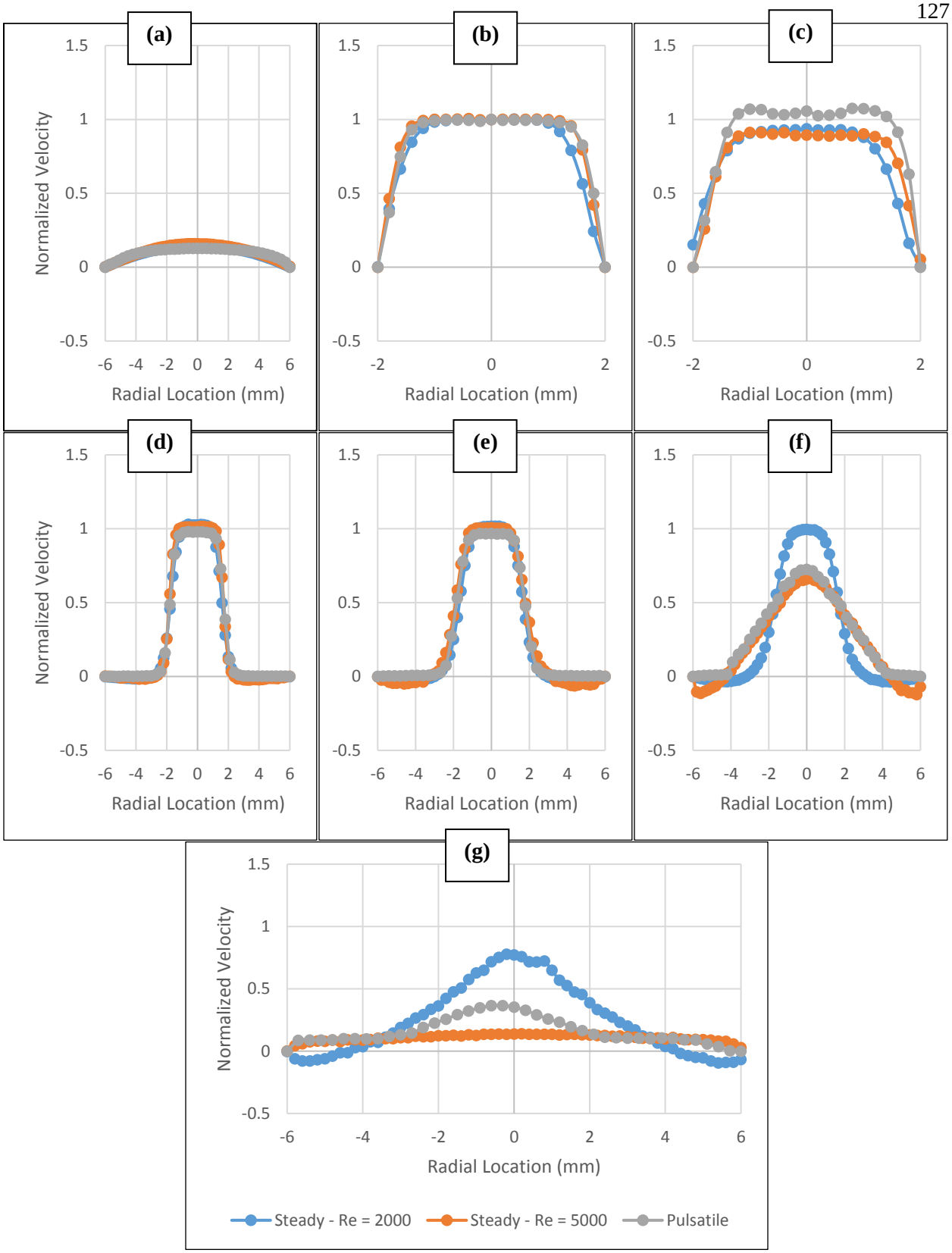

Figure 79. Comparison of Steady Data at Re2000 and Re5000 with Pulsatile Data during Peak Systole, all normalized by peak throat velocity, at (a) SE2, (b) SE5, (c) SE6, (d) SE7, (e) SE8, (f) SE10, (g) SE11

A computational study conducted by Walters *et al.*[67] found similar trends to those shown in Figure 80. A streamwise velocity contour and streamline plot generated using RANS k-ω SST in the sudden expansion orientation at a Reynolds number of 6500 is shown in Figure 79. As shown in the figure, a central jet develops in the area downstream of the sudden expansion, with recirculation zones outside of the jet. This central jet was observed in the steady flow results and during mid-acceleration, systole, and mid-deceleration for pulsatile flow. In addition, there were areas of recirculation downstream of the sudden expansion during steady flow and for mid-deceleration and diastole. Farther downstream of the sudden expansion, flow reattaches to the wall, a trend also shown in Figures 78f and 78g for steady and pulsatile flow.

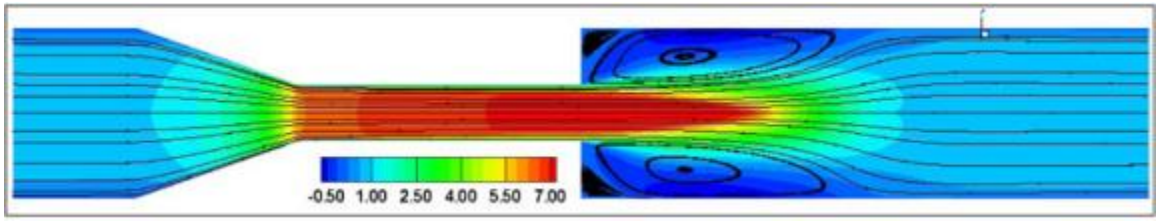

Figure 80. Streamwise Velocity Contours and Flow Streamlines Calculated using RANS k- ω SST in the Sudden Expansion Orientation at a Reynolds Number of 6500, Adapted from Walters et al. [67]

Figures 81 and 82 compare pulsatile data during peak systole with steady data taken at Reynolds numbers of 2000 and 5000 from Taylor *et al*. [57] in the conical diffuser orientation. The Reynolds number during peak systole is again 4300, and all data are normalized using Equations 37 and 38. In Figure 81, the systolic velocity curve is normalized using the mean throat velocity during peak systole, and the steady velocity curves are normalized using the mean throat velocities for their respective Reynolds numbers. In Figure 82, all three curves are normalized using the peak throat velocity for each curve's respective Reynolds number. All three curves are very similar at CD2, CD5, CD6, and CD7. At CD2 (Figures 81a and 82a), the flow for all three profiles is fully developed. At CD5 (Figures 81b and 82b), the flow profiles for all three curves are very blunted, as the fluid has just passed through the sudden contraction. At CD6 and CD7 (Figures 81c, 81d, 82c, and 82d), the profiles have become more parabolic for all three curves.

At CD8, CD9, CD10, and CD11 (Figures 81e – 81h and 82e – 82h) there is recirculation present for steady flow but not for peak systolic flow. Similar to the sudden expansion direction, the recirculation regions do not have time to develop during the short duration that flow is accelerating to peak systole.

Just as in the sudden expansion orientation, flow reattaches to the wall sooner for higher Reynolds numbers. At CD8, CD9, and CD10 (Figures 81e – 81g and 82e – 82g), the systolic velocity curve and the Re5000 curve are in various stages of reattachment, with the Re5000 curve closer to full reattachment at each plane. The Re2000 curve is still fully detached from the wall at CD8 and CD9, with a similar velocity to that seen in the throat region. At CD10, Re2000 is just beginning to reattach to the walls. At CD11 (Figures 81h and 82h), the Re5000 curve has fully reattached. The systolic velocity and Re2000 curves are still in the process of reattaching to the wall, with the systolic velocity curve closer to reaching fully developed flow than the Re2000 curve.

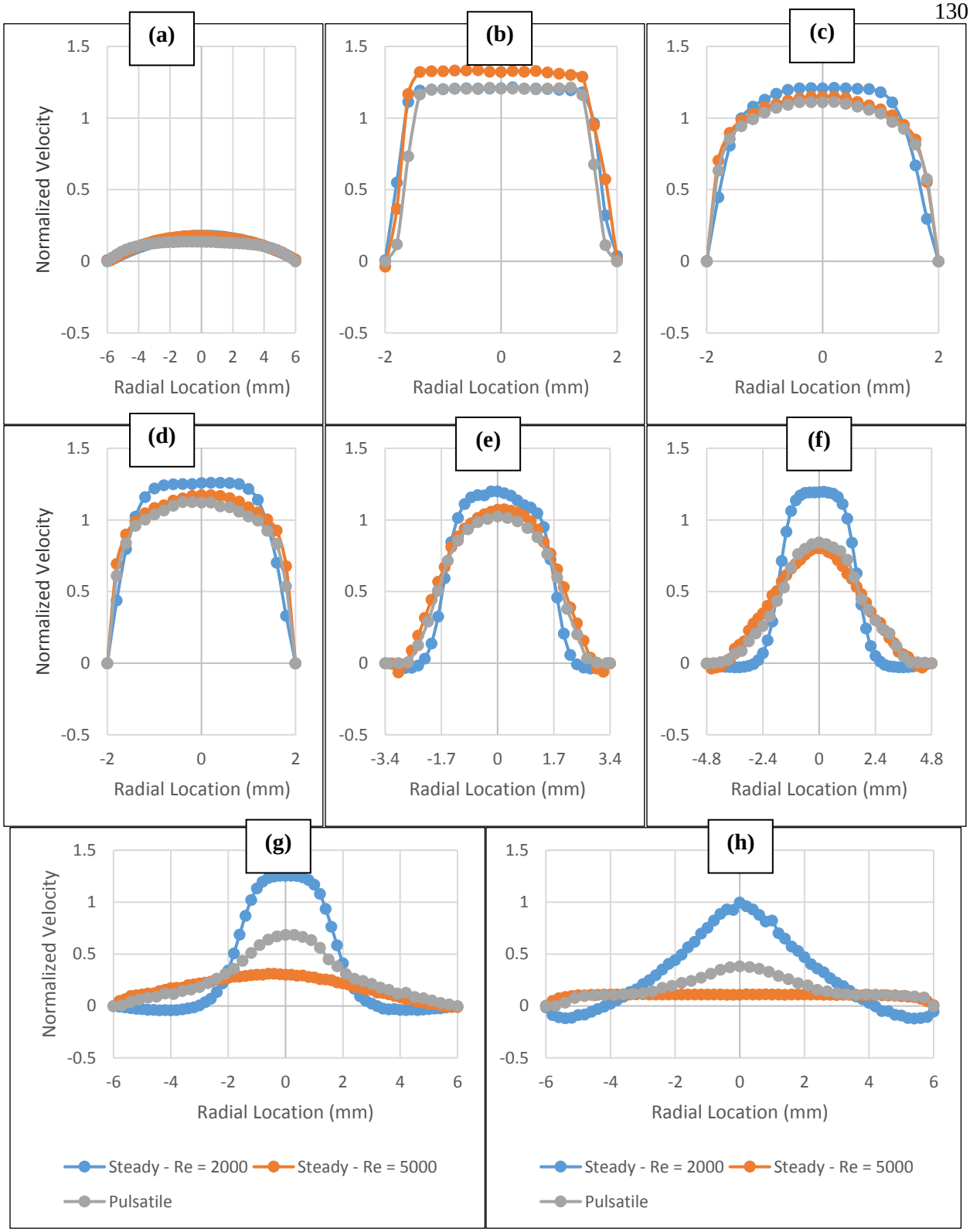

Figure 81. Comparison of Steady Data at Re2000 and Re5000 with Pulsatile Data during Peak Systole, all normalized by mean throat velocity, at (a) CD2, (b) CD5, (c) CD6, (d) CD7, (e) CD8, (f) CD9, (g) CD10, (h) CD11

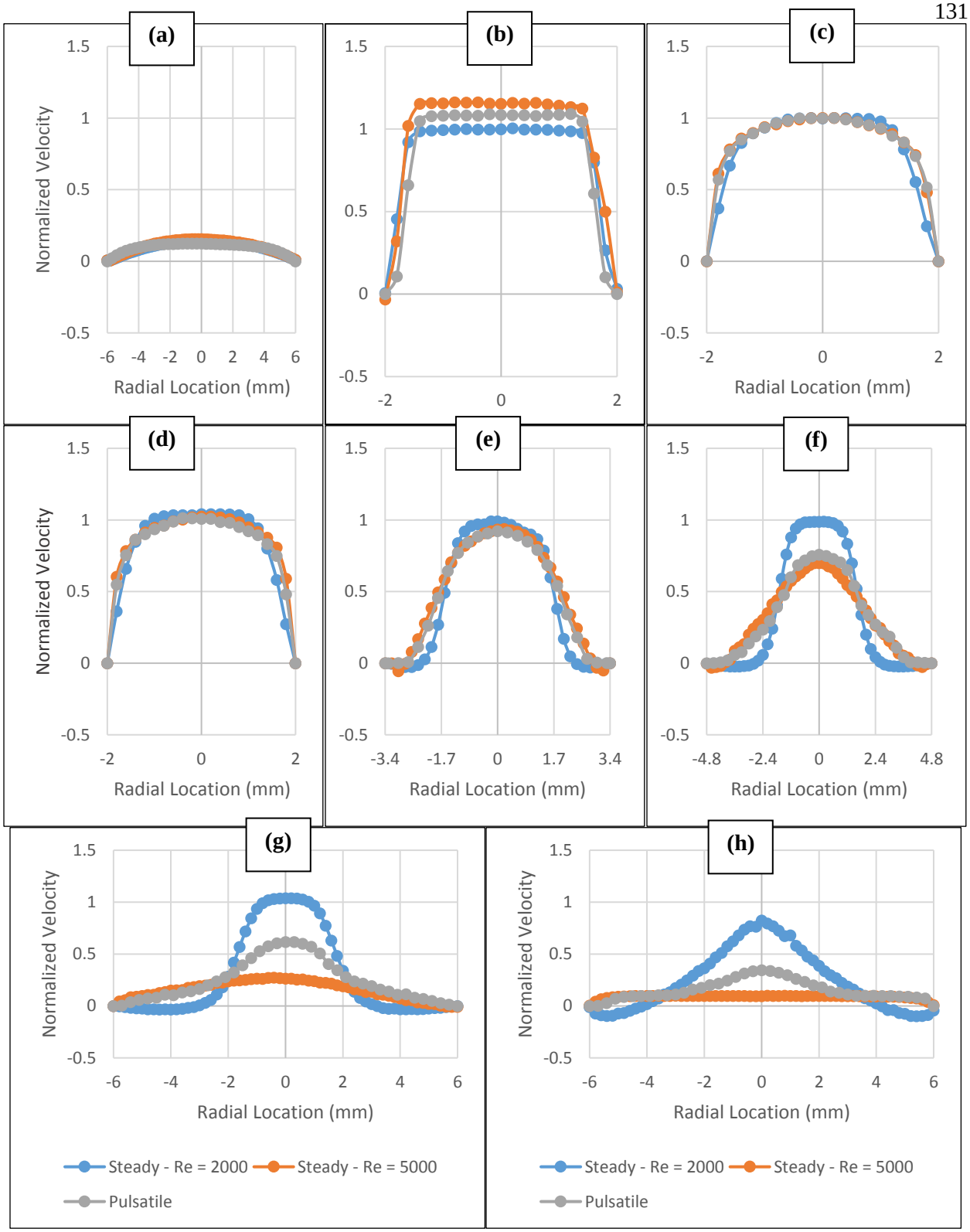

Figure 82. Comparison of Steady Data at Re2000 and Re5000 with Pulsatile Data during Peak Systole, all normalized by peak throat velocity, at (a) CD2, (b) CD5, (c) CD6, (d) CD7, (e) CD8, (f) CD9, (g) CD10, (h) CD11

6.2 Hemolysis Analysis

Hemolysis results from the exposure of red blood cells to a high enough Reynolds shear stress for a given exposure time. The threshold Reynolds shear stress values necessary to induce hemolysis are summarized in Table 1, and range from a minimum RSS of 150 Pa for an exposure time of 10^2 s [22] to a maximum RSS of 4000 Pa for an exposure time of 10^{-6} s [23]. Based on these threshold limits, multiple planes examined in this study present flow conditions that may induce hemolysis. SE8, SE10, SE11, CD5, CD6, CD7, CD8, CD9, and CD10 all have MRSSs that exceed 150 Pa during at least one portion of the cardiac cycle. Each of these planes also have significant PRS values. In addition, SE7, SE10, CD5, CD8, and CD9 all have systolic MRSSs greater than 400 Pa, a commonly cited value for the onset of hemolysis for an exposure time of 1ms [17].

The plots of MRSSs that exceed 400 Pa during peak systole in the sudden expansion orientation are given in Figure 83. At SE7 (Figure 83a), which is immediately downstream of the sudden expansion, the peak MRSS value of 471.47 Pa is located just outside of the recirculation zone. Farther downstream at SE10 (Figure 83b), shear stresses have increased across the central portion of the plane, and the peak MRSS value of 545.3 Pa occurs close to the centerline.

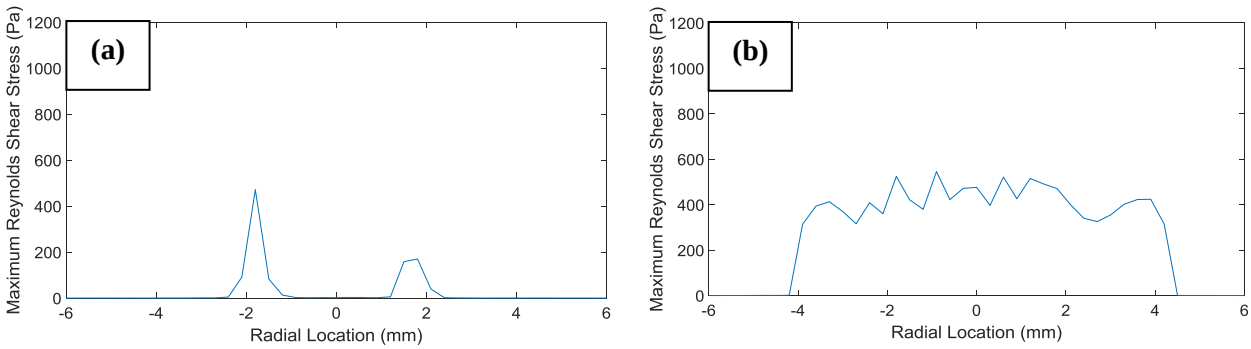

Figure 83. Systolic MRSS values that exceed 400 Pa in Sudden Expansion Orientation, at (s) SE7, and (b) SE10

Figure 84 shows the planes at which systolic MRSS values exceed 400 Pa in the conical diffuser orientation. Within the throat, at CD5 (Figure 84a), the peak MRSS value of 752.88 Pa occurs near the wall. MRSS values are also significant within the diffuser. At CD8 (Figure 84b), the peak MRSS value of 797.79 Pa is located at the border of the free shear layer. The same is true at CD9 (Figure 84c), although the MRSS profile has spread out and the peak value has decreased to 538.7 Pa.

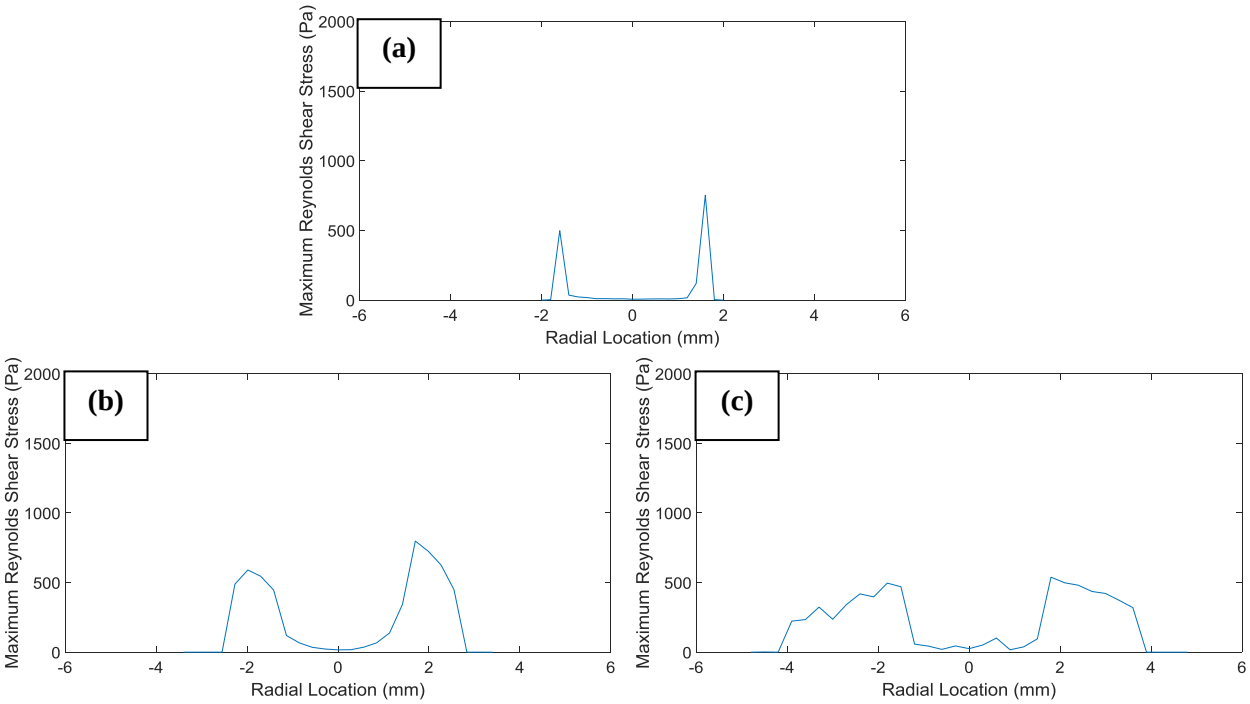

Figure 84. Systolic MRSS Values that Exceed 400 Pa in Conical Diffuser Orientation, at (a) CD5, (b) CD8, and (c) CD9.

Although MRSS values are not as high during the other phases of the cardiac cycle as they are during peak systole, there are several planes with significant shear stresses at other points in the cycle. Figure 85 shows the MRSS values that exceed 150 Pa during mid-deceleration. Within the diffuser at CD9 (Figure 85a), peak MRSS values are located just outside of the recirculation zone. Downstream of the diffuser at CD10 (Figure 85b), the MRSS values that are high enough to induce hemolysis are located at the center of the plane.

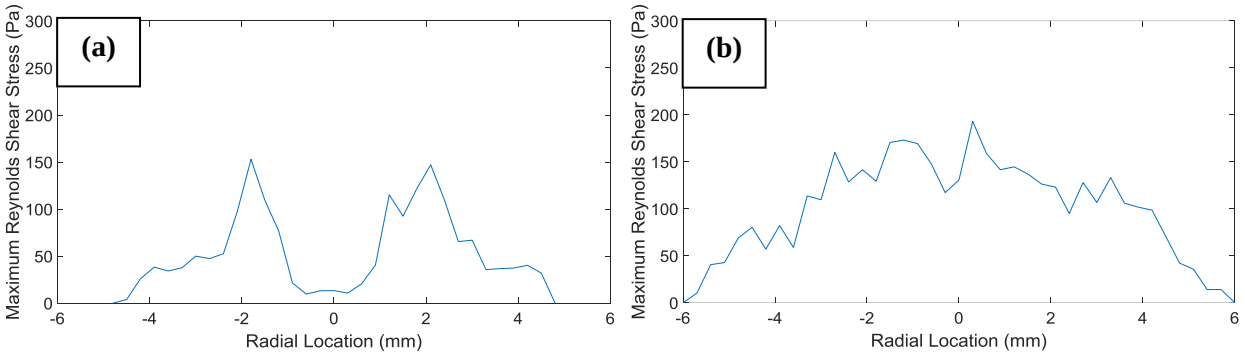

Figure 85. MRSS Values that Exceed 150 Pa during Mid-Deceleration, at (a) CD9, and (b) CD10

Figure 86 shows the MRSS values during diastole that exceed threshold hemolysis values for certain exposure times from literature. At each of these planes, (SE10, CD5, and CD8), the peak MRSS values are located within the recirculation zones that develop near the wall in the regions following the sudden expansion and the conical diffuser inlet. These values are noteworthy because they occur within slower moving flow regimes than the MRSS values shown in previous figures, meaning that the exposure times are greater.

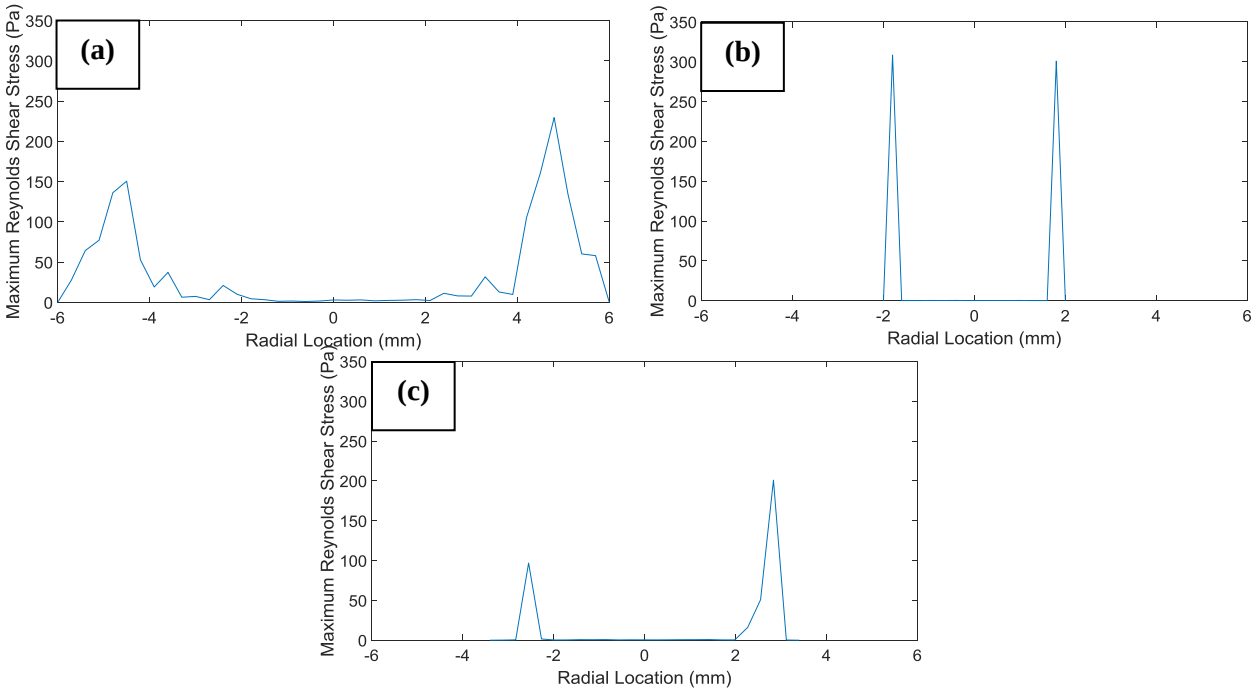

Figure 86. MRSS Values that Exceed 150 Pa during Diastole, at (a) SE10, (b) CD5, and (c) CD8

The elevated MRSS values in the areas downstream of the sudden expansion, in the conical diffuser, and in the area downstream of the conical diffuser are caused by the breakdown of the jet developed in the throat region [57]. The results given in Figures 83-86 indicate that sudden expansions and conical diffusers are problematic geometries that may induce hemolysis during pulsatile flow. However, since hemolysis is a function of both shear stress and exposure time, it is necessary to gain a better understanding of the effect of exposure time in order to draw conclusions about the likelihood of hemolysis in the nozzle model.

Herbertson *et al.* [68] measured hemolysis in the benchmark model in both orientations, and found higher levels of hemolysis in the conical diffuser orientation. That study concluded that the sudden contraction was the likely culprit of hemolysis. The fluid dynamics of any medical devices with similar geometries should be extensively studied and validated to ensure that they do not induce hemolysis. In addition, the elevated shear stresses within both the sudden expansion and conical diffuser orientations provide a useful benchmark to validate any CFD simulation package intending to predict blood damage.

Taylor *et al*. [57] also found that MRSS values were relatively low upstream of the throat. Within the throat at Re5000, shear stress was low in the sudden expansion orientation, but reached a peak of 2000 Pa in the conical diffuser orientation near the wall. Similarly in this study, elevated MRSS values were calculated near the walls of the throat in the conical diffuser orientation but not in the sudden expansion orientation. The maximum MRSS value within the throat was 752.88 Pa at CD5. Downstream of the throat in both orientations, similar to the results presented above, the previous study also found that shear stress was highest in the free shear layer at the edges of the jet at planes SE8 and CD8. During the breakdown of the jet at SE10, CD9, and CD10, Taylor *et al.* [57] found that shear stresses were elevated across the entire plane, which is the same trend observed in the present study. The peak MRSS values calculated downstream of the sudden expansion were 1150 Pa, somewhat higher than the peak value of 471.47 Pa calculated in this study. In the conical diffuser orientation, the peak MRSS value calculated by the previous study was 1350 Pa, again somewhat higher than the peak value of 797.79 Pa in this study.

Also similar to this study, Taylor *et al.* [57] found low levels of turbulence at SE11 and CD11, not exceeding 300 Pa at either plane. In this study, shear stresses were below 200 Pa at each of these planes. Although the Reynolds number used in the previous study is not significantly higher than that of the present study, turbulent flows scale nonlinearly with the Reynolds number [69], leading to the increase in MRSS between studies.

Walters *et al.* [67] used a dynamic hybrid Reynolds-averaged Navier-Stokes large eddy simulation to predict turbulent shear stresses in the sudden expansion orientation at a Reynolds number of 6500. A plot of the resolved turbulent shear stresses is given in Figure 87. The plot shows that maximum shear stresses occur at the boundary of the free shear layer downstream of the sudden expansion. This result is again supported by the present study, and by Taylor *et al* [57]. However, the magnitudes of the shear stresses predicted by Walters *et al.* [67] are lower than those predicted in this study. In addition, the values at most regions of the simulation were near zero, which was not true in this study.

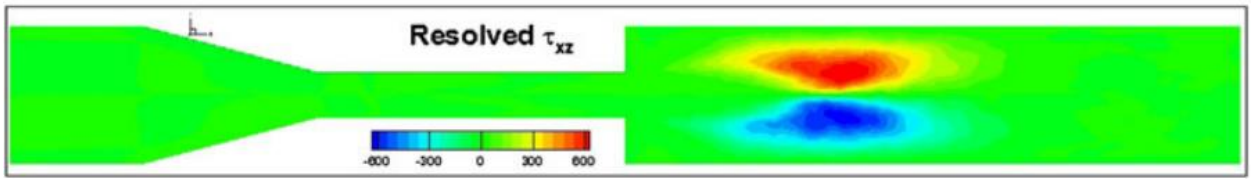

Figure 87. Resolved Turbulent Shear Stresses using DHRL for Re = 6500 in the Sudden Expansion Orientation, adapted from Walters *et al.* [67]

The results of the present study, Taylor *et al.* [57], and Walters *et al.* [67] indicate that for Reynolds numbers in the range used by the three studies (4300 – 6500), there are significant shear stresses downstream of the sudden expansion at the boundary of the free shear layer. As Taylor *et al.* [57] discussed, this is not true for lower Reynolds numbers. At Re2000, the peak shear stresses were located farther downstream of the sudden expansion at SE11, and peak values were at the center of the plane rather than at the boundary of the free shear layer. The results of the three studies indicate that at sufficiently high Reynolds numbers, the transition from the rapid central jet to the surrounding recirculation zone induces significant levels of turbulence.

A recent study of the HeartMateII rotary blood pump examined turbulence in the device, and found that TIs reach between 0.2 and 0.6 within certain regions [70], a similar level of turbulence to those given in Table 5, particularly during systole. Based on the MRSS values measured at the locations with elevated TIs in the benchmark nozzle model, these values indicate that the HeartMateII may induce hemolysis. In addition, the HeartMateII contains a diffuser, which this study has shown can induce problematic fluid dynamics. Indeed, in a clinical study of 115 patients with a HeartMateII, 7% of patients suffered hemolytic events 2-26 months after implantation [71]. The study of this device and others like it with properly validated CFD packages may help reduce blood damage.

6.3 Sudden Expansion Analysis

At the model inlet (SE2), the flow prolife is fully developed, agreeing well with previous LDV data. In addition, stresses and TIs are very low at the inlet, which is expected for laminar flow (the Reynolds numbers given above are for the throat; at the larger inlet diameter, the Reynolds number during systole is 1430). The systolic velocity profiles within the throat are blunted, and the throat is the only location with no regurgitant flow during diastole. Within the throat, PRSs, MRSSs, and TIs are all low, but VSSs and WSSs are higher in the throat than at any other plane.

Downstream of the sudden expansion, a jet develops at the center of the plane with a similar velocity profile to that of the throat. Significant areas of recirculation are present during diastole. Elevated PRSs, MRSSs, and TIs are located at the boundary of the free shear layer during mid-acceleration, systole, and mid-deceleration. During diastole, turbulence statistics are high within the recirculation regions. As the jet breaks down, turbulence characteristics are significant across the entire diameter of the plane during systole, and are higher than at any other point downstream of the sudden expansion. Farther downstream, where the flow profile is nearly reattached, turbulence decreases to levels similar to the nozzle inlet.

Turbulence intensities in the regions upstream and downstream of a sudden expansion were studied by Smyth [45]. As shown in Figure 88a, upstream of the sudden expansion, Smyth [45] found that peak TIs occurred near the wall. This result was replicated in this study, as shown in Figure 88b, which shows the axial TIs at SE5 within the throat region. Peak TIs reach 0.05 near the walls. These values are lower than those found by Smyth [45], which reached approximately 0.18 near the walls. At the center of the plane, TIs dropped to approximately 0.06 in Smyth's study [45], and 0.03 in the present study. The differences in the model geometry, the velocity used to normalize the TIs, the fluid properties, and the Reynolds number make it difficult to compare specific TIs between this study and that of Smyth [45]. However, the trends between the two studies are very similar.

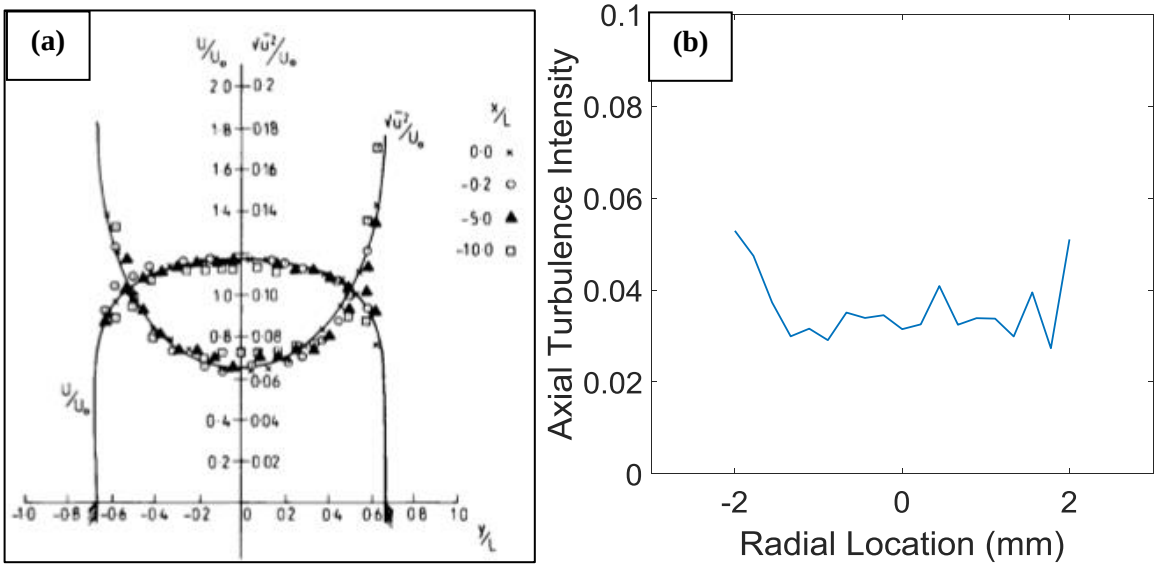

Figure 88. (a) Streamwise Velocity and Turbulence Intensity Upstream of Sudden Expansion adapted from Smyth [45], (b) Axial Turbulence Intensity during Peak Systole at SE5

Shown in Figure 89a, downstream of the sudden expansion, Smyth [45] found that turbulence intensities reached their peak values in the shear layer on the edges of the central jet, dropping in value at the center of the duct and near the walls. As shown in Figures 89b-e, the turbulence intensities calculated in this study immediately downstream of the sudden expansion followed the same trend. At SE7 (Figure

89b) and SE8 (Figure 89d), the axial turbulence intensities reached their peak values at the edges of the recirculation regions, at +/-2 mm from the center of the plane. The radial TIs for SE8 follow the same trend. Although the radial TIs at SE7 do not show this trend, the same result was found at this plane in Taylor *et al.* [57]. The maximum axial TIs were 0.44 and 0.33, and the maximum radial TIs were .02 and 0.15 for SE7 and SE8, respectively. These TIs exceed those in Taylor *et al.* [57], which found low levels of turbulence at SE7, and TIs around 0.25 at SE8. This is reasonable, as the mean velocity used to normalize the TIs is significantly lower in this study. The shapes of the axial and radial TI curves at SE8 are similar between the previous and current studies.

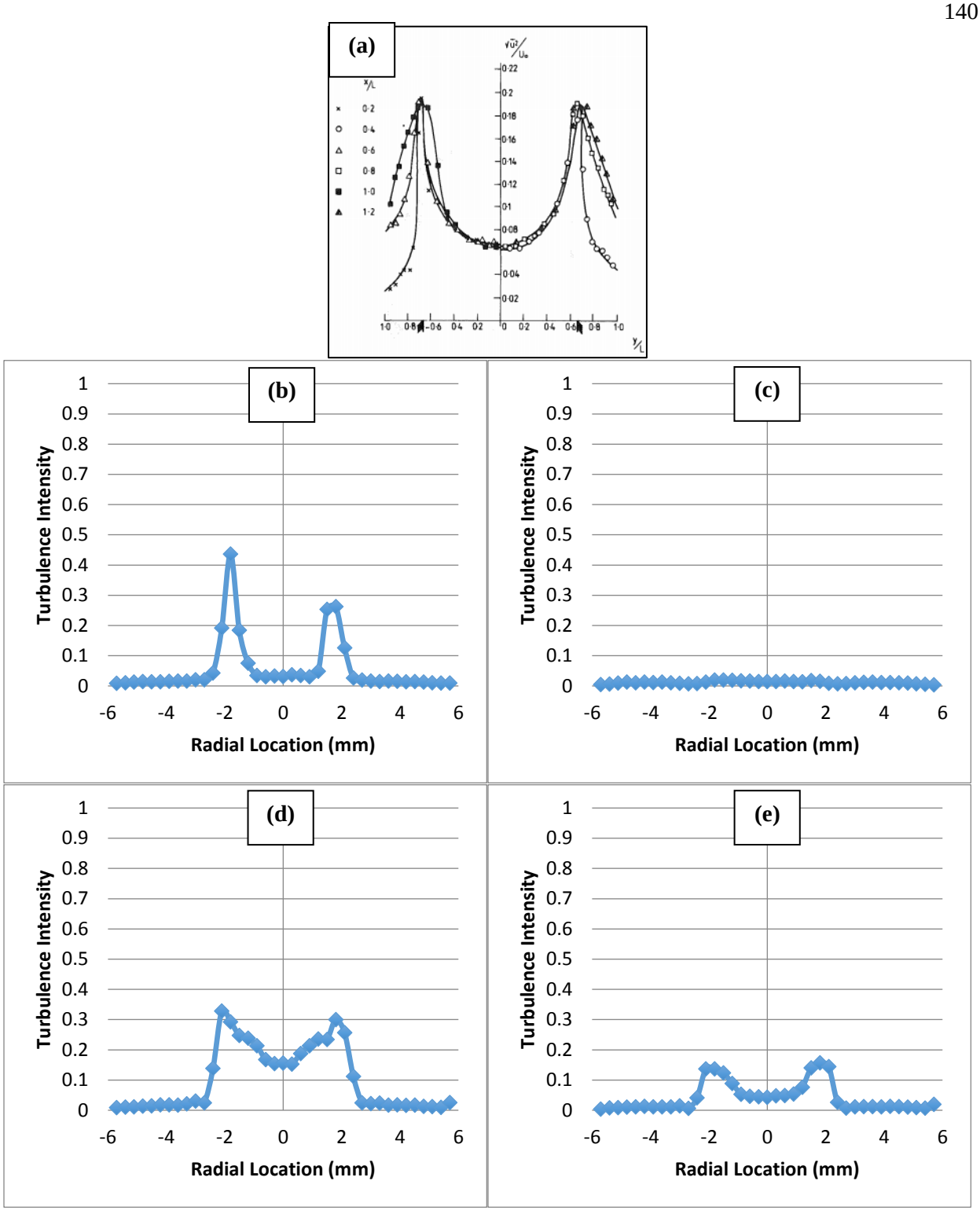

Figure 89. (a) Streamwise Turbulence Intensity downstream of Sudden Expansion, adapted from Smyth [45], and Systolic Turbulence Intensities Downstream of Sudden Expansion for, (b) Axial TI, SE7, (c) Radial TI, SE7, (d) Axial TI, SE8, (e) Radial TI, SE8

In regions following the reattachment point in the study conducted by Smyth [45], turbulence intensities had minimum values at the center of the plane, and reached maximum values nearer to the wall. Flow still had not reattached by SE11 in this study, so this trend was not observed.

Smyth [45] also found that the shear stress curves in the regions following the sudden expansion reached their maximum values at the edges of the separation zones. This trend also occurred in this study. As shown in Figure 90, Reynolds shear stresses at SE7 and SE8 downstream of the sudden expansion reached peak values at the edges of the recirculation regions.

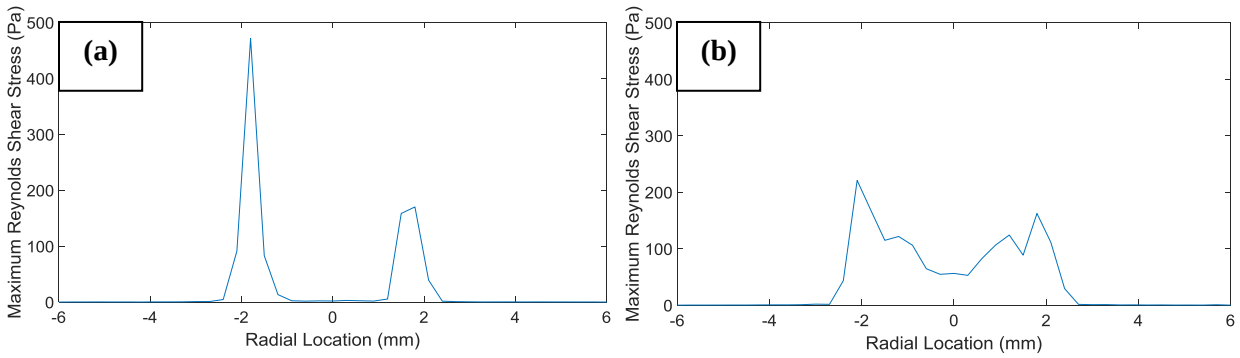

Figure 90. Reynolds Shear Stresses during Peak Systole at (a) SE7, and (b) SE8

6.4 Conical Diffuser Analysis

Similar to the sudden expansion orientation, flow at the nozzle inlet (CD2) is fully developed with negligible turbulence statistics. Within the throat, the velocity profile is again blunted in shape. PRSs, MRSSs, and TIs, are very high within the throat, particularly near the sudden contraction at CD5. These turbulence statistics are each an order of magnitude higher than the values calculated in the throat in the sudden expansion orientation, indicating that the rapid contraction that leads to the throat in the conical diffuser orientation generates significantly more turbulence than the gradual contraction in the sudden expansion orientation. The difference in turbulence statistics in the throat of the model in the sudden expansion orientation and conical diffuser orientation was also found by Taylor *et al.* [57].

Within the conical diffuser, the systolic flow profile separates from the wall. Areas of recirculation develop in the separation zone during diastole. Similar to the sudden expansion orientation, significant areas of turbulence are present at the edges of the separation regions. Turbulence gradually decreases as the fluid moves downstream and reattaches to the wall. The gradual expansion does not lessen the turbulence of fluid exiting the throat region in comparison to the sudden expansion. In fact, turbulence is somewhat higher exiting the conical diffuser than the sudden expansion, a result also found by Taylor *et al.* [57]. Turbulence may be higher in the regions downstream of the conical diffuser than the sudden expansion because rapid flow deceleration within the conical diffuser significantly increases shear-layer instabilities [72].

A study by Okwuobi and Azad [50], one result of which is given in Figure 91, showed that TIs immediately following a conical diffuser inlet are maximum near the wall. The maximum TIs shift gradually towards the center of the duct as the flow moves downstream. This trend is also seen in the present study in Figure 92. At CD8 (Figures 92a and 92b), located within the conical diffuser, peak TIs are very close to the walls. Turbulence intensities are also greater at CD8 than at any of the planes downstream. As fluid moves downstream, turbulence intensities gradually decrease. At CD9 (Figures 92c and 92d), the peak TIs have decreased and moved closer to the center of the plane. After exiting the diffuser at CD10 (Figures 92e and 92f), the peak TIs are again closer to the centerline. Finally, at CD11 (Figures 92g and 92h), the turbulence is greatly diminished, and the maximum value is near the centerline.

The TI curves at each of the planes following the conical diffuser in Taylor *et al.* [57] are similar in shape to those shown in Figure 92. Peak TIs in the present study are greater at CD8, CD9, and CD10 but are lower at CD11.

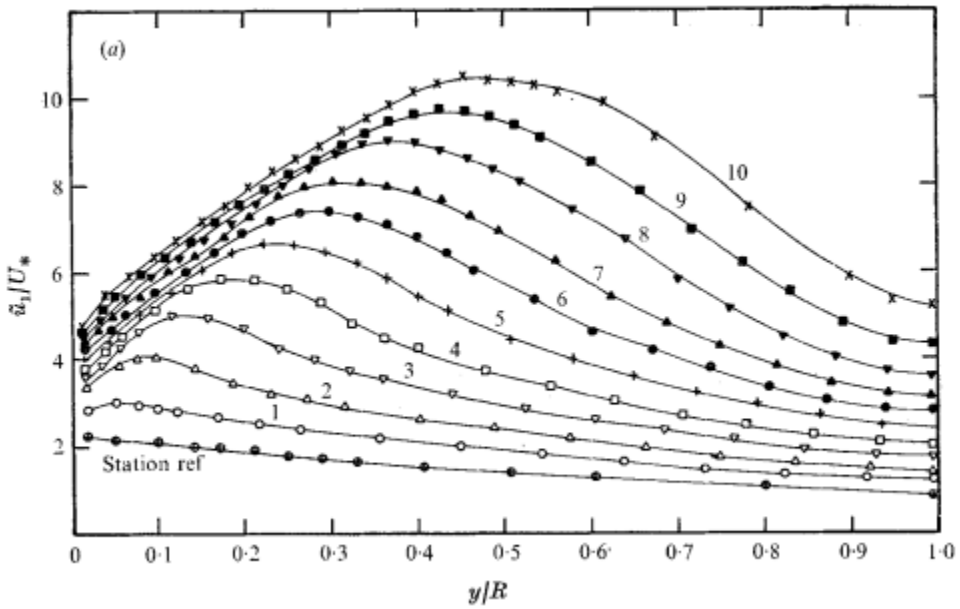

Figure 91. Turbulence Intensity Distribution, Adapted from Okwuobi and Azad [50]

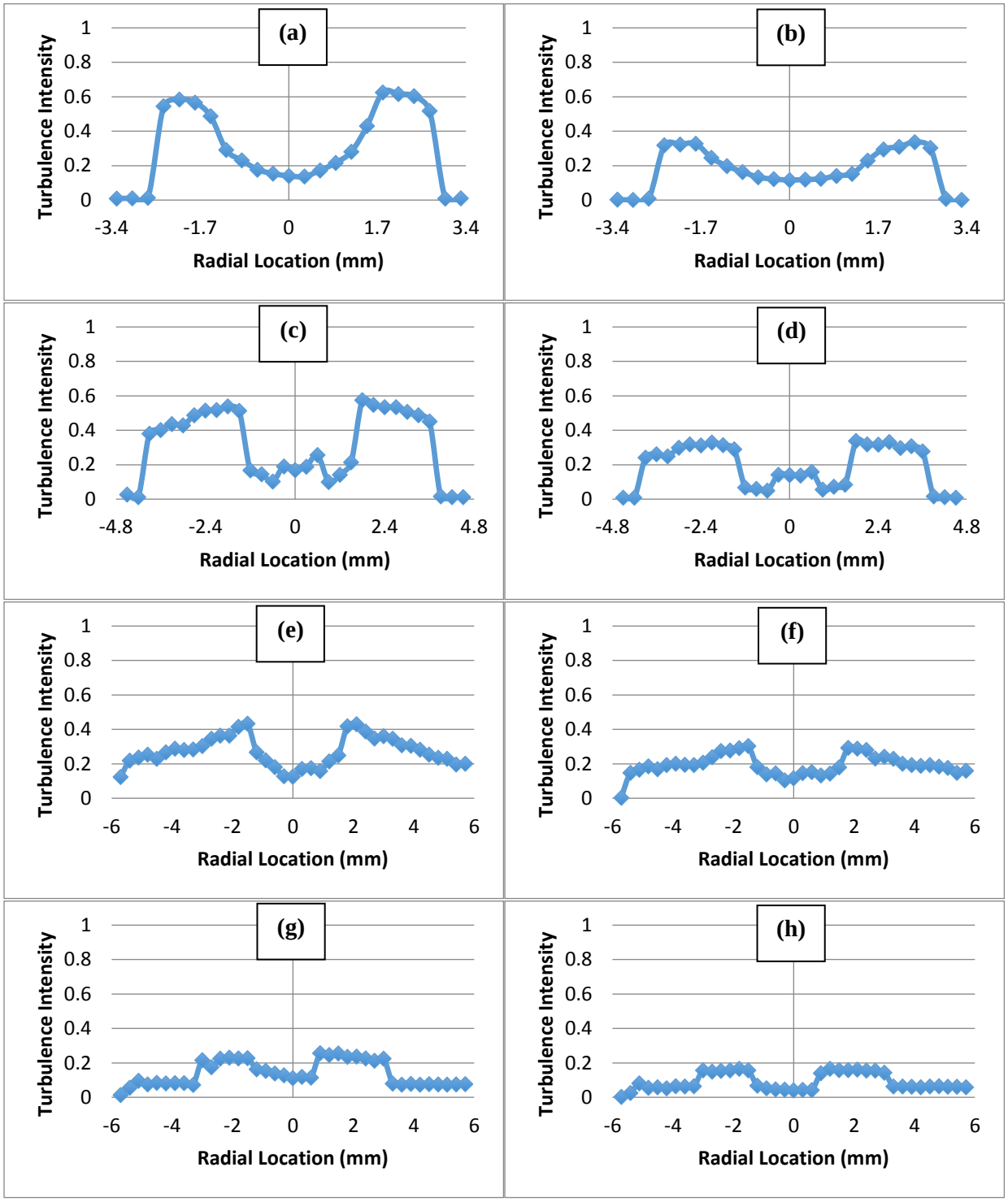

Figure 92. Turbulence Intensities during Peak Systole for (a) CD8, Axial TI, (b) CD8, Radial TI, (c) CD9, Axial TI, (d) CD9, Radial TI, (e) CD10, Axial TI, (f) CD10, Radial TI, (g) CD11, Axial TI, (h) CD11, Radial TI

During diastole, there was asymmetry between the recirculation regions in the conical diffuser orientation, an example of which is given in Figure 93. Similar asymmetry was detected by Taylor *et al.* [57] and Stewart *et al.* [38]. In Stewart *et al.* [38], asymmetries developed within the conical diffuser, and were diminished downstream. This same trend occurred in this study. These areas of asymmetry likely developed due to the adverse pressure gradient in the diffuser. They may also be caused by minor inlet flow asymmetries, such as slight misalignment of the inlet tubing, nozzle throat, cone, and nozzle outlet [38].

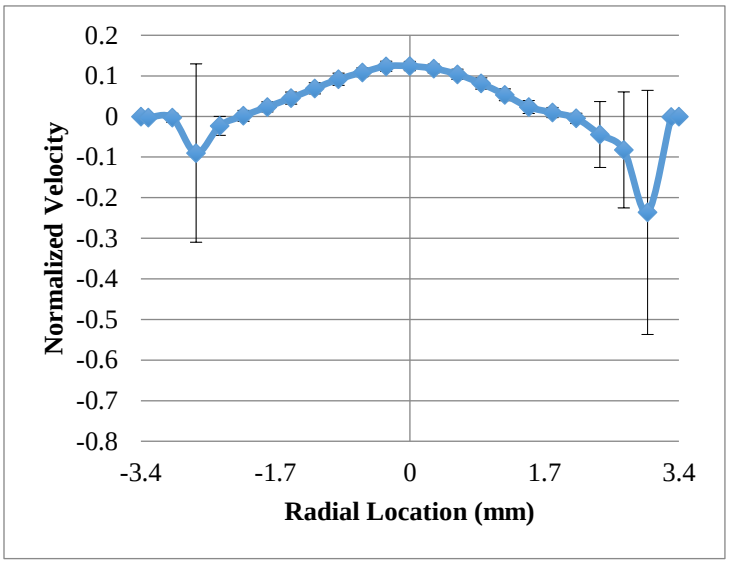

Figure 93. Asymmetry at CD8 during Diastole

6.5 Viscous Shear Stresses and Wall Shear Stresses

The viscous shear stresses and wall shear stresses during systole are similar to those calculated by Taylor *et al.* [57]. Like the previous study, the VSSs presented in this study are an order of magnitude lower than the calculated maximum Reynolds shear stresses. Due to our inability to calculate axial viscous normal stresses from the velocity data, it was impossible to convert the viscous shear stresses to their maximum values, as was done for the Reynolds shear stresses. This difference in magnitude

suggests that maximum and principal stress values should be calculated when possible, so that the coordinate system used for data collection does not bias the results.

The percent error between the wall shear stresses calculated in this study during systole at the model inlet and theoretical wall shear stresses for fully developed flow was 20.09% for the sudden expansion orientation and 12.34% for the conical diffuser orientation. These values are similar to the error calculated for the previous LDV and PIV data, which ranged from 8-40% [57]. The uncertainty in the Reynolds number, and the limitations imposed by LDV's spatial resolution which only allow the walls to be found within ± 17.5 μm, produce an uncertainty of 20%. Standard deviations are higher at planes within the throat where the assumption of a linear near-wall velocity is less valid [57].

6.6 Study Limitations

Some limitations of LDV include statistical bias due to random particle arrival rate across the probe volume, difficulty measuring high temperature flows, problems measuring the boundary layer due to issues with stray light, and inability to collect measurements at low turbulence levels [58]. In addition, the velocities that were measured in this study were taken in a 2D plane, so some flow asymmetries may not have been fully characterized. Another limitation was our inability to calculate maximum viscous shear stresses. Finally, WSS calculations depended on the assumption of a linear near-wall velocity profile [57], so for planes in which this assumption is less valid, WSS calculations are less accurate.

Chapter 7

Conclusions

The FDA benchmark model was evaluated under pulsatile flow using LDV in order to collect a large dataset that can contribute to the broader effort of validating computational fluid dynamics. Fifteen pertinent planes within the model were evaluated in both the sudden expansion and the conical diffuser orientation in order to obtain data from multiple geometries. The high spatial and temporal resolution of LDV enabled the comprehensive collection of velocity data in the nozzle model undergoing pulsatile flow, and the subsequent calculation of Reynolds stresses and turbulence intensities. Velocity, Reynolds stress, and turbulence intensity data were presented for mid-acceleration, systole, mid-deceleration, and diastole at each plane, and locations with significant turbulence were discussed. CFD simulations studying hemolysis and platelet activation in the nozzle model can compare results to this dataset of Reynolds shear stresses to help validate their accuracy.

The results from this study and those of Taylor *et al.* [57] indicate that sudden expansion and conical diffuser geometries induce high levels of turbulence which can lead to blood damage. The study of turbulence in biomedical devices is crucial to prevent serious complications like hemolysis. The dataset collected in this study, in conjunction with data collected previously using this and other models, will assist in the development of accurate CFD simulations, ultimately improving the ability of scientists and engineers to design and develop novel medical devices.

Future studies should evaluate the benchmark model using different Reynolds numbers under pulsatile flow, providing data from multiple flow regimes. In addition, models with different geometries should be studied to generate a diverse set of data with which to compare to CFD.

BIBLIOGRAPHY

[1] A. S. Go *et al.*, *Heart Disease and Stroke Statistics--2014 Update: A Report From the American Heart Association*, vol. 129, no. 3. 2014.

[2] T. Lee, "Mitral Valve Disease," *Case-Based Rev. Cardiothorac. Surg.*, pp. 1–5, 2004.

[3] M. G. Beckman, W. C. Hooper, S. E. Critchley, and T. L. Ortel, "Venous Thromboembolism," *Am. J. Prev. Med.*, vol. 38, no. 4, pp. S495–S501, 2010.

[4] CDC *et al.*, "Nanocrystalline calcium phosphate ceramics in biomedical engineering," *J. Mater. Chem.*, vol. 113, no. 1, pp. 441–449, 2002.

[5] M. Slaughter *et al.*, "Advanced heart failure treated with continuous-flow left ventricular assist device.," *N. Engl. J. Med.*, vol. 361, no. 23, pp. 2241–51, 2009.

[6] J. E. Sousa, "Four-Year Angiographic and Intravascular Ultrasound Follow-Up of Patients Treated With Sirolimus-Eluting Stents," *Circulation*, vol. 111, no. 18, pp. 2326–2329, 2005.

[7] C. M. Shaw, L. B. Scorza, P. N. Waybill, H. Singh, and F. C. Lynch, "Optional Vena Cava Filter Use in the Elderly Population," *Jvir*, vol. 22, no. 6, pp. 824–828, 2011.

[8] Y. P. Chiang, J. Chikwe, A. J. Moskowitz, S. Itagaki, D. H. Adams, and N. N. Egorova, "Survival and long-term outcomes following bioprosthetic vs mechanical aortic valve replacement in patients aged 50 to 69 years.," *Jama*, vol. 312, no. 13, pp. 1323–9, 2014.

[9] A. Platis and D. F. Larson, "CardioWest temporary total artificial heart," *Perfusion*, vol. 24, no. 5, pp. 341–347, 2009.

[10] A. K. Mankad *et al.*, "Persistent Anemia in Patients Supported With the Total Artificial

Heart: Hemolysis and Ineffective Erythropoiesis," *J. Card. Fail.*, vol. 17, no. 8, p. S42, 2011.

[11] R. C. Starling *et al.*, "Unexpected Abrupt Increase in Left Ventricular Assist Device Thrombosis," *N. Engl. J. Med.*, vol. 370, no. 1, pp. 33–40, 2014.

[12] S. Sponga, C. Nalli, A. Casonato, and E. Charbonneau, "Severe upper gastrointestinal bleeding in Heartmate II induced by acquired von Willebrand deficiency: anticoagulation management.," *Ann. Thorac. Surg.*, vol. 94, no. 2, pp. e41-3, 2012.

[13] D. Maragiannis, N. Gramze, and B. Ramlawi, "Prosthetic mitral valve thrombosis," no. 3, 2015.

[14] A. Koster *et al.*, "Alterations in coagulation after implantation of a pulsatile Novacor LVAD and the axial flow MicroMed DeBakey LVAD.," *Ann Thorac Surg*, vol. 70, no. 2, pp. 533–537, 2000.

[15] L. O. Thompson, M. Loebe, and G. P. Noon, "What Price Support? Ventricular Assist Device Induced Systemic Response," *ASAIO J.*, vol. 49, no. 5, pp. 518–526, 2003.

[16] K. B. Chandran, S. E. Rittgers, and A. P. Yoganathan, *Biofluid Mechanics: The Human Circulation*, 2nd ed. Boca Raton, FL: CRC Press, 2012.

[17] A. M. Sallam and N. H. Hwang, "Human red blood cell hemolysis in a turbulent shear flow: contribution of Reynolds shear stresses.," *Biorheology*, vol. 21(6), pp. 783–797, 1984.

[18] C. G. Nevaril, J. D. Hellums, C. P. Alfrey, and E. C. Lynch, "Physical Effects in Red Blood Cell Trauma," vol. 15, no. 5, pp. 707–711.

[19] P. C. Lu, H. C. Lai, and J. S. Liu, "A reevaluation and discussion on the threshold limit for hemolysis in a turbulent shear flow," *J. Biomech.*, vol. 34, no. 10, pp. 1361–1364, 2001.

[20] M. Grigioni, C. Daniele, G. D. Avenio, and V. Barbaro, “A discussion on the threshold limit for hemolysis related to Reynolds shear stress,” vol. 32, pp. 1107–1112, 1999.

[21] S. P. Sutera and M. H. Mehrjardi, “Deformation and fragmentation of human red blood cells in turbulent shear flow.,” *Biophys. J.*, vol. 15, no. 1, pp. 1–10, 1975.

[22] L. Leverett, J. Hellums, C. Alfrey, and E. C. Lynch, “Red blood cell damage by shear stress,” *Biophys. J.*, vol. 12, pp. 257–273, 1972.

[23] R. J. Forstrom, “A new measure of erythrocyte membrane strength: the jet fragility test,” University of Minnesota, 1969.

[24] K. H. Fraser, M. E. Taskin, B. P. Griffith, and Z. J. Wu, “The use of computational fluid dynamics in the development of ventricular assist devices.,” *Med. Eng. Phys.*, vol. 33, no. 3, pp. 263–280, 2011.

[25] M. Giersiepen, L. Wurzinger, R. Opitz, and H. Reul, “Estimation of shear stressrelated blood damage in heart valve prosthesis-in vitro comparison of 25 aortic valves,” *Int J Artif Organs*, vol. 13, pp. 300–306, 1990.

[26] A. Garon and M.-I. Farinas, “Fast three-dimensional numerical hemolysis approximation.,” *Artif. Organs*, vol. 28, no. 11, pp. 1016–25, 2004.

[27] M. Grigioni, U. Morbiducci, G. D’Avenio, G. Di Benedetto, and C. Del Gaudio, “A novel formulation for blood trauma prediction by a modified power-law mathematical model,” *Biomech. Model. Mechanobiol.*, vol. 4, no. 4, pp. 249–260, 2005.

[28] Y. Alemu and D. Bluestein, “Flow-induced Platelet Activation and Damage Accumulation in a Mechanical Heart Valve: Numerical Studies,” *Artif. Organs*, vol. 31, no. 9, pp. 677–688, 2007.

[29] Y. Chen, T. L. Kent, and M. K. Sharp, “Testing of Models of Flow-Induced Hemolysis in

Blood Flow Through Hypodermic Needles," *Artif. Organs*, vol. 37, no. 3, pp. 256–266, 2013.

[30] G. Heuser and R. Opitz, "A Couette Viscometer for Short Time Shearing in Blood," *Biorheology*, vol. 17, no. 17–24, 1980.

[31] L. Goubergrits and K. Affeld, "Numerical estimation of blood damage in artificial organs," *Artif. Organs*, vol. 28, no. 5, pp. 499–507, 2004.

[32] D. Arora, M. Behr, and M. Pasquali, "A tensor-based measure for estimating blood damage," *Artif. Organs*, vol. 28, no. 11, pp. 1002–1015, 2004.

[33] A. Arvand, M. Hormes, and H. Reul, "A validated computational fluid dynamics model to estimate hemolysis in a rotary blood pump.," *{A}rtif {O}rgans*, vol. 29, no. 7, pp. 531–540, 2005.

[34] Y. Chen and M. K. Sharp, "A Strain-Based Flow-Induced Hemolysis Prediction Model Calibrated by In Vitro Erythrocyte Deformation Measurements," *Artif. Organs*, vol. 35, no. 2, pp. 145–156, 2011.

[35] P. Hariharan *et al.*, "Multilaboratory Particle Image Velocimetry Analysis of the FDA Benchmark Nozzle Model to Support Validation of Computational Fluid Dynamics Simulations," vol. 133, no. APRIL, pp. 1–14, 2011.

[36] "FDA's Critical Path Initiative," 2014. [Online]. Available: http://www.fda.gov/ScienceResearch/SpecialTopics/CriticalPathInitiative/ucm076689.htm. [Accessed: 05-Dec-2015].

[37] S. F. C. Stewart *et al.*, "Assessment of CFD Performance in Simulations of an Idealized Medical Device: Results of FDA's First Computational Interlaboratory Study," *Cardiovasc. Eng. Technol.*, vol. 3, no. 2, pp. 139–160, 2012.

[38] S. F. C. Stewart *et al.*, “Results of FDA’s First Interlaboratory Computational Study of a Nozzle with a Sudden Contraction and Conical Diffuser,” *Cardiovasc. Eng. Technol.*, vol. 4, no. 4, pp. 374–391, 2013.

[39] M. T. Hinds, Y. J. Park, S. a. Jones, D. P. Giddens, and B. Rita Alevriadou, “Local hemodynamics affect monocytic cell adhesion to a three-dimensional flow model coated with E-selectin,” *J. Biomech.*, vol. 34, no. 1, pp. 95–103, 2001.

[40] B. R. Patel, “Separated Internal Flows,” *Handbook of Fluid Dynamics and Fluid Machinery*. John Wiley & Sons, pp. 519–537, 1996.

[41] G. N. Rocha, R. J. Poole, and P. J. Oliveira, “Bifurcation phenomena in viscoelastic flows through a symmetric 1:4 expansion,” *J. Nonnewton. Fluid Mech.*, vol. 141, no. 1, pp. 1–17, 2007.

[42] F. Durst, A. Melling, and J. H. Whitelaw, “Low Reynolds number flow over a plane symmetric sudden expansion,” *J. Fluid Mech.*, vol. 64, pp. 111–128, 1974.

[43] E. O. Macagno and T.-K. Hung, “Computational and experimental study of a captive annular eddy,” *J. Fluid Mech.*, vol. 28, no. 1967, pp. 43–64, 1967.

[44] B. F. Armaly, F. Durst, J. C. F. Pereira, and B. Schönung, “Experimental and theoretical investigation of backward-facing step flow,” *J. Fluid Mech.*, vol. 127, no. 1, p. 473, 1983.

[45] R. Smyth, “Turbulent Flow Over a Plane Symmetric Sudden Expansion,” *J. Fluids Eng.*, vol. 101, no. 3, p. 348, 1979.

[46] B. R. Patel, “Diffusers,” *Handbook of Fluid Dynamics and Fluid Machinery*. John Wiley & Sons, pp. 2024–2039, 1996.

[47] R. D. Blevins, “Nozzles, Diffusers, and Venturis,” *Applied Fluid Dynamics Handbook*. pp. 144–163, 1986.

[48] D. C. Wisler, “Airfoils and the Diffusion Process,” *Handbook of Fluid Dynamics*. CRC Press, pp. 40–8, 1998.

[49] G. Sovran and E. D. Klomp, “Experimentally determined optimum geometries for rectilinear diffusers with rectangular, conical or annular cross-section,” *Fluid Mech. Intern. Flow*, p. 270, 1967.

[50] O. Pa and A. Rs, “Turbulence i n a conical diffuser with fully developed f l o w at entry,” vol. 57, 1973.

[51] J. T. Baldwin, S. Deutsch, H. L. Petrie, and J. M. Tarbell, “Determination of principal reynolds stresses in pulsatile flows after elliptical filtering of discrete velocity measurements.,” *J. Biomech. Eng.*, vol. 115, no. 4A, pp. 396–403, 1993.

[52] J. Baldwin, “An Investigation of the Mean Fluid Velocity and Reynolds Stress Fields within an Artificial Heart Ventricle,” The Pennsylvania State University, 1990.

[53] C. T. Crowe, D. F. Elger, B. C. Williams, and J. A. Robertson, *Engineering Fluid Mechanics*, 9th ed. John Wiley & Sons, 2009.

[54] H. Tennekes and J. Lumley, *A First Course in Turbulence*. Cambridge: MIT Press, 1972.

[55] P. K. Kundu, I. M. Cohen, and D. R. Dowling, *Fluid Mechanics*, 6th ed. Elsevier Inc., 2016.

[56] B. Lieber and D. Giddens, “Estimation of Reynolds Stresses in Pulsatile Disturbed Flows,” in *39th ACEMB meeting*, 1986.

[57] J. O. Taylor *et al.*, “Analysis of Transitional and Turbulent Flow Through the FDA Benchmark Nozzle Model Using Laser Doppler Velocimetry,” *Cardiovasc. Eng. Technol.*, vol. 7, no. 3, pp. 191–209, 2016.

[58] A. Boutier, *Laser Velocimetry in Fluid Mechanics*. Somerset, US: Wiley-ISTE, 2013.

[59] TSI, “Phase Doppler Particle Analyzer (PDPA)/ Laser Doppler Velocimeter (LDV) Operations Manual,” no. November, p. 177, 2014.

[60] C. T. Crowe, J. D. Schwarzkopf, M. Sommerfeld, and Y. Tsuji, *Multiphase Flows within Droplets and Particles*, Second. Boca Raton: CRC Press, 2012.

[61] TSI, “LDV Installation Manual,” no. July, 2011.

[62] “Operator’s Manual The Innova ® 70C Series Ion Laser,” Santa Clara, CA.

[63] “LDV / PDPA System : Model FSA 3500/4000, Signal Processor Model PDM1000, Photo Detector Module,” 2005.

[64] TSI, “Phase Doppler Particle Analyzers LDV / PDPA System :,” no. July, 2011.

[65] TSI, “TR / TM Series Fiberoptic Probes,” no. November, 2005.

[66] J. T. Baldwin, S. Deutsch, D. B. Geselowitz, and J. M. Tarbell, “LDA measurements of mean velocity and Reynolds stress fields within an artificial heart ventricle.,” *J. Biomech. Eng.*, vol. 116, no. 2, pp. 190–200, 1994.

[67] D. K. Walters, S. Bhushan, M. F. Alam, and D. S. Thompson, “Investigation of a dynamic hybrid RANS/LES modelling methodology for finite-volume CFD simulations,” *Flow, Turbul. Combust.*, vol. 91, no. 3, pp. 643–667, 2013.

[68] L. H. Herbertson *et al.*, “Multilaboratory study of flow-induced hemolysis using the FDA benchmark nozzle model,” *Artif. Organs*, vol. 39, no. 3, pp. 237–248, 2015.

[69] P. GARAUD and G. I. OGILVIE, “A model for the nonlinear dynamics of turbulent shear flows,” *J. Fluid Mech.*, vol. 530, pp. 145–176, 2005.

[70] C. Y. Schüle, K. Affeld, M. Kossatz, C. O. Paschereit, and U. Kertzscher, “Turbulence measurements in an axial rotary blood pump with laser Doppler velocimetry,” *Int. J. Artif. Organs*, vol. 40, no. 3, pp. 109–117, 2017.

[71] T. Hasin *et al.*, “The Role of Medical Management for Acute Intravascular Hemolysis in Patients Supported on Axial Flow LVAD,” *ASAIO J.*, vol. 60, no. 1, pp. 9–14, 2014.

[72] V. SHTERN and F. HUSSAIN, “Effect of deceleration on jet instability,” *J. Fluid Mech.*, vol. 480, p. S0022112002003646, 2003.

Appendix A – Steady Flow Velocity Data

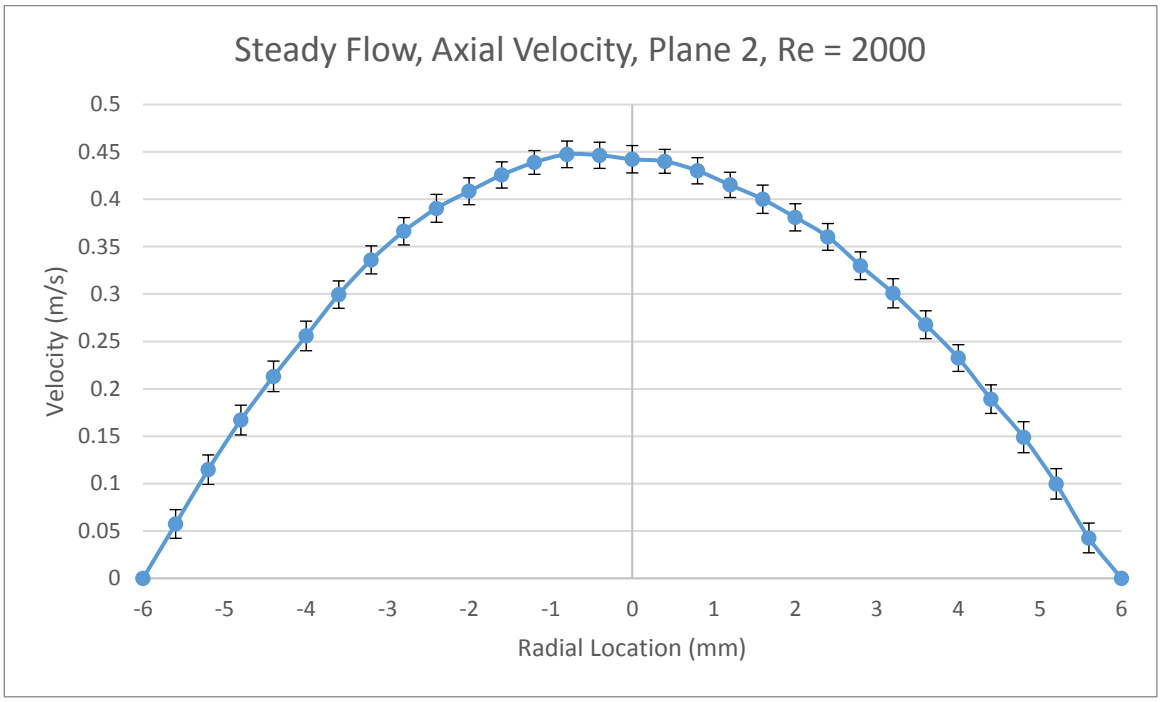

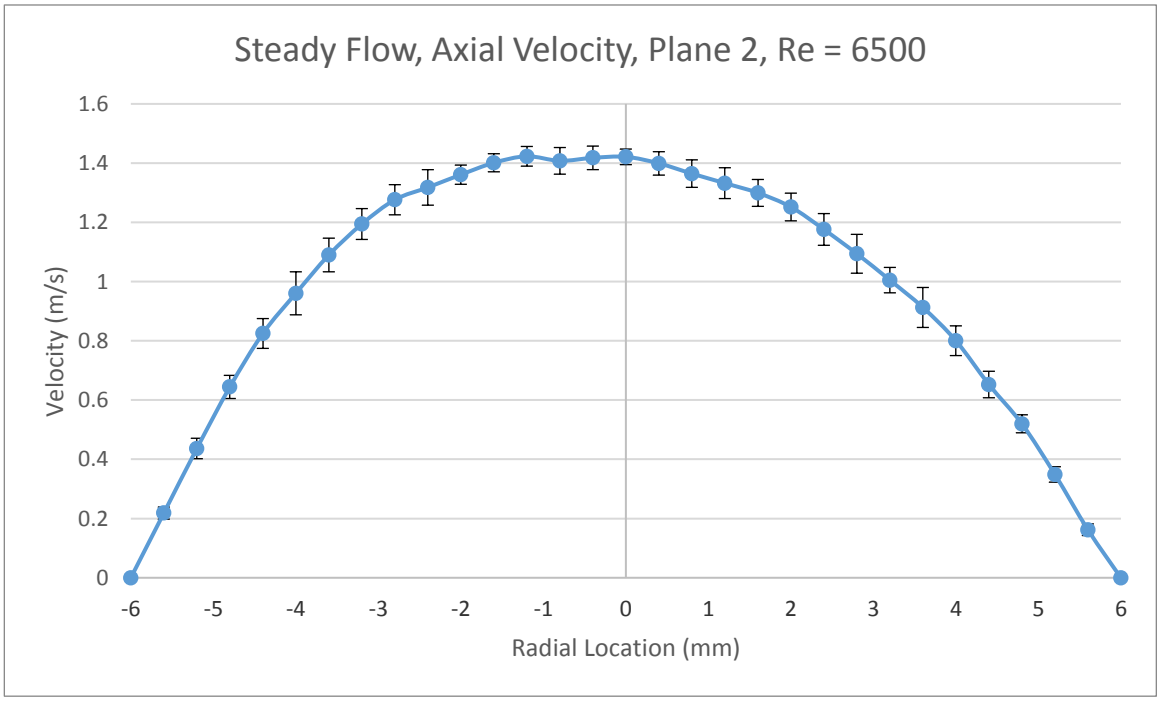

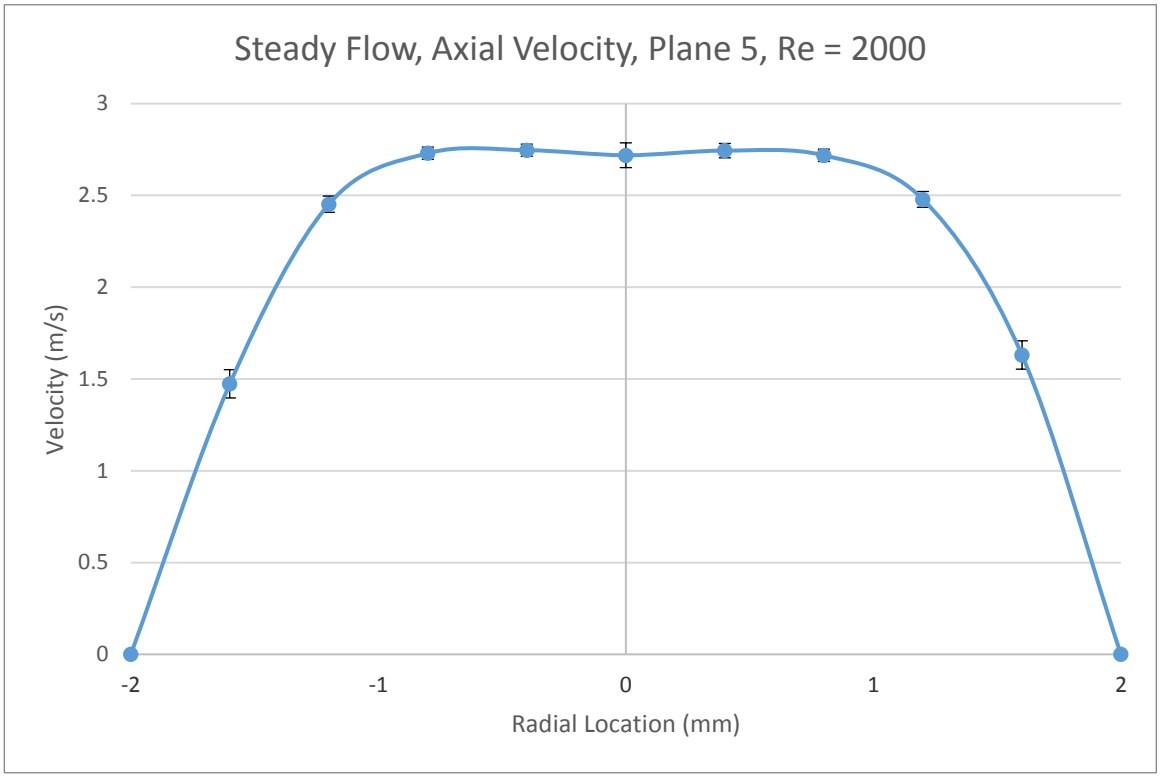
Steady Flow, Axial Velocity, Plane 5, Re = 2000
Velocity (m/s)
3
2.5
2
1.5
1
0.5
0
-2
-1
0
1
2
Radial Location (mm)

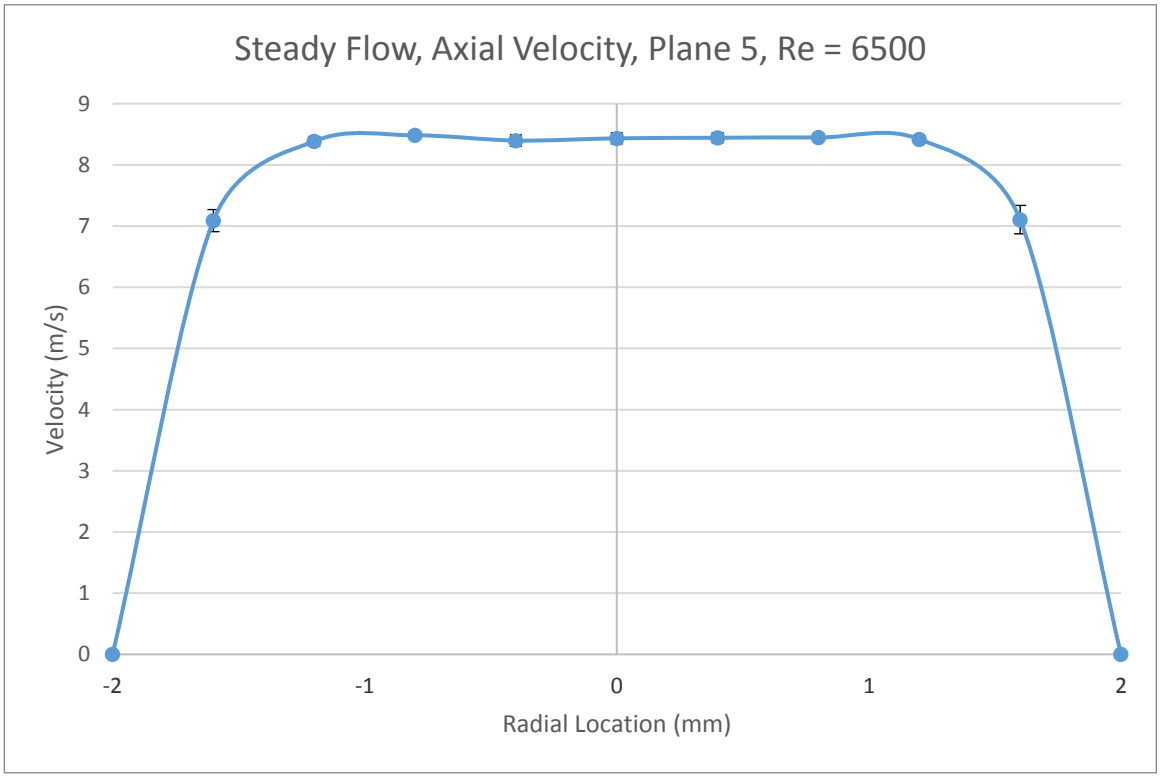
Steady Flow, Axial Velocity, Plane 5, Re = 6500
Velocity (m/s)
9
8
7
6
5
4
3
2
1
0
-2
-1
0
1
2
Radial Location (mm)

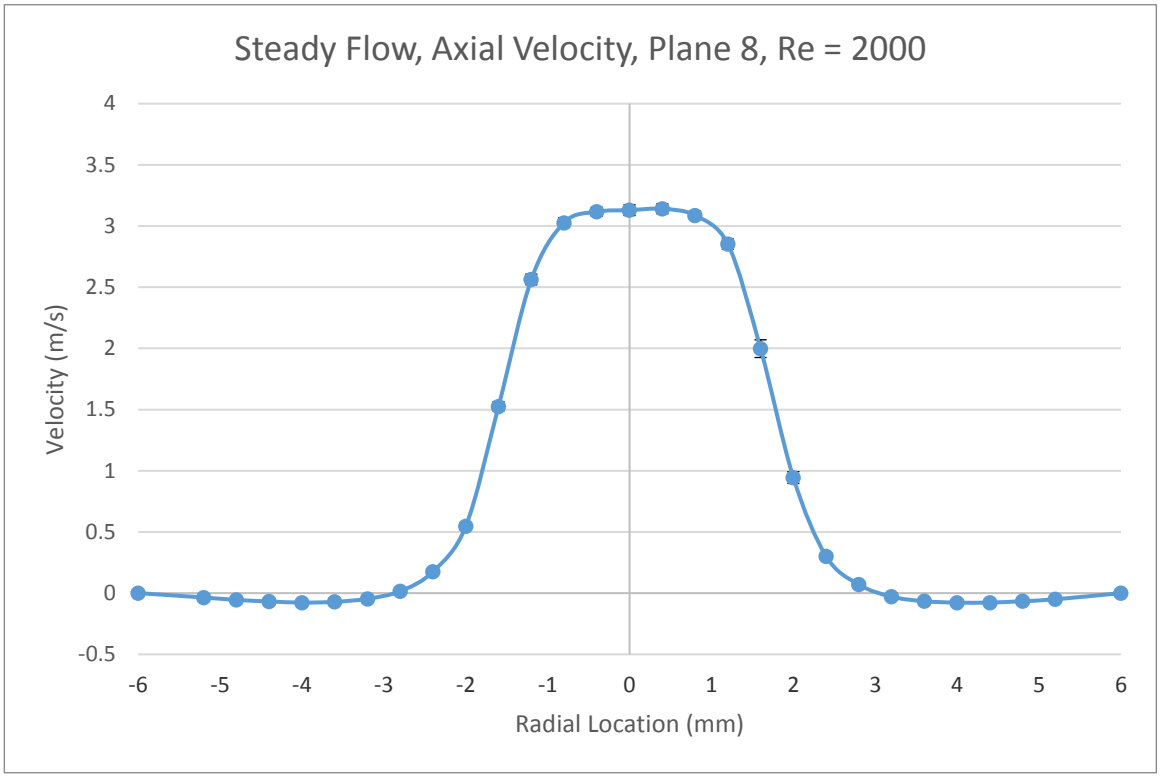
Steady Flow, Axial Velocity, Plane 8, Re = 2000
Velocity (m/s)
4
3.5
3
2.5
2
1.5
1
0.5
0
-0.5
-6
-5
-4
-3
-2
-1
0
1
2
3
4
5
6
Radial Location (mm)

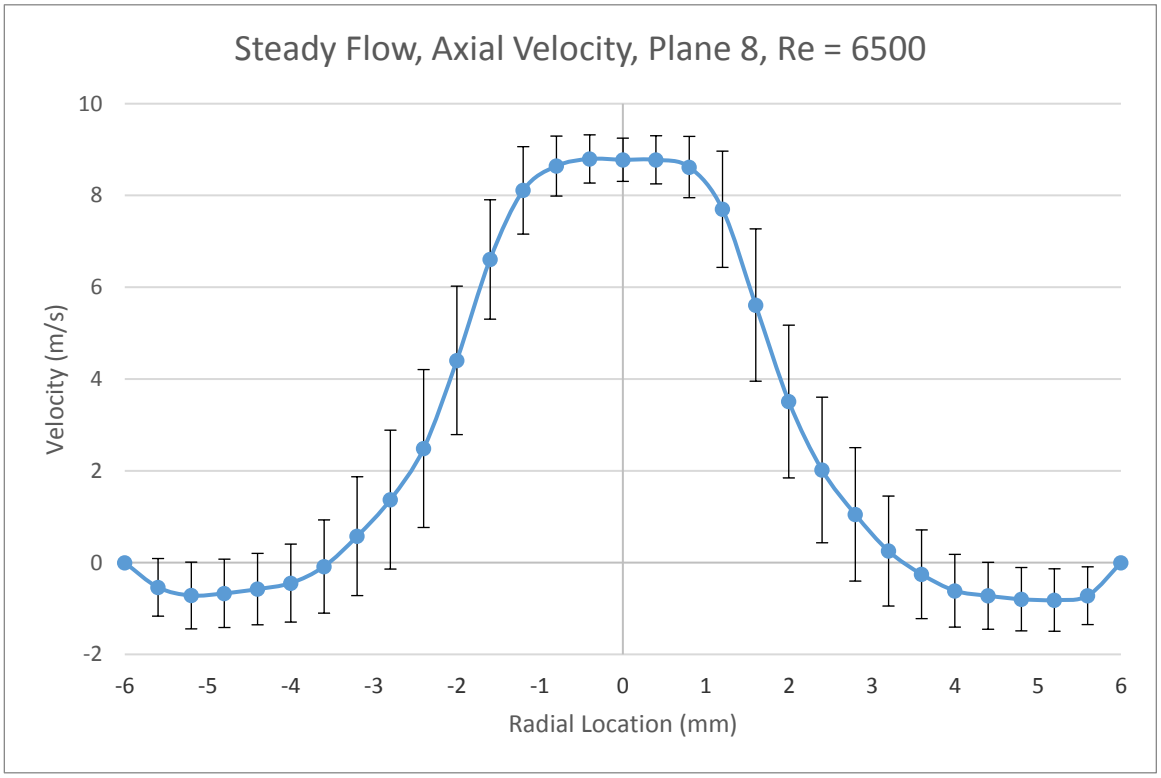
Steady Flow, Axial Velocity, Plane 8, Re = 6500
Velocity (m/s)
10
8
6
4
2
0
-2
-6
-5
-4
-3
-2
-1
0
1
2
3
4
5
6
Radial Location (mm)

Appendix B – Radial Velocity, RSS, RNSs, and TIs for Pulsatile Flow Data

Appendix B.1 – Sudden Expansion Plane 2

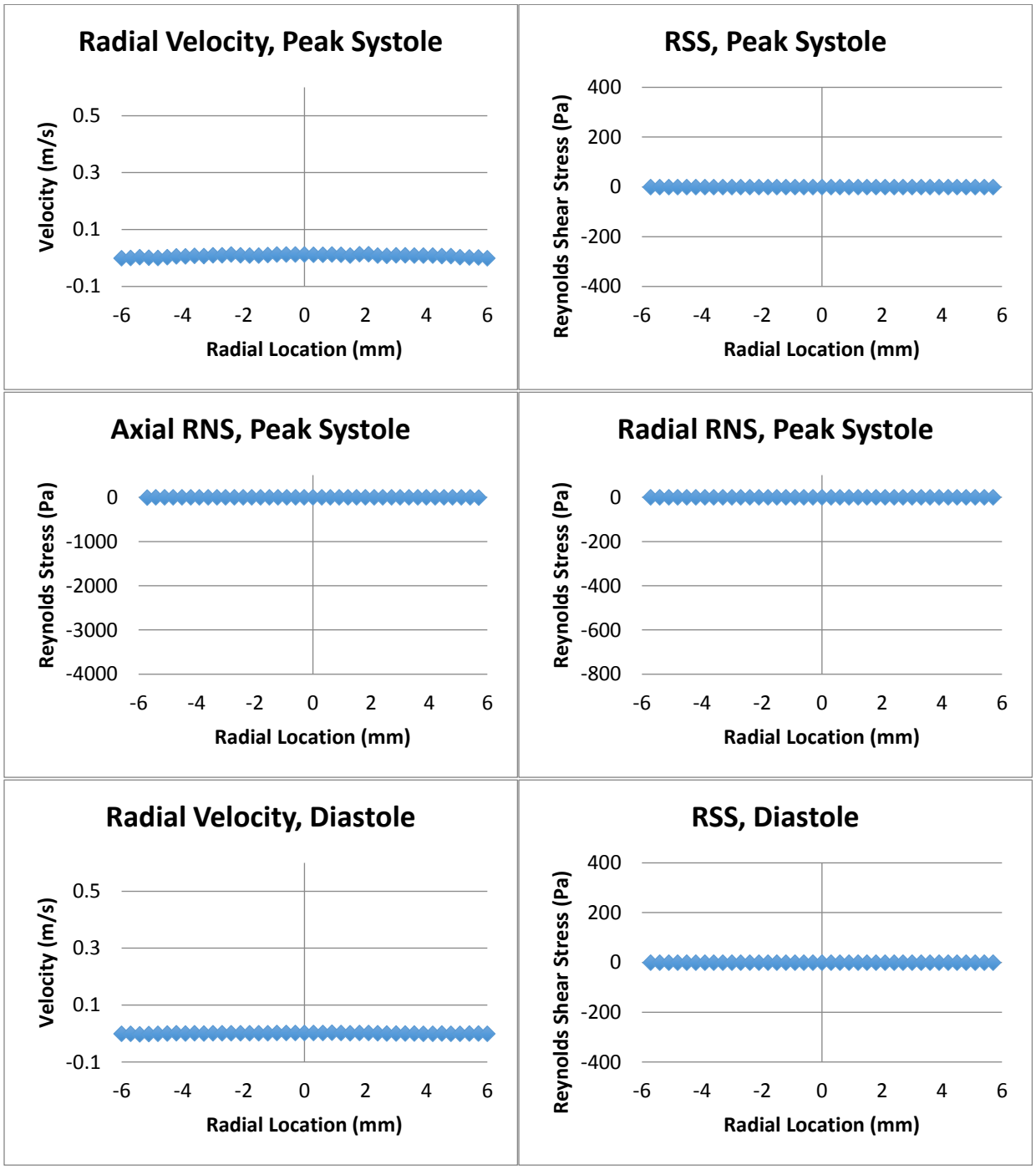

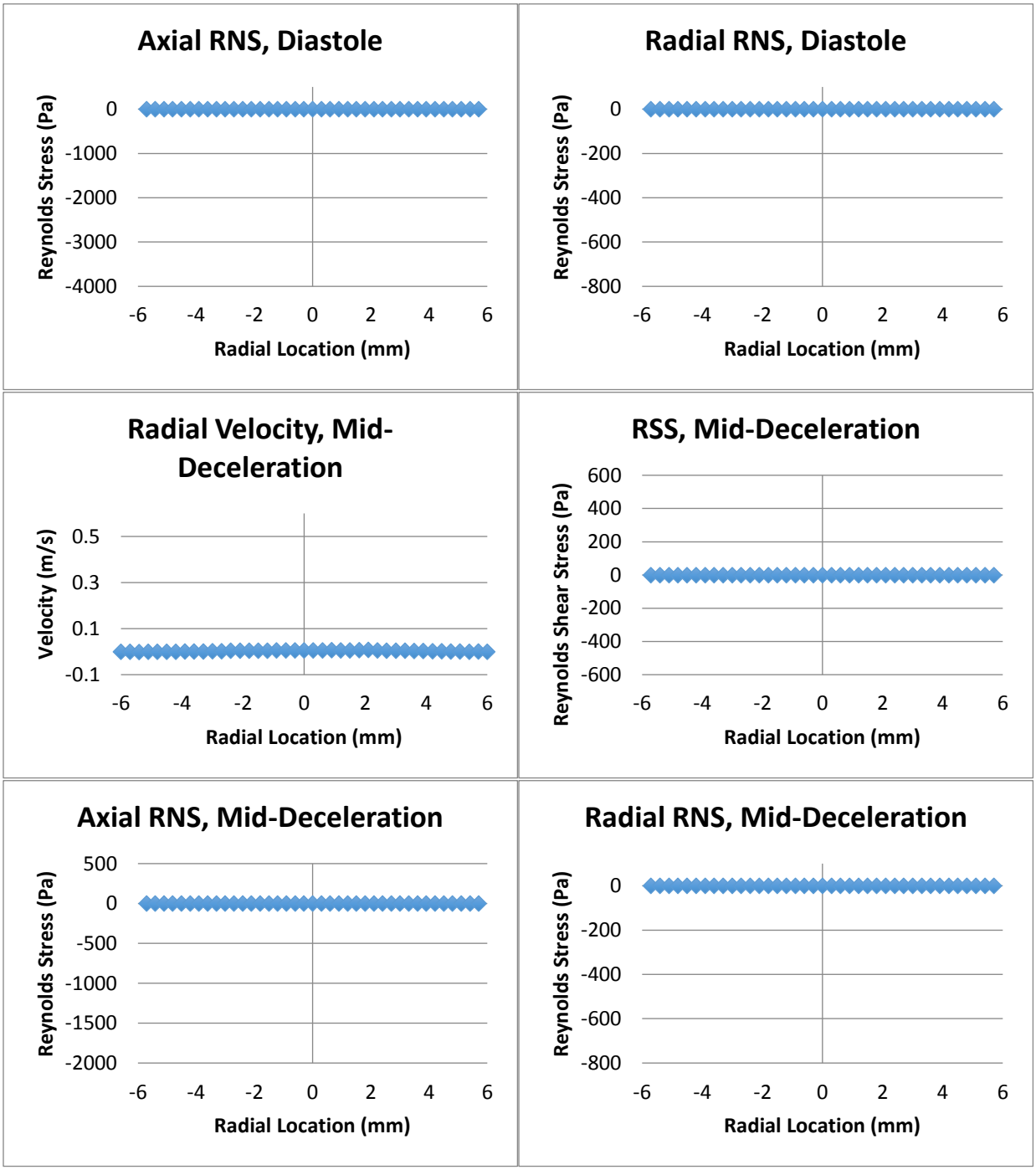
Axial RNS, Diastole
Reynolds Stress (Pa)
0
-1000
-2000
-3000
-4000
-6 -4 -2 0 2 4 6
Radial Location (mm)
Radial RNS, Diastole
Reynolds Stress (Pa)
0
-200
-400
-600
-800
-6 -4 -2 0 2 4 6
Radial Location (mm)
Radial Velocity, Mid-Deceleration
Velocity (m/s)
0.5
0.3
0.1
-0.1
-6 -4 -2 0 2 4 6
Radial Location (mm)
RSS, Mid-Deceleration
Reynolds Shear Stress (Pa)
600
400
200
0
-200
-400
-600
-6 -4 -2 0 2 4 6
Radial Location (mm)
Axial RNS, Mid-Deceleration
Reynolds Stress (Pa)
500
0
-500
-1000
-1500
-2000
-6 -4 -2 0 2 4 6
Radial Location (mm)
Radial RNS, Mid-Deceleration
Reynolds Stress (Pa)
0
-200
-400
-600
-800
-6 -4 -2 0 2 4 6
Radial Location (mm)

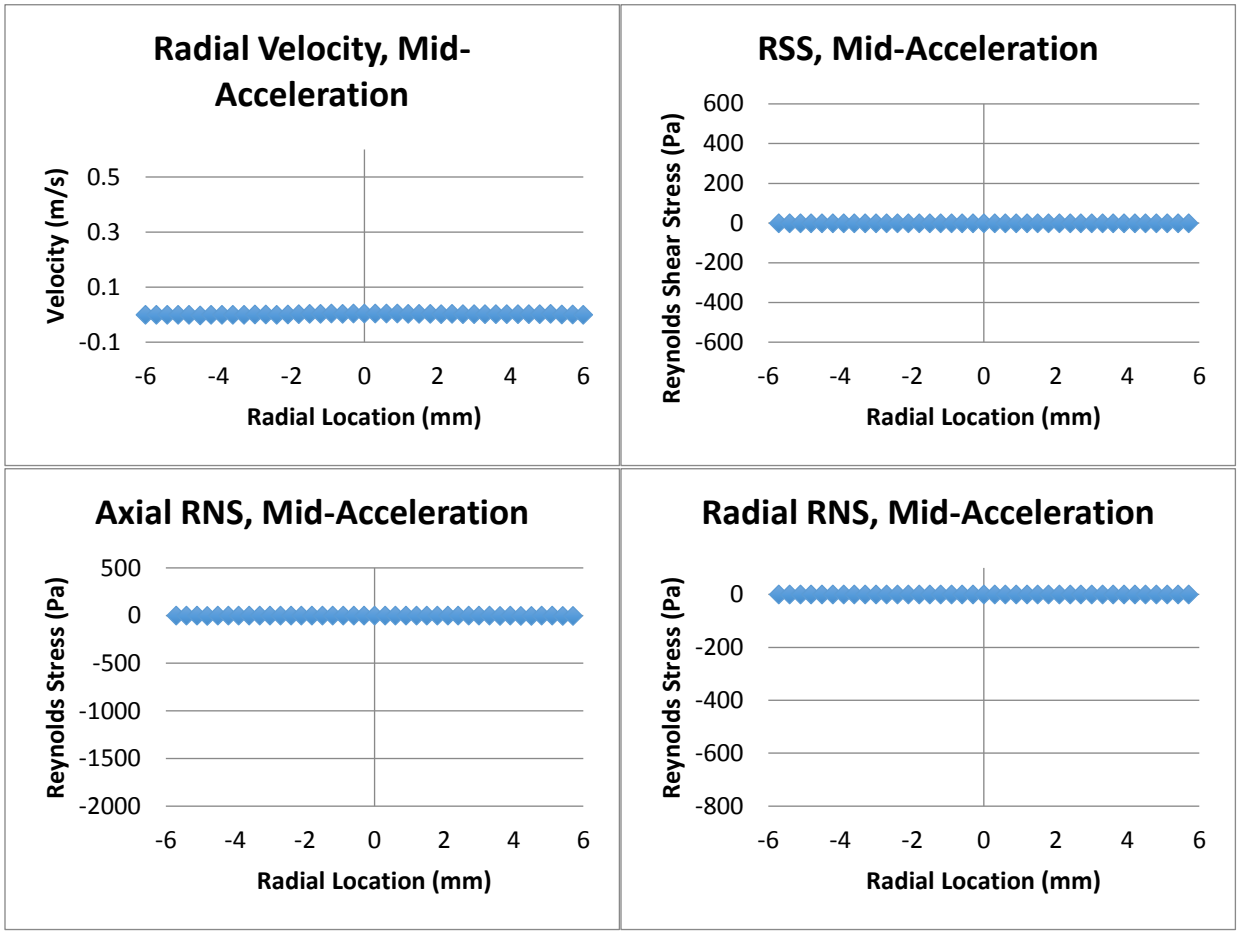
Radial Velocity, Mid-Acceleration
Velocity (m/s)
0.5
0.3
0.1
-0.1
-6
-4
-2
0
2
4
6
Radial Location (mm)
RSS, Mid-Acceleration
Reynolds Shear Stress (Pa)
600
400
200
0
-200
-400
-600
-6
-4
-2
0
2
4
6
Radial Location (mm)
Axial RNS, Mid-Acceleration
Reynolds Stress (Pa)
500
0
-500
-1000
-1500
-2000
-6
-4
-2
0
2
4
6
Radial Location (mm)
Radial RNS, Mid-Acceleration
Reynolds Stress (Pa)
0
-200
-400
-600
-800
-6
-4
-2
0
2
4
6
Radial Location (mm)

Appendix B.2 – Sudden Expansion Plane 5

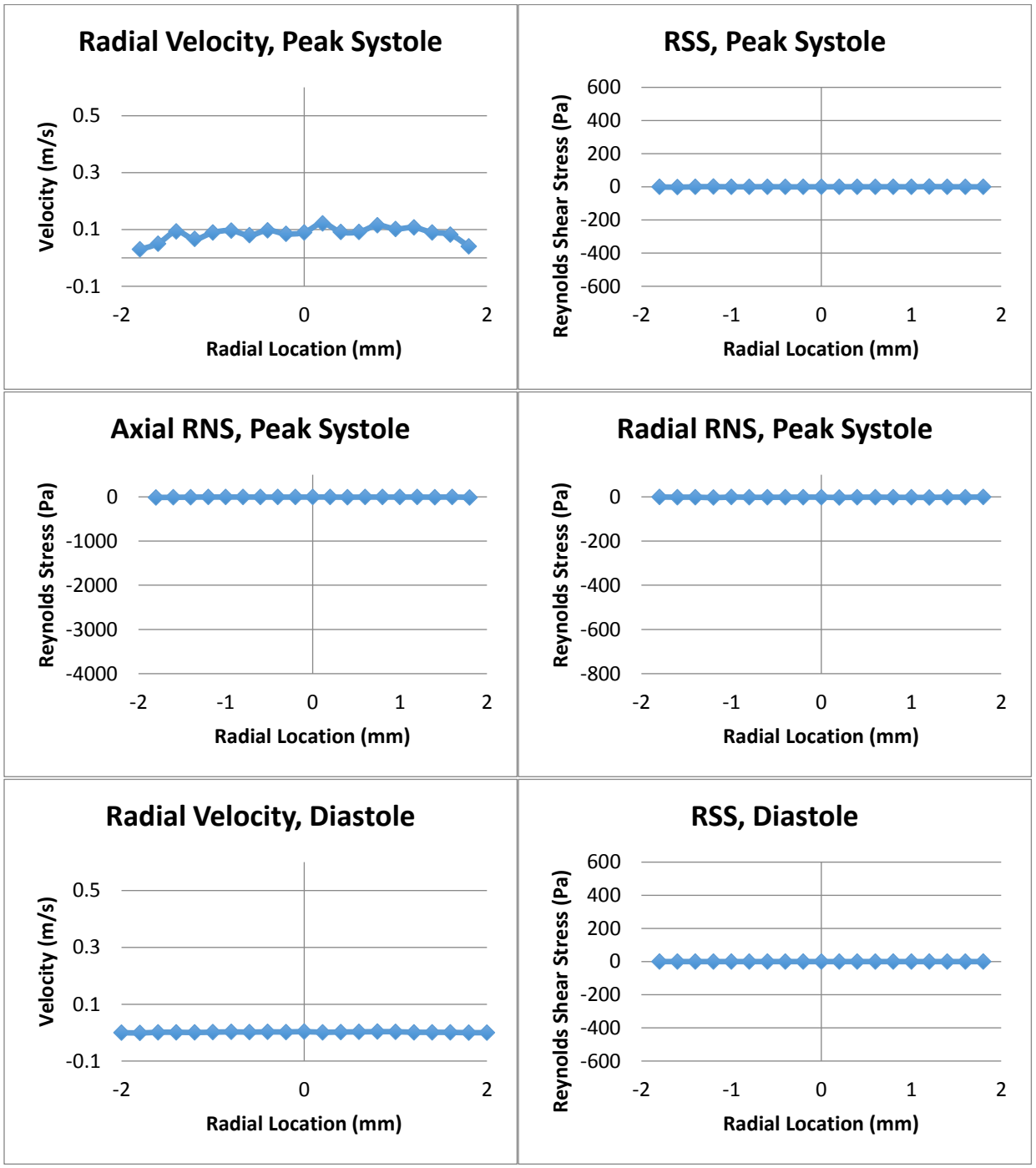

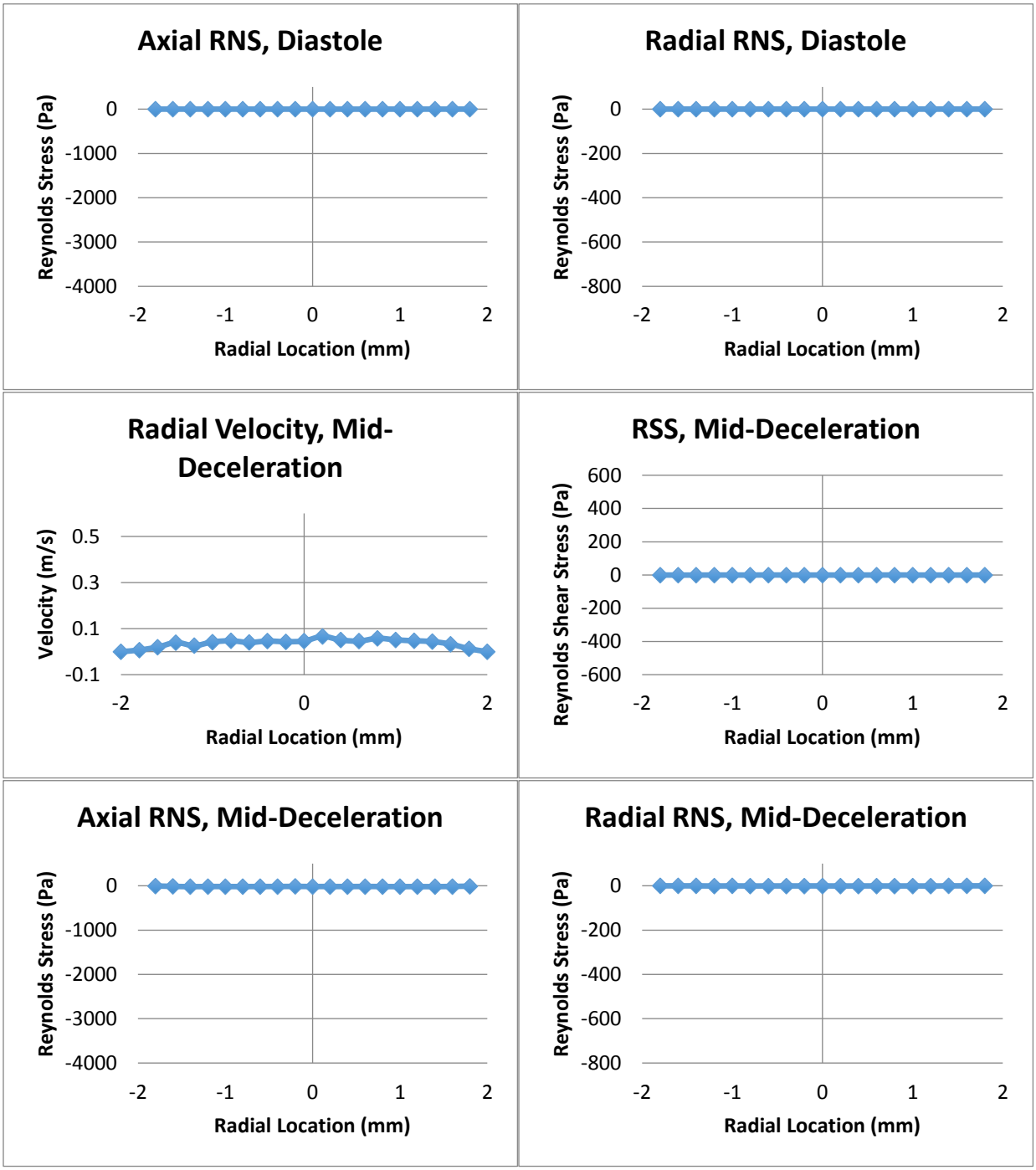
Axial RNS, Diastole
Reynolds Stress (Pa)
0
-1000
-2000
-3000
-4000
-2
-1
0
1
2
Radial Location (mm)
Radial RNS, Diastole
Reynolds Stress (Pa)
0
-200
-400
-600
-800
-2
-1
0
1
2
Radial Location (mm)
Radial Velocity, Mid-Deceleration
Velocity (m/s)
0.5
0.3
0.1
-0.1
-2
0
2
Radial Location (mm)
RSS, Mid-Deceleration
Reynolds Shear Stress (Pa)
600
400
200
0
-200
-400
-600
-2
-1
0
1
2
Radial Location (mm)
Axial RNS, Mid-Deceleration
Reynolds Stress (Pa)
0
-1000
-2000
-3000
-4000
-2
-1
0
1
2
Radial Location (mm)
Radial RNS, Mid-Deceleration
Reynolds Stress (Pa)
0
-200
-400
-600
-800
-2
-1
0
1
2
Radial Location (mm)

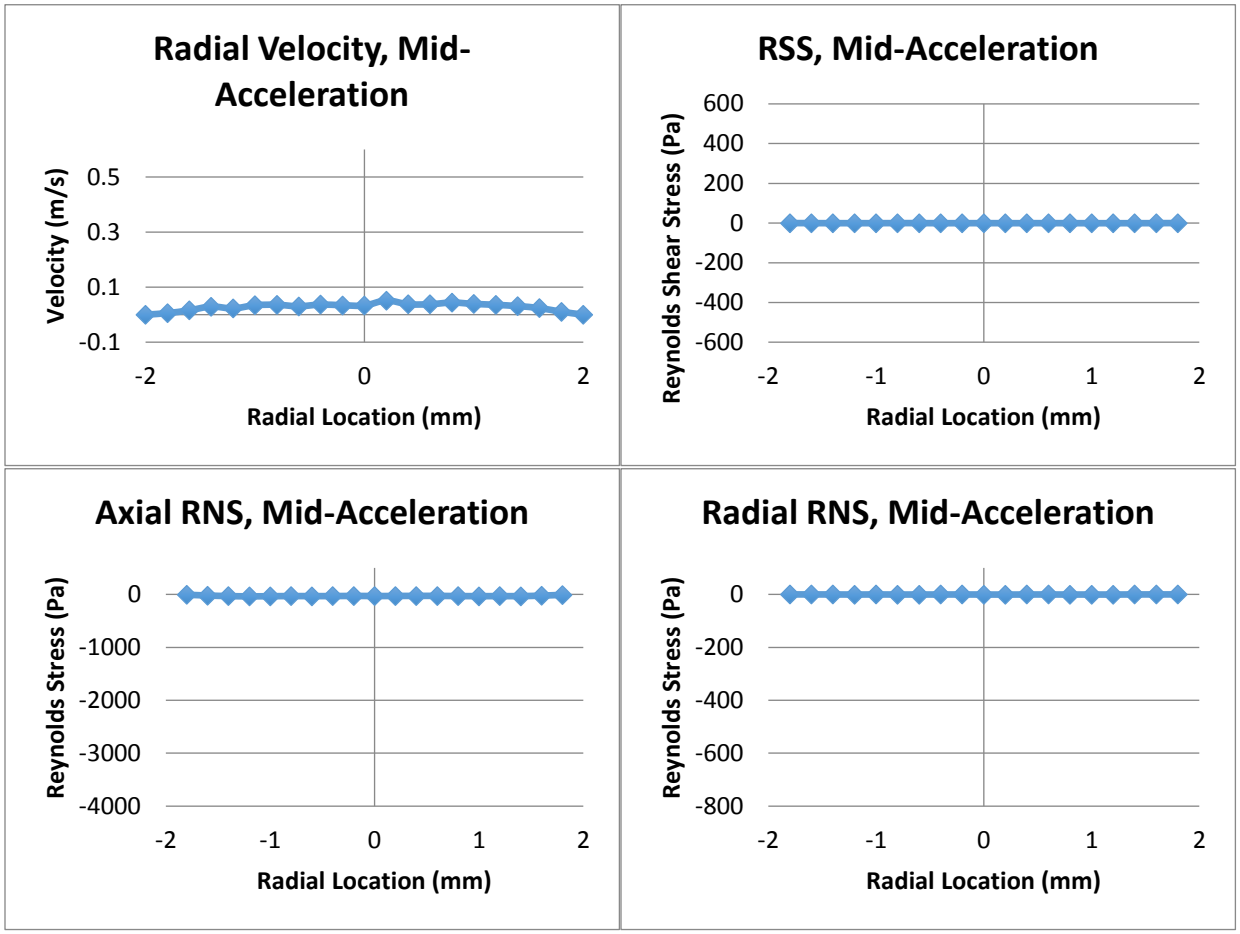
Radial Velocity, Mid-Acceleration
Velocity (m/s)
0.5
0.3
0.1
-0.1
-2
0
2
Radial Location (mm)
RSS, Mid-Acceleration
Reynolds Shear Stress (Pa)
600
400
200
0
-200
-400
-600
-2
-1
0
1
2
Radial Location (mm)
Axial RNS, Mid-Acceleration
Reynolds Stress (Pa)
0
-1000
-2000
-3000
-4000
-2
-1
0
1
2
Radial Location (mm)
Radial RNS, Mid-Acceleration
Reynolds Stress (Pa)
0
-200
-400
-600
-800
-2
-1
0
1
2
Radial Location (mm)

Appendix B.3 – Sudden Expansion Plane 6

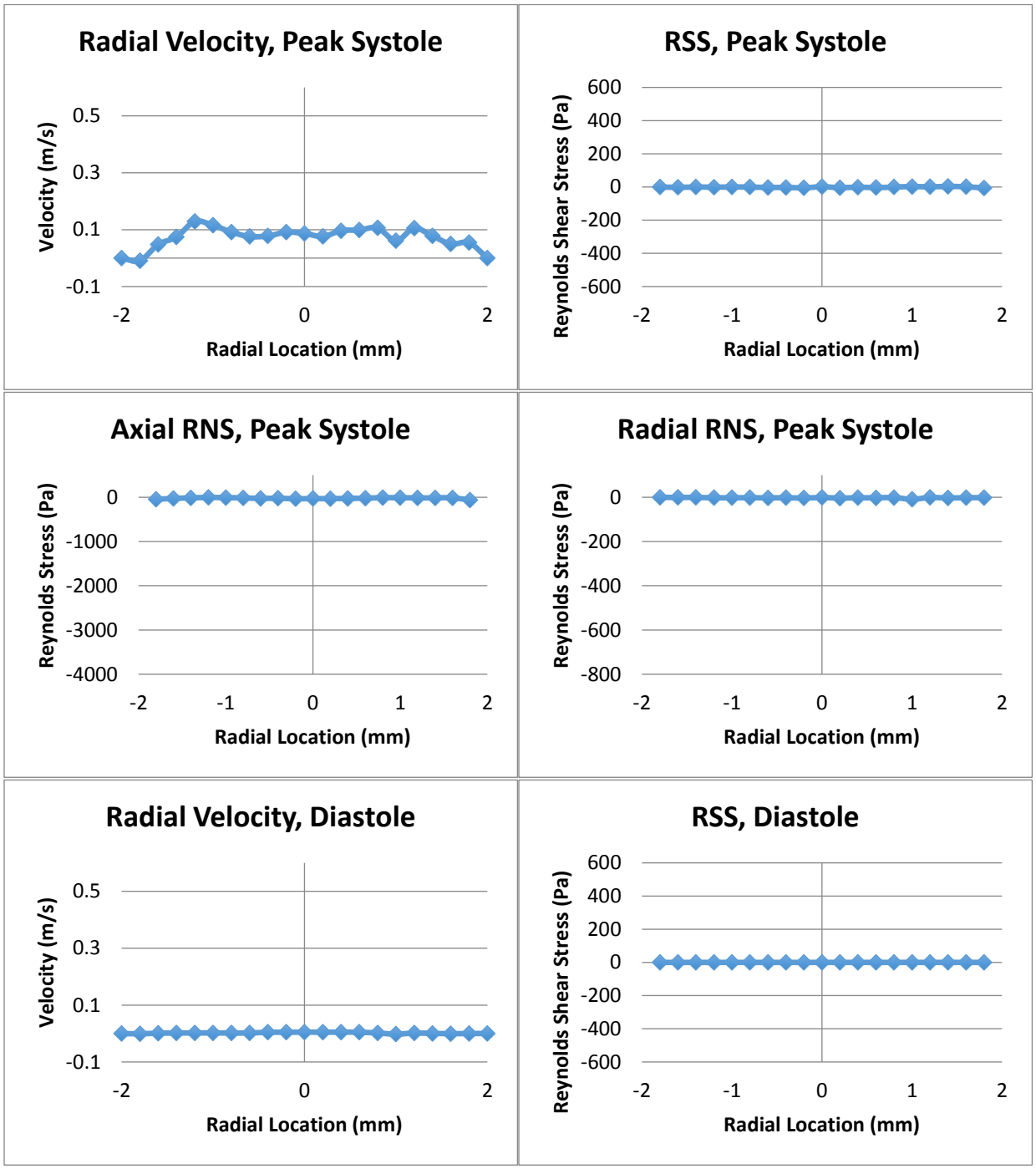

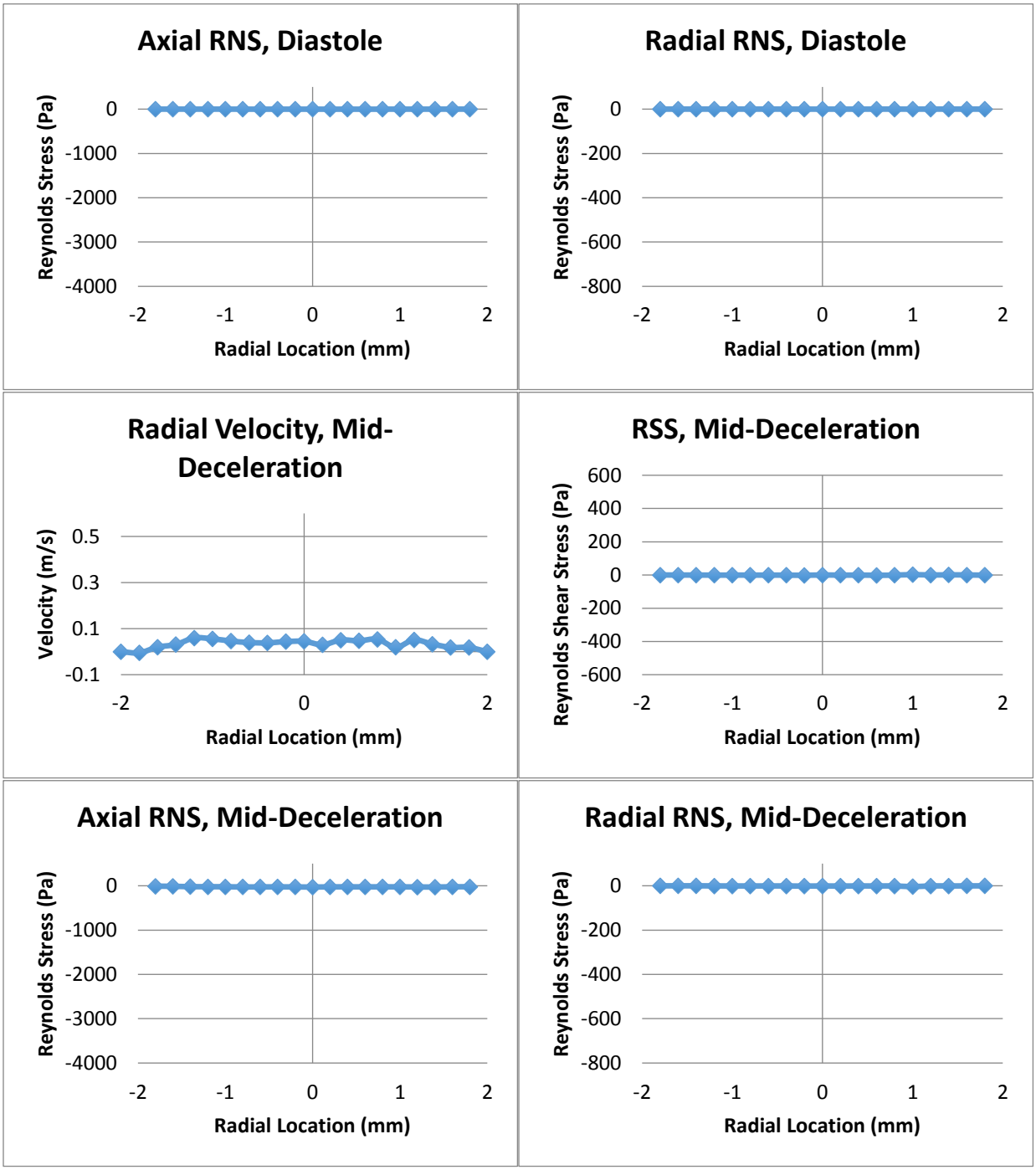
Axial RNS, Diastole
Reynolds Stress (Pa)
0
-1000
-2000
-3000
-4000
-2
-1
0
1
2
Radial Location (mm)
Radial RNS, Diastole
Reynolds Stress (Pa)
0
-200
-400
-600
-800
-2
-1
0
1
2
Radial Location (mm)
Radial Velocity, Mid-Deceleration
Velocity (m/s)
0.5
0.3
0.1
-0.1
-2
0
2
Radial Location (mm)
RSS, Mid-Deceleration
Reynolds Shear Stress (Pa)
600
400
200
0
-200
-400
-600
-2
-1
0
1
2
Radial Location (mm)
Axial RNS, Mid-Deceleration
Reynolds Stress (Pa)
0
-1000
-2000
-3000
-4000
-2
-1
0
1
2
Radial Location (mm)
Radial RNS, Mid-Deceleration
Reynolds Stress (Pa)
0
-200
-400
-600
-800
-2
-1
0
1
2
Radial Location (mm)

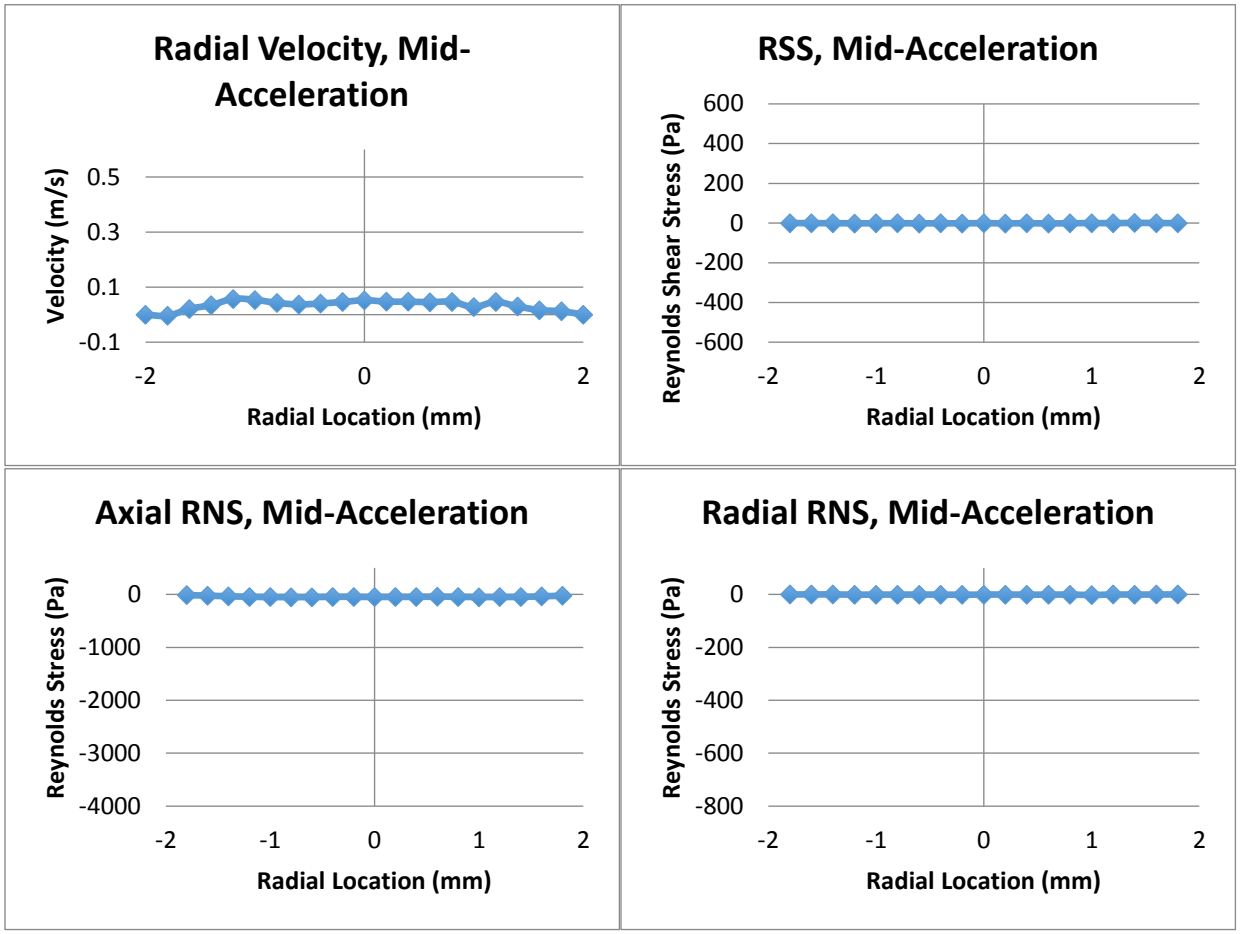
Radial Velocity, Mid-Acceleration
Velocity (m/s)
0.5
0.3
0.1
-0.1
-2
0
2
Radial Location (mm)
RSS, Mid-Acceleration
Reynolds Shear Stress (Pa)
600
400
200
0
-200
-400
-600
-2
-1
0
1
2
Radial Location (mm)
Axial RNS, Mid-Acceleration
Reynolds Stress (Pa)
0
-1000
-2000
-3000
-4000
-2
-1
0
1
2
Radial Location (mm)
Radial RNS, Mid-Acceleration
Reynolds Stress (Pa)
0
-200
-400
-600
-800
-2
-1
0
1
2
Radial Location (mm)

Appendix B.4 – Sudden Expansion Plane 7

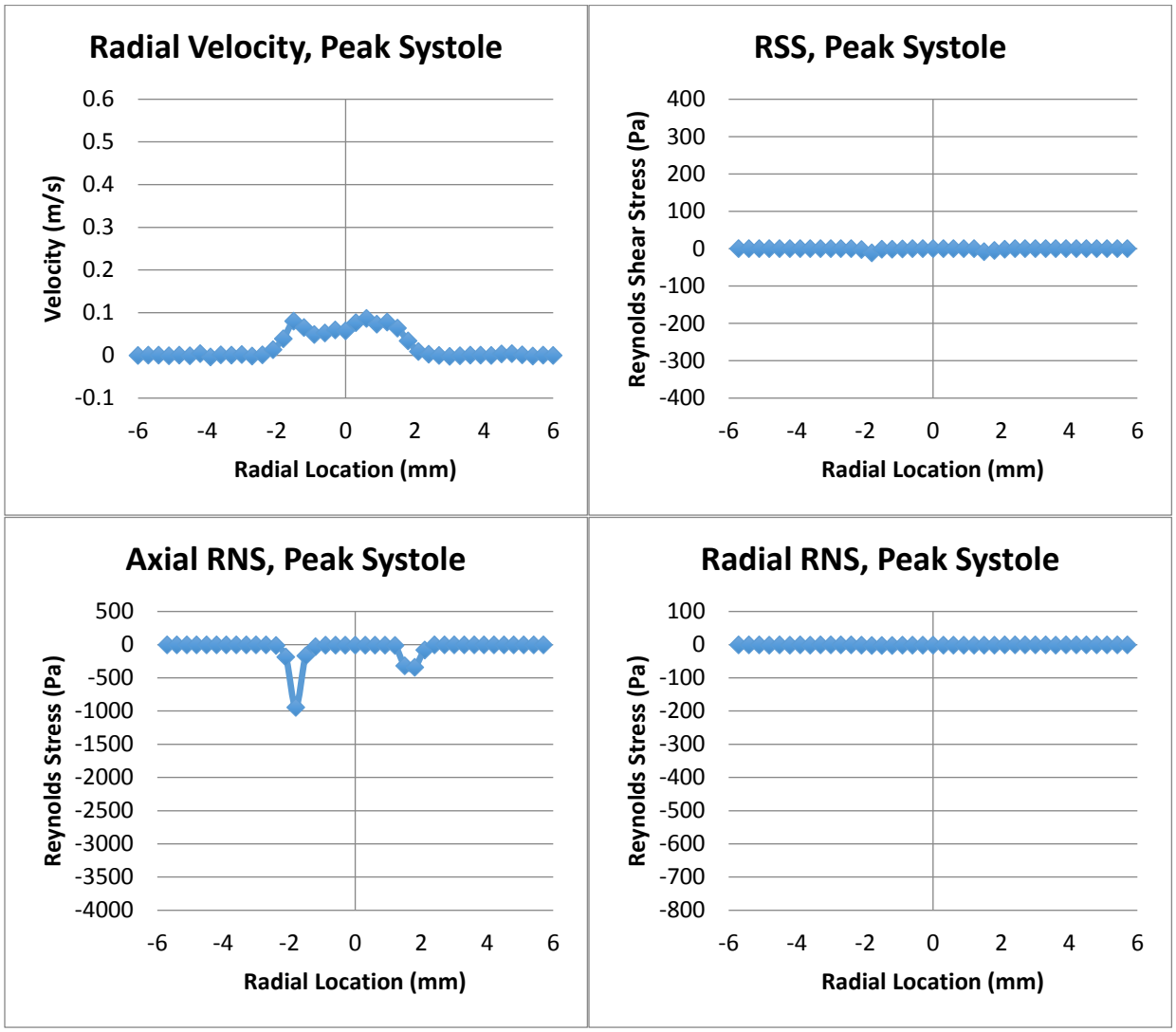

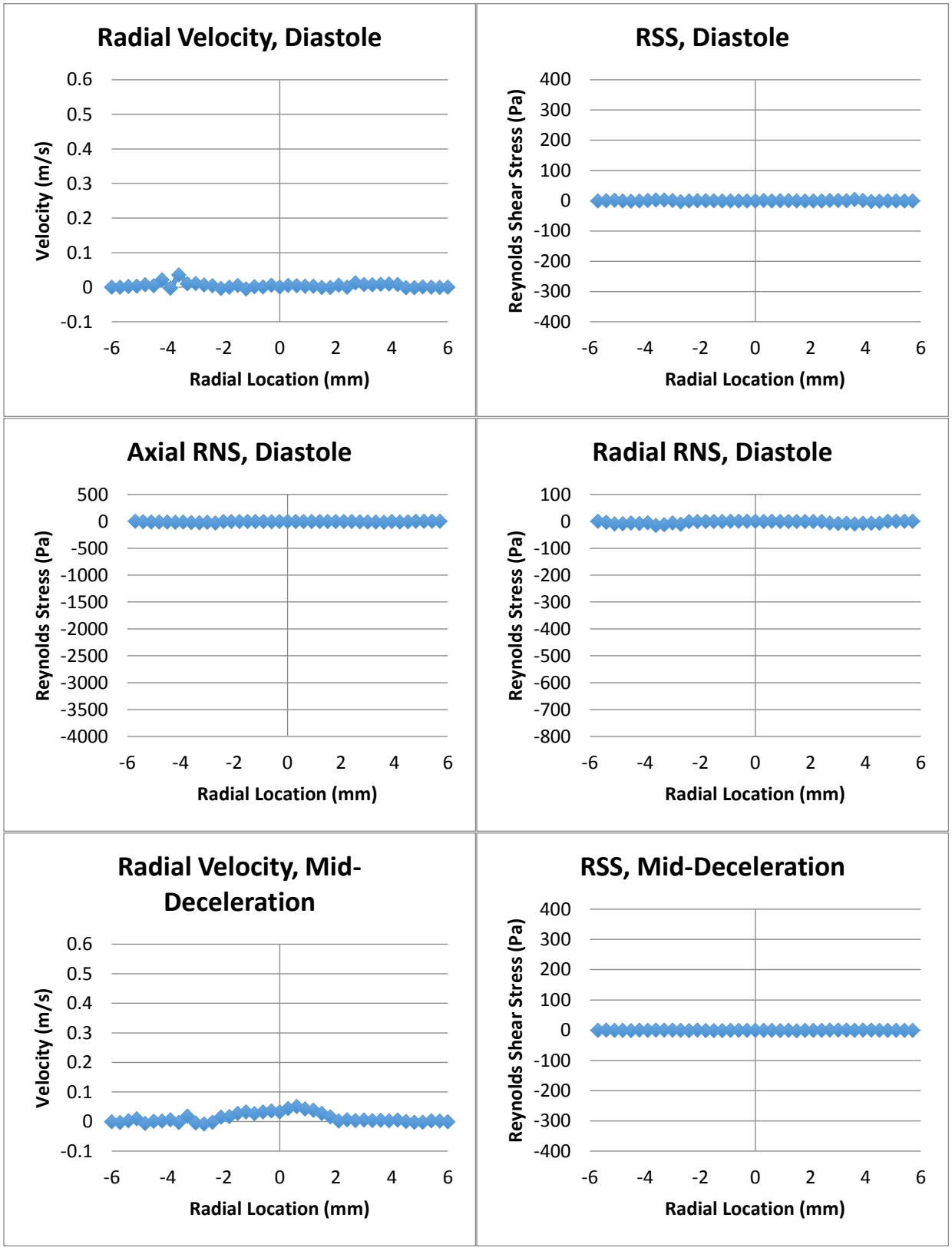
Radial Velocity, Diastole
Velocity (m/s)
0.6
0.5
0.4
0.3
0.2
0.1
0
-0.1
-6 -4 -2 0 2 4 6
Radial Location (mm)
RSS, Diastole
Reynolds Shear Stress (Pa)
400
300
200
100
0
-100
-200
-300
-400
-6 -4 -2 0 2 4 6
Radial Location (mm)
Axial RNS, Diastole
Reynolds Stress (Pa)
500
0
-500
-1000
-1500
-2000
-2500
-3000
-3500
-4000
-6 -4 -2 0 2 4 6
Radial Location (mm)
Radial RNS, Diastole
Reynolds Stress (Pa)
100
0
-100
-200
-300
-400
-500
-600
-700
-800
-6 -4 -2 0 2 4 6
Radial Location (mm)
Radial Velocity, Mid-Deceleration
Velocity (m/s)
0.6
0.5
0.4
0.3
0.2
0.1
0
-0.1
-6 -4 -2 0 2 4 6
Radial Location (mm)
RSS, Mid-Deceleration
Reynolds Shear Stress (Pa)
400
300
200
100
0
-100
-200
-300
-400
-6 -4 -2 0 2 4 6
Radial Location (mm)

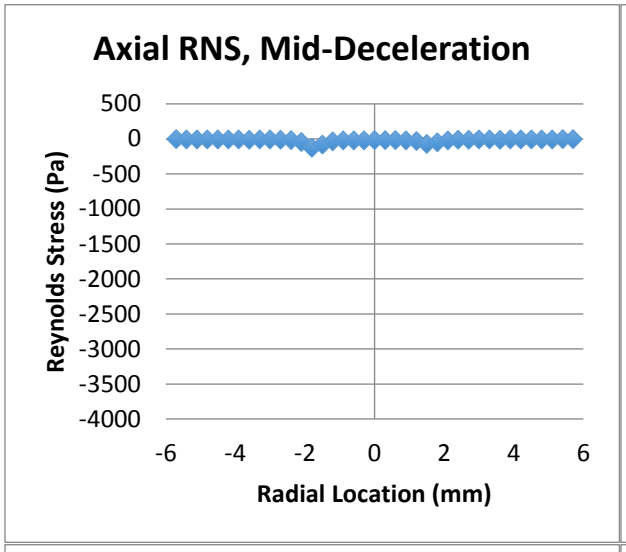
Axial RNS, Mid-Deceleration
Reynolds Stress (Pa)
500
0
-500
-1000
-1500
-2000
-2500
-3000
-3500
-4000
-6
-4
-2
0
2
4
6
Radial Location (mm)

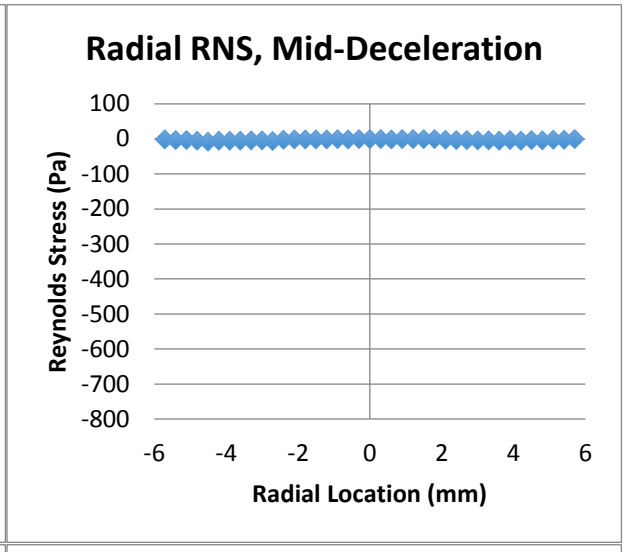
Radial RNS, Mid-Deceleration
Reynolds Stress (Pa)
100
0
-100
-200
-300
-400
-500
-600
-700
-800
-6
-4
-2
0
2
4
6
Radial Location (mm)

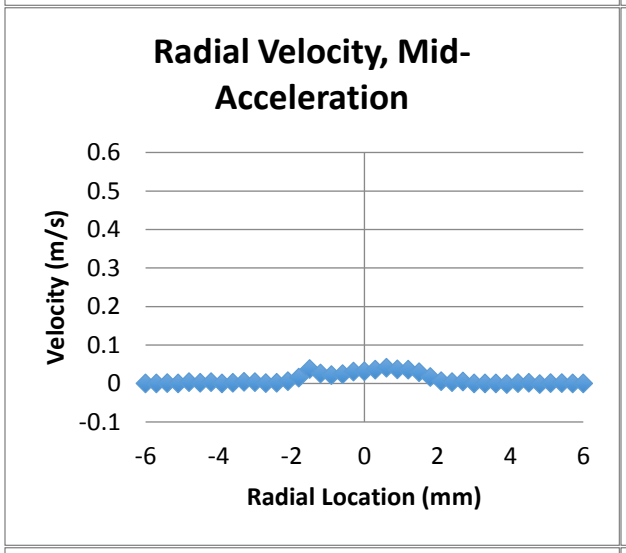
Radial Velocity, Mid-Acceleration
Velocity (m/s)
0.6
0.5
0.4
0.3
0.2
0.1
0
-0.1
-6
-4
-2
0
2
4
6
Radial Location (mm)

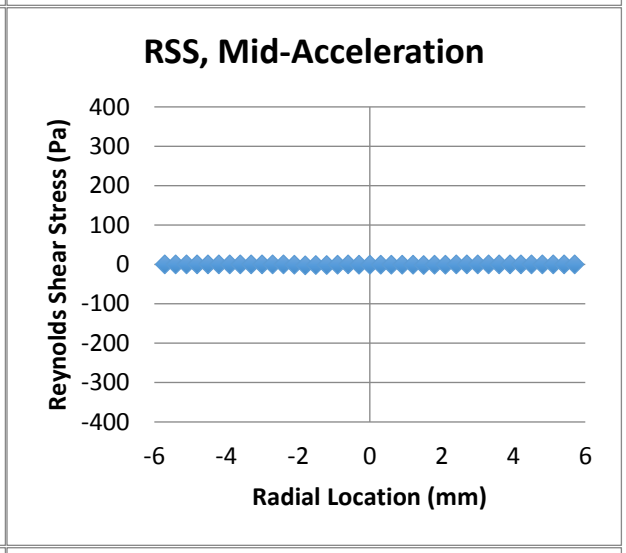
RSS, Mid-Acceleration
Reynolds Shear Stress (Pa)
400
300
200
100
0
-100
-200
-300
-400
-6
-4
-2
0
2
4
6
Radial Location (mm)

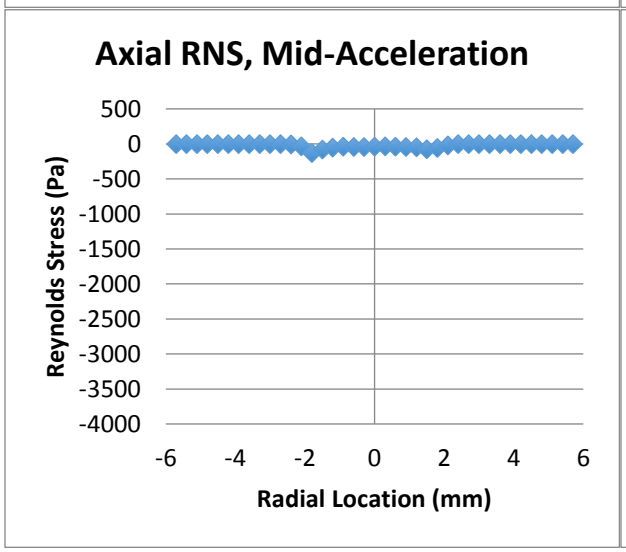
Axial RNS, Mid-Acceleration
Reynolds Stress (Pa)
500
0
-500
-1000
-1500
-2000
-2500
-3000
-3500
-4000
-6
-4
-2
0
2
4
6
Radial Location (mm)

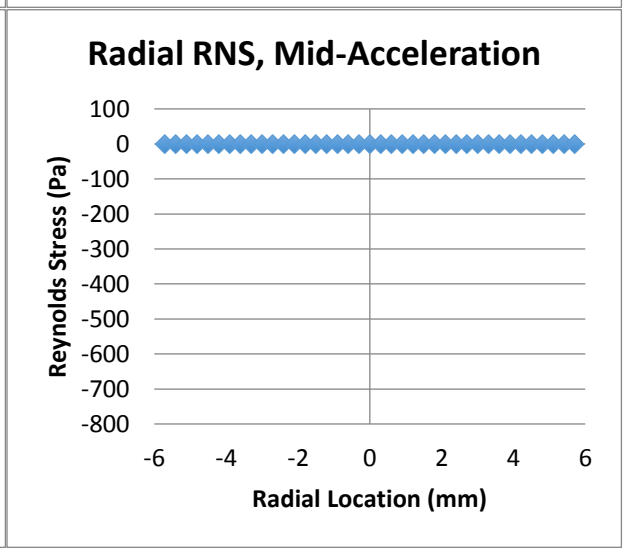
Radial RNS, Mid-Acceleration
Reynolds Stress (Pa)
100
0
-100
-200
-300
-400
-500
-600
-700
-800
-6
-4
-2
0
2
4
6
Radial Location (mm)

Appendix B.5 – Sudden Expansion Plane 8

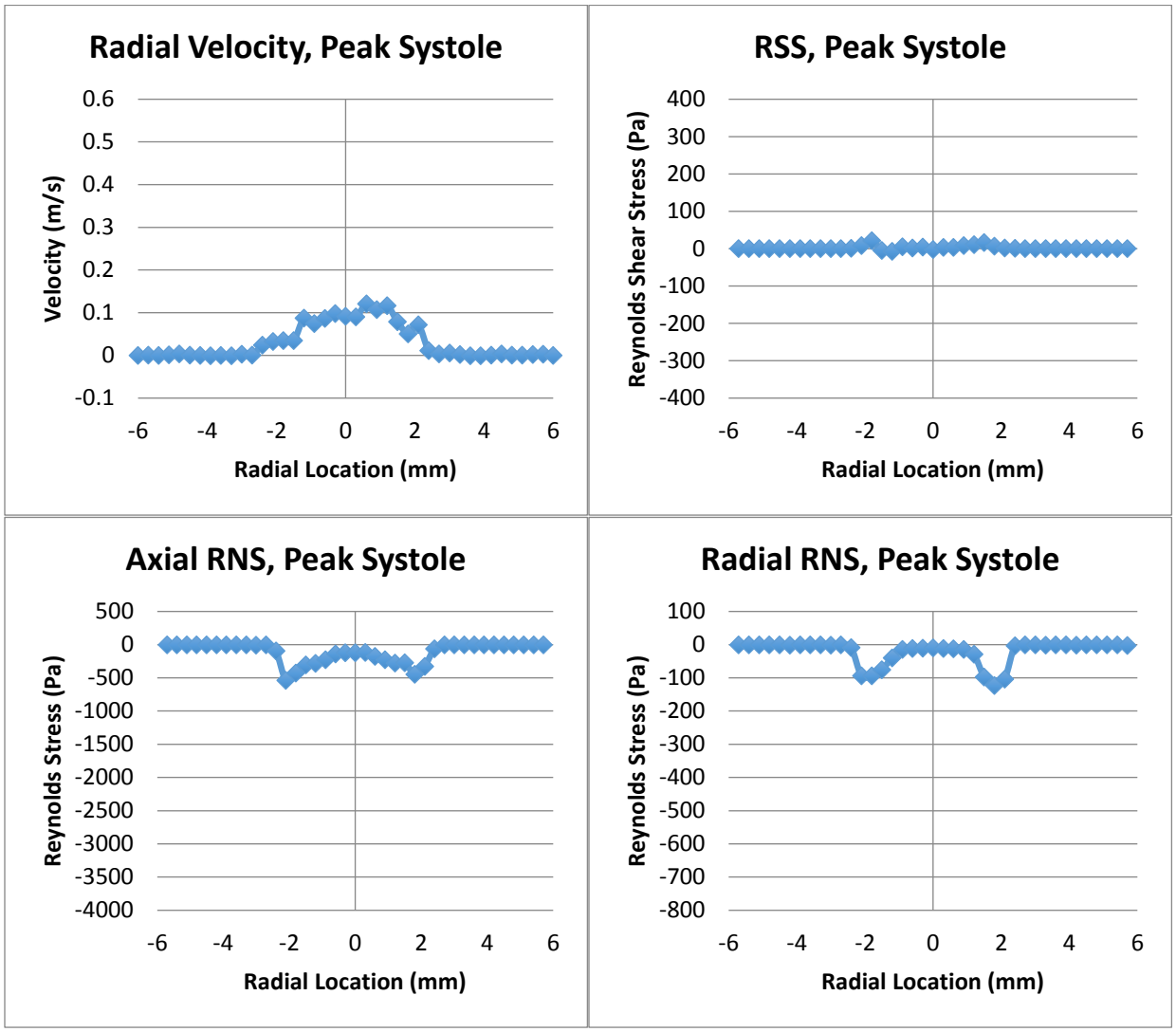

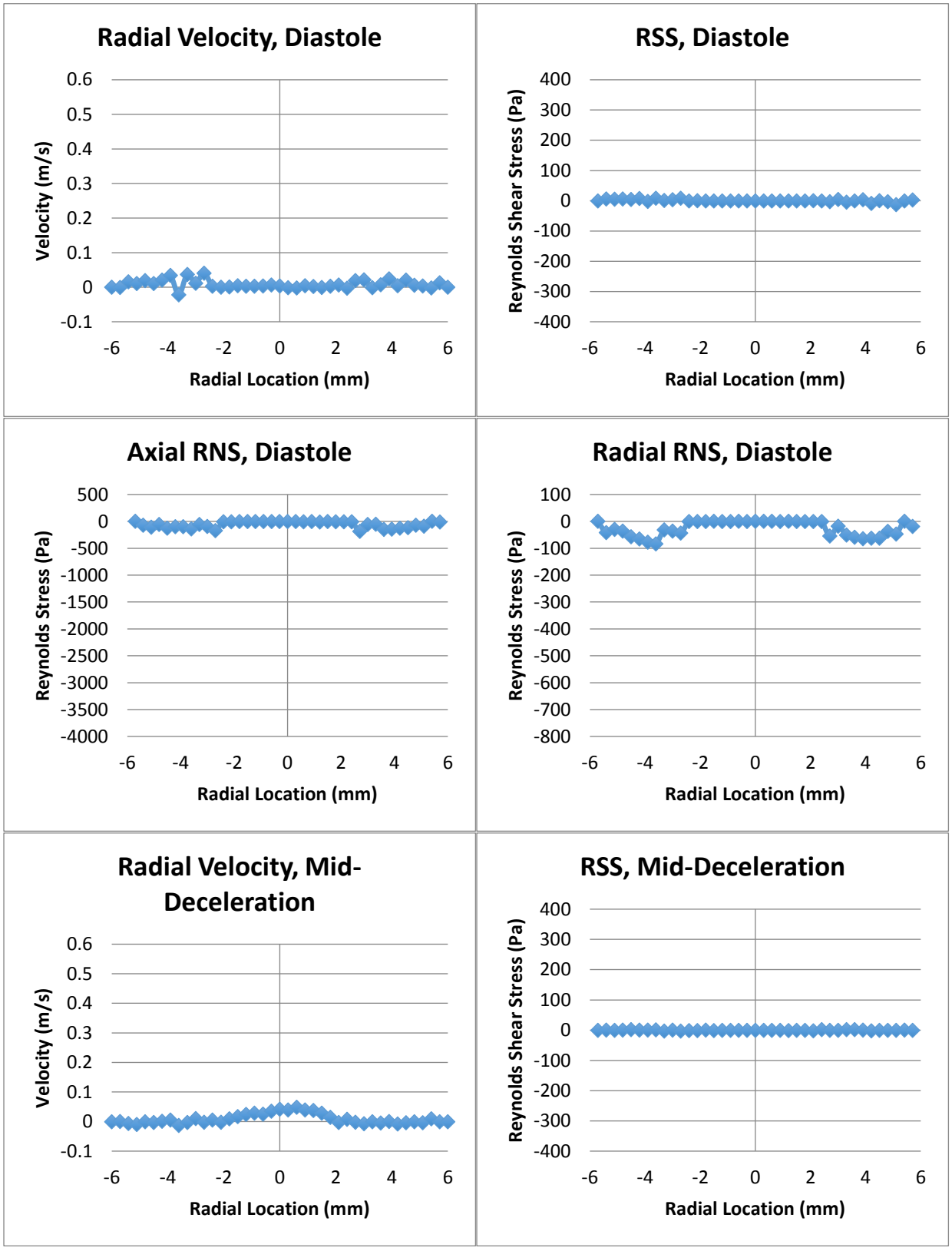
Radial Velocity, Diastole
Velocity (m/s)
0.6
0.5
0.4
0.3
0.2
0.1
0
-0.1
-6 -4 -2 0 2 4 6
Radial Location (mm)
RSS, Diastole
Reynolds Shear Stress (Pa)
400
300
200
100
0
-100
-200
-300
-400
-6 -4 -2 0 2 4 6
Radial Location (mm)
Axial RNS, Diastole
Reynolds Stress (Pa)
500
0
-500
-1000
-1500
-2000
-2500
-3000
-3500
-4000
-6 -4 -2 0 2 4 6
Radial Location (mm)
Radial RNS, Diastole
Reynolds Stress (Pa)
100
0
-100
-200
-300
-400
-500
-600
-700
-800
-6 -4 -2 0 2 4 6
Radial Location (mm)
Radial Velocity, Mid-Deceleration
Velocity (m/s)
0.6
0.5
0.4
0.3
0.2
0.1
0
-0.1
-6 -4 -2 0 2 4 6
Radial Location (mm)
RSS, Mid-Deceleration
Reynolds Shear Stress (Pa)
400
300
200
100
0
-100
-200
-300
-400
-6 -4 -2 0 2 4 6
Radial Location (mm)

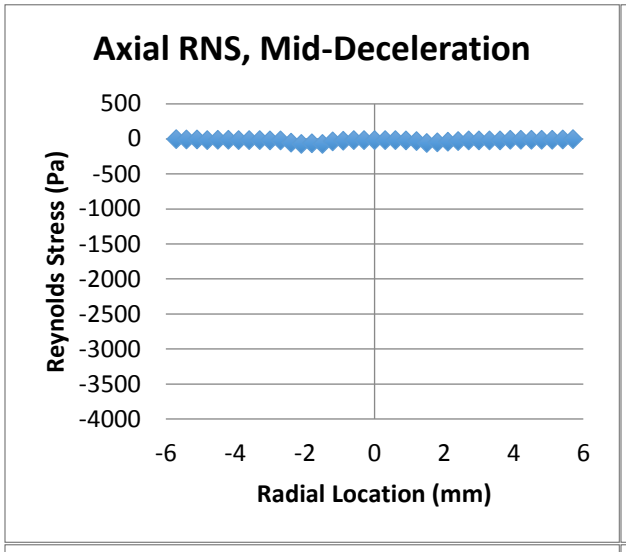
Axial RNS, Mid-Deceleration
Reynolds Stress (Pa)
500
0
-500
-1000
-1500
-2000
-2500
-3000
-3500
-4000
-6 -4 -2 0 2 4 6
Radial Location (mm)

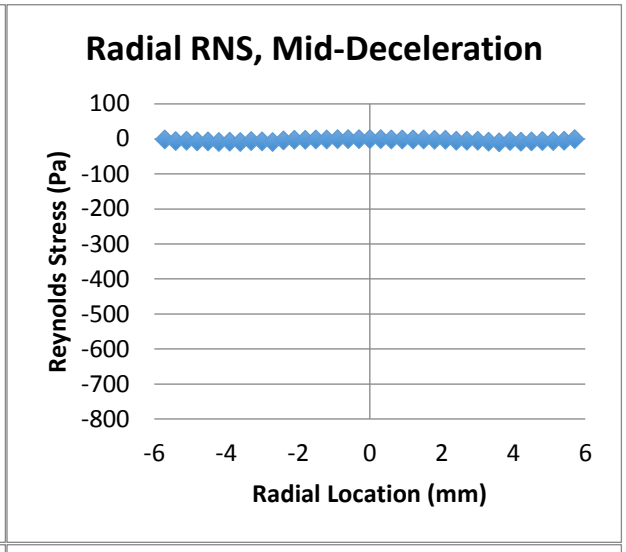
Radial RNS, Mid-Deceleration
Reynolds Stress (Pa)
100
0
-100
-200
-300
-400
-500
-600
-700
-800
-6 -4 -2 0 2 4 6
Radial Location (mm)

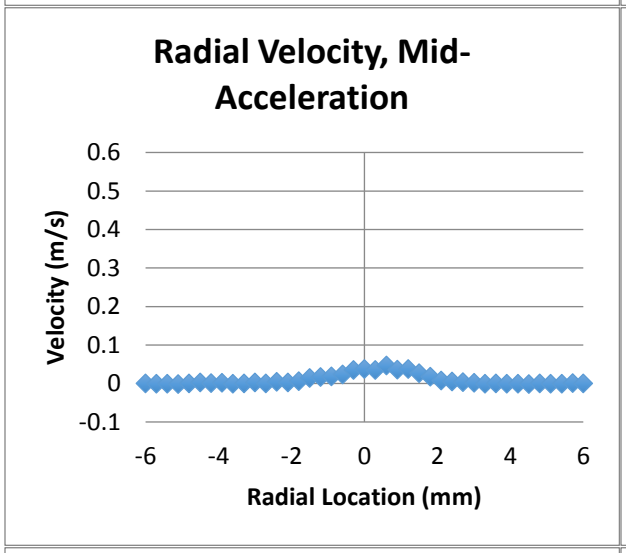
Radial Velocity, Mid-Acceleration
Velocity (m/s)
0.6
0.5
0.4
0.3
0.2
0.1
0
-0.1
-6 -4 -2 0 2 4 6
Radial Location (mm)

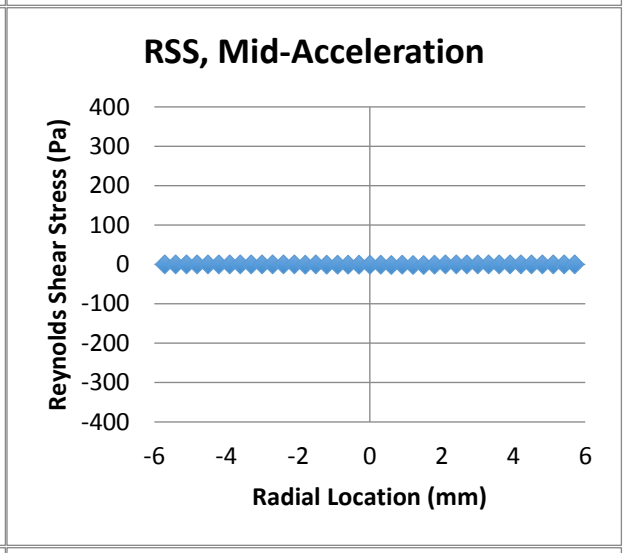
RSS, Mid-Acceleration
Reynolds Shear Stress (Pa)
400
300
200
100
0
-100
-200
-300
-400
-6 -4 -2 0 2 4 6
Radial Location (mm)

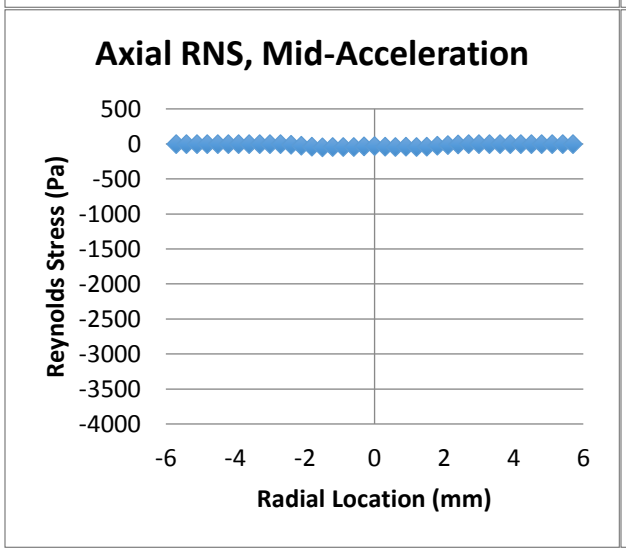
Axial RNS, Mid-Acceleration
Reynolds Stress (Pa)
500
0
-500
-1000
-1500
-2000
-2500
-3000
-3500
-4000
-6 -4 -2 0 2 4 6
Radial Location (mm)

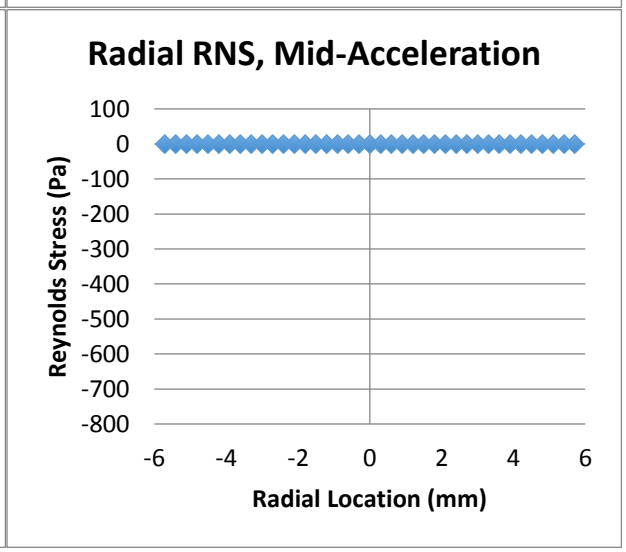
Radial RNS, Mid-Acceleration
Reynolds Stress (Pa)
100
0
-100
-200
-300
-400
-500
-600
-700
-800
-6 -4 -2 0 2 4 6
Radial Location (mm)

Appendix B.6 – Sudden Expansion Plane 10

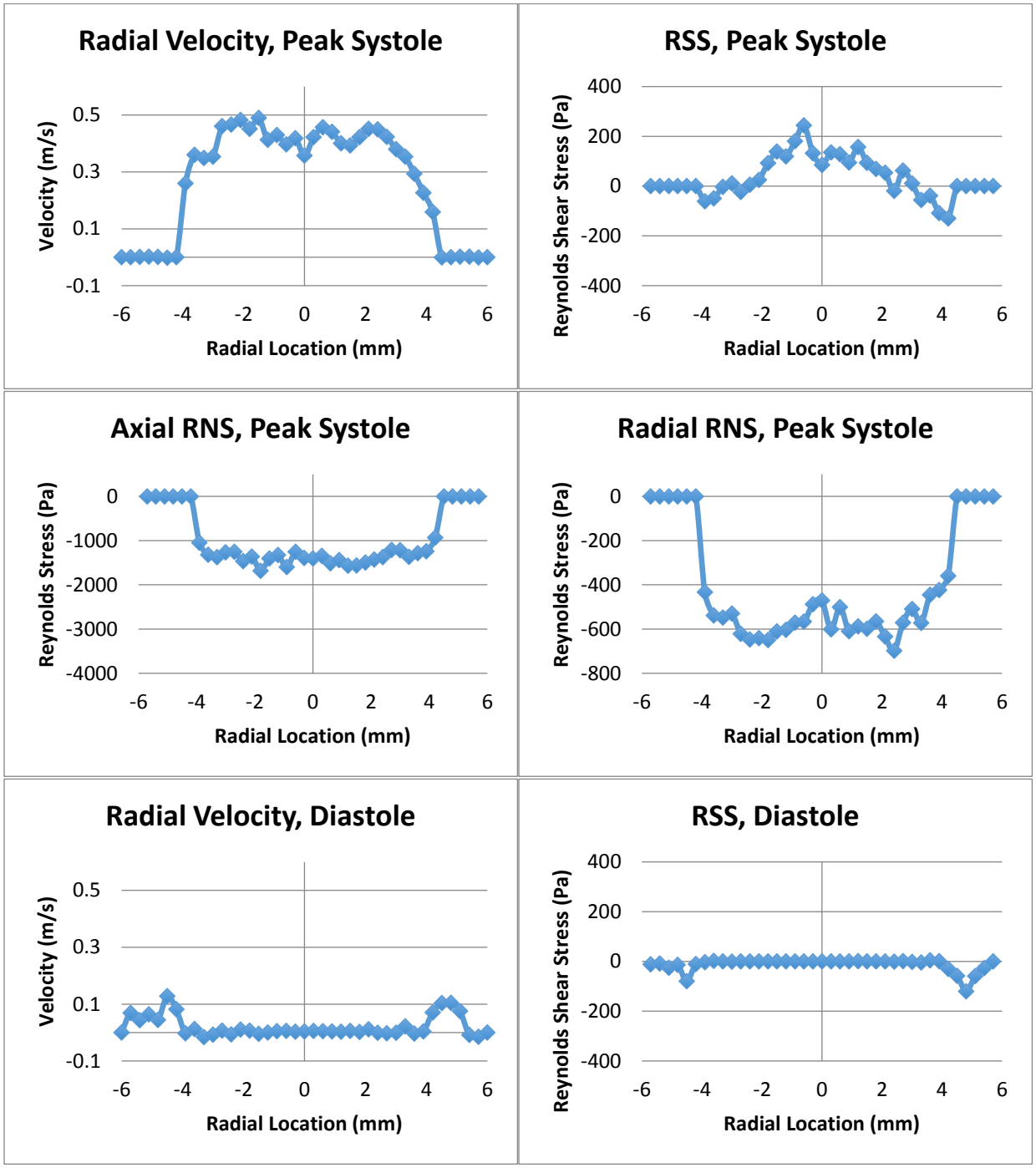

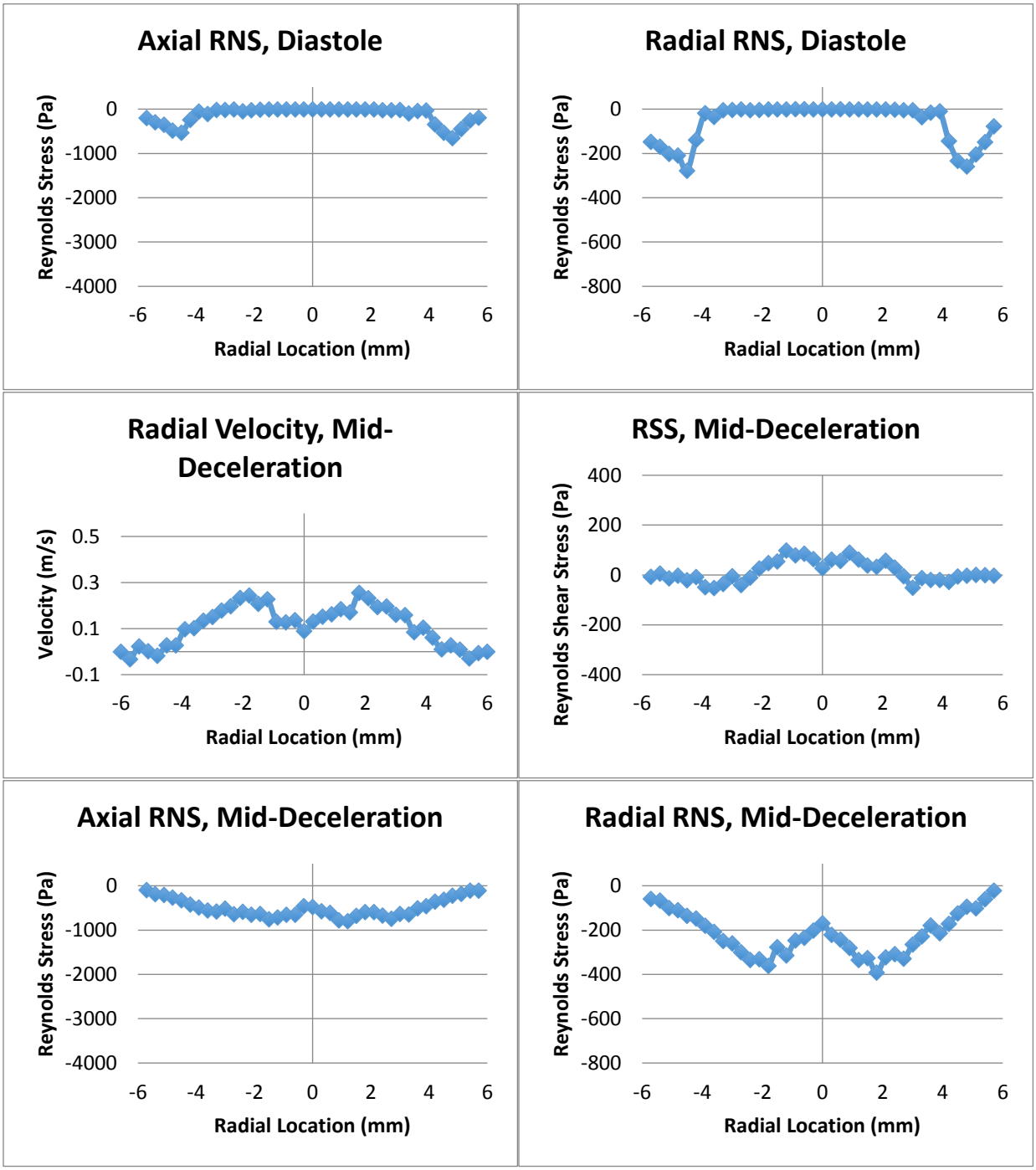
Axial RNS, Diastole
Reynolds Stress (Pa)
0
-1000
-2000
-3000
-4000
-6 -4 -2 0 2 4 6
Radial Location (mm)
Radial RNS, Diastole
Reynolds Stress (Pa)
0
-200
-400
-600
-800
-6 -4 -2 0 2 4 6
Radial Location (mm)
Radial Velocity, Mid-Deceleration
Velocity (m/s)
0.5
0.3
0.1
-0.1
-6 -4 -2 0 2 4 6
Radial Location (mm)
RSS, Mid-Deceleration
Reynolds Shear Stress (Pa)
400
200
0
-200
-400
-6 -4 -2 0 2 4 6
Radial Location (mm)
Axial RNS, Mid-Deceleration
Reynolds Stress (Pa)
0
-1000
-2000
-3000
-4000
-6 -4 -2 0 2 4 6
Radial Location (mm)
Radial RNS, Mid-Deceleration
Reynolds Stress (Pa)
0
-200
-400
-600
-800
-6 -4 -2 0 2 4 6
Radial Location (mm)

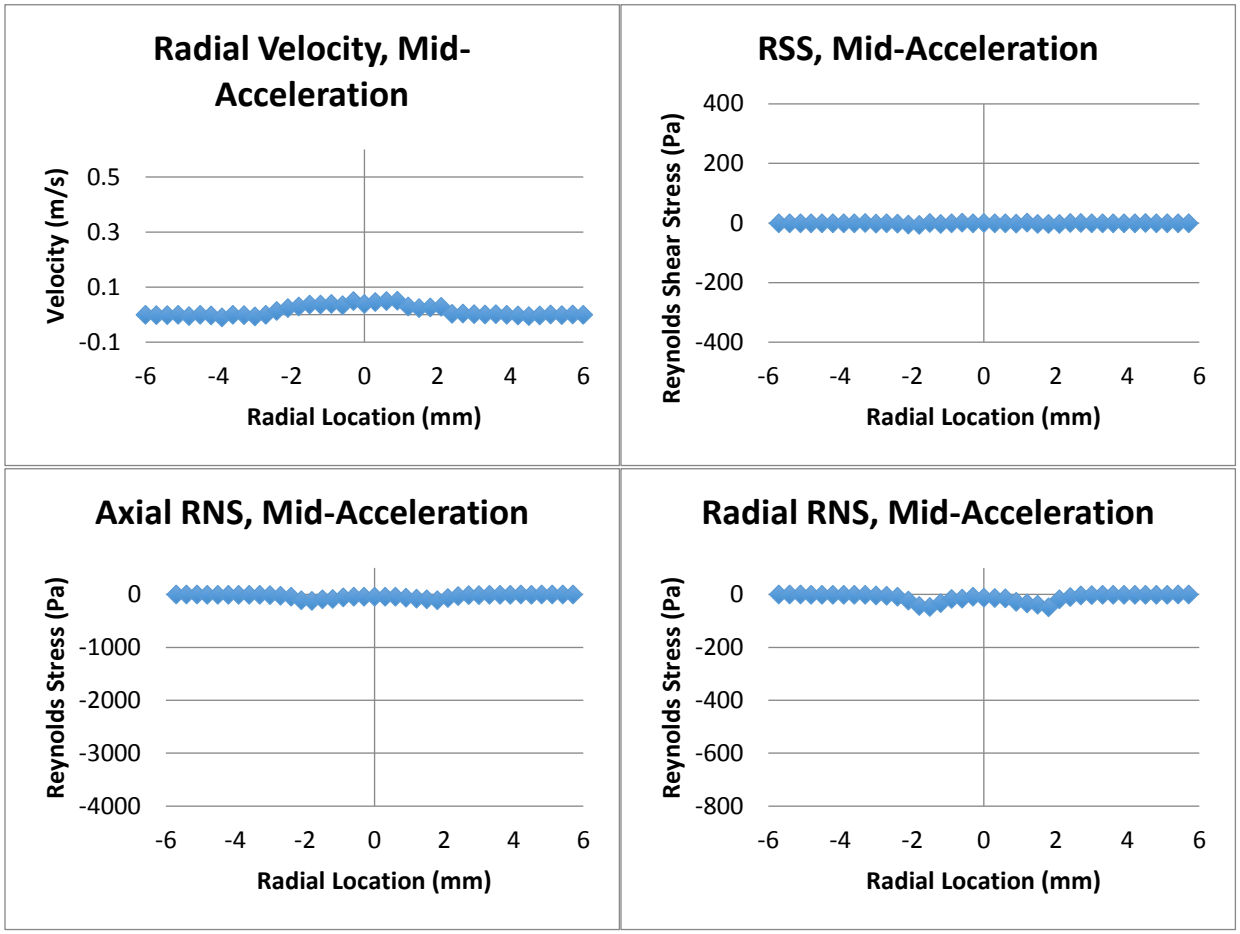
Radial Velocity, Mid-Acceleration
Velocity (m/s)
0.5
0.3
0.1
-0.1
-6
-4
-2
0
2
4
6
Radial Location (mm)
RSS, Mid-Acceleration
Reynolds Shear Stress (Pa)
400
200
0
-200
-400
-6
-4
-2
0
2
4
6
Radial Location (mm)
Axial RNS, Mid-Acceleration
Reynolds Stress (Pa)
0
-1000
-2000
-3000
-4000
-6
-4
-2
0
2
4
6
Radial Location (mm)
Radial RNS, Mid-Acceleration
Reynolds Stress (Pa)
0
-200
-400
-600
-800
-6
-4
-2
0
2
4
6
Radial Location (mm)

Appendix B.7 – Sudden Expansion Plane 11

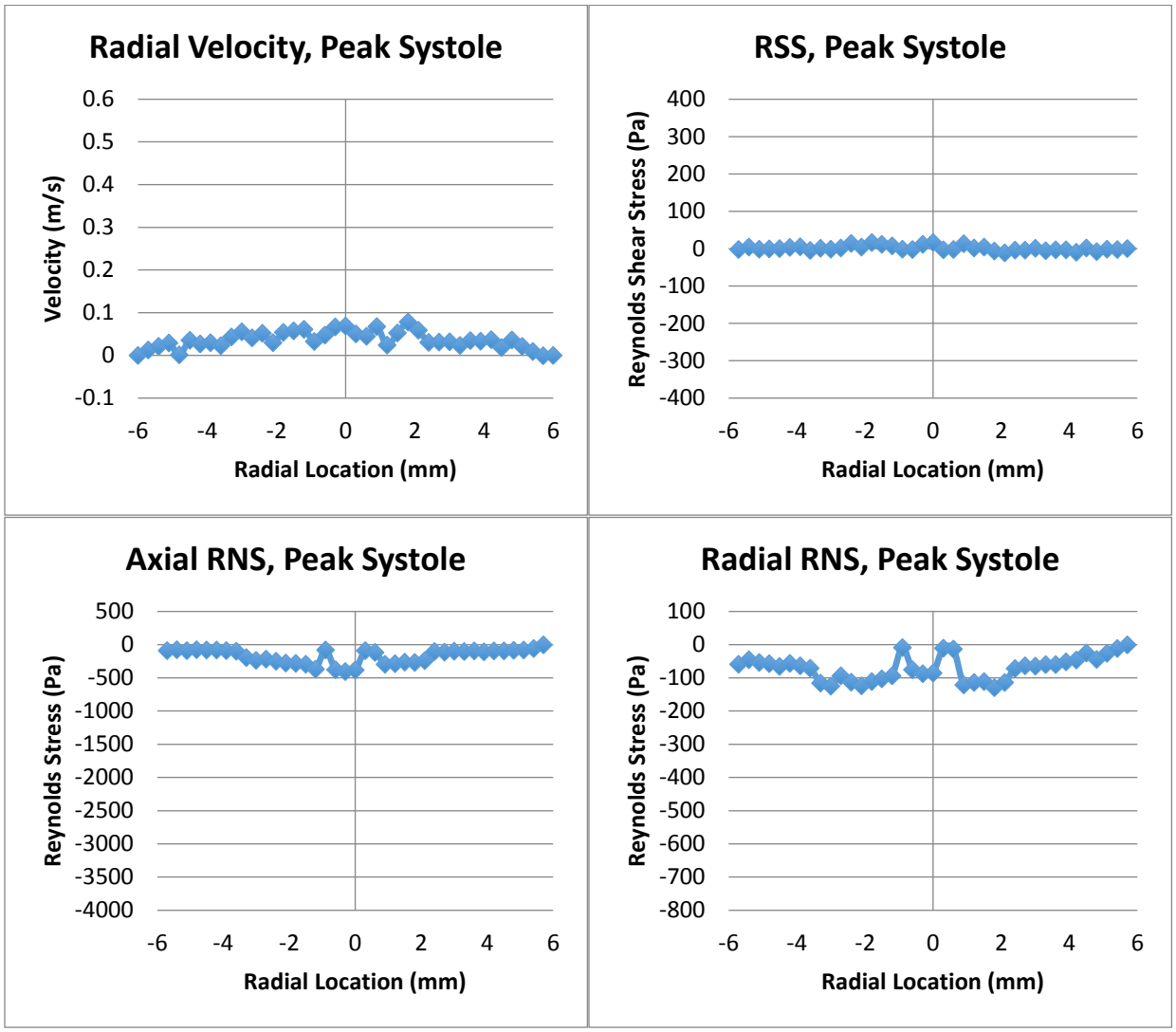

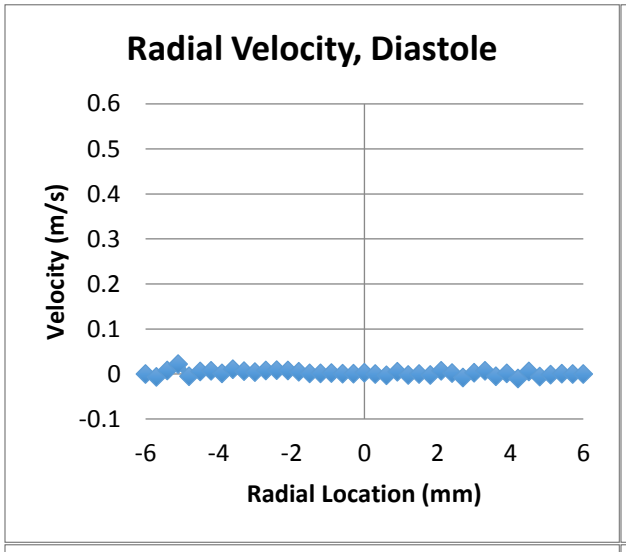
Radial Velocity, Diastole
Velocity (m/s)
0.6
0.5
0.4
0.3
0.2
0.1
0
-0.1
-6 -4 -2 0 2 4 6
Radial Location (mm)

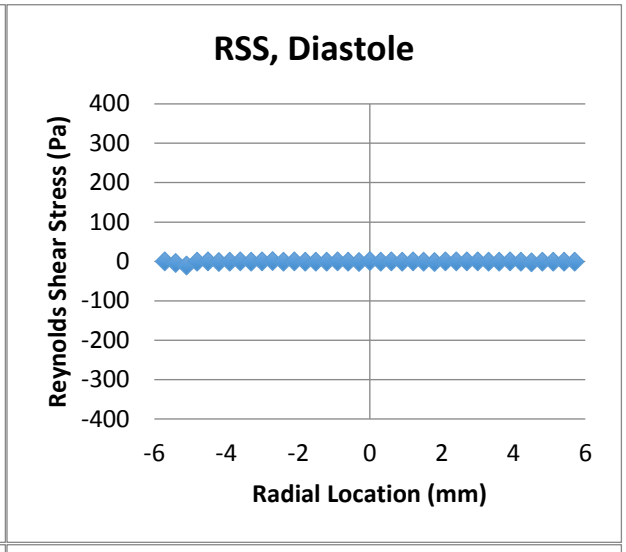
RSS, Diastole
Reynolds Shear Stress (Pa)
400
300
200
100
0
-100
-200
-300
-400
-6 -4 -2 0 2 4 6
Radial Location (mm)

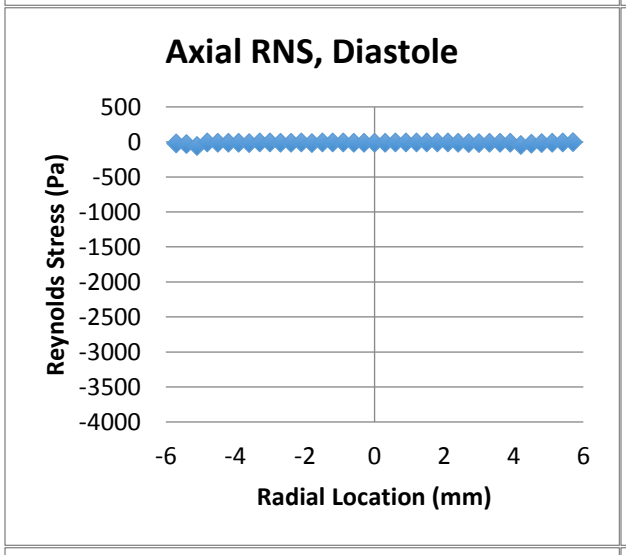
Axial RNS, Diastole
Reynolds Stress (Pa)
500
0
-500
-1000
-1500
-2000
-2500
-3000
-3500
-4000
-6 -4 -2 0 2 4 6
Radial Location (mm)

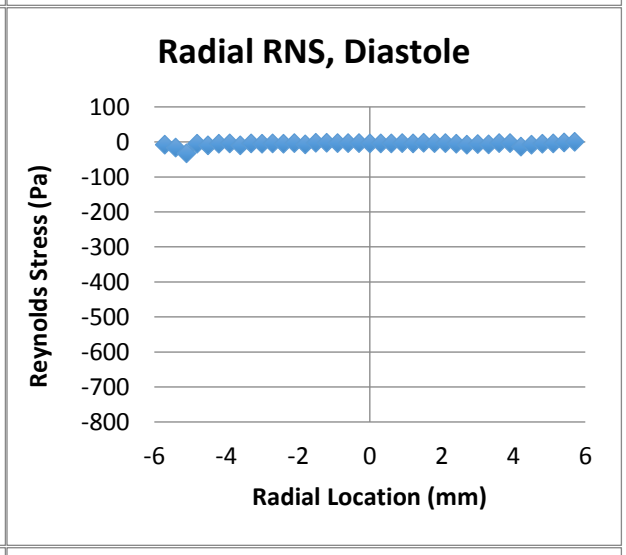
Radial RNS, Diastole
Reynolds Stress (Pa)
100
0
-100
-200
-300
-400
-500
-600
-700
-800
-6 -4 -2 0 2 4 6
Radial Location (mm)

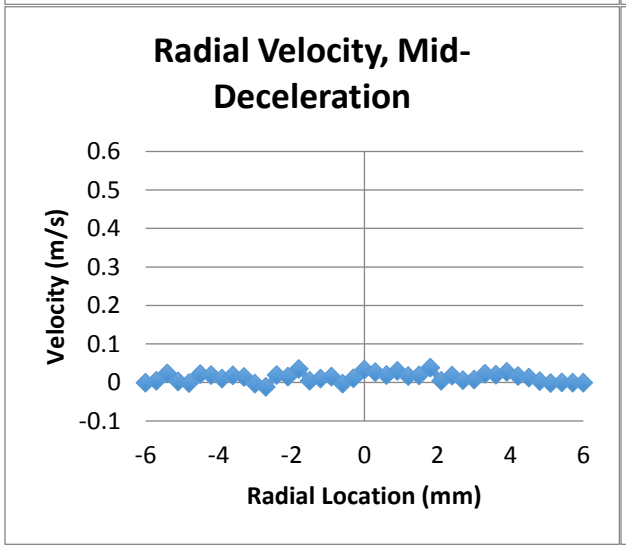
Radial Velocity, Mid-Deceleration
Velocity (m/s)
0.6
0.5
0.4
0.3
0.2
0.1
0
-0.1
-6 -4 -2 0 2 4 6
Radial Location (mm)

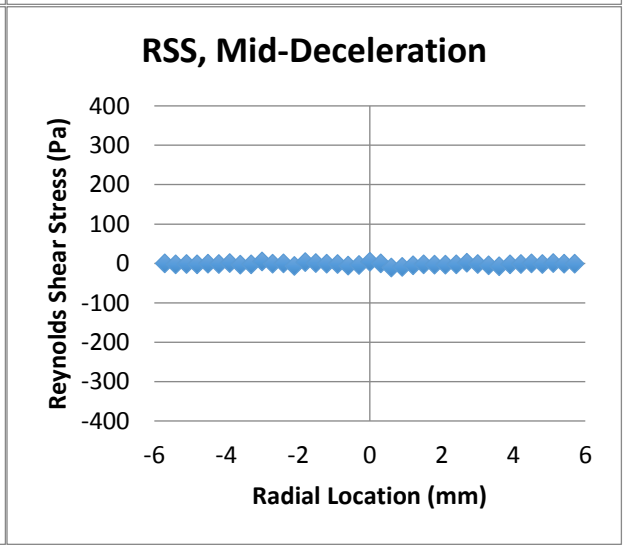
RSS, Mid-Deceleration
Reynolds Shear Stress (Pa)
400
300
200
100
0
-100
-200
-300
-400
-6 -4 -2 0 2 4 6
Radial Location (mm)

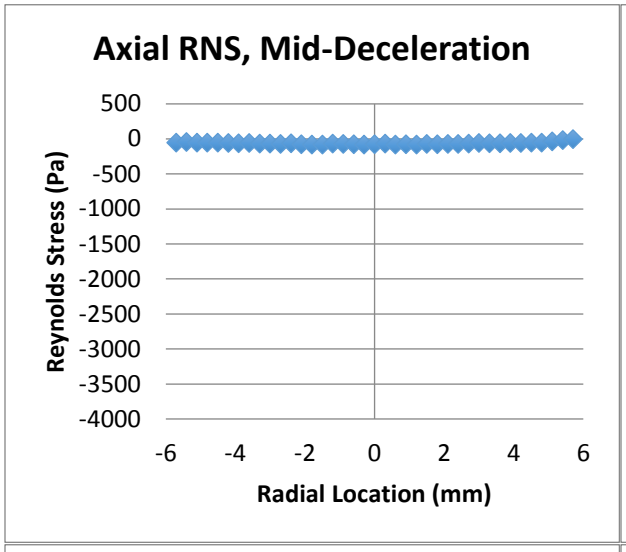
Axial RNS, Mid-Deceleration
Reynolds Stress (Pa)
500
0
-500
-1000
-1500
-2000
-2500
-3000
-3500
-4000
-6
-4
-2
0
2
4
6
Radial Location (mm)

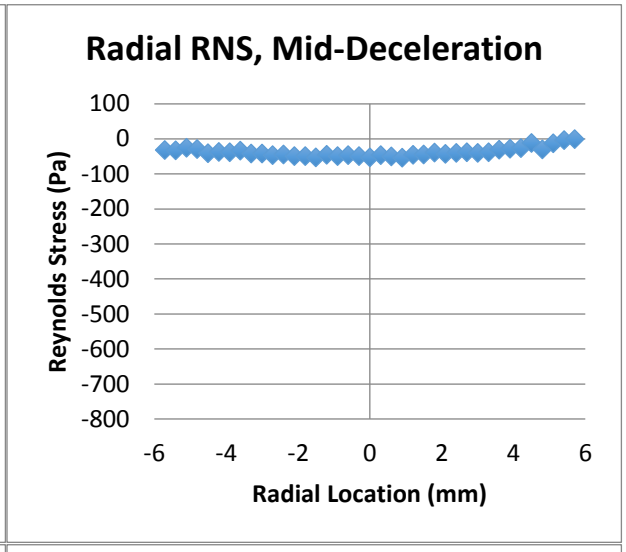
Radial RNS, Mid-Deceleration
Reynolds Stress (Pa)
100
0
-100
-200
-300
-400
-500
-600
-700
-800
-6
-4
-2
0
2
4
6
Radial Location (mm)

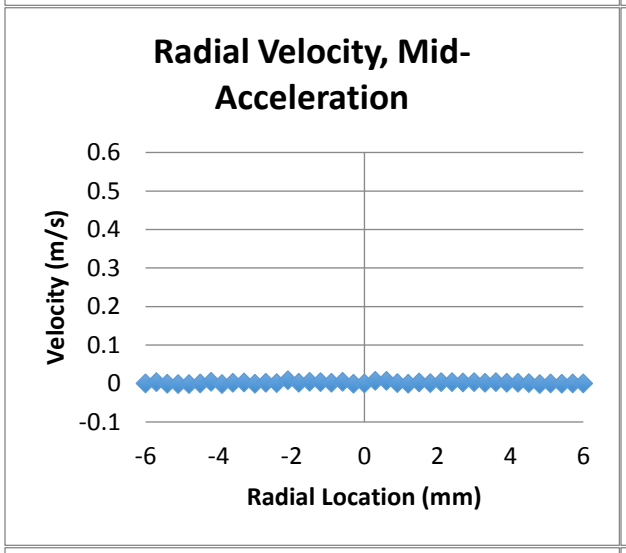
Radial Velocity, Mid-Acceleration
Velocity (m/s)
0.6
0.5
0.4
0.3
0.2
0.1
0
-0.1
-6
-4
-2
0
2
4
6
Radial Location (mm)

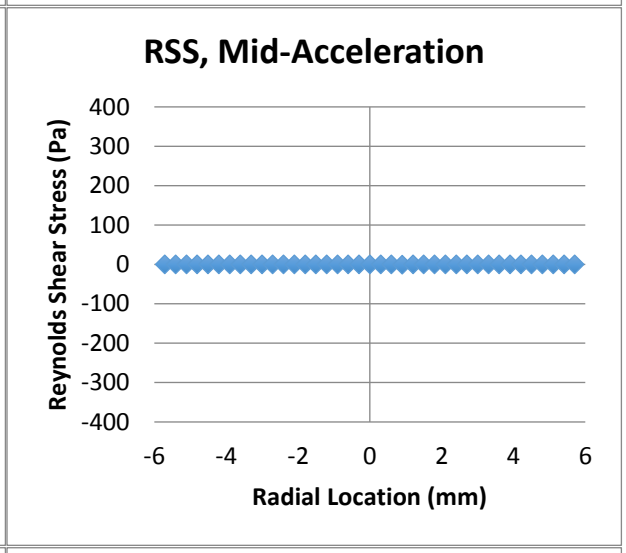
RSS, Mid-Acceleration
Reynolds Shear Stress (Pa)
400
300
200
100
0
-100
-200
-300
-400
-6
-4
-2
0
2
4
6
Radial Location (mm)

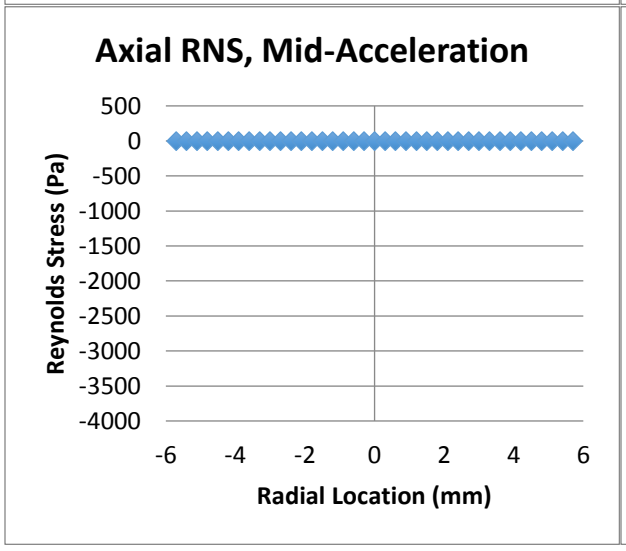
Axial RNS, Mid-Acceleration
Reynolds Stress (Pa)
500
0
-500
-1000
-1500
-2000
-2500
-3000
-3500
-4000
-6
-4
-2
0
2
4
6
Radial Location (mm)

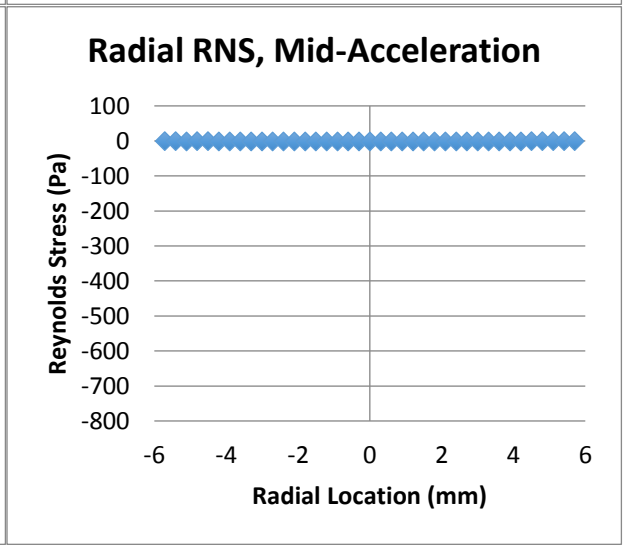
Radial RNS, Mid-Acceleration
Reynolds Stress (Pa)
100
0
-100
-200
-300
-400
-500
-600
-700
-800
-6
-4
-2
0
2
4
6
Radial Location (mm)

Appendix B.8 – Conical Diffuser Plane 2

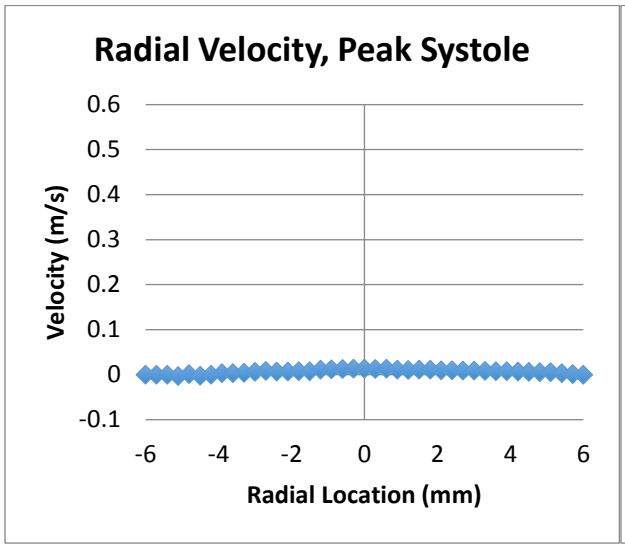

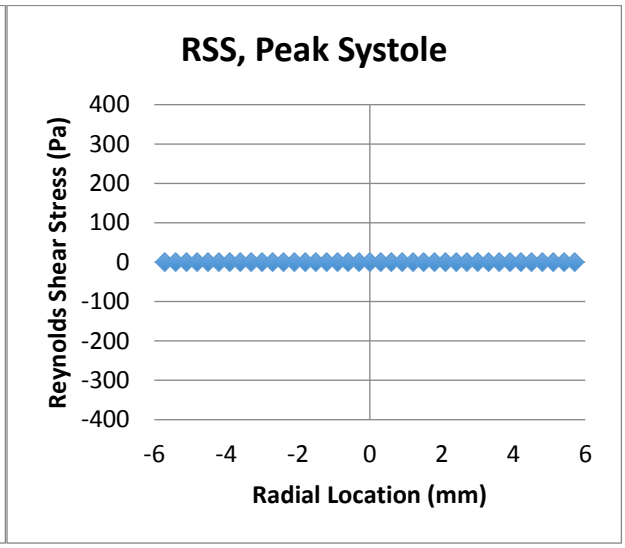

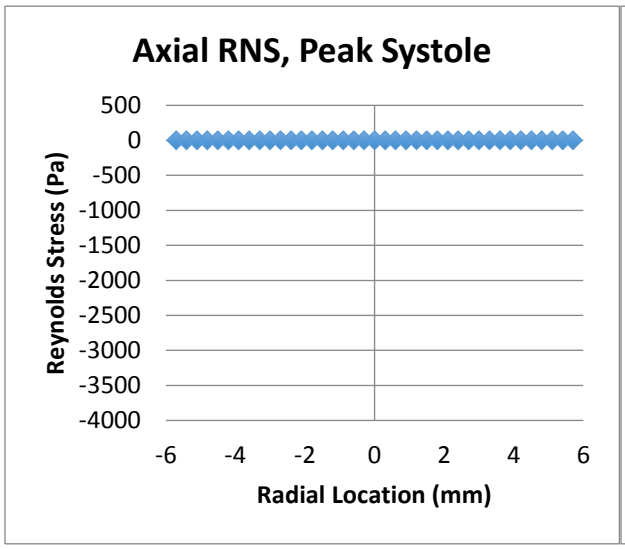

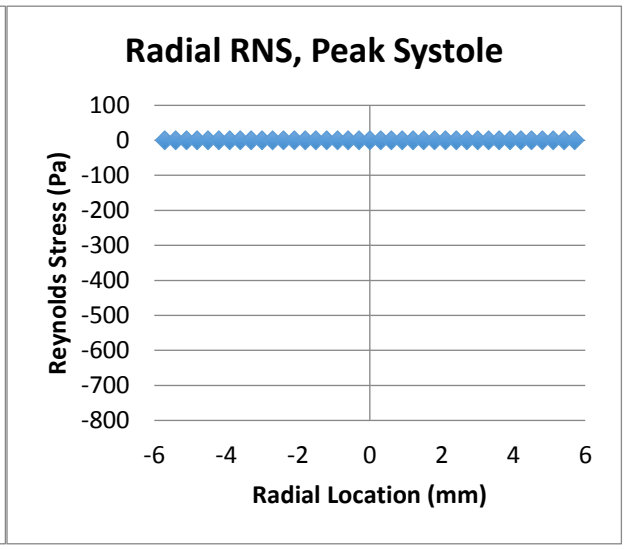

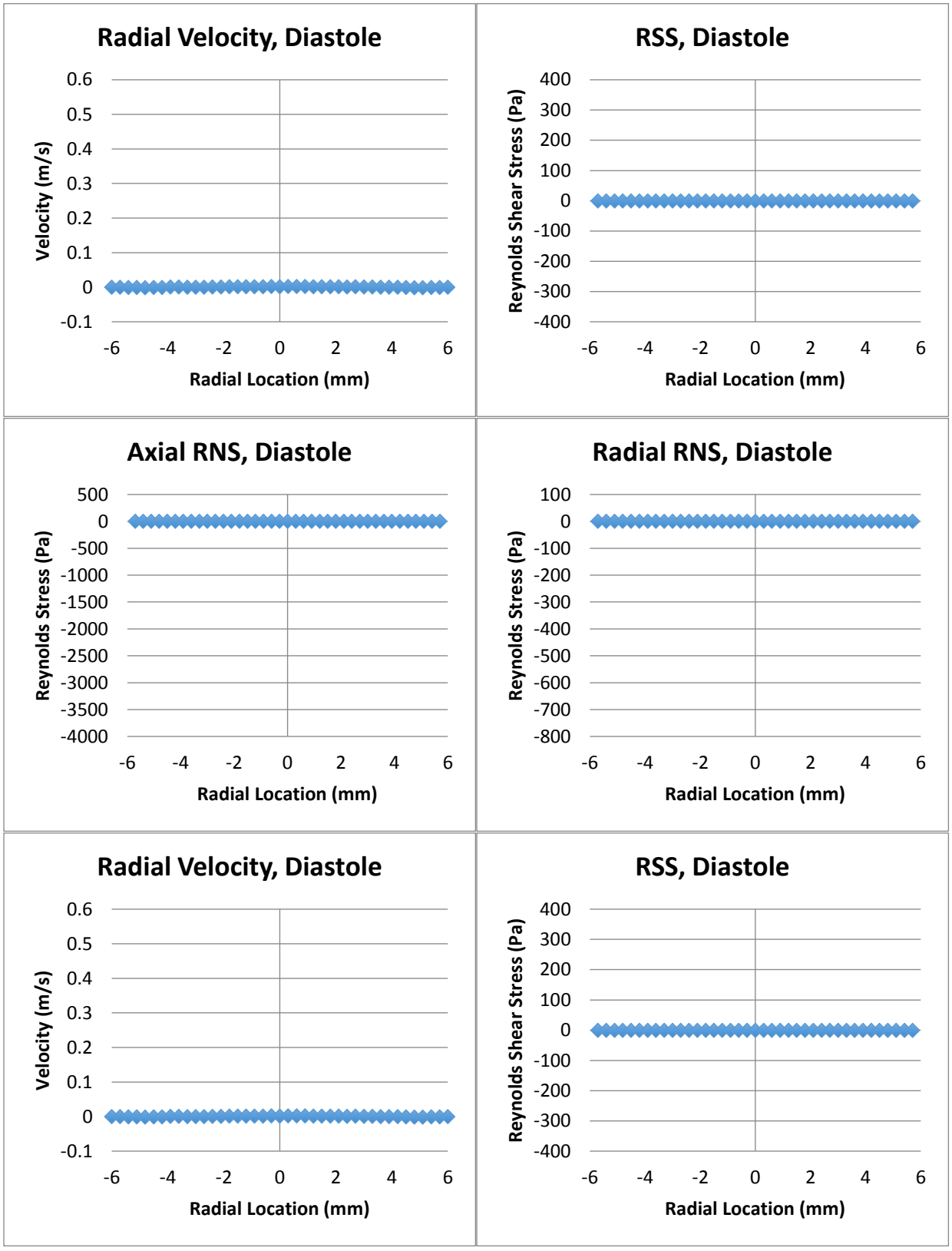
Radial Velocity, Diastole
Velocity (m/s)
0.6
0.5
0.4
0.3
0.2
0.1
0
-0.1
-6 -4 -2 0 2 4 6
Radial Location (mm)
RSS, Diastole
Reynolds Shear Stress (Pa)
400
300
200
100
0
-100
-200
-300
-400
-6 -4 -2 0 2 4 6
Radial Location (mm)
Axial RNS, Diastole
Reynolds Stress (Pa)
500
0
-500
-1000
-1500
-2000
-2500
-3000
-3500
-4000
-6 -4 -2 0 2 4 6
Radial Location (mm)
Radial RNS, Diastole
Reynolds Stress (Pa)
100
0
-100
-200
-300
-400
-500
-600
-700
-800
-6 -4 -2 0 2 4 6
Radial Location (mm)
Radial Velocity, Diastole
Velocity (m/s)
0.6
0.5
0.4
0.3
0.2
0.1
0
-0.1
-6 -4 -2 0 2 4 6
Radial Location (mm)
RSS, Diastole
Reynolds Shear Stress (Pa)
400
300
200
100
0
-100
-200
-300
-400
-6 -4 -2 0 2 4 6
Radial Location (mm)

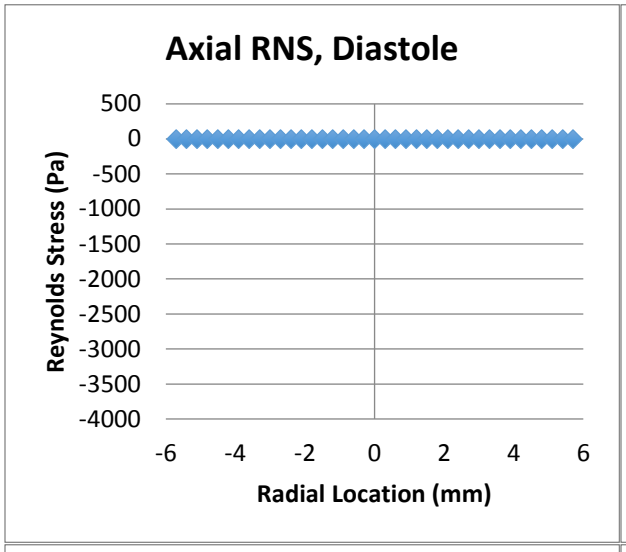
Axial RNS, Diastole
Reynolds Stress (Pa)
500
0
-500
-1000
-1500
-2000
-2500
-3000
-3500
-4000
-6
-4
-2
0
2
4
6
Radial Location (mm)

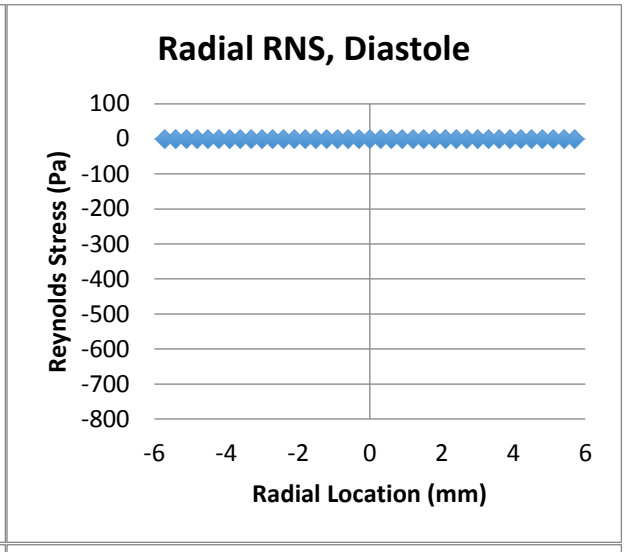
Radial RNS, Diastole
Reynolds Stress (Pa)
100
0
-100
-200
-300
-400
-500
-600
-700
-800
-6
-4
-2
0
2
4
6
Radial Location (mm)

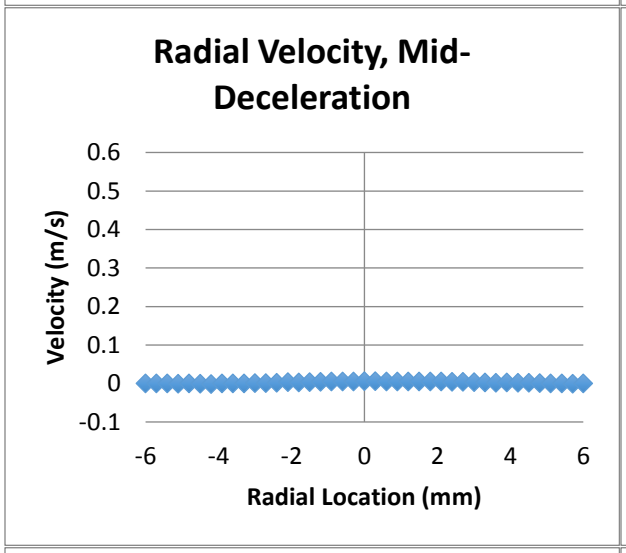
Radial Velocity, Mid-Deceleration
Velocity (m/s)
0.6
0.5
0.4
0.3
0.2
0.1
0
-0.1
-6
-4
-2
0
2
4
6
Radial Location (mm)

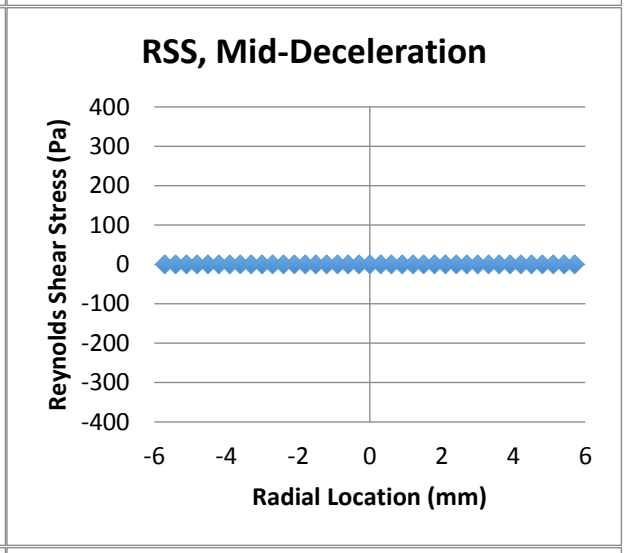
RSS, Mid-Deceleration
Reynolds Shear Stress (Pa)
400
300
200
100
0
-100
-200
-300
-400
-6
-4
-2
0
2
4
6
Radial Location (mm)

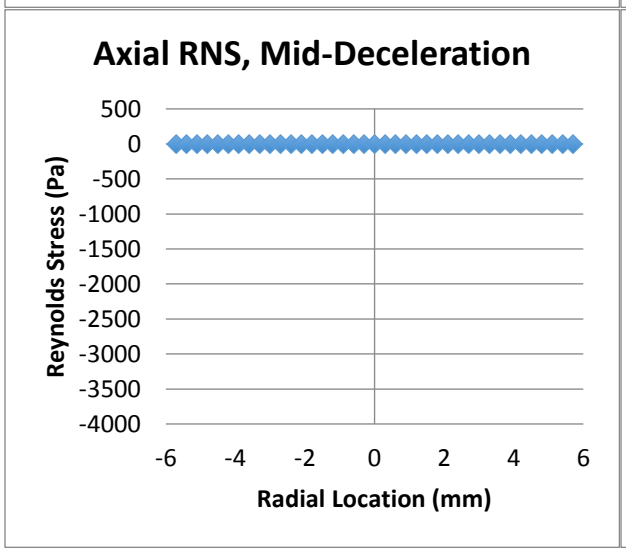
Axial RNS, Mid-Deceleration
Reynolds Stress (Pa)
500
0
-500
-1000
-1500
-2000
-2500
-3000
-3500
-4000
-6
-4
-2
0
2
4
6
Radial Location (mm)

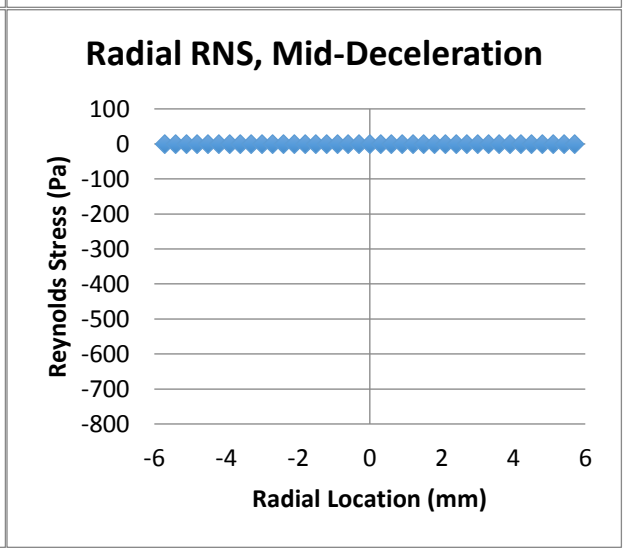
Radial RNS, Mid-Deceleration
Reynolds Stress (Pa)
100
0
-100
-200
-300
-400
-500
-600
-700
-800
-6
-4
-2
0
2
4
6
Radial Location (mm)

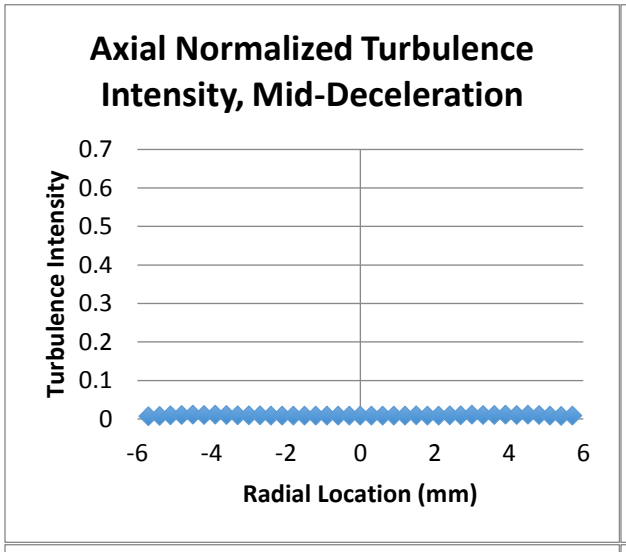
Axial Normalized Turbulence Intensity, Mid-Deceleration
Turbulence Intensity
0.7
0.6
0.5
0.4
0.3
0.2
0.1
0
-6
-4
-2
0
2
4
6
Radial Location (mm)

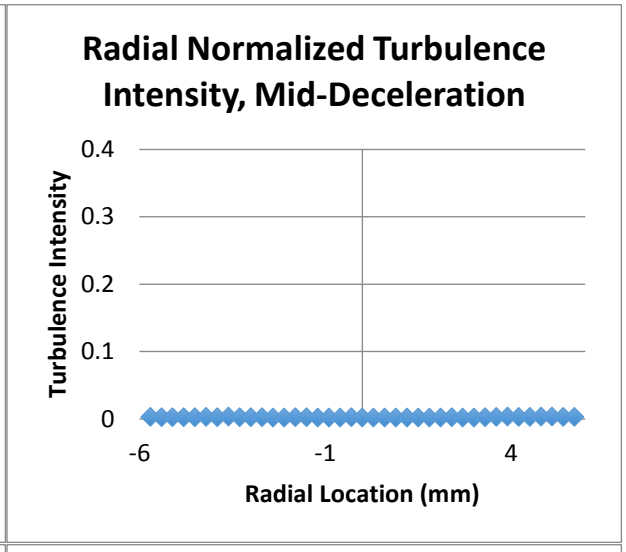
Radial Normalized Turbulence Intensity, Mid-Deceleration
Turbulence Intensity
0.4
0.3
0.2
0.1
0
-6
-1
4
Radial Location (mm)

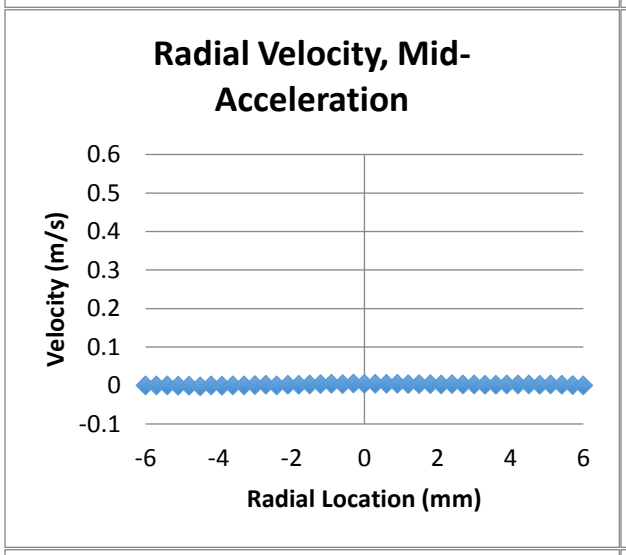
Radial Velocity, Mid-Acceleration
Velocity (m/s)
0.6
0.5
0.4
0.3
0.2
0.1
0
-0.1
-6
-4
-2
0
2
4
6
Radial Location (mm)

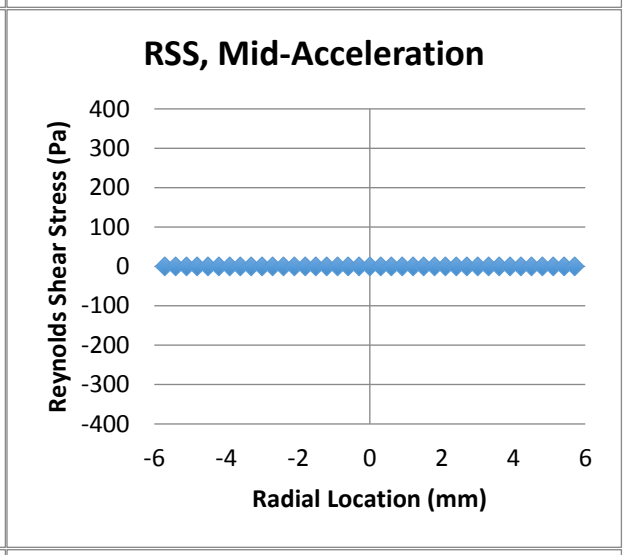
RSS, Mid-Acceleration
Reynolds Shear Stress (Pa)
400
300
200
100
0
-100
-200
-300
-400
-6
-4
-2
0
2
4
6
Radial Location (mm)

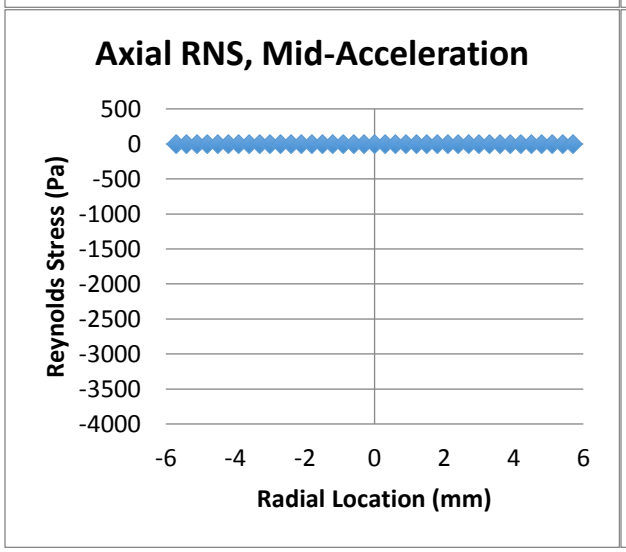
Axial RNS, Mid-Acceleration
Reynolds Stress (Pa)
500
0
-500
-1000
-1500
-2000
-2500
-3000
-3500
-4000
-6
-4
-2
0
2
4
6
Radial Location (mm)

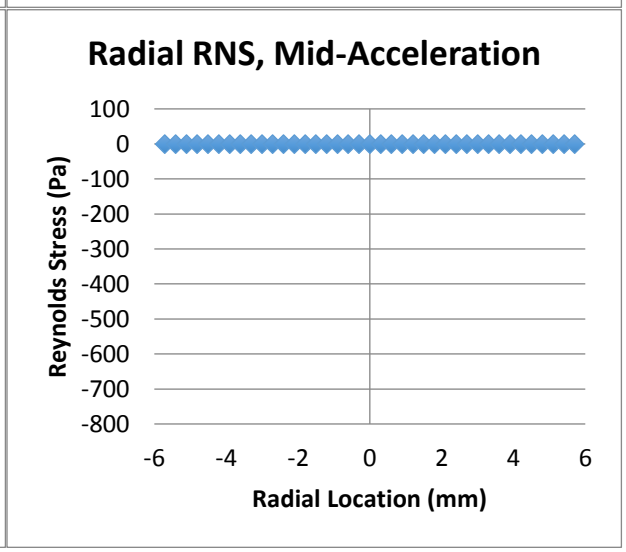
Radial RNS, Mid-Acceleration
Reynolds Stress (Pa)
100
0
-100
-200
-300
-400
-500
-600
-700
-800
-6
-4
-2
0
2
4
6
Radial Location (mm)

Appendix B.9 – Conical Diffuser Plane 5

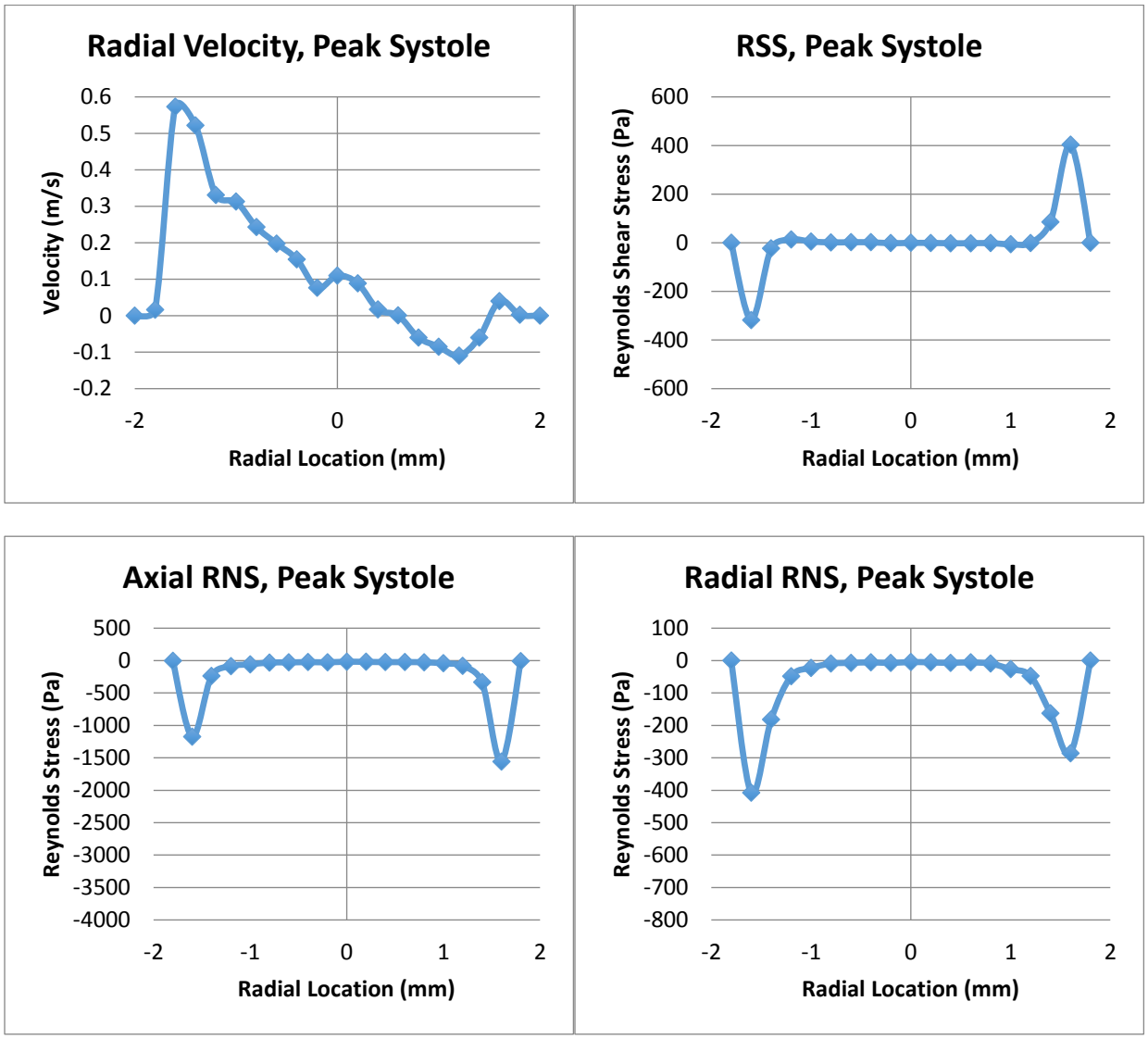

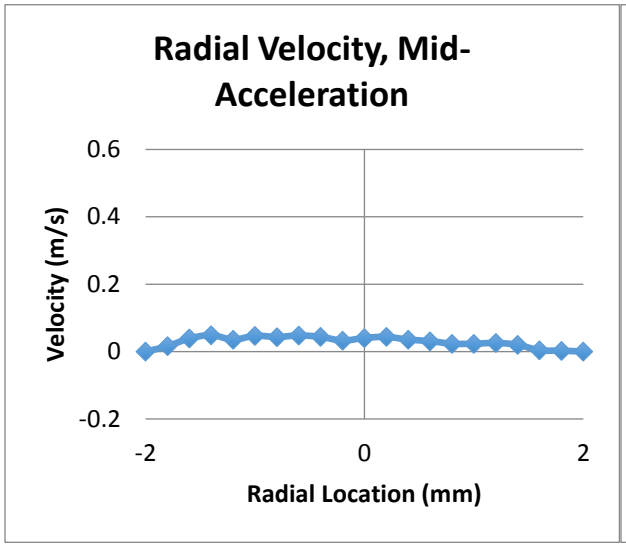
Radial Velocity, Mid-Acceleration
Velocity (m/s)
0.6
0.4
0.2
0
-0.2
-2
0
2
Radial Location (mm)

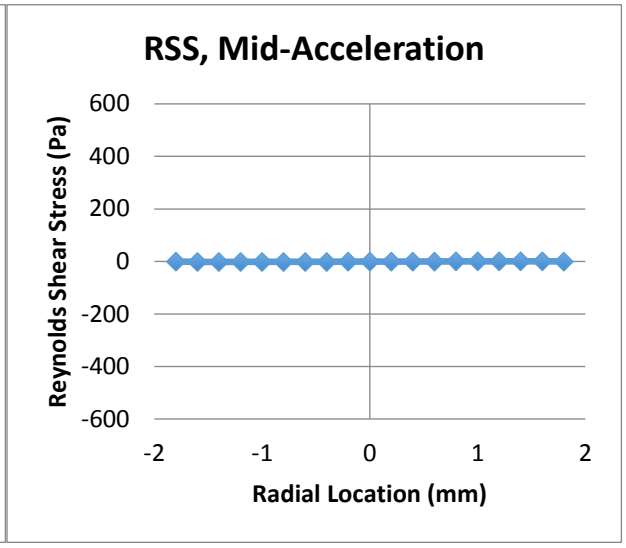
RSS, Mid-Acceleration
Reynolds Shear Stress (Pa)
600
400
200
0
-200
-400
-600
-2
-1
0
1
2
Radial Location (mm)

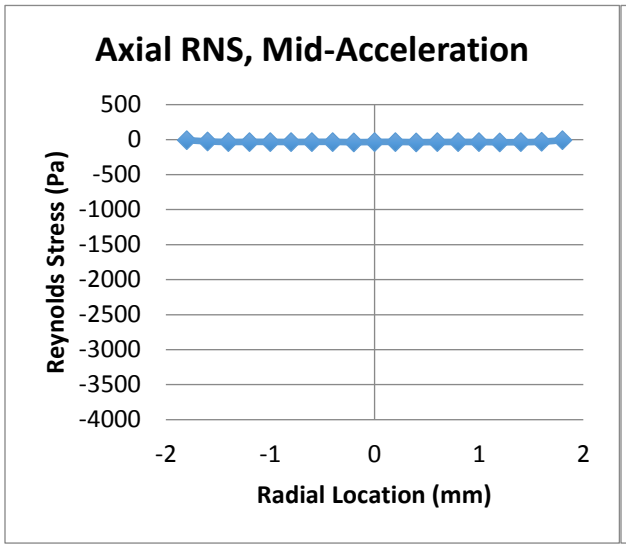
Axial RNS, Mid-Acceleration
Reynolds Stress (Pa)
500
0
-500
-1000
-1500
-2000
-2500
-3000
-3500
-4000
-2
-1
0
1
2
Radial Location (mm)

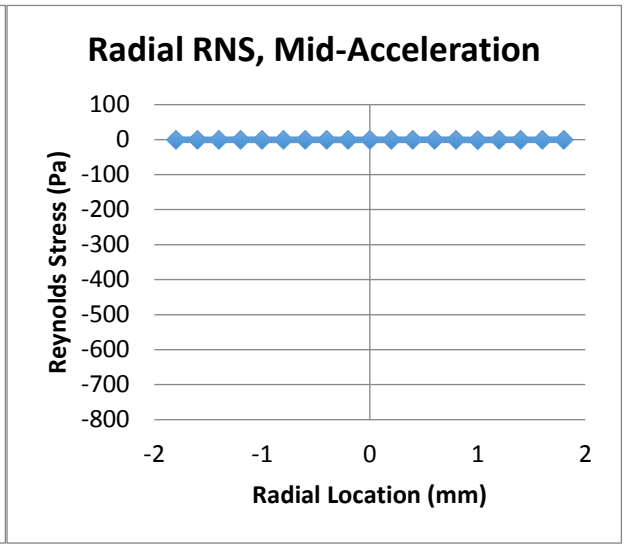
Radial RNS, Mid-Acceleration
Reynolds Stress (Pa)
100
0
-100
-200
-300
-400
-500
-600
-700
-800
-2
-1
0
1
2
Radial Location (mm)

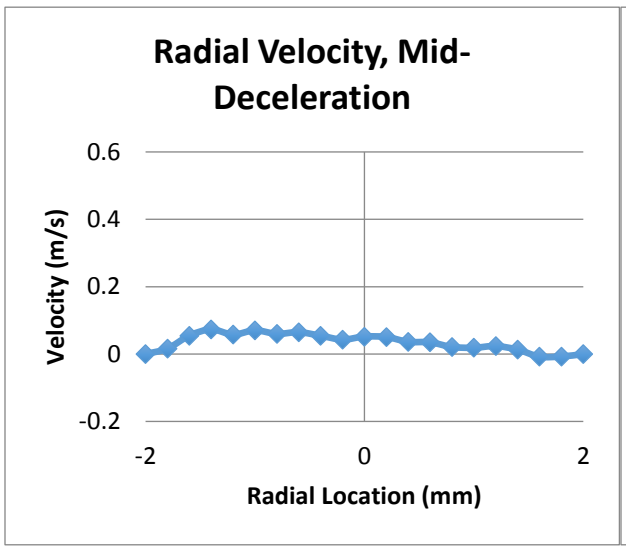
Radial Velocity, Mid-Deceleration
Velocity (m/s)
0.6
0.4
0.2
0
-0.2
-2
0
2
Radial Location (mm)

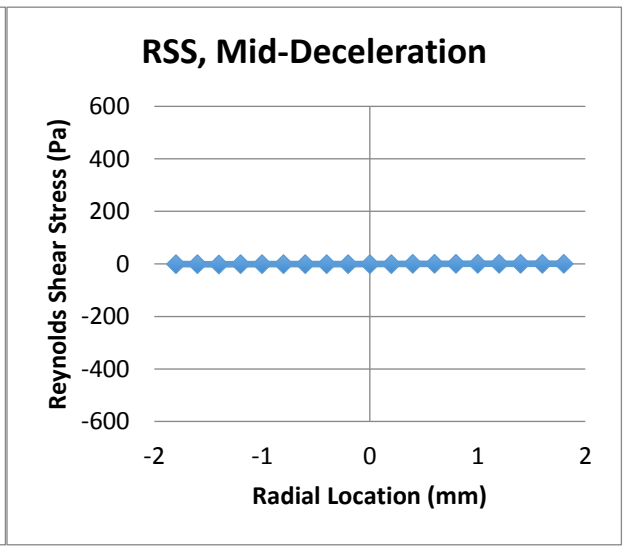
RSS, Mid-Deceleration
Reynolds Shear Stress (Pa)
600
400
200
0
-200
-400
-600
-2
-1
0
1
2
Radial Location (mm)

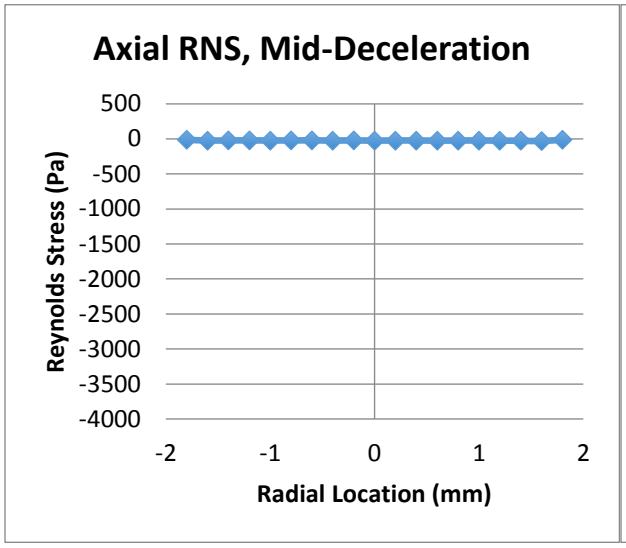
Axial RNS, Mid-Deceleration
Reynolds Stress (Pa)
500
0
-500
-1000
-1500
-2000
-2500
-3000
-3500
-4000
-2
-1
0
1
2
Radial Location (mm)

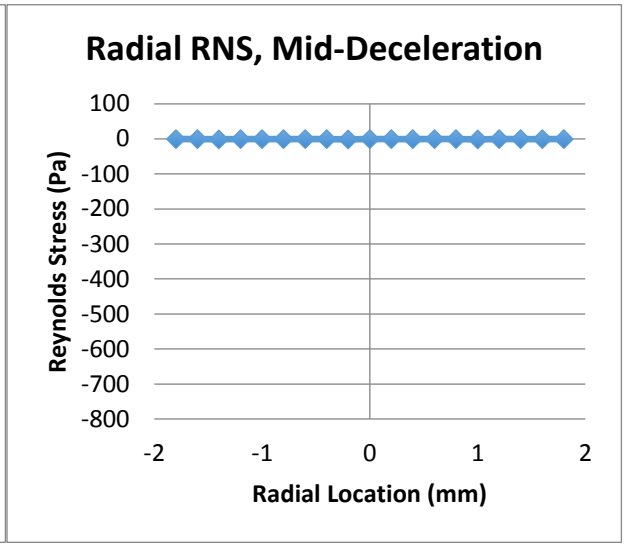
Radial RNS, Mid-Deceleration
Reynolds Stress (Pa)
100
0
-100
-200
-300
-400
-500
-600
-700
-800
-2
-1
0
1
2
Radial Location (mm)

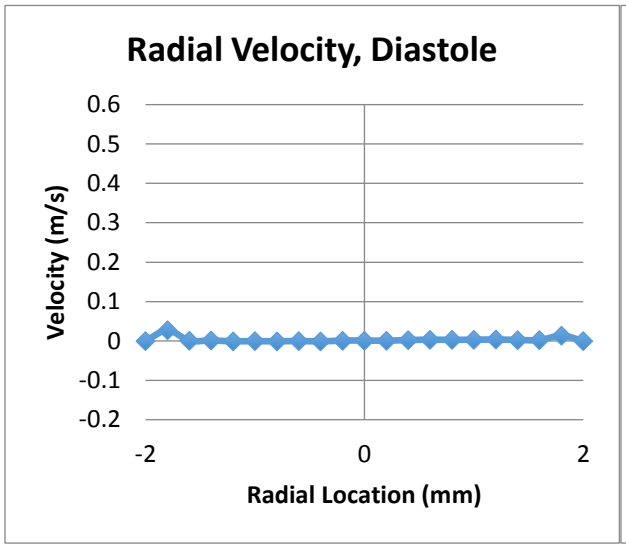
Radial Velocity, Diastole
Velocity (m/s)
0.6
0.5
0.4
0.3
0.2
0.1
0
-0.1
-0.2
-2
0
2
Radial Location (mm)

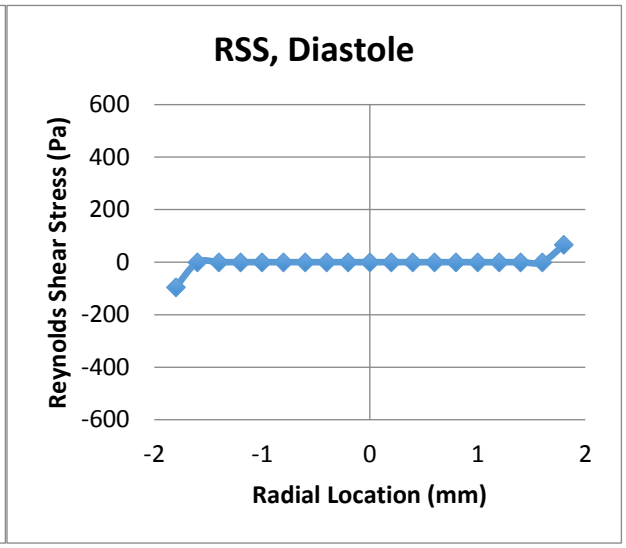
RSS, Diastole
Reynolds Shear Stress (Pa)
600
400
200
0
-200
-400
-600
-2
-1
0
1
2
Radial Location (mm)

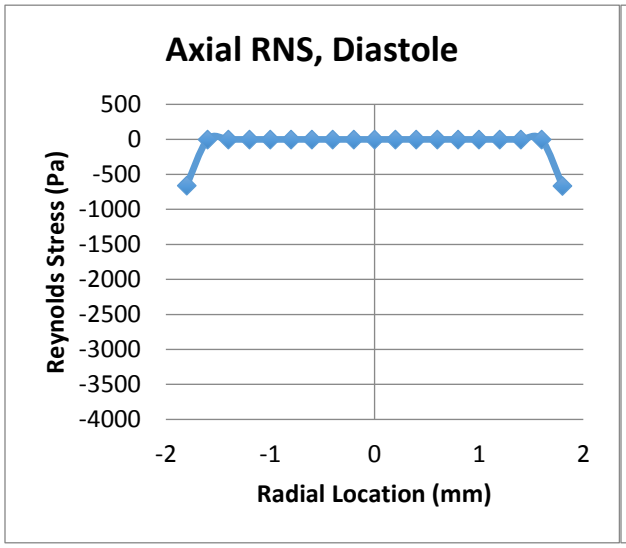
Axial RNS, Diastole
Reynolds Stress (Pa)
500
0
-500
-1000
-1500
-2000
-2500
-3000
-3500
-4000
-2
-1
0
1
2
Radial Location (mm)

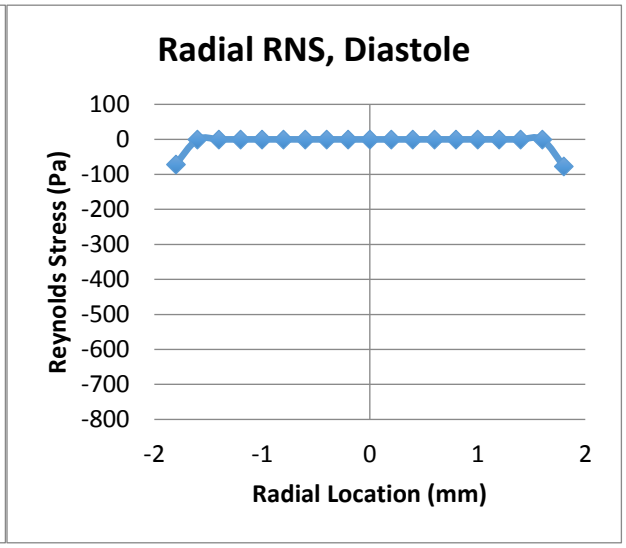
Radial RNS, Diastole
Reynolds Stress (Pa)
100
0
-100
-200
-300
-400
-500
-600
-700
-800
-2
-1
0
1
2
Radial Location (mm)

Appendix B.10 – Conical Diffuser Plane 6

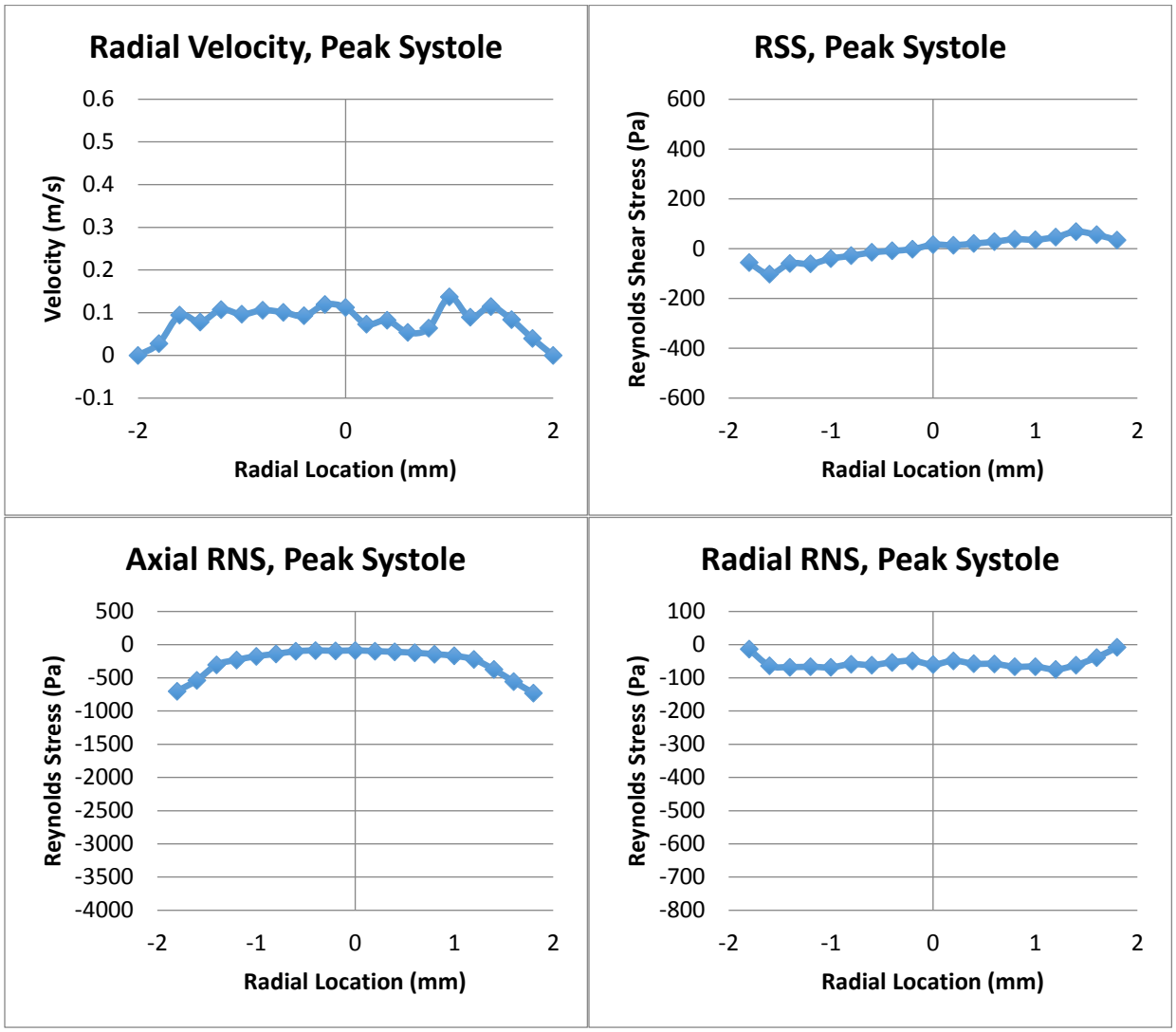

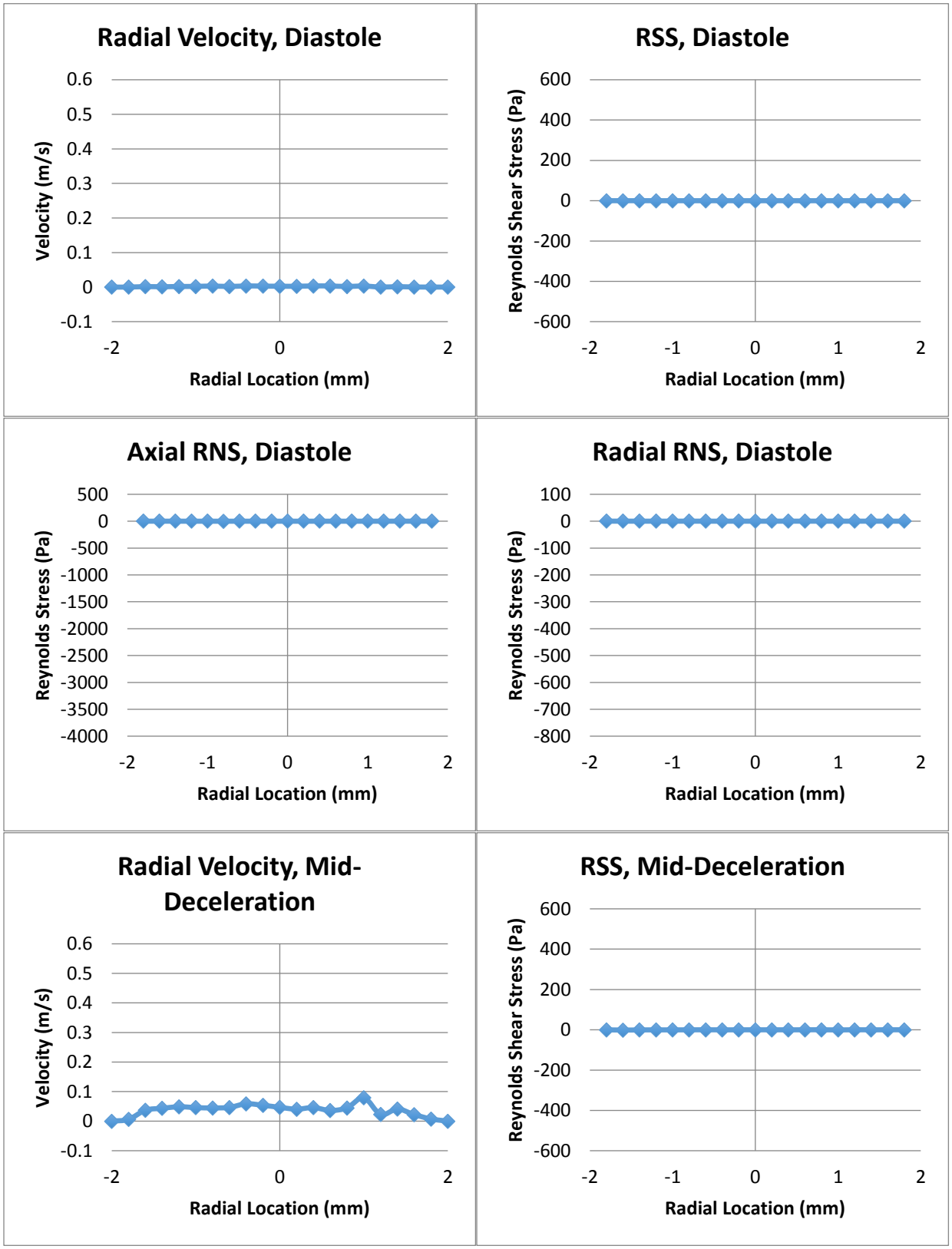
Radial Velocity, Diastole
Velocity (m/s)
0.6
0.5
0.4
0.3
0.2
0.1
0
-0.1
-2
0
2
Radial Location (mm)
RSS, Diastole
Reynolds Shear Stress (Pa)
600
400
200
0
-200
-400
-600
-2
-1
0
1
2
Radial Location (mm)
Axial RNS, Diastole
Reynolds Stress (Pa)
500
0
-500
-1000
-1500
-2000
-2500
-3000
-3500
-4000
-2
-1
0
1
2
Radial Location (mm)
Radial RNS, Diastole
Reynolds Stress (Pa)
100
0
-100
-200
-300
-400
-500
-600
-700
-800
-2
-1
0
1
2
Radial Location (mm)
Radial Velocity, Mid-Deceleration
Velocity (m/s)
0.6
0.5
0.4
0.3
0.2
0.1
0
-0.1
-2
0
2
Radial Location (mm)
RSS, Mid-Deceleration
Reynolds Shear Stress (Pa)
600
400
200
0
-200
-400
-600
-2
-1
0
1
2
Radial Location (mm)

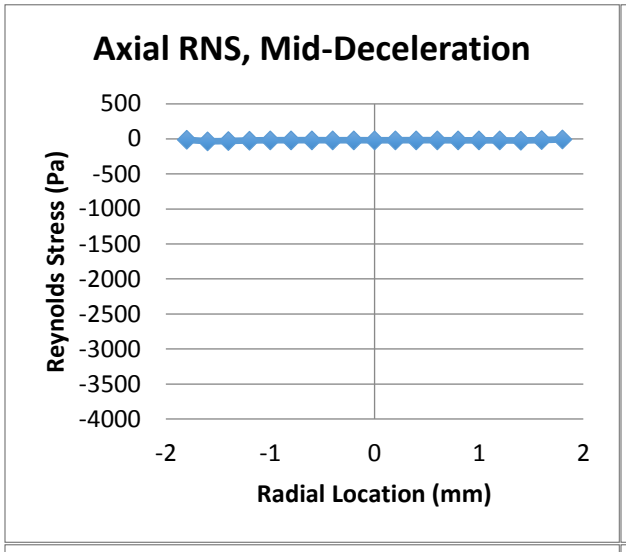
Axial RNS, Mid-Deceleration
Reynolds Stress (Pa)
500
0
-500
-1000
-1500
-2000
-2500
-3000
-3500
-4000
-2
-1
0
1
2
Radial Location (mm)

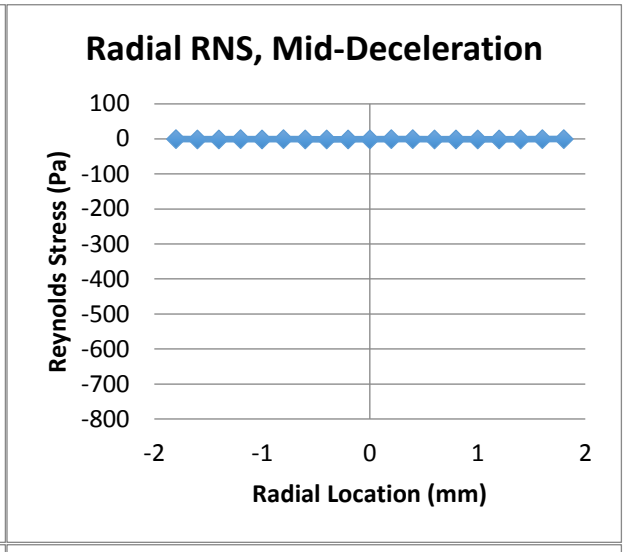
Radial RNS, Mid-Deceleration
Reynolds Stress (Pa)
100
0
-100
-200
-300
-400
-500
-600
-700
-800
-2
-1
0
1
2
Radial Location (mm)

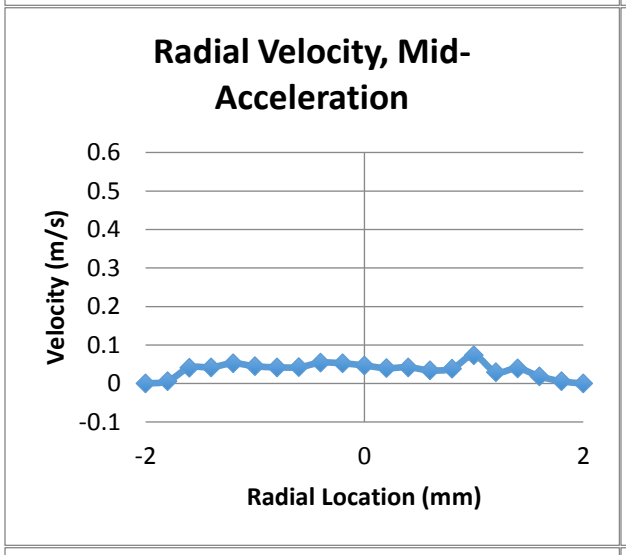
Radial Velocity, Mid-Acceleration
Velocity (m/s)
0.6
0.5
0.4
0.3
0.2
0.1
0
-0.1
-2
0
2
Radial Location (mm)

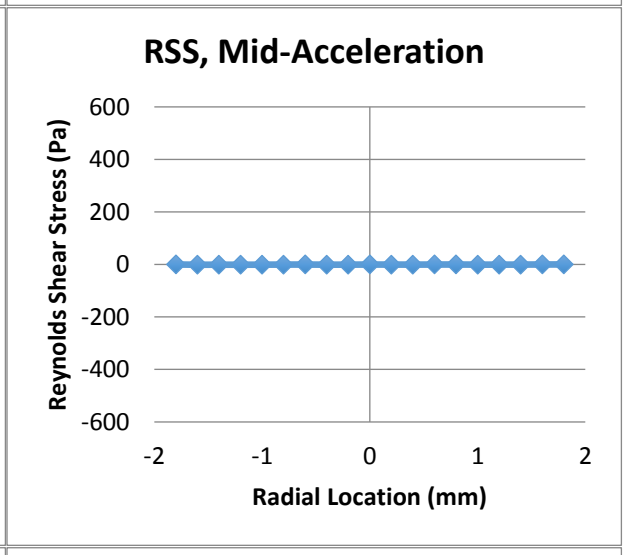
RSS, Mid-Acceleration
Reynolds Shear Stress (Pa)
600
400
200
0
-200
-400
-600
-2
-1
0
1
2
Radial Location (mm)

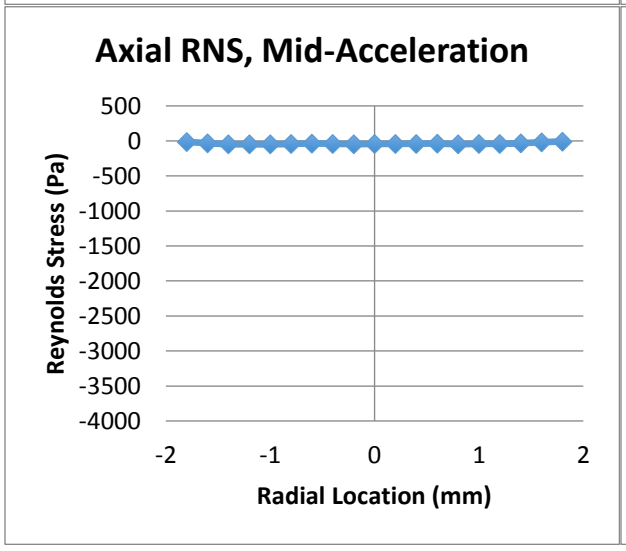
Axial RNS, Mid-Acceleration
Reynolds Stress (Pa)
500
0
-500
-1000
-1500
-2000
-2500
-3000
-3500
-4000
-2
-1
0
1
2
Radial Location (mm)

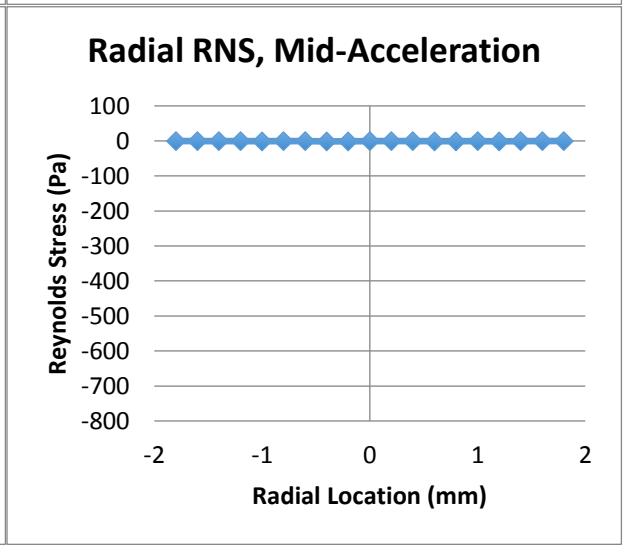
Radial RNS, Mid-Acceleration
Reynolds Stress (Pa)
100
0
-100
-200
-300
-400
-500
-600
-700
-800
-2
-1
0
1
2
Radial Location (mm)

Appendix B.11 – Conical Diffuser Plane 7

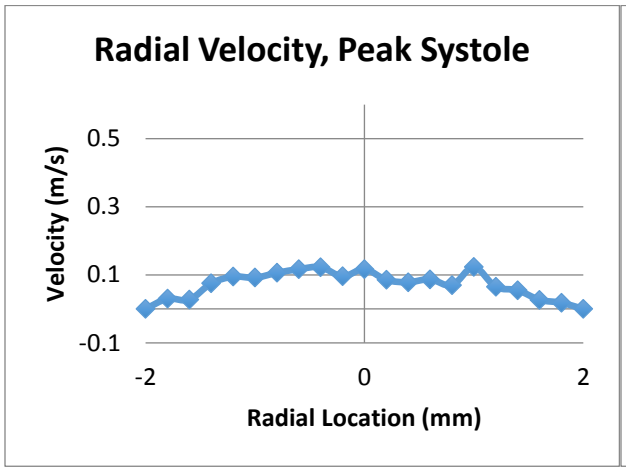

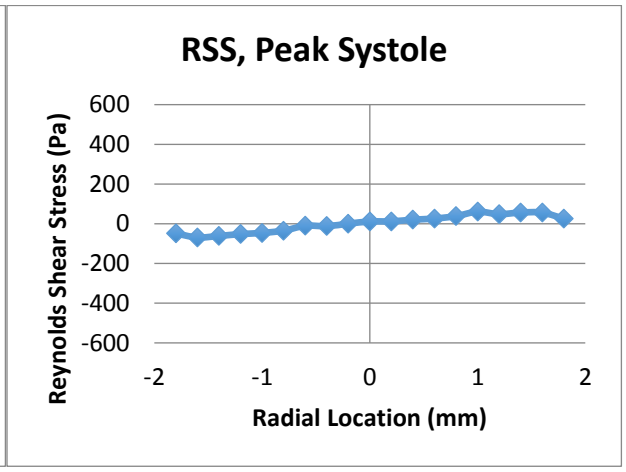

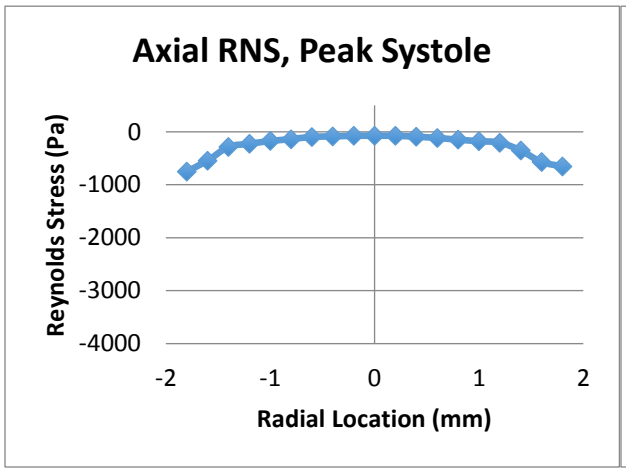

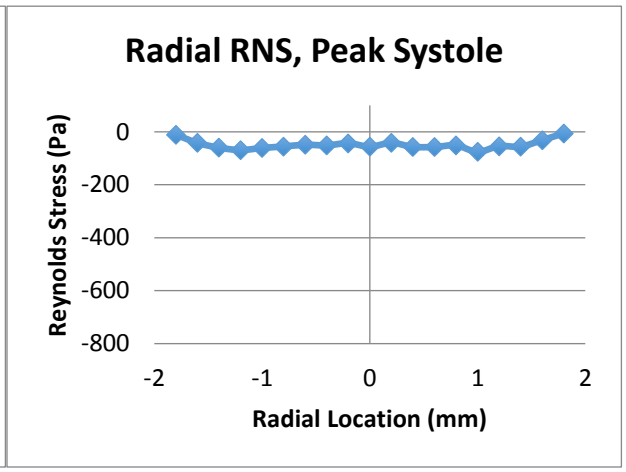

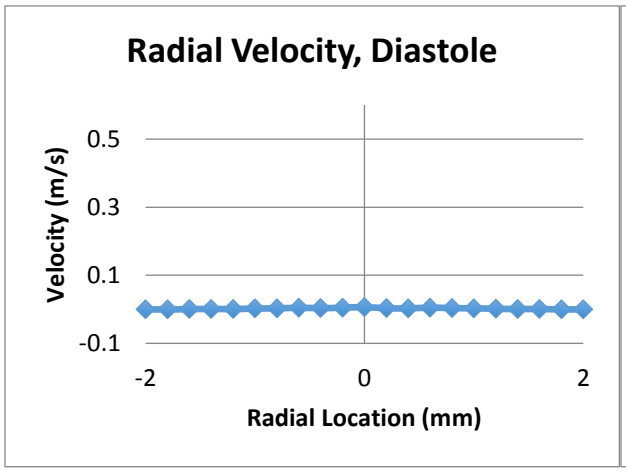

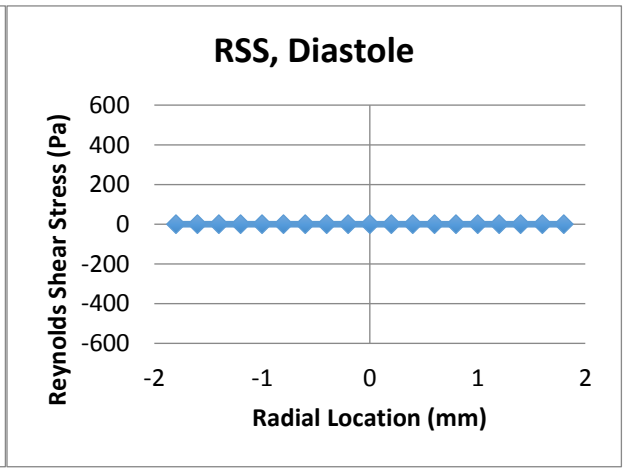

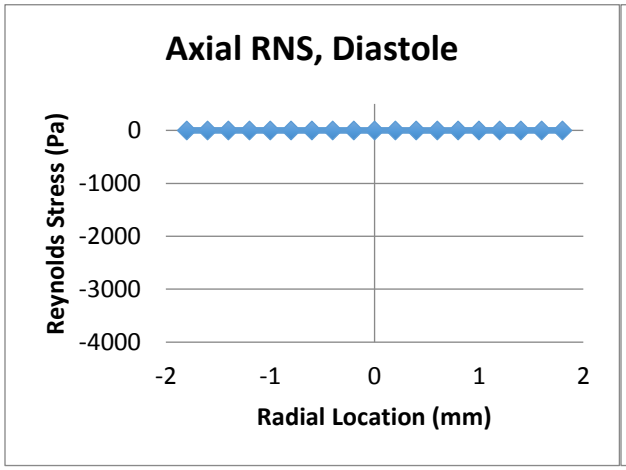
Axial RNS, Diastole
Reynolds Stress (Pa)
0
-1000
-2000
-3000
-4000
-2
-1
0
1
2
Radial Location (mm)

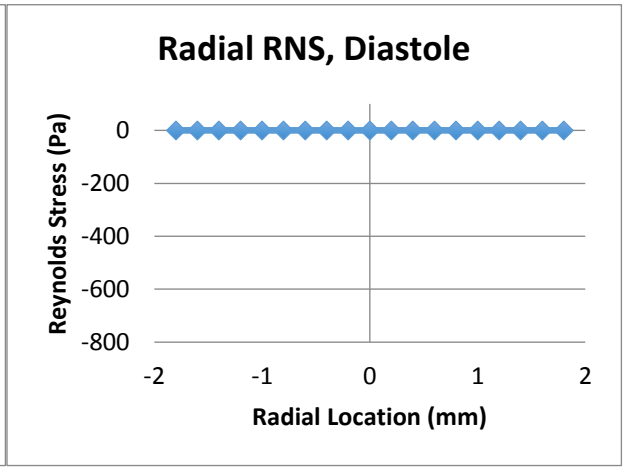
Radial RNS, Diastole
Reynolds Stress (Pa)
0
-200
-400
-600
-800
-2
-1
0
1
2
Radial Location (mm)

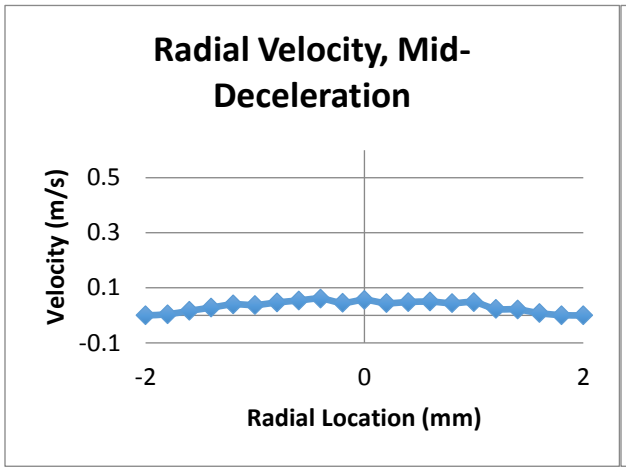
Radial Velocity, Mid-Deceleration
Velocity (m/s)
0.5
0.3
0.1
-0.1
-2
0
2
Radial Location (mm)

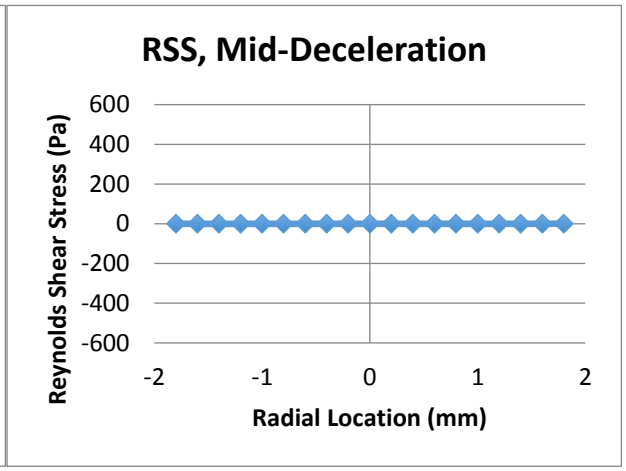
RSS, Mid-Deceleration
Reynolds Shear Stress (Pa)
600
400
200
0
-200
-400
-600
-2
-1
0
1
2
Radial Location (mm)

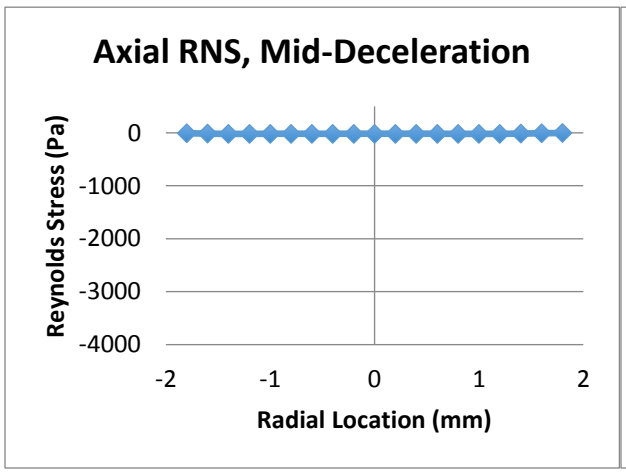
Axial RNS, Mid-Deceleration
Reynolds Stress (Pa)
0
-1000
-2000
-3000
-4000
-2
-1
0
1
2
Radial Location (mm)

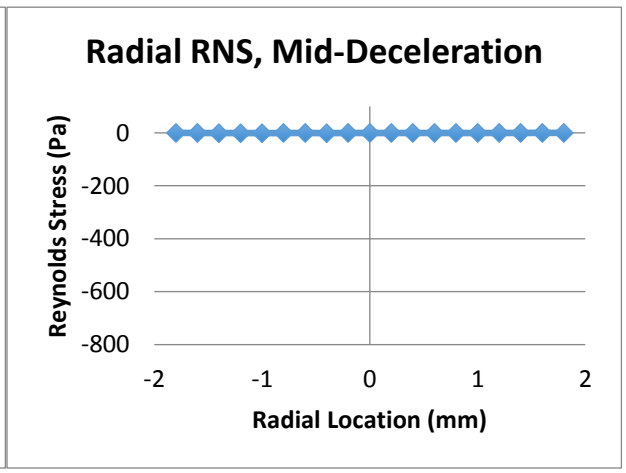
Radial RNS, Mid-Deceleration
Reynolds Stress (Pa)
0
-200
-400
-600
-800
-2
-1
0
1
2
Radial Location (mm)

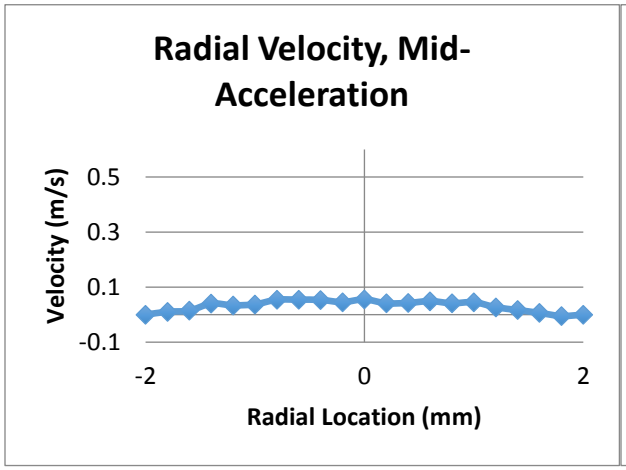
Radial Velocity, Mid-Acceleration
Velocity (m/s)
0.5
0.3
0.1
-0.1
-2
0
2
Radial Location (mm)

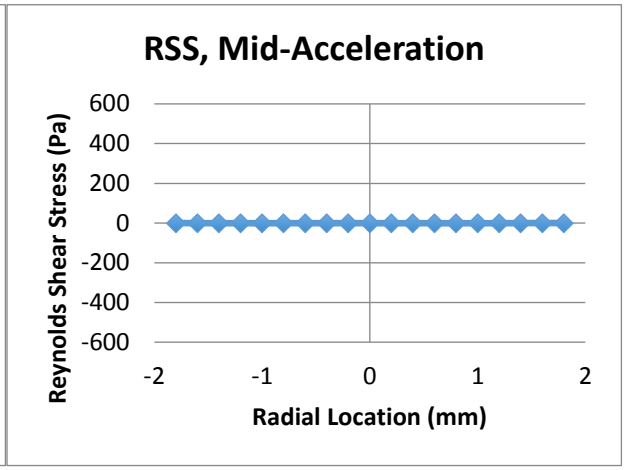
RSS, Mid-Acceleration
Reynolds Shear Stress (Pa)
600
400
200
0
-200
-400
-600
-2
-1
0
1
2
Radial Location (mm)

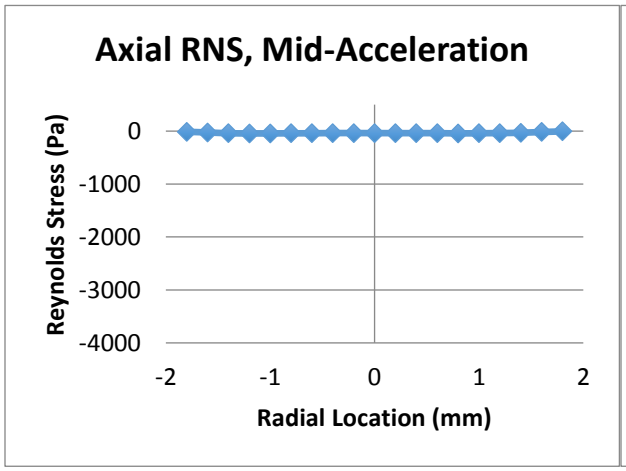
Axial RNS, Mid-Acceleration
Reynolds Stress (Pa)
0
-1000
-2000
-3000
-4000
-2
-1
0
1
2
Radial Location (mm)

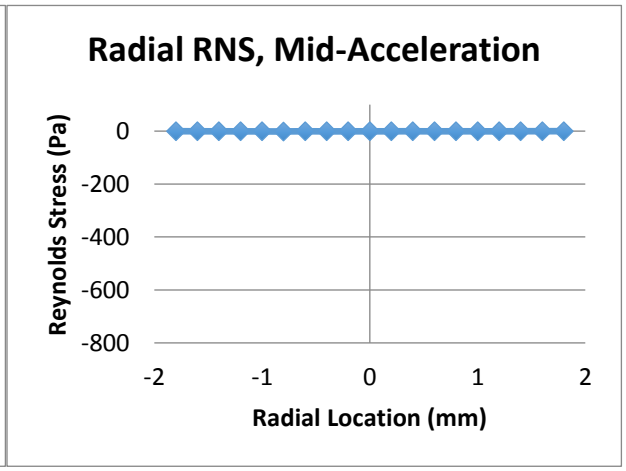
Radial RNS, Mid-Acceleration
Reynolds Stress (Pa)
0
-200
-400
-600
-800
-2
-1
0
1
2
Radial Location (mm)

Appendix B.12 – Conical Diffuser Plane 8

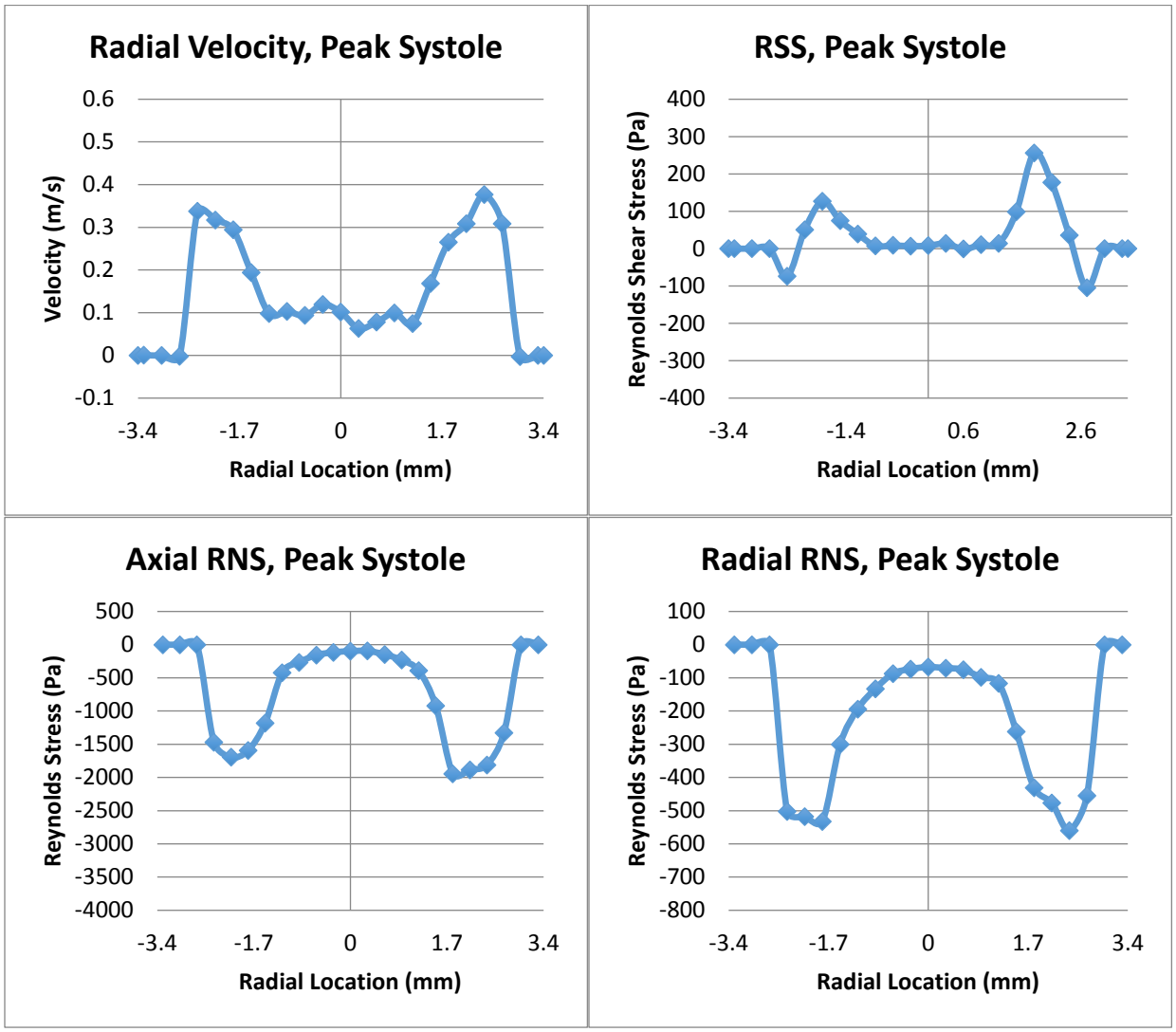

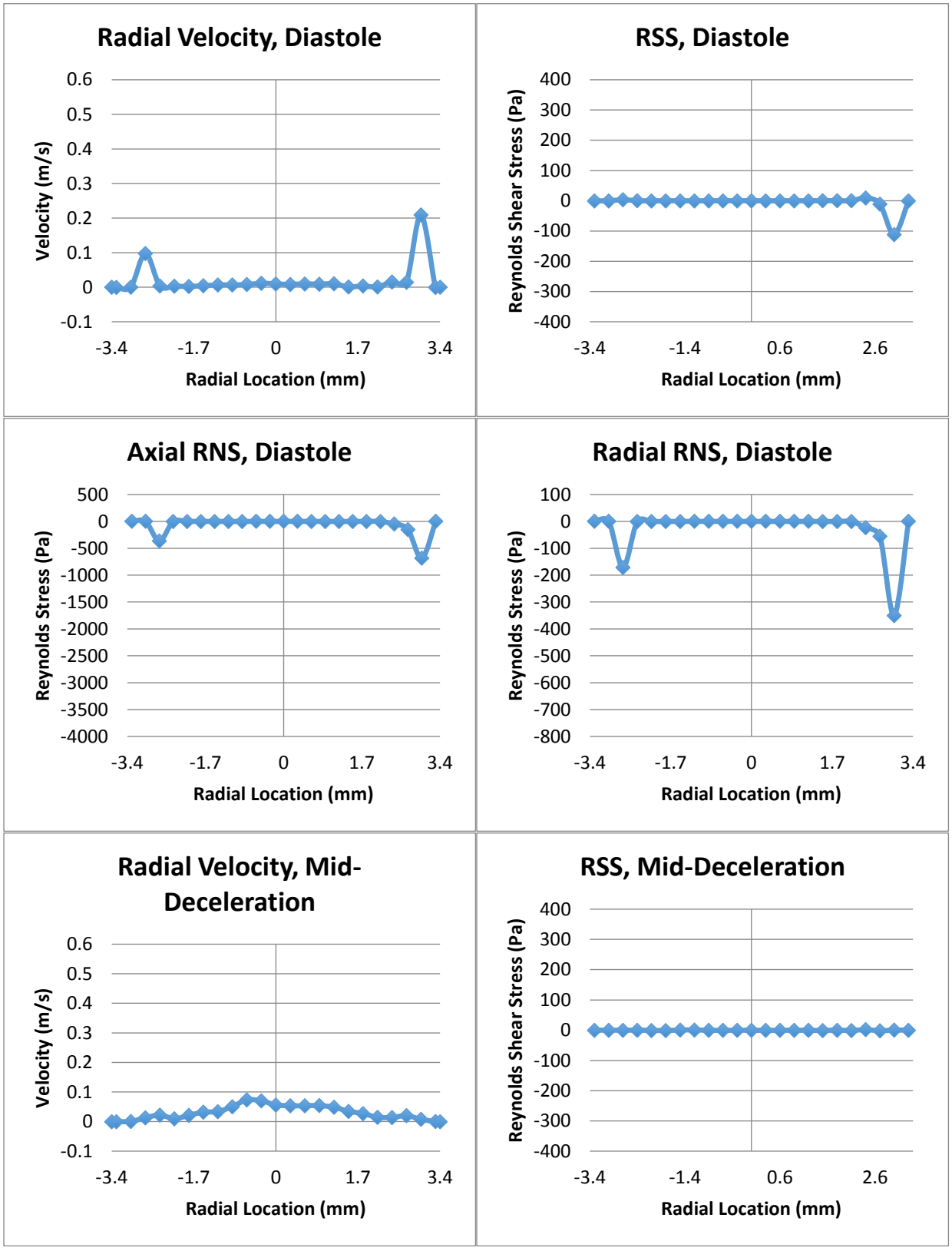
Radial Velocity, Diastole
Velocity (m/s)
0.6
0.5
0.4
0.3
0.2
0.1
0
-0.1
-3.4
-1.7
0
1.7
3.4
Radial Location (mm)
RSS, Diastole
Reynolds Shear Stress (Pa)
400
300
200
100
0
-100
-200
-300
-400
-3.4
-1.4
0.6
2.6
Radial Location (mm)
Axial RNS, Diastole
Reynolds Stress (Pa)
500
0
-500
-1000
-1500
-2000
-2500
-3000
-3500
-4000
-3.4
-1.7
0
1.7
3.4
Radial Location (mm)
Radial RNS, Diastole
Reynolds Stress (Pa)
100
0
-100
-200
-300
-400
-500
-600
-700
-800
-3.4
-1.7
0
1.7
3.4
Radial Location (mm)
Radial Velocity, Mid-Deceleration
Velocity (m/s)
0.6
0.5
0.4
0.3
0.2
0.1
0
-0.1
-3.4
-1.7
0
1.7
3.4
Radial Location (mm)
RSS, Mid-Deceleration
Reynolds Shear Stress (Pa)
400
300
200
100
0
-100
-200
-300
-400
-3.4
-1.4
0.6
2.6
Radial Location (mm)

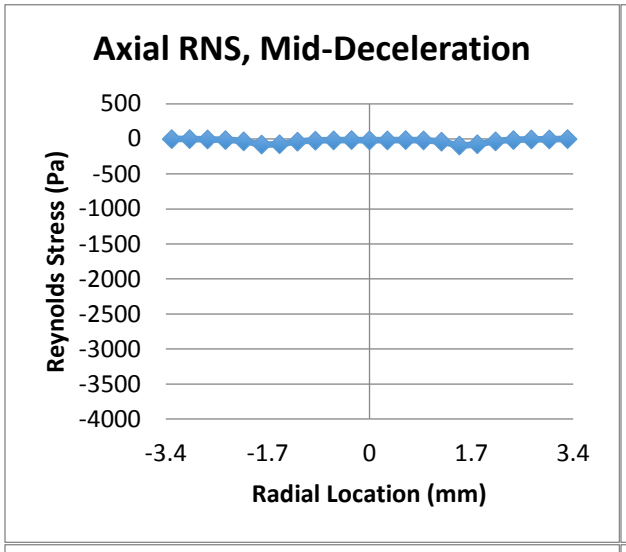
Axial RNS, Mid-Deceleration
Reynolds Stress (Pa)
500
0
-500
-1000
-1500
-2000
-2500
-3000
-3500
-4000
-3.4
-1.7
0
1.7
3.4
Radial Location (mm)

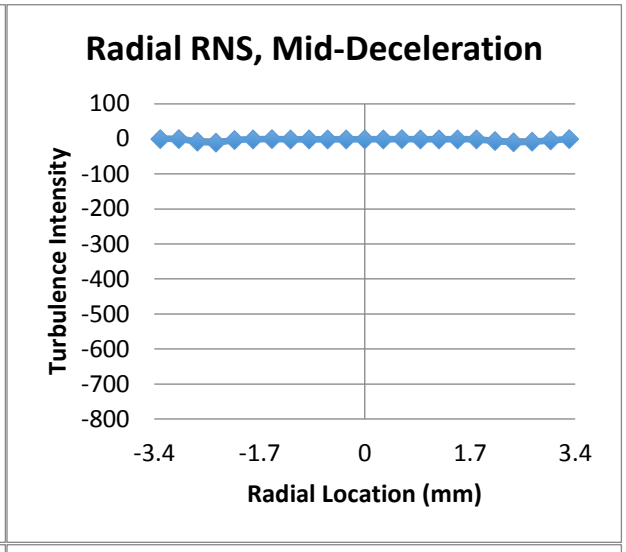
Radial RNS, Mid-Deceleration
Turbulence Intensity
100
0
-100
-200
-300
-400
-500
-600
-700
-800
-3.4
-1.7
0
1.7
3.4
Radial Location (mm)

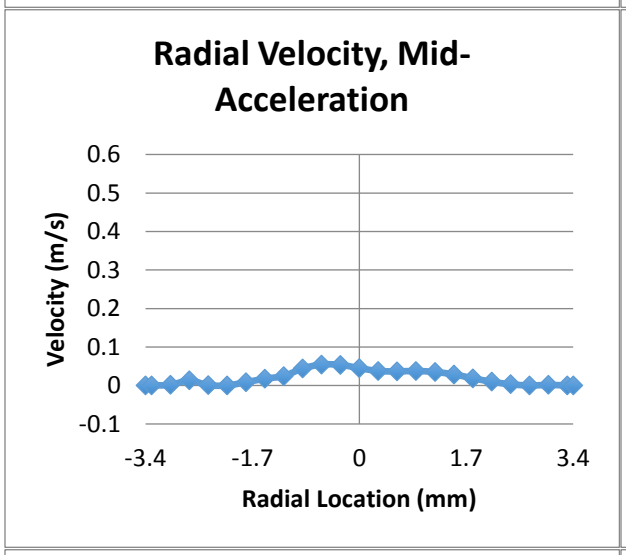
Radial Velocity, Mid-Acceleration
Velocity (m/s)
0.6
0.5
0.4
0.3
0.2
0.1
0
-0.1
-3.4
-1.7
0
1.7
3.4
Radial Location (mm)

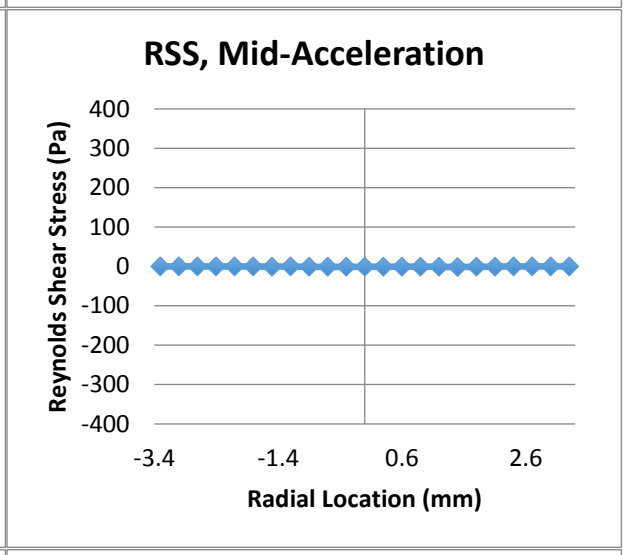
RSS, Mid-Acceleration
Reynolds Shear Stress (Pa)
400
300
200
100
0
-100
-200
-300
-400
-3.4
-1.4
0.6
2.6
Radial Location (mm)

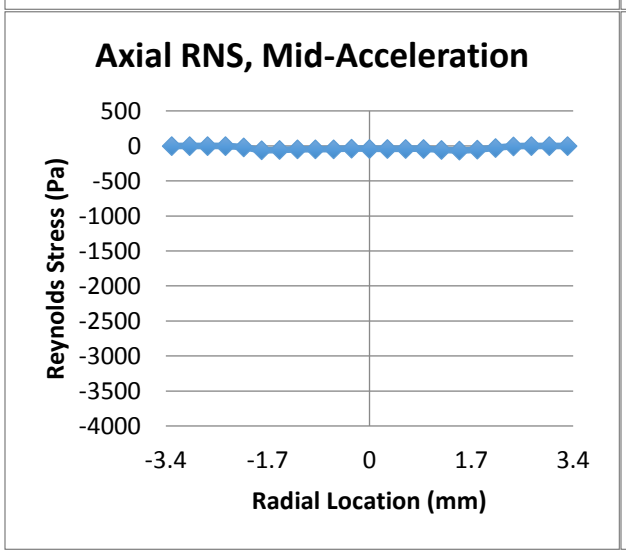
Axial RNS, Mid-Acceleration
Reynolds Stress (Pa)
500
0
-500
-1000
-1500
-2000
-2500
-3000
-3500
-4000
-3.4
-1.7
0
1.7
3.4
Radial Location (mm)

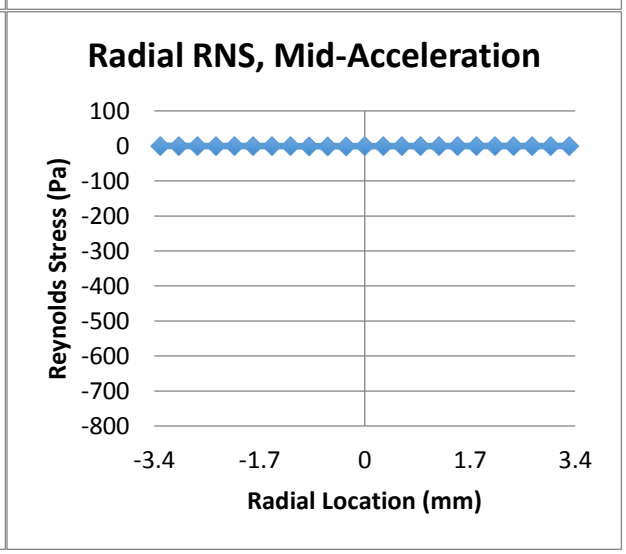
Radial RNS, Mid-Acceleration
Reynolds Stress (Pa)
100
0
-100
-200
-300
-400
-500
-600
-700
-800
-3.4
-1.7
0
1.7
3.4
Radial Location (mm)

Appendix B.13 – Conical Diffuser Plane 9

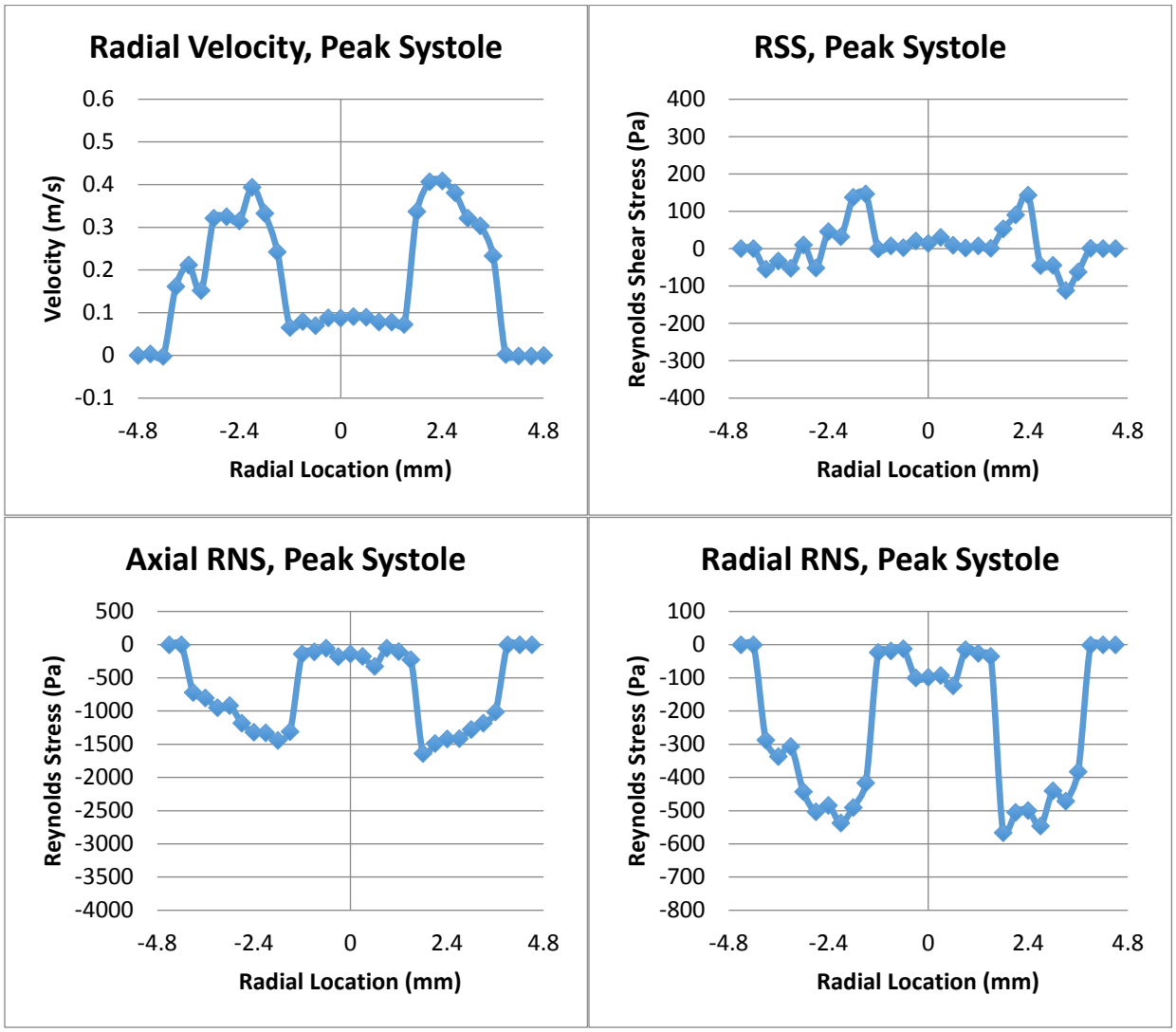

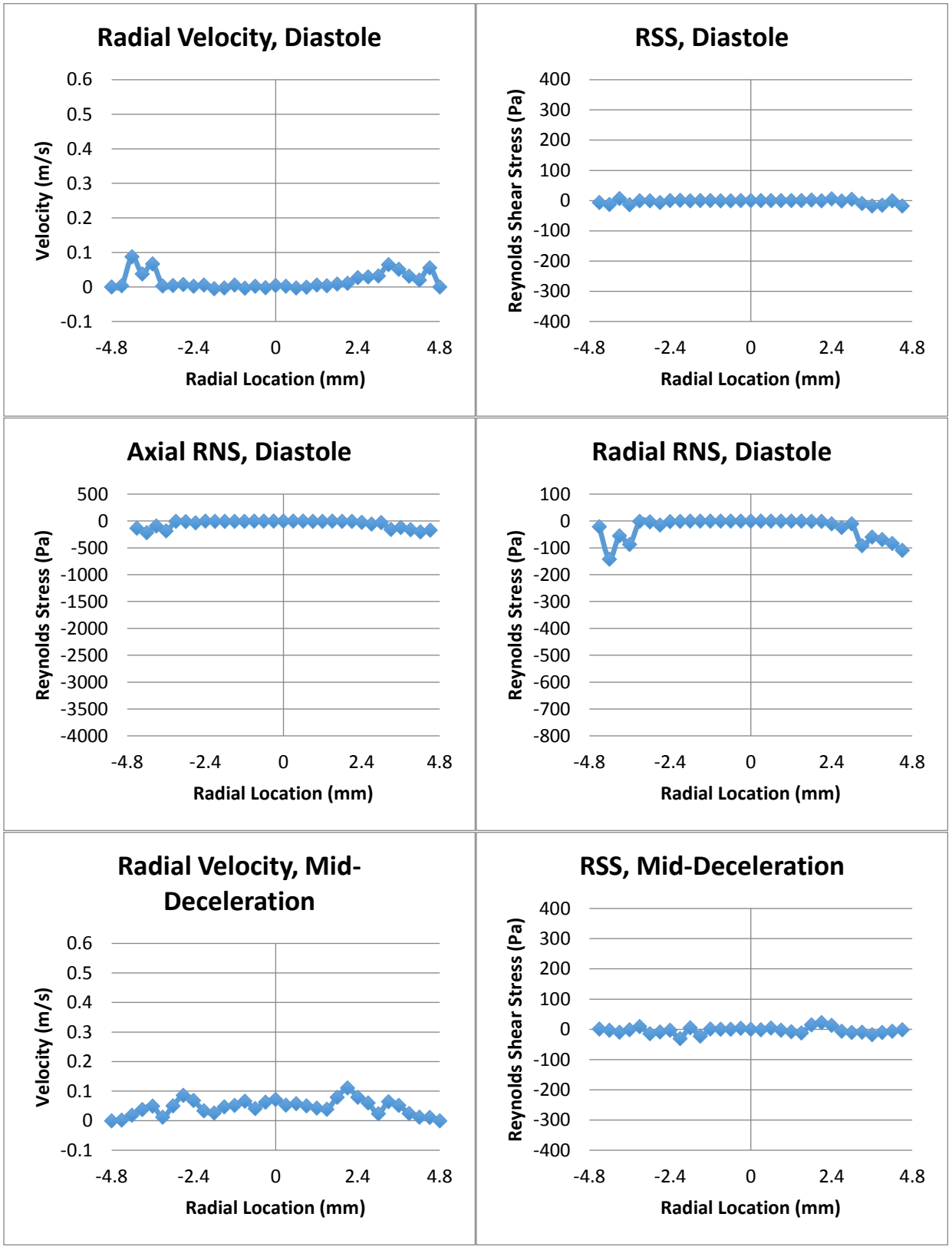
Radial Velocity, Diastole
Velocity (m/s)
0.6
0.5
0.4
0.3
0.2
0.1
0
-0.1
-4.8
-2.4
0
2.4
4.8
Radial Location (mm)
RSS, Diastole
Reynolds Shear Stress (Pa)
400
300
200
100
0
-100
-200
-300
-400
-4.8
-2.4
0
2.4
4.8
Radial Location (mm)
Axial RNS, Diastole
Reynolds Stress (Pa)
500
0
-500
-1000
-1500
-2000
-2500
-3000
-3500
-4000
-4.8
-2.4
0
2.4
4.8
Radial Location (mm)
Radial RNS, Diastole
Reynolds Stress (Pa)
100
0
-100
-200
-300
-400
-500
-600
-700
-800
-4.8
-2.4
0
2.4
4.8
Radial Location (mm)
Radial Velocity, Mid-Deceleration
Velocity (m/s)
0.6
0.5
0.4
0.3
0.2
0.1
0
-0.1
-4.8
-2.4
0
2.4
4.8
Radial Location (mm)
RSS, Mid-Deceleration
Reynolds Shear Stress (Pa)
400
300
200
100
0
-100
-200
-300
-400
-4.8
-2.4
0
2.4
4.8
Radial Location (mm)

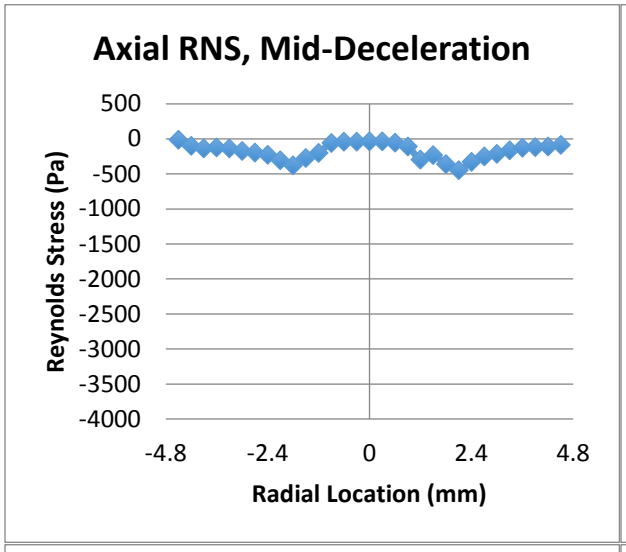
Axial RNS, Mid-Deceleration
Reynolds Stress (Pa)
500
0
-500
-1000
-1500
-2000
-2500
-3000
-3500
-4000
-4.8
-2.4
0
2.4
4.8
Radial Location (mm)

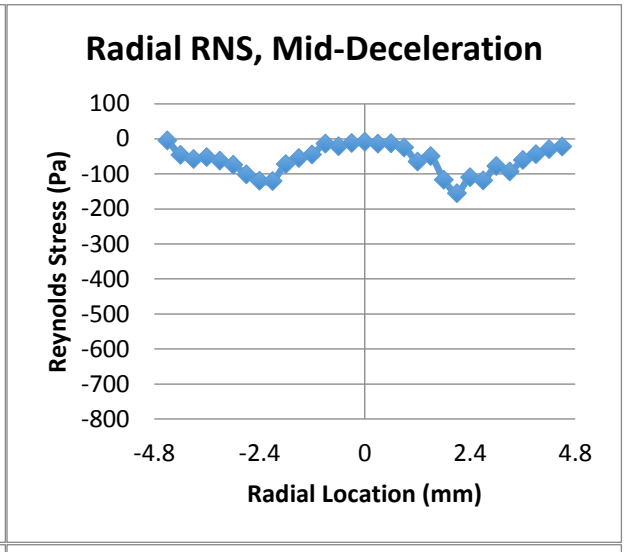
Radial RNS, Mid-Deceleration
Reynolds Stress (Pa)
100
0
-100
-200
-300
-400
-500
-600
-700
-800
-4.8
-2.4
0
2.4
4.8
Radial Location (mm)

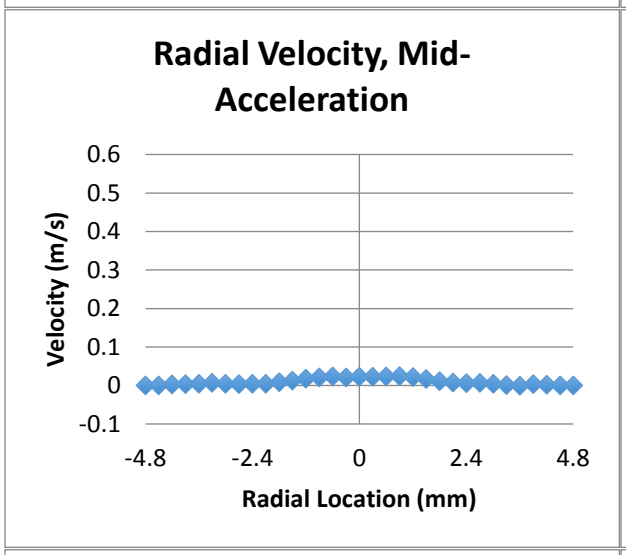
Radial Velocity, Mid-Acceleration
Velocity (m/s)
0.6
0.5
0.4
0.3
0.2
0.1
0
-0.1
-4.8
-2.4
0
2.4
4.8
Radial Location (mm)

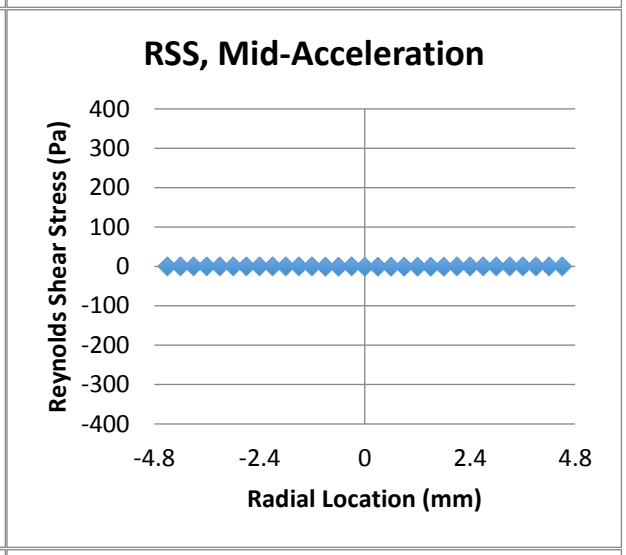
RSS, Mid-Acceleration
Reynolds Shear Stress (Pa)
400
300
200
100
0
-100
-200
-300
-400
-4.8
-2.4
0
2.4
4.8
Radial Location (mm)

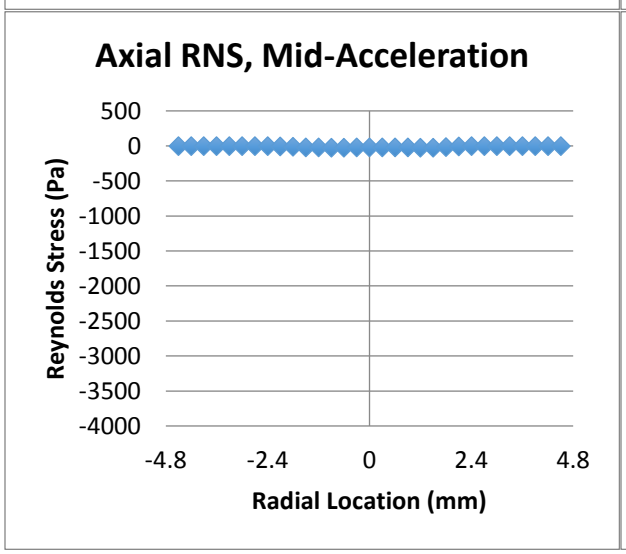
Axial RNS, Mid-Acceleration
Reynolds Stress (Pa)
500
0
-500
-1000
-1500
-2000
-2500
-3000
-3500
-4000
-4.8
-2.4
0
2.4
4.8
Radial Location (mm)

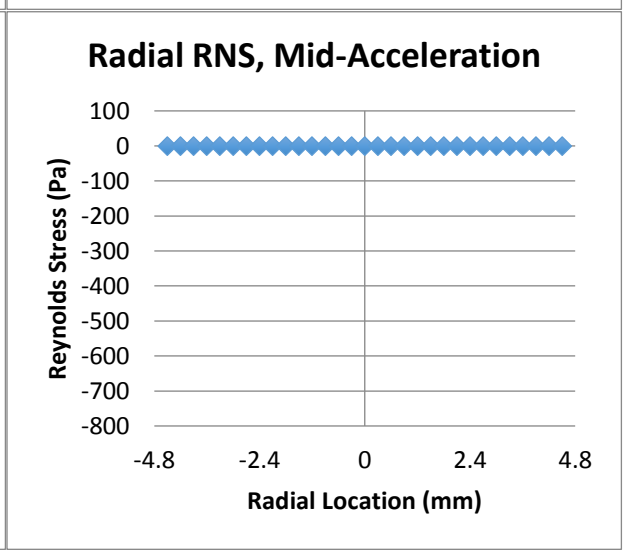
Radial RNS, Mid-Acceleration
Reynolds Stress (Pa)
100
0
-100
-200
-300
-400
-500
-600
-700
-800
-4.8
-2.4
0
2.4
4.8
Radial Location (mm)

Appendix B.14 – Conical Diffuser Plane 10

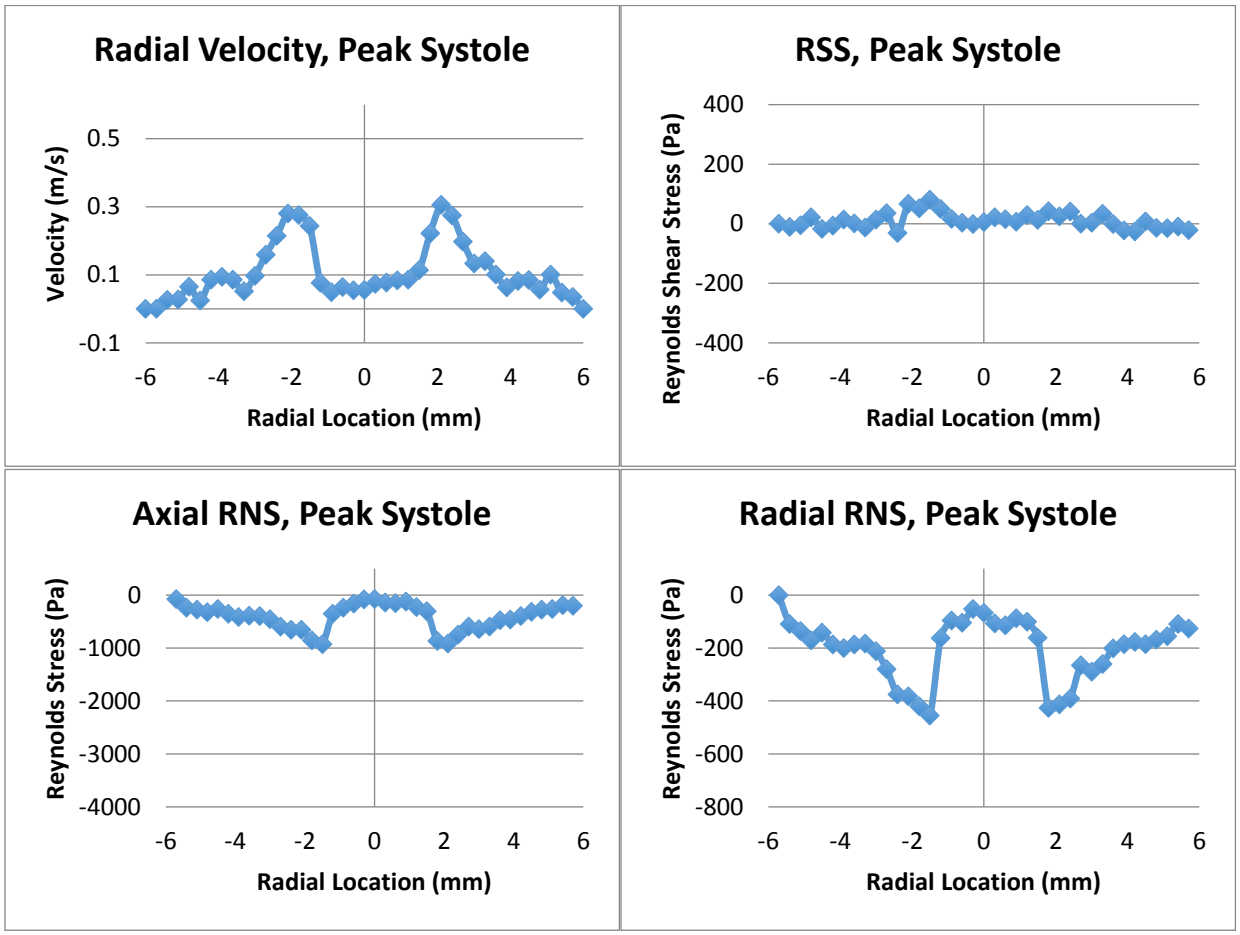

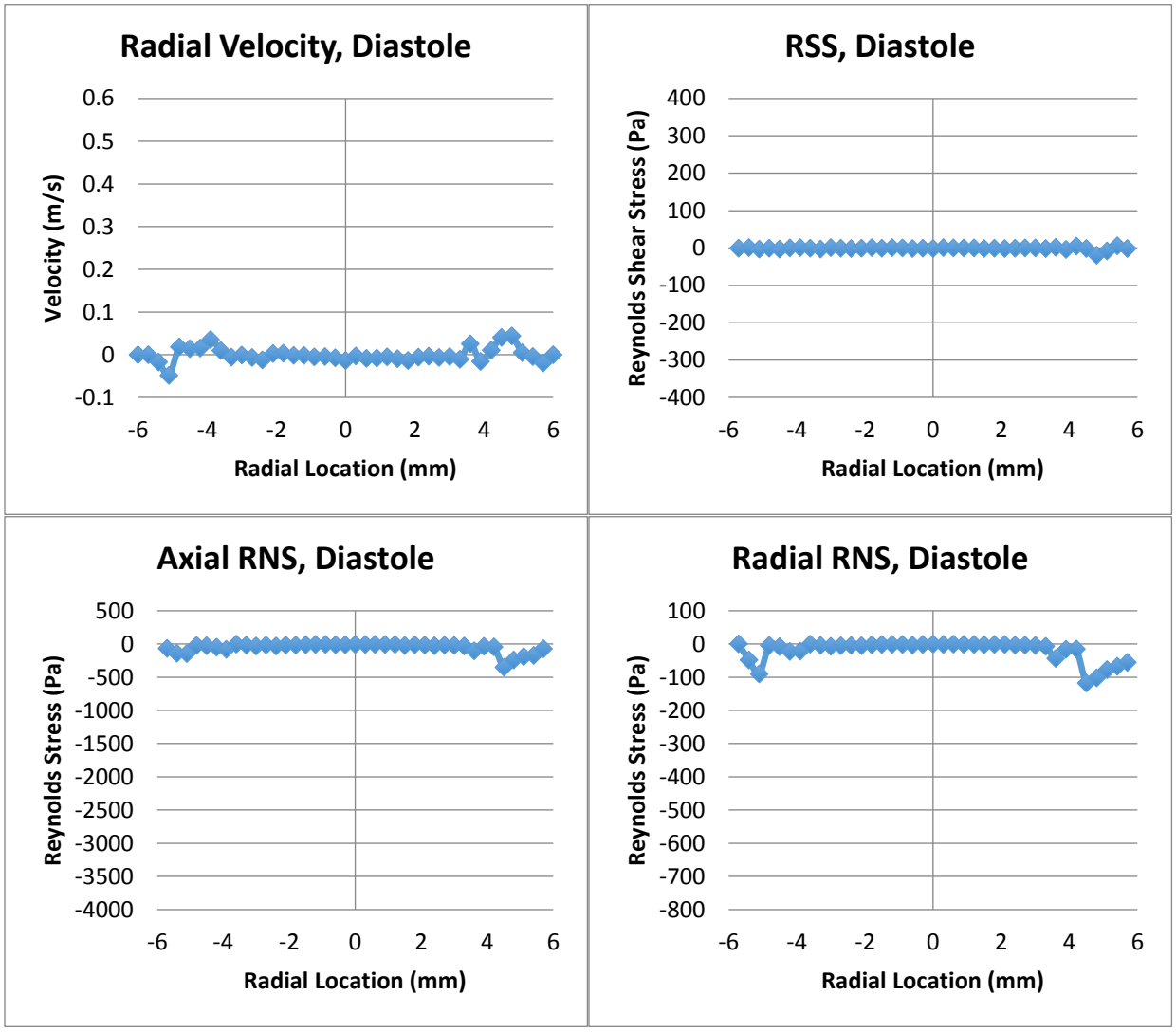
Radial Velocity, Diastole
Velocity (m/s)
0.6
0.5
0.4
0.3
0.2
0.1
0
-0.1
-6 -4 -2 0 2 4 6
Radial Location (mm)
RSS, Diastole
Reynolds Shear Stress (Pa)
400
300
200
100
0
-100
-200
-300
-400
-6 -4 -2 0 2 4 6
Radial Location (mm)
Axial RNS, Diastole
Reynolds Stress (Pa)
500
0
-500
-1000
-1500
-2000
-2500
-3000
-3500
-4000
-6 -4 -2 0 2 4 6
Radial Location (mm)
Radial RNS, Diastole
Reynolds Stress (Pa)
100
0
-100
-200
-300
-400
-500
-600
-700
-800
-6 -4 -2 0 2 4 6
Radial Location (mm)

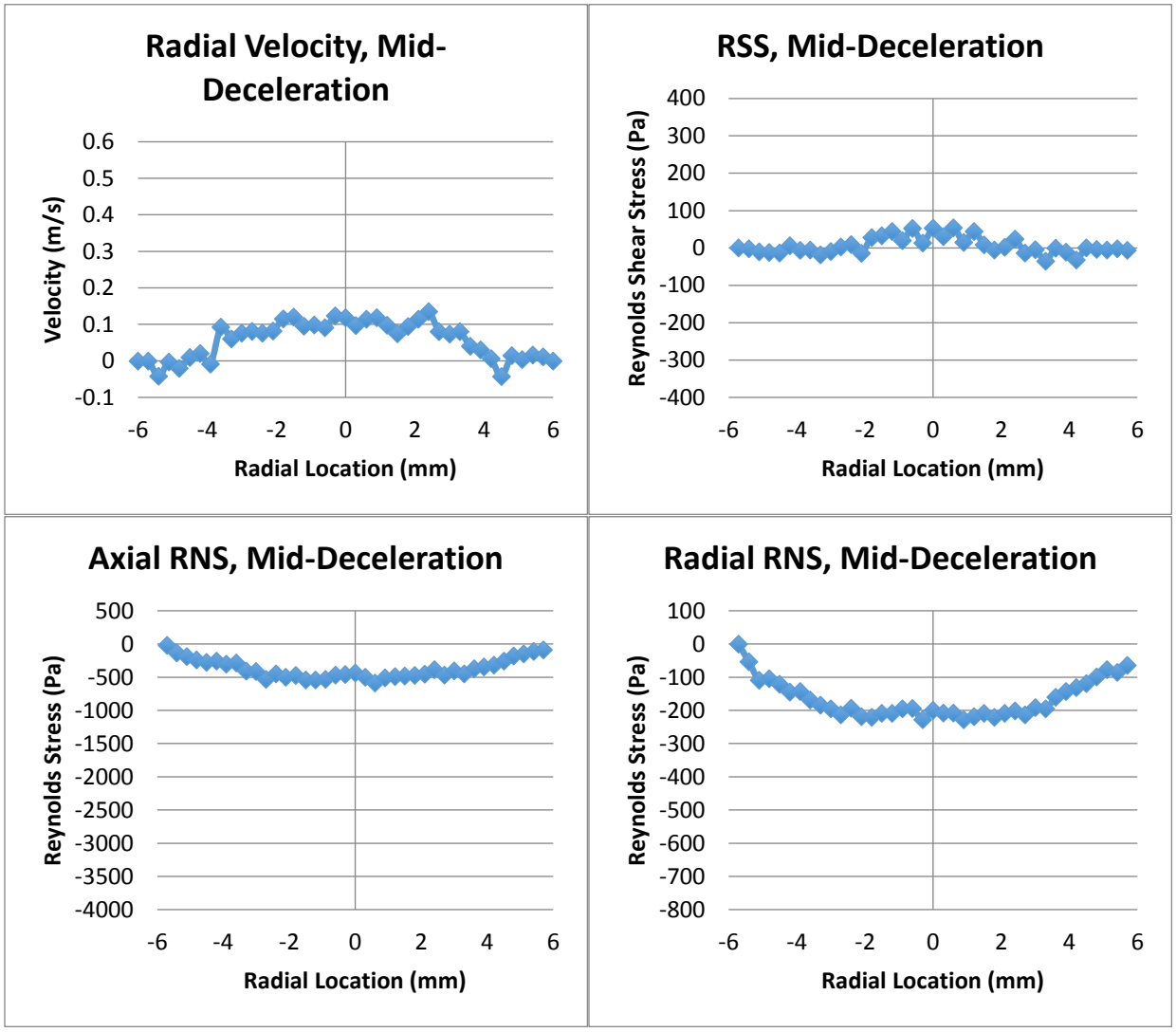
Radial Velocity, Mid-Deceleration
Velocity (m/s)
0.6
0.5
0.4
0.3
0.2
0.1
0
-0.1
-6 -4 -2 0 2 4 6
Radial Location (mm)
RSS, Mid-Deceleration
Reynolds Shear Stress (Pa)
400
300
200
100
0
-100
-200
-300
-400
-6 -4 -2 0 2 4 6
Radial Location (mm)
Axial RNS, Mid-Deceleration
Reynolds Stress (Pa)
500
0
-500
-1000
-1500
-2000
-2500
-3000
-3500
-4000
-6 -4 -2 0 2 4 6
Radial Location (mm)
Radial RNS, Mid-Deceleration
Reynolds Stress (Pa)
100
0
-100
-200
-300
-400
-500
-600
-700
-800
-6 -4 -2 0 2 4 6
Radial Location (mm)

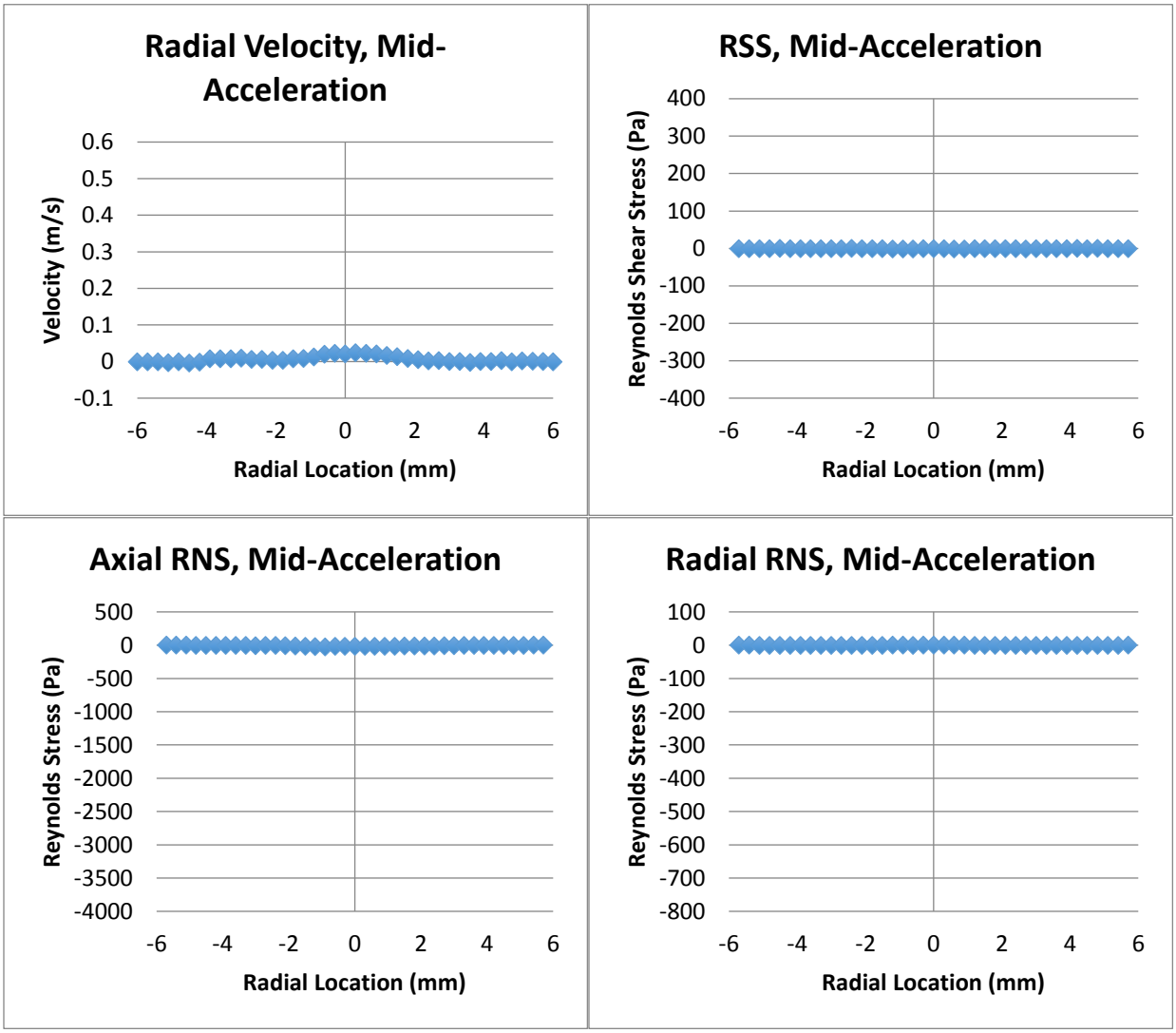
Radial Velocity, Mid-Acceleration
Velocity (m/s)
0.6
0.5
0.4
0.3
0.2
0.1
0
-0.1
-6 -4 -2 0 2 4 6
Radial Location (mm)
RSS, Mid-Acceleration
Reynolds Shear Stress (Pa)
400
300
200
100
0
-100
-200
-300
-400
-6 -4 -2 0 2 4 6
Radial Location (mm)
Axial RNS, Mid-Acceleration
Reynolds Stress (Pa)
500
0
-500
-1000
-1500
-2000
-2500
-3000
-3500
-4000
-6 -4 -2 0 2 4 6
Radial Location (mm)
Radial RNS, Mid-Acceleration
Reynolds Stress (Pa)
100
0
-100
-200
-300
-400
-500
-600
-700
-800
-6 -4 -2 0 2 4 6
Radial Location (mm)

Appendix B.15 – Conical Diffuser Plane 11

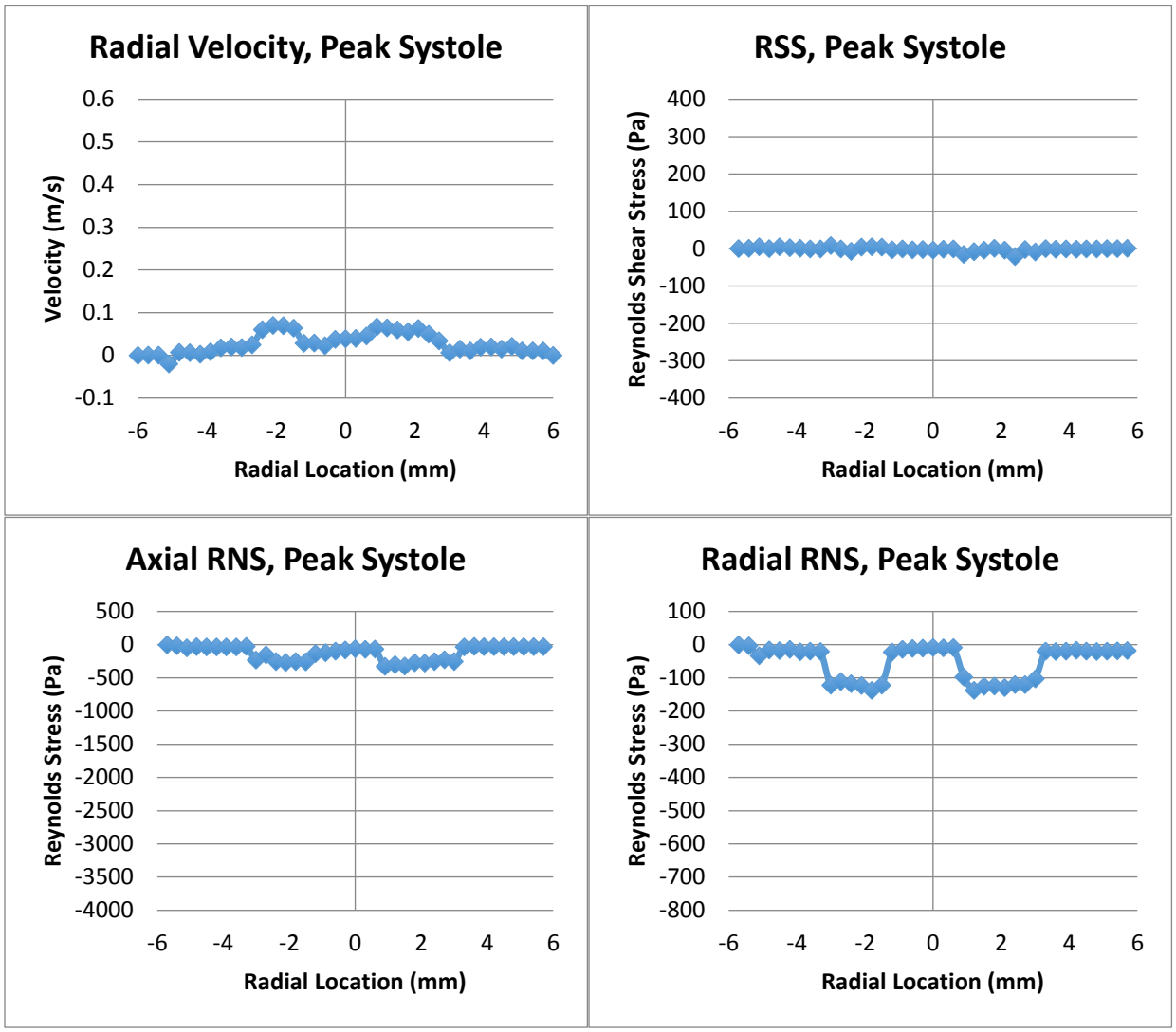

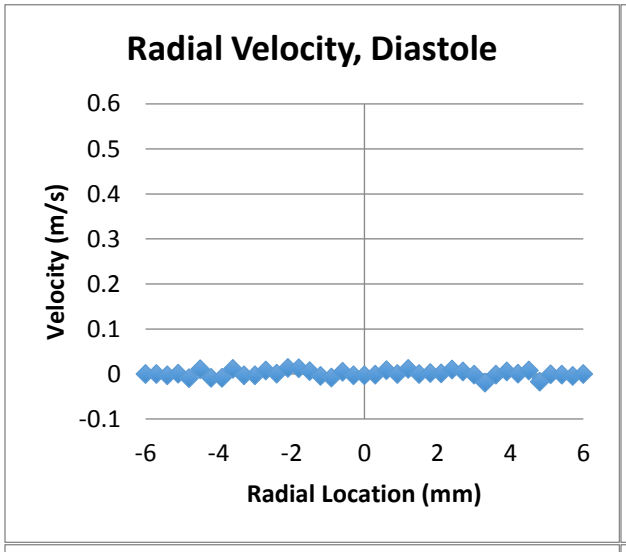
Radial Velocity, Diastole
Velocity (m/s)
0.6
0.5
0.4
0.3
0.2
0.1
0
-0.1
-6 -4 -2 0 2 4 6
Radial Location (mm)

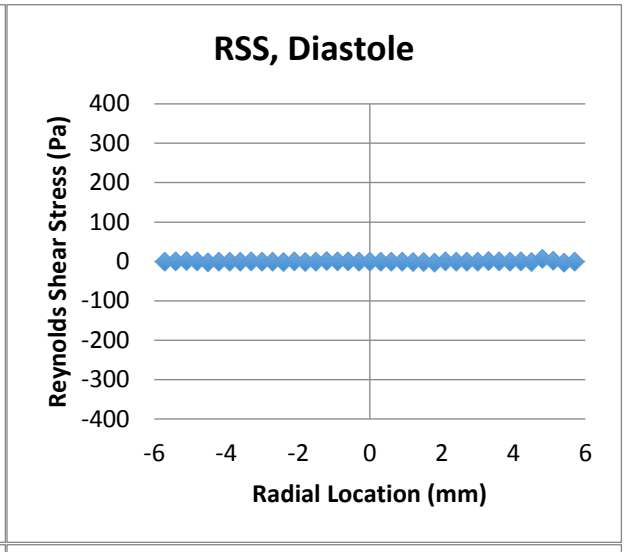
RSS, Diastole
Reynolds Shear Stress (Pa)
400
300
200
100
0
-100
-200
-300
-400
-6 -4 -2 0 2 4 6
Radial Location (mm)

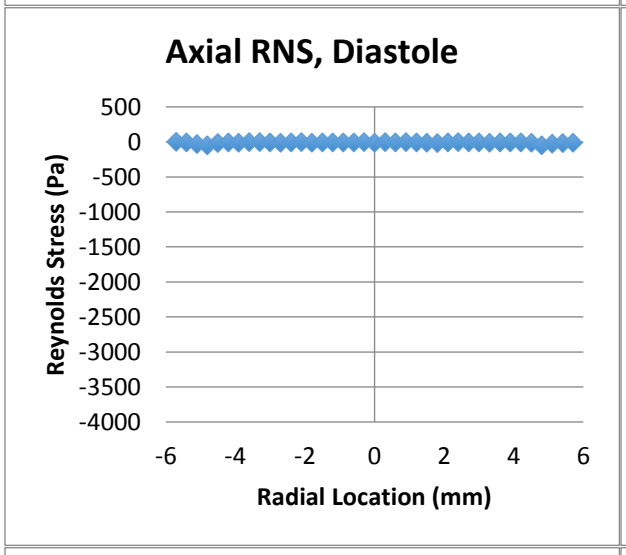
Axial RNS, Diastole
Reynolds Stress (Pa)
500
0
-500
-1000
-1500
-2000
-2500
-3000
-3500
-4000
-6 -4 -2 0 2 4 6
Radial Location (mm)

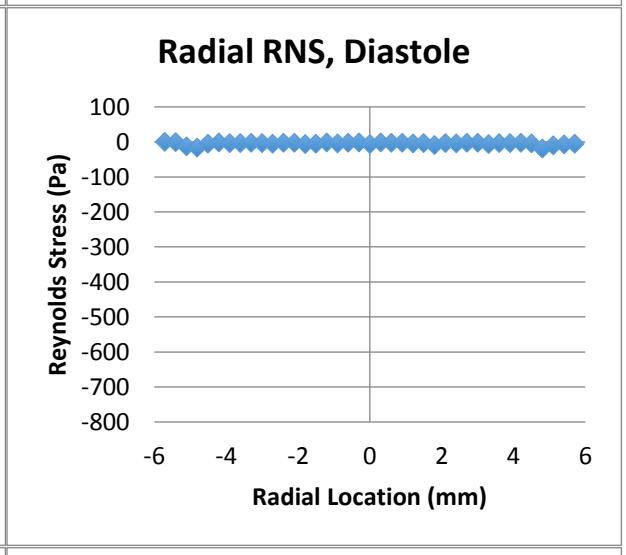
Radial RNS, Diastole
Reynolds Stress (Pa)
100
0
-100
-200
-300
-400
-500
-600
-700
-800
-6 -4 -2 0 2 4 6
Radial Location (mm)

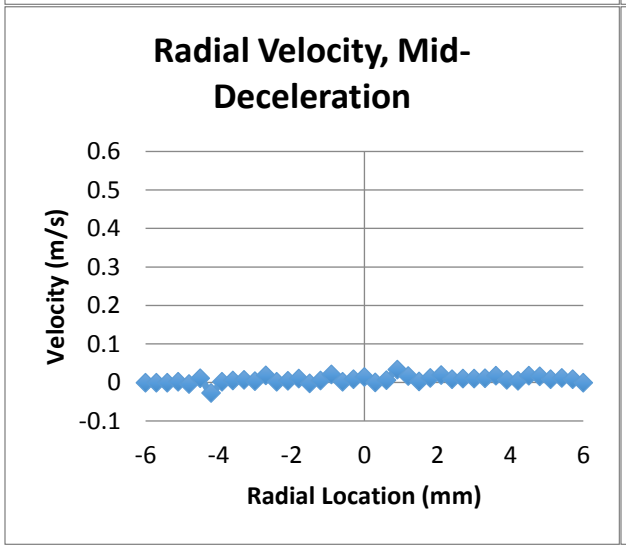
Radial Velocity, Mid-Deceleration
Velocity (m/s)
0.6
0.5
0.4
0.3
0.2
0.1
0
-0.1
-6 -4 -2 0 2 4 6
Radial Location (mm)

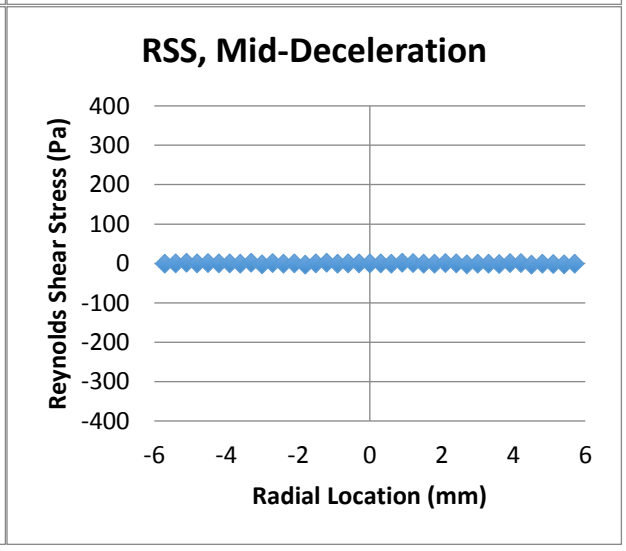
RSS, Mid-Deceleration
Reynolds Shear Stress (Pa)
400
300
200
100
0
-100
-200
-300
-400
-6 -4 -2 0 2 4 6
Radial Location (mm)

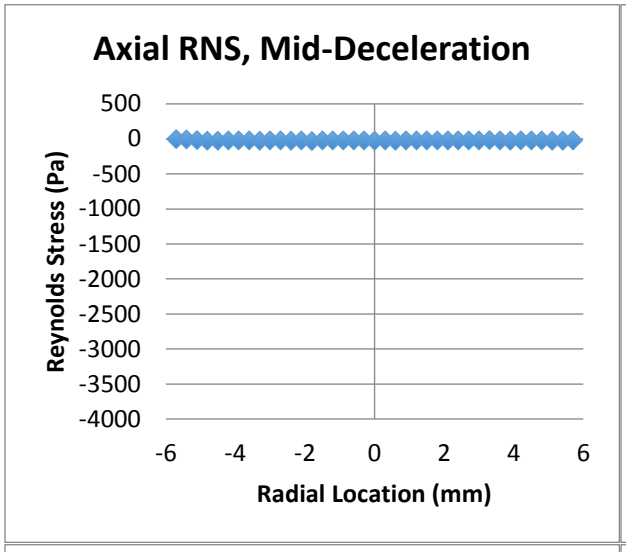
Axial RNS, Mid-Deceleration
Reynolds Stress (Pa)
500
0
-500
-1000
-1500
-2000
-2500
-3000
-3500
-4000
-6 -4 -2 0 2 4 6
Radial Location (mm)

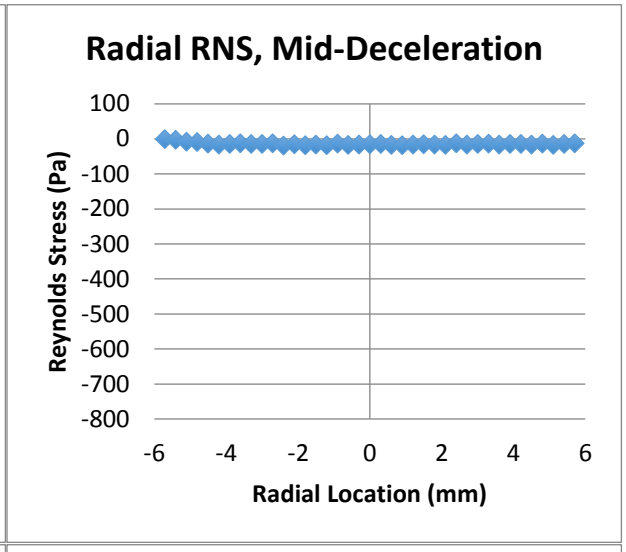
Radial RNS, Mid-Deceleration
Reynolds Stress (Pa)
100
0
-100
-200
-300
-400
-500
-600
-700
-800
-6 -4 -2 0 2 4 6
Radial Location (mm)

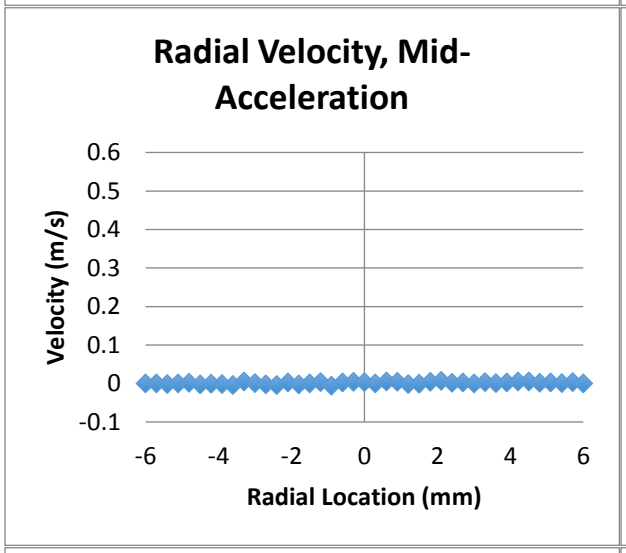
Radial Velocity, Mid-Acceleration
Velocity (m/s)
0.6
0.5
0.4
0.3
0.2
0.1
0
-0.1
-6 -4 -2 0 2 4 6
Radial Location (mm)

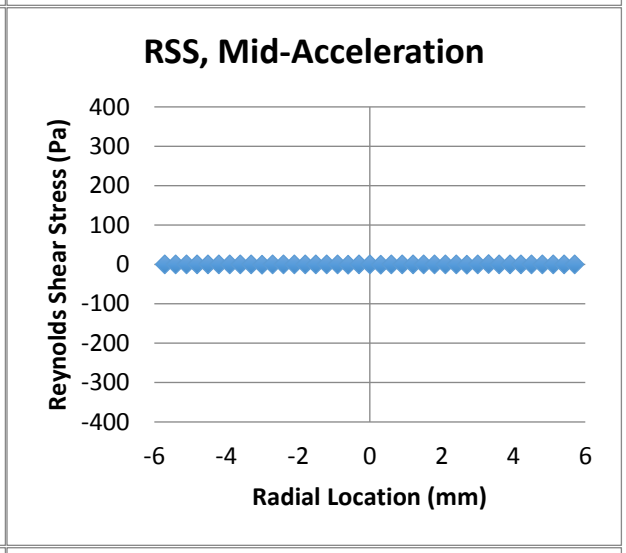
RSS, Mid-Acceleration
Reynolds Shear Stress (Pa)
400
300
200
100
0
-100
-200
-300
-400
-6 -4 -2 0 2 4 6
Radial Location (mm)

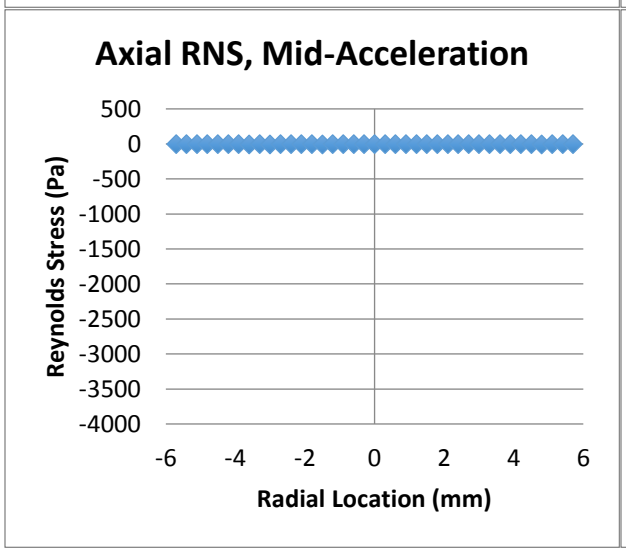
Axial RNS, Mid-Acceleration
Reynolds Stress (Pa)
500
0
-500
-1000
-1500
-2000
-2500
-3000
-3500
-4000
-6 -4 -2 0 2 4 6
Radial Location (mm)

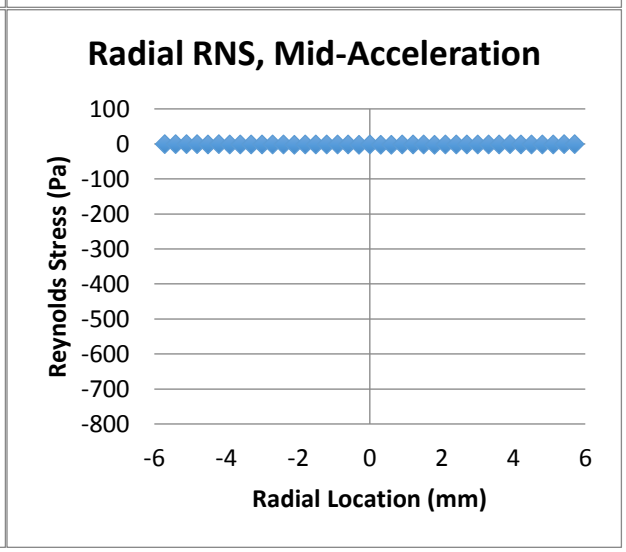
Radial RNS, Mid-Acceleration
Reynolds Stress (Pa)
100
0
-100
-200
-300
-400
-500
-600
-700
-800
-6 -4 -2 0 2 4 6
Radial Location (mm)

ACADEMIC VITA

Academic Vita of Joshua Kessler
Josh.kessler93@gmail.com

Education: The Pennsylvania State University
Major(s) and Minor(s): Biomedical Engineering and Mechanical Engineering
Honors:

Thesis Title: Fluid Dynamic Study of the FDA Benchmark Model under Pulsatile Flow
Thesis Supervisor: Keefe B. Manning

Work Experience
Summer 2015
Manufacturing Development Intern
Improved a fiber optics manufacturing process
TE Connectivity – Middletown, PA
David Skotek

Summer 2014
Product Engineering Intern
Developed a new product that prevents intravenous catheter associated infections
B. Braun Medical – Allentown, PA
Dawn Kentner

Summer 2012 – Summer 2013
Software Engineering Intern
Developed a program to remotely calibrate phones running an application called Gammapix
Image Insight – East Hartford, CT
Gordon Drukier

Grants Received:
Erickson Discovery Grant, from the Office of Undergraduate Education

Awards:
The President's Freshman Award, The President Sparks Award, the Evan Pugh Scholar Award

Professional Memberships:
Phi Kappa Phi

Publications:
Drukier, G. Kessler, J. Rubenstein, Y. and Rubenstein, E. “Crowd-Sourced Calibration of Uncontrolled Radiation Detectors.” IEEE

International Education (including service-learning abroad):
Tecnun, University of Navarra, Spain